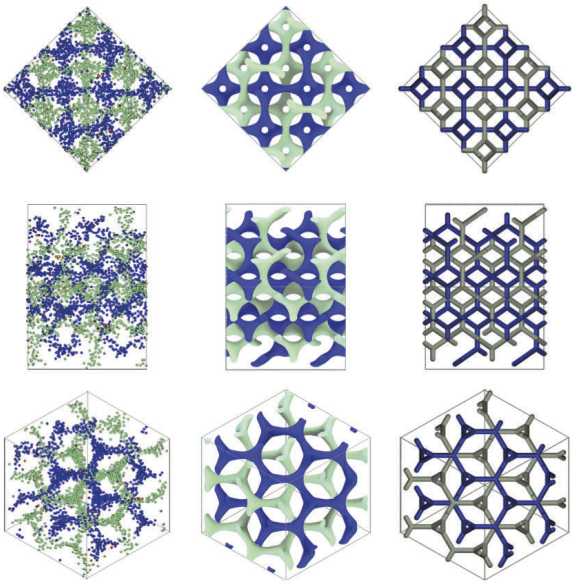

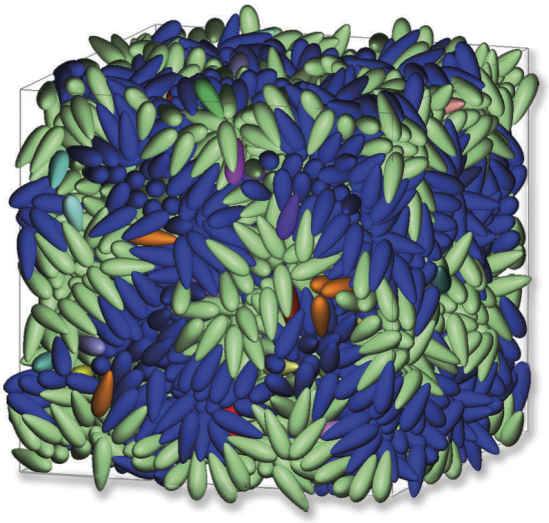

FAU Forschungen, Reihe B, Medizin, Naturwissenschaft, Technik 32

Philipp W. A. Schönhöfer

Entropically driven self-assembly of pear-shaped nanoparticles

FAU UNIVERSITY PRESS

Philipp W. A. Schönhöfer

Entropically driven self-assembly of pear-shaped nanoparticles

FAU Forschungen, Reihe B
Medizin, Naturwissenschaft, Technik
Band 32

Herausgeber der Reihe:
Wissenschaftlicher Beirat der FAU University Press

Philipp W. A. Schönhöfer

Entropically driven self-assembly of pear-shaped nanoparticles

Erlangen
FAU University Press
2019

Bibliografische Information der Deutschen Nationalbibliothek:
Die Deutsche Nationalbibliothek verzeichnet diese Publikation in der Deutschen Nationalbibliografie; detaillierte bibliografische Daten sind im Internet über http://dnb.d-nb.de abrufbar.

Bitte zitieren als
Schönhöfer, Philipp W. A. 2019. *Entropically driven self-assembly of pear-shaped nanoparticles.* FAU Forschungen, Reihe B, Medizin, Naturwissenschaft, Technik Band 32.
Erlangen: FAU University Press, DOI: 10.25593/978-3-96147-269-7.

Der vollständige Inhalt des Buchs ist als PDF über den OPUS Server der Friedrich-Alexander-Universität Erlangen-Nürnberg abrufbar:
https://opus4.kobv.de/opus4-fau/home

Verlag und Auslieferung:

FAU University Press, Universitätsstraße 4, 91054 Erlangen

Druck: docupoint GmbH

ISBN: 978-3-96147-268-0 (Druckausgabe)
eISBN: 978-3-96147-269-7 (Online-Ausgabe)
ISSN: 2198-8102
DOI: 10.25593/978-3-96147-269-7

Entropically driven self-assembly of pear-shaped nanoparticles

Entropie-dominierte Selbstorganisationsprozesse birnenförmiger Teilchensysteme

Der Naturwissenschaftlichen Fakultät
der Friedrich-Alexander-Universität
Erlangen-Nürnberg

zur

Erlangung des Doktorgrades Dr. rer. nat.

vorgelegt von

Philipp Wilhelm Albert Schönhöfer

aus Erlangen

Als Dissertation genehmigt

von der Naturwissenschaftlichen Fakultät
der Friedrich-Alexander-Universität Erlangen-Nürnberg

Tag der mündlichen Prüfung: 25. Juli 2019
Vorsitzender des Promotionsorgans: Prof. Dr. Georg Kreimer
Gutachter: Prof. Dr. Klaus Mecke
Prof. Dr. Hartmut Löwen
Prof. Dr. Peter Harrowell

Diese Arbeit ist Teil eines Cotutelle Verfahrens

zwischen der Naturwissenschaftlichen Fakultät
der Friedrich-Alexander-Universität Erlangen-Nürnberg
und der School of Engineering and Information Technology
der Murdoch University, Perth

Abstract

This thesis addresses the entropically driven colloidal self-assembly of pear-shaped particle ensembles, including the formation of nanostructures based on triply periodic minimal surfaces, in particular of the Ia$\bar{3}$d gyroid. One of the key results is that the formation of the Ia$\bar{3}$d gyroid, reported earlier in the so-called pear hard Gaussian overlap (PHGO) approximation and confirmed here, is due to a slight non-additivity of that potential; this phase does not form in pears with true hard-core potential.

First, we computationally study the PHGO system and present the phase diagram of pears with an aspect ratio of 3 in terms of global density and particle shape (degree of taper), containing gyroid, isotropic, nematic and smectic phases. We confirm that it is adequate to interpret the gyroid as a warped smectic bilayer phase. The collective behaviour to arrange into interdigitated sheets with negative Gauss curvature, from which the gyroid results, is investigated through correlations of (Set-)Voronoi cells and local curvature. This geometric arrangement within the bilayers suggests a fundamentally different stabilisation mechanism of the pear gyroid phase compared to those found in both lipid-water and di-block copolymer systems forming the Ia$\bar{3}$d gyroid.

The PHGO model is only an approximation for hard-core interactions, and we additionally investigate, by much slower simulations, pear-assemblies with true hard-core interactions (HPR). We find that HPR phase diagram only contains isotropic and nematic phases, but neither gyroid nor smectic phases. To understand this shape sensitivity more profoundly, the depletion interactions of both models are studied in two pear-shaped colloids dissolved in a hard sphere solvent. The HPR particles act as one would expect from a geometric analysis of the excluded-volume minimisation, whereas the PHGO particles show deviations from this expectation. These differences are attributed to the unusual angle dependency of the (non-additive) contact function and, more so, to small overlaps induced by the approximation.

For the PHGO model, we further demonstrate that the addition of a small concentration of hard spheres ("solvent") drives the system towards a $Pn\bar{3}m$ diamond phase. This result is explained by the greater spatial heterogeneity of the diamond geometry compared to the gyroid where additional material is needed to relieve packing frustration. In contrast to copolymer systems, however, the solvent mostly aggregates near the diamond minimal surface, driven by the non-additivity of the PHGO pears. At high solvent concentrations, the mixture phase separates into "inverse" micelle-like structures with the blunt ends at the micellar centres and thin ends pointing outwards. The micelles themselves spontaneously cluster, indicative of a hierarchical self-assembly process for bicontinuous structures.

Finally, we develop a density functional for hard solids of revolution (including pears) within the framework of fundamental measure theory. It is applied to low-density ensembles of pear-shaped particles, where we analyse their response near a hard substrate. A complex orientational ordering close to the wall is predicted, which is directly linked to the particle shape and gives insight into adsorption processes of asymmetric particles. This predicted behaviour and the differences between the PHGO and HPR model are confirmed by MC simulations.

Zusammenfassung

Diese Doktorarbeit befasst sich mit der Selbstorganisation entropisch getriebener, birnen-förmiger Kolloidteilchen. Hierbei wird besonders auf die Bildung von Nanostrukturen eingegangen, die auf dreifach-periodischen Minimalflächen und insbesondere auf der Ia$\bar{3}$d Gyroid Minimalfläche fußen. Eines unserer wichtigsten Ergebnisse besteht aus der Erkenntnis, dass die spontane Bildung der Ia$\bar{3}$d Gyroid Struktur, von welcher in früheren Studien über die *pear hard Gaussian overlap* (PHGO) Annäherung berichtet wurde und die hier bestätigt wurde, auf geringfügig nicht-additive Eigenschaften dieses Potentials zurückzuführen ist; in Systemen mit Teilchen von perfekt harter Birnenform wird dieser dreifach-periodische Flüssigkristallzustand nicht beobachtet.

Zuerst untersuchen wir mit Hilfe von Computersimulationen das PHGO System, bei dem wir das Phasendiagram von Birnen-Teilchen mit Aspektverhältnis 3 präsentieren. Dieses ist in Abhängigkeit der globalen Dichte und der Teilchenform (Teilchenverjüngung) angegeben und beinhaltet sowohl gyroide, isotrope, nematische, als auch smektische Phasen. Wir bestätigen, dass die Gyroidphase als gekrümmte smektische Bilagenphase gedeutet werden kann. Das kollektive Verhalten der Birnenteilchen, sich in verzahnte Schichten mit negativer Gausskrümmung, aus der der Gyroid resultiert, anzuordnen, wird erkundet, indem ein Zusammenhang zwischen den zugrundeliegenden Mengen Voronoi Zellen und den lokal Krümmungen gezogen wird. Die geometrische Anordnung in den Bilagen weist auf fundamental unterschiedliche Stabilisierungsmechanismen zwischen der von birnenförmigen Teilchen erzeugten Ia$\bar{3}$d Gyroidstruktur und derer, welche in Lipid-Wasser Mischungen oder in Diblockcopolymeren beobachtet wurden.

Da es sich bei dem PHGO-Modell um eine Näherung der Birnenform handelt, untersuchen wir zusätzlich in viel langsameren Simulationen die Selbstorganisation von Teilchen mit perfekt harter Birnenform (HPR-Modell). Das Phasendiagram der HPR-Teilchen besteht lediglich aus isotropen und nematischen Zuständen, wobei weder der Gyroid noch smektische Annordnungen beobachtet werden. Um die Anfälligkeit gegenüber der

Teilchenform näher zu beleuchten, behandeln wir die entropische effektive Anziehung zweier Birnenteilchen durch Depletion beider Modelle in einer Lösung harter Kugeln. Es zeigt sich, dass sich die HPR-Teilchen genau nach geometrischen Vorhersagen richten, die wir zuvor durch Berechnungen des Verdrängungsvolumens der Teilchen tätigen, wohingegen die PHGO Birnen Unterschiede zu diesen Erwartungen aufweisen. Diese Abweichungen sind auf die ungewöhnliche Winkelabhängigkeit der (nicht-additiven) Kontaktfunktion und auf die, durch die Annäherung enstehenden, kleinen Überlappungen zurückzuführen.

Im PHGO Modell zeigen wir darüberhinaus, dass sich bei Hinzunahme geringer Konzentrationen harter Kugeln eine $Pn\bar{3}m$ Diamantphase einstellt (basierend auf der Schwarz D Minimalfläche). Dieses Ergebnis beruht auf der größeren räumlichen Heterogenität der Diamantgeometrie verglichen mit dem Gyroid, wodurch zusätzliches Material benötigt wird, um geometrische Frustration zu überwinden. Im Gegensatz zu Copolymersystemen sammeln sich die Füllteilchen meist nahe der Minimalfläche des Diamanten, was wiederum in dem nicht-additiven Charakter der PHGO-Kontaktfunktion begründet ist. Bei hohen Konzentrationen, stellt sich eine Phasenseparation ein, in welcher sich die Birnen in mizellenähnlichen Strukturen anordnen. Hier bilden die dicken Enden der Birnen die Mitte, wohingegen die Spitzen der Birnen nach außen zeigen. Die Mizellen erzeugen selbst größere Mesostrukturen, was auf eine mögliche hierarchisch aufgebaute Selbstorganisation der bikontinuierlichen Strukturen hindeutet.

Schlussendlich entwickeln wir ein Dichtefunktional im Rahmen von *Fundamental Measure Theory* für allgemeine harte Rotationskörper, in denen die Birnen als Spezialfall enthalten sind. Dieses wird auf ein System von Birnenteilchen bei geringer Dichte angewendet, wobei wir das Verhalten der Teilchen an einer harten Wand untersuchen. Dabei sagen wir eine komplizierte Richtungsanordnung nahe der Wand voraus, welche direkt mit der Teilchenform in Zusammenhang gebracht werden kann und Einsicht in Adsorptionsprozesse nichtsymmetrischer Kolloide gibt. Das prognostizierte Verhalten der Teilchen und die Unterschiede zwischen PHGO und HPR Modell werden durch Monte Carlo Simulationen bestätigt.

Publications

Parts of this PhD project have already been published in peer-reviewed journals:

P. W. A. Schönhöfer, L. J. Ellison, M. Marechal, D. J. Cleaver, G. E. Schröder-Turk
Purely entropic self-assembly of the bicontinuous $Ia\bar{3}d$ gyroid-phase
Interface Focus 7, 20160161 (2017).

S. Weis, P. W. A. Schönhöfer, F. M. Schaller, M. Schröter, G. E. Schröder-Turk
Pomelo, a tool for computing generic Set Voronoi diagrams of aspherical particles of arbitrary shape
EPJ Web of Conferences 140, 06007 (2017).

P. W. A. Schönhöfer, G. E. Schröder-Turk, M. Marechal
Density functional theory for hard uniaxial particles: Complex ordering of pear-shaped and spheroidal particles near a substrate
Journal of Chemical Physics 148(12), 124104 (2018).

P. W. A. Schönhöfer, D. J. Cleaver, G. E. Schröder-Turk
Double diamond phase in pear-shaped nanoparticle systems with hard sphere solvent
Journal of Physics D: Applied Physics 51(46), 464003 (2018).

M. A. Klatt, J. Lovrić, D. Chen, S. C. Kapfer, F. M. Schaller, P. W. A. Schönhöfer, B. S. Gardiner, A.-S. Smith, G. E. Schröder-Turk, S. Torquato
Universal hidden order in amorphous cellular geometries
Nature Communications 10(1), 811 (2019).

The publications are highlighted again in the respective chapters in which their content is addressed.

Contents

1 Self-assembly of bicontinuous nanostructures

> *"Great things are done by a series of small things brought together."*
>
> – Vincent Van Gogh

The focus of this thesis is the complex three-dimensional nanostructures known as bicontinuous phases and in particular their genesis in entropic systems. This chapter introduces this research field by giving a brief overview of select aspects of nanoscience and nanomaterials. To establish the general paradigm of this thesis – the core role of geometry for soft-matter physics, we first discuss the use of functional nanomaterials and the special connection between geometry and physics (Sec. 1.1). Afterwards, the geometry behind bicontinuous phases, namely triply periodic minimal surfaces, is introduced (Sec. 1.2). The last section (Sec. 1.3) outlines the occurrence of such minimal surface morphologies in chemistry, biology and soft matter physics.

1.1 Nanostructures: Functional spatial geometries

Why is steel harder than iron? What gives a kitchen sponge its squishy consistency? Why do strawberries appear red and what makes peacock feathers extraordinarily colourful? Often the physical properties of objects can be derived from the features of the molecules they are made of. Strawberries, for instance, owe their bright red colour to anthocyanin pigments: chemicals which absorb all but the red light [1]. Also the hardness of steel is mainly governed by its carbon or alloy content [2]. However, many fascinating effects in materials science, for instance, the mechanical properties of the sponge or the colour of peacocks, cannot be reduced directly to the chemical compounds of substances, but are contingent instead on the internal structure and arrangement of those molecules.

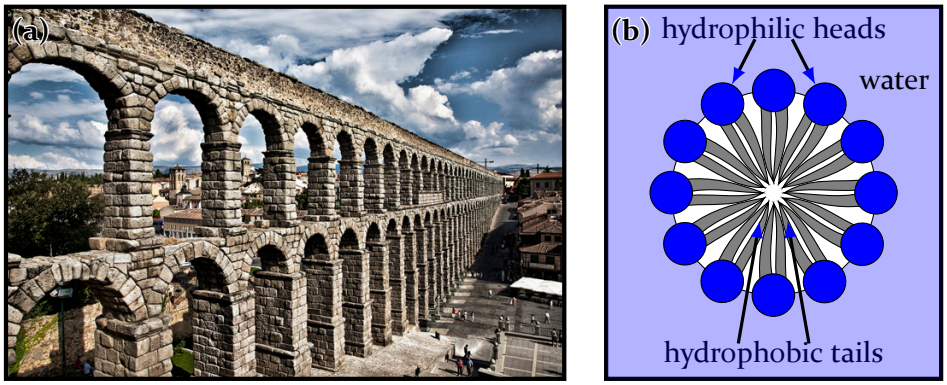

Figure 1.1: Two structures representing the construction method for complex geometries out of multiple constituents for different length-scales. (a) The aqueduct de Sagovia in the centre of Spain. Its arches embody the concepts of geometry in Roman architecture (photo credit: Felver Alfonzo [4]). (b) A sketch of lipids forming a micelle structure in a mixture with water.

The importance of patterns and structures on the physics of materials has been recognised for a long time. Already the ancient Romans applied geometrical concepts to build monumental structures, beautifully demonstrated in the arches of their aqueducts (see Fig. 1.1a). The specific arrangement of single stones leads to a pressure distribution which binds the loose constituents and additionally increases the tolerance to heavy loads. At the least when Kepler stated "Ubi materia, ibi geometria!"[1] 400 years ago in one of his tractates *De fundamentis astrologiae certioribus* [3], the inseparable bond between geometry and matter and its special relation to patterns have been fully acknowledged by physicists.

Today geometry plays a crucial role in understanding physical phenomena. For instance, the percolating nature of permeable rocks can be explained by the arrangement and topology of embedded cavities. Those voids form complex hollow tunnel systems allowing liquids or gases to spread from the top to the bottom of the rock [5], or they can store fluids, which is of great importance in the gas or oil industry [6]. Similarly, the perforations alter the mechanical properties of the rocks [7]. Similar mechanisms are found in the kitchen sponge, where small pores within the cellulose fabric cause both the sponge's softness and its high liquid absorption. Another example is the stability of granular packings, which is crucial for the fundamental mechanisms

[1] "Where there is matter, there is geometry!"

of landslides of debris or finely grained soil around seismic areas and also explains the difference between a nearly solid sand surface and liquid-like quicksand [8, 9, 10]. The arrangement of particles within the packing is a key determinant that governs the static, mechanical and dynamic (flow) properties of such systems [11, 12].

On a much smaller, microscopic scale, patterns play a significant role likewise in biology. Even before the first *nanostructures*, that is patterns with a typical length scale up to 1 μm, were found, D'Arcy Thompson established in his book *On Growth and Form* (first published in 1917 [13]) the thinking that biology and biological materials are informed by geometry on any imaginable length-scale. Since then, a plethora of different nanostructures with highly diverse functions have been discovered in nature. The overwhelming number of structures in animals and plants allows only for a limited selection of examples which we can give in the following list (see also Fig. 1.2, Fig. 1.3 and Fig. 1.4). However, even this glimpse into the world of nano- and microstructures illustrates their impressive variety and versatility.

- The Lotus effect of ultra-hydrophobic leaves is based on microscopically small spikes on the surface, which decrease the contact surface between the leaf and a water droplet significantly and so prevent the wetting of the surface [14].
- In the eyes of moths, a nano-grated array of knobs prevents the accretion of unwanted particles like pollen or dust [15]. Moreover, this particular pattern achieves additional anti-reflective properties [16].
- Oriental hornets use grooves in their exoskeleton to harvest the energy of light [17], which might explain their heightened activity under a UV source [18].
- Planktonic types of microalgae, called diatoms, are known to build porous silica shells [19]. These shells or "frustules" are produced for protection without hindering the algae's photosynthetic abilities (in fact the shells even enhance the production of oxygen [20]) and exhibit a great diversity of forms as depicted in Fig. 1.2a.
- The skin of snakes is designed to facilitate a frictionless forward motion combined with high friction in the backward direction [21]. This friction anisotropy is caused by 400 nm wide "hairs", called microfibrils.

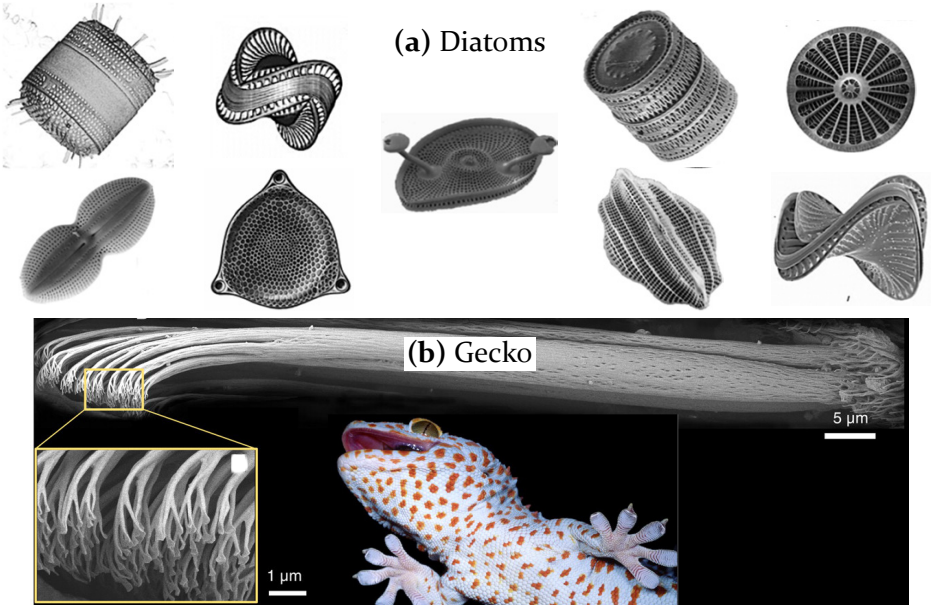

Figure 1.2: The functionality and variety of nanostructures in biological systems displayed by two representative examples. (a) Microscopic diatoms form protective silica shells with a great variety of different morphologies (adapted with permission from [19]). (b) The feet of geckos are covered with thin hairs, called setae, which give the gecko its adhesive properties (adapted with permission from [22]).

- Geckos are able to climb extremely smooth objects because of similarly small hairs on their feet, called setae designed to increase their adhesive properties [22, 23] (see Fig. 1.2b).

Perhaps the influence of nanostructures is best "visualised" by the phenomenon of structural (or interference) color [24, 25, 26, 27]. Here colour is produced by the interplay of visible light and microscopically small structures on the same length scale, so-called photonic crystals, rather than by chemical pigments. Most people are familiar with this optical effect as they admired it in their childhood in the stunning array of colours of soap bubbles and oil films (see Fig. 1.3a). Their appearance is not explained by chemistry. On the one hand, the bubble is multicoloured and even changes colour over time and with viewing angle. On the other hand, the soap solution on its own – for example in a vial – is usually fully transparent without any sign of colour. Instead of pigments, the incident light interacts with the thin liquid soap film of the bubble which encapsulates air and separates it from the outside. As the film acts as two interfaces between the liquid and

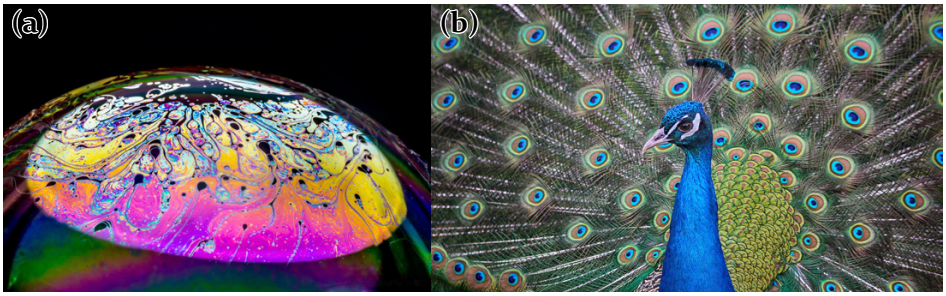

Figure 1.3: Structural color demonstrated on (a) soap bubbles (photo credit: Pashminu [29]) and (b) barbules in the eye pattern of peacock feathers (photo credit: Marco Roosnik [30]). In both cases microscopic structures on the scale of visible light generate the coloration.

air-domain, light reflects from both interfaces and forms two separate waves travelling different distances. This enhances the colour of a certain wavelength, due to constructive interference. The wavelengths that are amplified and, more importantly, the resulting apparent colours are both controlled by the thickness of the film. Given that the film thickness is between 200 nm and 1200 nm [28], this is the most commonly known nanoscale effect.

Flora and fauna utilize similar techniques for color creation by producing complex nanostructures [24, 25, 31, 32, 33, 34, 35, 36, 37, 38, 39, 40, 41, 42, 43, 44]. For example, some flowers have developed a deliberately disordered nanostructure which predominantly scatters light in the blue-UV range to attract bees, which are sensitive to exactly this wavelength [31]. Also the feathers of peacocks exhibit an elaborate pattern on the nanoscale, which imbues the bird with its piedness [24, 32] (see Fig. 1.3b). Additionally, these structures induce a much more complex optical effect, namely an angle dependency of colour appearance called iridescence [25, 33, 34, 35]. Not only in other birds [25, 36], but also in insects [37, 38, 39, 40], which might unfold the greatest diversity of nanostructures [41], arachnoids [42] and cephalopods [43], a magnificent range of structural color creating patterns has been detected.

1.2 Triply-periodic minimal surface structures

This thesis is focused on one of the most complex, but simultaneously highly symmetric and most ordered class of geometries, whose, among others, optical properties have raised major interest amongst both biologists and

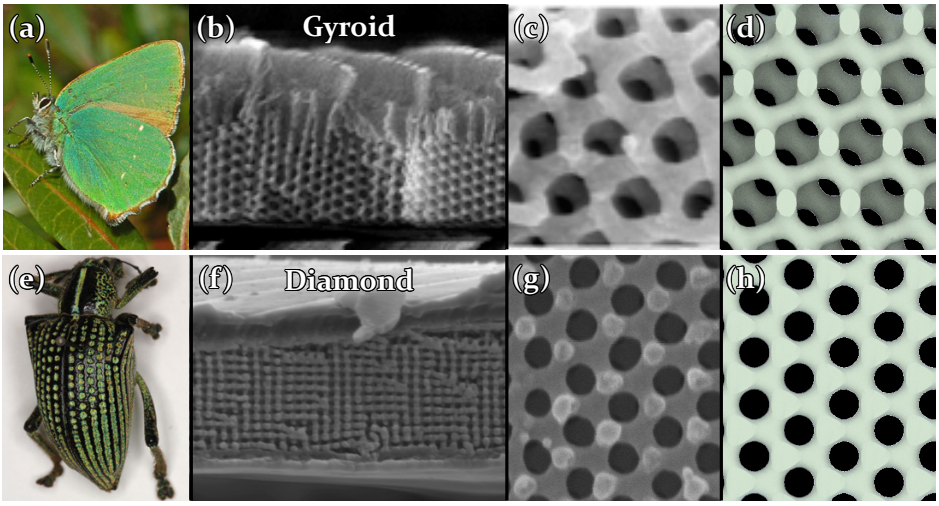

Figure 1.4: Nanostructures creating structural color in the *Callophrys rubi* butterfly (a-c) and the *Entimus imperialis* weevil (e-f). Light microscopy shows that the wings (b) and pits (f) are built out of multi-faceted scales. Electron microscopy of their wing and pit scales, respectively, reveals two triply-periodic minimal surface structures (see Sec. 1.2), the single gyroid in the [110]-direction (b,c) with lattice constant a_{SG} = 311 nm [45] and the single diamond in the {100}- (f) and {111}-direction (g) with lattice constant a_{SD} = 445 nm [37]. For comparison computer models of the single gyroid (d) and single diamond (h) are shown (reproduced with permission from Ref. [46] (a-c) and Ref. [38] (e-g)).

physicists. Two representatives, which demonstrate this complexity, have been observed in certain butterflies (the so-called single gyroid [46, 47]) and weevils (the so-called single diamond [37, 38]) and are depicted in Fig. 1.4. By performing electron microscopy, it becomes apparent that the scales of the wings of the butterfly and the scales of the pits of the weevil both display a chitinous network-like geometry. In both cases, the nanostructures are responsible for the green appearance of the wings/scales and can be attributed to bicontinuous triply-periodic minimal surfaces (TPMS) [48, 49, 50, 51, 52].

The most famous members of TPMSs, the gyroid ($Ia\bar{3}d$ symmetry), diamond or Schwarz-D surface ($Pn\bar{3}m$ symmetry) and also the primitive or Schwarz-P surface ($Im\bar{3}m$), are ubiquitously found in biological and chemical systems and are depicted in Fig. 1.5. These three surfaces partition space into two identical (up to mirror reflections) and interwoven domains, which are often alternatively visualised as two intertwined, periodic and highly symmetric labyrinth-like sub-volumes and, hence, are referred to as *bicontinuous*. In the butterfly and weevil system in Fig. 1.4 the gyroid and diamond surface,

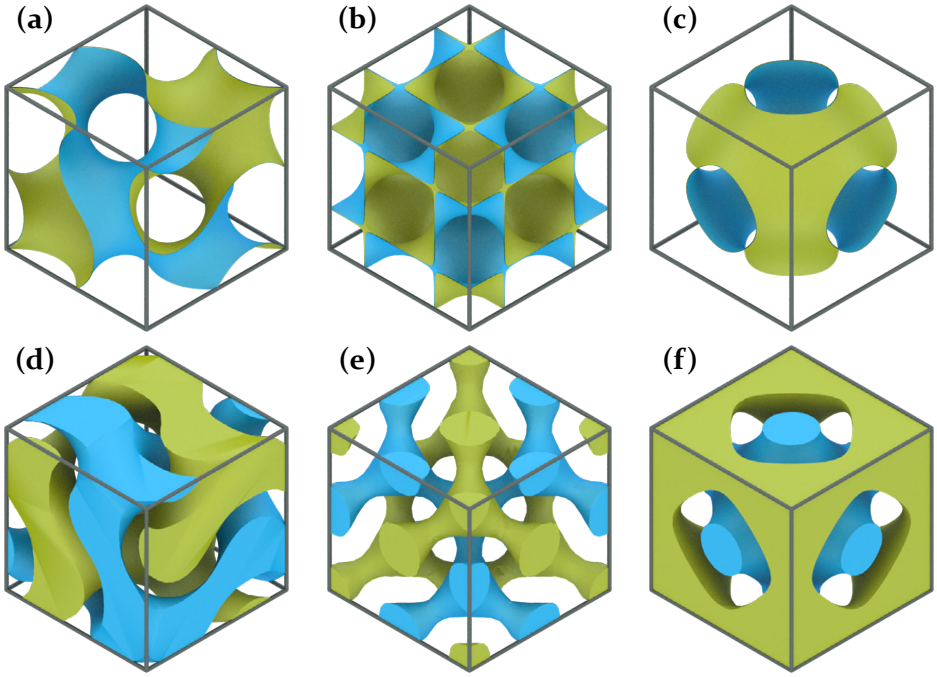

Figure 1.5: The three most common triply-periodic minimal surface structures occurring in nature and soft matter: (a+d) gyroid, (b+e) diamond, (c+f) primitive. At the top, the TPMS surfaces are shown which divide space into two equally sized subdomains. At the bottom, the alternative depiction of the two intertwined non-intersecting labyrinth-like domains is indicated. The domains are represented by filling the smaller channels of their CMC companions [53, 54, 55].

for example, separate the chitin network from the air filled channel and generates a single gyroid and single diamond structure, respectively.

The auxiliary "single" in single gyroid or single diamond refers to the different chemical compounds of the two sub-volumes in these systems leading to a different symmetry group than the surface structures on which they are based.[2] The individual channel networks of the gyroid are also known as "srs"-networks, named after the $SrSi_2$ crystal [56]. This specific structure is of special interest as it is chiral (with a 4-fold screw axis in the {100}-direction and a 3-fold screw axis in {111}-direction [55]) and has even been argued to be the simplest interconnected chiral network with cubic symmetry [56]. The

[2]The single gyroid has the symmetry group $I4_132$, the single diamond the space group $Fd\bar{3}m$, and the single primitive the space group $Pm\bar{3}m$.

"double" gyroid, where the two channels are not distinguishable and the structure has the same symmetry group as the attributable surface, contains two srs-networks with opposite handedness and, therefore, is overall achiral [57].

1.2.1 Mathematical description

In mathematical terms, *minimal surfaces* are defined as surfaces of zero mean curvature H. This implies that every point p on the surface is a saddle point and the principal curvatures, κ_1 and κ_2, differ only in sign. In terms of Gaussian curvature K – the product of both principle curvatures – these surfaces are hyperbolic, and so

$$\begin{aligned} H(p) &= \frac{1}{2}(\kappa_1(p) + \kappa_2(p)) = 0 \\ K(p) &= \kappa_1(p) \cdot \kappa_2(p) \leq 0 \quad \forall p \in \text{TPMS}. \end{aligned} \tag{1.1}$$

The "minimal" feature refers to the surface being a critical point of the area functional, constrained by the boundary conditions in terms of variations due to normal deformations [58]. In other words, minimal surfaces are local optima, where the surface area is minimised subject to sufficiently simple boundary conditions embedded within the surface. Hence minimal surfaces are special cases of constant-mean-curvature surfaces (CMC) where the mean curvature is constant but not zero necessarily. Classic examples for minimal surfaces are again soap films which form catenoid minimal surfaces between two rings due to surface tension (see Fig. 1.6).

Triply-periodic minimal surfaces are a special class of minimal surfaces that are invariant under a discrete set of translations which determine the Euclidean space and can be assigned to a crystallographic symmetry group. Despite the great variety of TPMSs with different symmetries only a limited class of these surfaces are not self-intersecting and even fewer (especially gyroid, diamond, and primitive) have shown their importance in living organisms [37, 38, 46, 47, 59, 60, 61, 62, 63, 64] and synthetic materials [65, 66, 67, 68, 69, 70, 71, 72, 73, 74, 75, 76, 77, 78, 79, 80].

Some of these bicontinuous gyroid, diamond or primitive structures are technically not minimal surface structures but belong to one of their constant mean-curvature (CMC) companions [53, 54, 55]. These surfaces share the

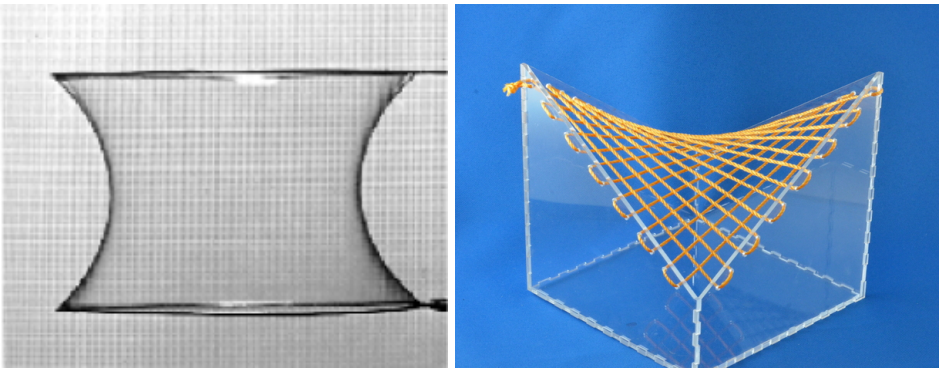

Figure 1.6: Two classic examples of minimal surfaces. Left: A soap film minimises the surface area between two parallel rings. The emerging minimal surface is the catenoid (Photo credit: EPINET [81]). Right: A braided mesh spanned over four of six edges of a regular tetrahedron (photo credit: AGPapa [82]). By tightening the mesh it eventually forms a minimal surface which is the fundamental surface patch of the diamond minimal surface (see Fig. 1.5).

same topology as their parents, however, vary in terms of the volume fraction between the two separate channel domains. Even though $H(p)$ is constant for all points p on the CMC surface, it is unequal to 0 unless the CMC surface is congruent with the TPMS itself. The CMC companions can also be created by minimising the surface area, with the difference that a constraint of the fixed volume ratio between the divided subdomains has to be included.

Triply-periodic minimal surfaces were first discovered in 1856 by Amandus Schwarz [83] in the form of the D-surface. He noticed that a soap film spanned across a quadrilateral frame, consisting of four edges of a regular tetrahedron, can be smoothly and infinitely continued with other soap films creating the same surface patches (see Fig. 1.6). This is due to the fact that every TPMS can be constructed out of a smallest fundamental piece or "Flächenstück" under consideration of the symmetry group. For surfaces with mirror and two-fold in-surface rotations, these patches are often bounded by straight lines or mirror planes. Using this idea, Schwarz later accomplished to formulate, with input from Riemann and Weierstrass [48, 51], an analytical expression for a couple of TPMS including the diamond and also the primitive surface. They were able to connect holomorphic functions $R(\omega)$, which are complex differentiable functions at every point $\omega \in \mathbb{C}$, with minimal surfaces [48]. In particular, it was shown that for all $R(\omega)$ there exists a minimal surface which is embedded in space by $\mathbf{x} = (x, y, z)$ where

$$
\begin{aligned}
x(\bar{\omega}) &= \mathrm{Re} \int_0^{\bar{\omega}} \mathrm{e}^{\mathrm{i}\theta_B}(1-\omega^2)R(\omega)\mathrm{d}\omega \\
y(\bar{\omega}) &= \mathrm{Im} \int_0^{\bar{\omega}} \mathrm{e}^{\mathrm{i}\theta_B}(1+\omega^2)R(\omega)\mathrm{d}\omega \\
z(\bar{\omega}) &= \mathrm{Re} \int_0^{\bar{\omega}} \mathrm{e}^{\mathrm{i}\theta_B}(2\omega)R(\omega)\mathrm{d}\omega,
\end{aligned}
\tag{1.2}
$$

with the Bonnet angle θ_B. This *Weierstrass representation* is still a powerful tool to generate and visualise TPMS [84, 85, 86]. As this procedure gives a more accurate representation of the TPMS, we will favour the Weierstrass approach over the nodal approximation of Eq. (1.5) to depict the surfaces in this thesis.

The gyroid was first described by Alan Schoen nearly 100 years later during his studies on TPMS and their Weierstrass representation [52, 87]. The gyroid, diamond, and primitive surface share the same holomorphic function, called the Weierstrass function [85, 86, 87, 88]

$$
R(\omega) = \frac{1}{\sqrt{\omega^8 - 14\omega^4 + 1}}. \tag{1.3}
$$

and only differ in θ_B. Hence, the Bonnet angle can be seen as a parameter to transform the surface from a diamond where $\theta_B = 0$, to a gyroid where $\theta_B = \operatorname{arccot} \frac{\mathrm{K}(1/4)}{\mathrm{K}(3/4)} \approx 38°$ with K being the complete elliptical integral of the first kind, to the primitive surface where $\theta_B = \frac{\pi}{2}$ [87].

Since then many other TPMS have been introduced [53, 89], but they do not receive the same attention in physics and biology as their three relatives because they are found less frequently, if at all. It is believed that the gyroid, diamond, and primitive surfaces are more likely to be obtained in nature and chemistry as they exhibit the lowest inhomogeneity of Gaussian curvature [70, 90, 91]. This makes them the closest attempt to embed a manifold with constant negative Gaussian curvature in Euclidean space (see Sec. 8.1 for a more in-depth discussion).

Gyroid-like surfaces and TPMS are still of interest in contemporary mathematical research. For example, Fujimori and Weber [92] recently introduced an alternative construction method for TPMS surfaces based on a Schwarz-Christoffel formula for periodic polygons. Similarly, Chen [93] identified

some minimal surfaces as minimal twins of TPMS. Also, new minimal surfaces have been described within the last two years, for instance, by deforming already known TPMS embeddings sufficiently [94, 95] or generating area-minimising interfaces between the quartz network and its dual [96]. For the latter a powerful software-tool called *Surface Evolver* [97, 98] is used which minimises the energy (for example area) of surfaces for given constraints.

1.2.2 Nodal approximation

A convenient way to approximate a TPMS is by the nodal surface of a Fourier series [99, 100, 101]

$$0 = \Psi(\mathbf{x}) = \sum_{\mathbf{k}} F(\mathbf{k}) \cos[2\pi\mathbf{k}\cdot\mathbf{x} - \alpha(\mathbf{k})], \tag{1.4}$$

where $\mathbf{k}$ is the reciprocal lattice vector, $\alpha(\mathbf{k})$ is a phase shift and $F(\mathbf{k})$ is an amplitude. Also the TPMS can be satisfactorily reproduced by truncating the Fourier series to the leading term, which gives the so-called *nodal approximation* of the gyroid, diamond and primitive surface [102]

$$\begin{aligned}
\text{gyroid:}\quad & 0 = \sin\frac{2\pi x}{a}\cdot\cos\frac{2\pi y}{a} + \sin\frac{2\pi y}{a}\cdot\cos\frac{2\pi z}{a} + \sin\frac{2\pi z}{a}\cdot\cos\frac{2\pi x}{a}\\
\text{diamond:}\quad & 0 = \cos\frac{2\pi x}{a}\cdot\cos\frac{2\pi y}{a}\cdot\cos\frac{2\pi z}{a} - \sin\frac{2\pi x}{a}\cdot\sin\frac{2\pi y}{a}\cdot\sin\frac{2\pi z}{a}\\
\text{primitive:}\quad & 0 = \cos\frac{2\pi x}{a} + \cos\frac{2\pi y}{a} + \cos\frac{2\pi z}{a},
\end{aligned} \tag{1.5}$$

where a is the crystallographic lattice parameter (periodicity) of the surface. With the nodal representation, also the CMC companions of these surfaces can be approximated by replacing 0 on the left-hand side of the equations Eq. (1.5) with a constant ϵ. Here the constant ϵ acts as a control parameter to shift the size proportions of the sub-volumes (but not in a strictly linear fashion [103]). The orange and blue channels in Fig. 1.5 are, for example, constructed by filling the minority domain of each CMC, which is approximated by a nodal equation with $\epsilon = 1$ and $\epsilon = -1$, respectively.

To picture the essential geometry of the domains, TPMS are often represented by a skeletal network [90] or the medial axis of the minimal surfaces (see [104] for a review). This medial surface (or axis) is a geometric

construction that produces a centred skeleton of the original shape. For the case of bicontinuous structures, it represents a generalised line graph that also provides a robust definition of local domain (or channel) size and hence relates to questions of chain stretching frustration and geometric homogeneity [70, 90, 91, 105]. For an object defined by its bounding surface, for every surface point p with surface normal vector $n(p)$, the corresponding medial surface point is defined as $p + d_{\mathrm{MS}}(p) \cdot n(p)$. The medial surface distance function $d_{\mathrm{MS}}(p)$ describes the distance from p to the corresponding centre of the channel.

1.3 Triply-periodic minimal surfaces in chemistry and nature

The ambition to mimic highly complex and functional nanostructures like the TPMS found in living organisms marks one of the pillars of today's research in bio- and soft matter physics. Due to their geometry and topology, TPMS and the corresponding CMCs are attractive for application in optics, where they can function, for instance, as beamsplitters [106, 107], photo-sensors [108, 109] or on-chip chiro-optical devices [110]. But they also raise interest for their transport [111, 112, 113, 114] and mechanical properties [115, 116, 117, 118] and even have been suggested for a new way of energy storage [119, 120, 121, 122, 123]. Next to the efforts expended in understanding how certain nanostructures manipulate these material properties, particularly the pursuit of the astonishing efficiency and variety of mechanisms which nature developed, is a driving force of many recent studies.

For the construction of gyroid-like structures on the nano-scale, scientists have developed, in the course of this, various methods which can be separated into two general categories. In top-down approaches the networks are manufactured directly out of certain materials. The techniques which are listed as bottom-up strategies, on the other hand, are inspired by nature, where microparticles collectively assemble into complex morphologies.

1.3.1 Top-down assembly methods

The most straightforward methods for preparing nearly arbitrarily sized nanostructures, including the gyroid or diamond networks, are categorised as top-down approaches. These strategies are essential to create new types

of meta-materials with tailored photonic or mechanical properties (see Ref. [124] for a recent review focused on gyroid-like structures generated with top-down approaches). Traditionally, lithography has been the most reliable route for preparing TPMS nanostructures with the top-down approach. The idea of these techniques is simply speaking to carve void space into a block of material using a photon or electron beam. In the case of interference lithography, for example, the three-dimensional network is shaped by the superposition of coherent light in a photo-reactive substance [125]. In particular, photonic crystals with different morphologies have been manufactured using multi-beam/holographic [126] and phase-mask lithography [127, 128], also including TPMS structures [129, 130, 131, 132]. These lithography techniques, however, are subject to limitations in terms of their requirement on a substrate, the obtainable geometries and the feasible dimensions of the final object. Typically they are also associated with complex optical setups. Other known methods, like atomic layer deposition [133, 134] and cuprous oxide electrodeposition [135] have similar issues regarding their efficiency and restriction to create structures of high complexity.

Nowadays many of these problems have been alleviated through the advances made in 3D nanoprinting. Especially multiphoton lithography, also known as direct laser writing (DLW), [136, 137] and super-resolution photo-induced-inhibition nanolithography (SPIN) [138, 139] provide the greatest combination of speed, precision, and flexibility. With these two methods, yet another degree of complexity can be added to the already intricate morphology of the srs [106] or double gyroid [140]. In particular, multi-srs networks, where 2-srs [141], 4-srs [56, 142], 8-srs [143, 144] or even more like-handed srs networks are intertwined, have been built. Hereby, the chiral nature of the srs-networks opened a new path for achieving interesting topological and optical phenomena, such as Weyl points (topological monopoles of the Berry-flux) [140, 145], circular dichroism effects [56, 106] and optical activity [56, 143].

Another great benefit of DLW, SPIN and top-down approaches, in general, is the layout flexibility of the used material. The incorporation of different materials is of great interest in modern-day nanofabrication, for example, to alter the refractive index of the optical material or the elasticity of scaffolds. Next to the already mentioned photo-sensitive polymers, gyroidal nanostructures have also been created from ceramic [140], chalcogenide glasses [147, 148, 149], and graphene [150]. Moreover, metallic gyroids have been

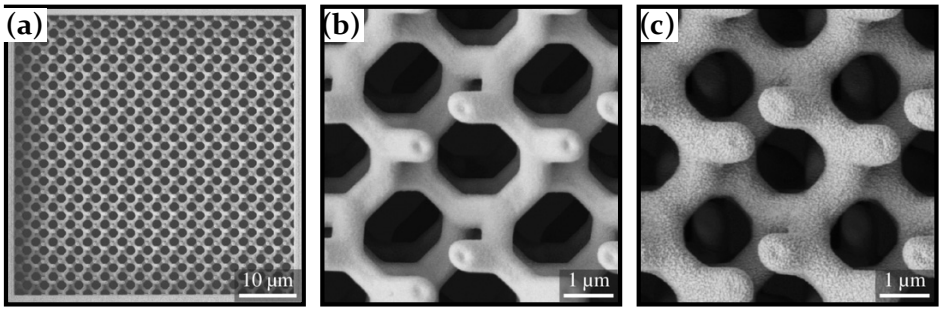

Figure 1.7: (a) A 50 μm×50 μm srs-network nanostructure created out of a plastic coverslip using direct laser writing. A close-up of the same structure before (b) and after (c) the surface is coated with silver particles. The figure is adopted from Ref. [146].

fabricated using DWL and electroless metallization [146] (see Fig. 1.7) or layer-by-layer deposition [124] on a polymer template.

1.3.2 Bottom-up assembly methods

Bottom-up approaches, which are the focus of this work, resort to a similar idea like the Romans for building aqueducts. Like the differently shaped stone bricks, small nanoparticles adopting suitable shapes act as building blocks to form long-ranged complex geometries (see Fig. 1.1). In particular, *self-assembly* (that is, the spontaneous and collective arrangement of multiple nanoparticles into ordered microstructures) has proven to be a fundamental design strategy to generate elaborate bio-inspired patterns. First, the method of particles forming complex configurations without any external input (like electromagnetic fields, or in contrast to the aqueduct: manpower) makes this bottom-up procedure much more energetically cost-effective than top-down strategies. Secondly, we can hope to fabricate nanomaterials on a much larger scale than it is otherwise achievable. The butterfly C. rubi, for example, produces several cm^2 of gyroid structure, where the top-down DLW method is limited to $(10\,\mu\mathrm{m})^2$ samples [151]. Molecules and nanoparticles which self-assemble into diffusive ordered configurations are often categorised as liquid crystals.

Liquid crystal phases

Liquid crystals (LC), also known as *mesogens*, and their applications have become indispensable in today's everyday life. May it be their implementation

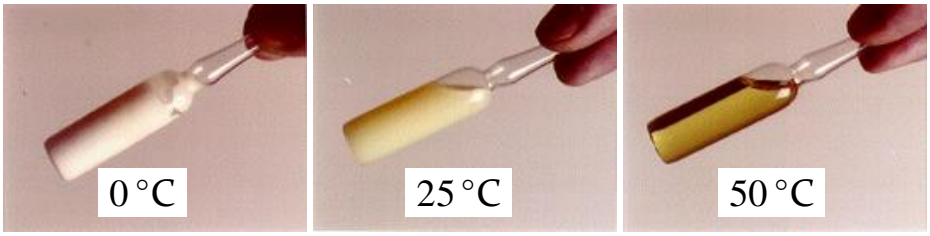

Figure 1.8: A cholesteric liquid crystal (MBBA) passes through three different phases (photo credit: Feodor Oestreicher [152]) . For low temperatures, the liquid crystal is in a solid phase. By supplying heat the system transitions into a mesophase which is revealed as a milky liquid. By raising the temperature further the liquid turns transparent and the liquid crystal adopts the isotropic phase.

in many of our electronic devices as a crucial part of liquid crystal displays (LCD) [153, 154], or their value as a tool to detect heat sources in medicine [155] and electrical engineering [156], LCs have proven to be of great importance in technology. Typically, liquid crystals are defined as anisotropic particles or molecules which exhibit additional, more complicated phases in between the liquid and crystalline state, see e.g. Ref. [157]. These so-called mesophases (μέσος; greek mesos: "middle") display features characteristic of both liquid and solid matter. Elongated molecules with liquid-like flowing dynamics which simultaneously can be assigned some sort of solid-like anisotropy in terms of their orientational order are prime examples of liquid crystals. The term liquid crystal or "flowing crystal" was introduced by Otto Lehmann in 1890 [158] after Friedrich Reinitzer observed this duality of states in derivates of cholesterol [159]. Even then, though not fully understood, their influence on optical features became apparent. Reinitzer observed two phase transitions. One from the solid to a milky liquid-like mesophase. At the other one the liquid turned transparent (see Fig. 1.8).

Commonly, the mesophases are classified into four different types: nematic, smectic and cholesteric (see Fig. 1.9). This classification is traceable to their description by Georg Friedel in 1922 [160]. The common LC phases are in the notation used in Ref. [157].

- The *nematic phase* (νήμα; greek nema: "thread") is characterized by its long-range orientational and only short-range translational order. This means that the particles are homogeneously distributed within the system like a liquid, however, possess an overall orientational alignment. The direction that is defined by the preferred orientation is

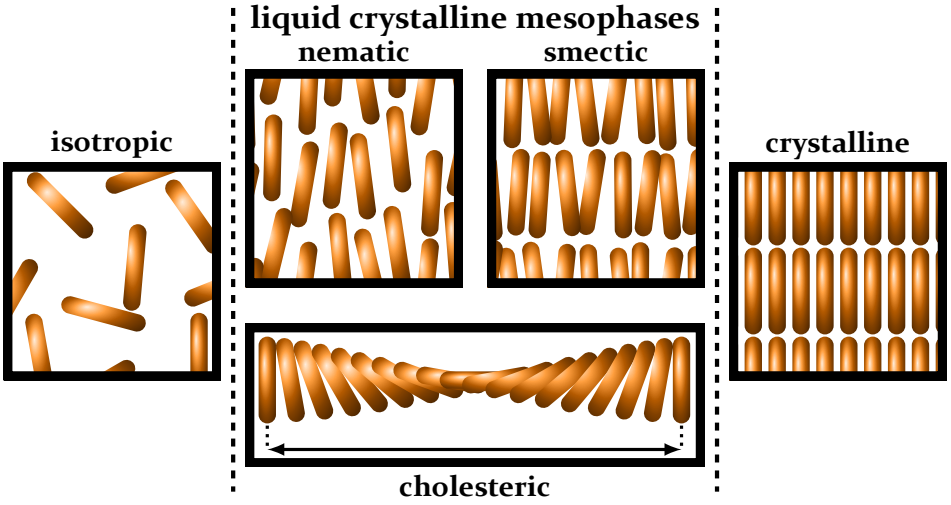

Figure 1.9: The three classes of thermotropic mesophases between the isotropic and the solid/crystalline phase. (a) The nematic phase exhibiting no translational but orientational order. (b) The cholesteric phase characterized by an additional chirality of the director. (c) The smectic phase combining both translational order in one dimension and orientational order.

called the director. Usually, the orientational alignment occurs along the major axis of the particles. Orientational order along the smaller axes has also been observed, often referred to as discotic or columnar phases as they also often form columns which themselves can arrange in different two-dimensional patterns (hexagons, rectangles) at higher concentrations[161].

- On introducing an overall chirality to the nematic system, the phase is defined as *cholesteric*. This phase was the one discovered by Reinitzer in cholesterol [159], hence the name. Here the director changes along a direction perpendicular to the director in a corkscrew-shaped fashion. This is manifested in a twist of the particles and simultaneously by the formation of layers with different orientation of the director.

- The *smectic phase* (σμῆγμα; greek smégma: "soap" due to their soap-like behaviour) differs from the other two by exhibiting some degree of translational order. Like in the nematic phase the particles align along a director, however, they also assemble into two-dimensional stacks/sheets. Within the different sheets the particles are still distributed randomly and diffuse like a liquid, yet, the formation of the

sheets indicates a one-dimensional positional order. If the particles are layered in the same direction as the director the smectic phase is indicated by smectic-A. If the director does not coincide with the layer-normal the phase is called smectic-C [157].[3]

All of the phases mentioned above are typically associated with *thermotropic* molecules. Here the occurrence of the different phases is highly dependent on the temperature T of the system. However, liquid crystals of another type have shown themselves to be able to form more complex phases – including TPMS phases. These *lyotropic* LCs consist of mesogens dissolved in a suitable solvent (typically a simple liquid or mixture of simple liquids). Hence, the mesophases are more dependent on the concentration between mesogen and solvent rather than the temperature of the system, which only plays a subordinate role.

Lipid bilayer structures

An example of LCs which famously adopt bicontinuous structures are the lyotropic phases of amphiphilic lipids [65, 66]. These molecules consist of a solvophilic head and a solvophobic tail end – therefore the term amphiphilic (αμφις; greek amphis: "both") – such that the lipids favour to face the solvent with their head rather than their tail part. Bicontinuous structures in pure water-lipid-systems without excess water were first reported by Luzzati [162]. The bicontinuous phase is a mesophase between a lamellar phase, where bilayers of lipids and water create alternating planar sheets (dry conditions), and the hexagonal columnar phase where lipids enclose infinite water cylinders in a hexagonal pattern (high water content) [163]. On diluting the hexagonal phase further, lipids arrange into spherical "micelle" clusters with the solvophobic moiety in the center of the micelle (see Fig. 1.1b). In the bicontinuous phase, the lipids form curved bilayers which are draped around the minimal surface and act as a matrix separating two aqueous domains [65, 67, 164]. Here the tails of the lipids meet at the curved minimal surface such that the head groups face the water domain, similar to the arrangement in the lamellar phase (see Fig. 1.10c). At a low concentration of water, the symmetry of the two domains can be assigned to the gyroid structure. Increasing the water content leads to the formation of the diamond structure [163, 165]. Similarly, the introduction of proteins to the gyroid phase can stabilise a diamond configuration [166]. This is explained

[3] However, if there are additional correlations, also further classification is possible.

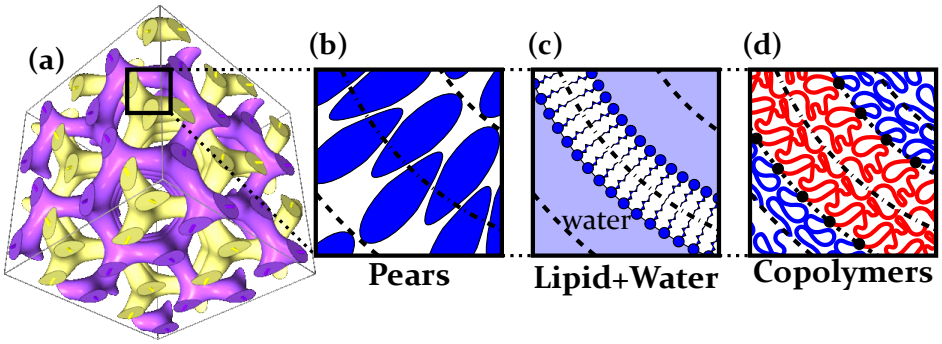

Figure 1.10: The three different arrangements within the gyroid phase (a) generated by tapered liquid crystalline pears, (b) lipids in a mixture with water, (c) and di-block copolymers (d). The pears, lipids and di-block copolymers create bilayers draped aroung the gyroid minimal surface (- -).

by the greater spatial heterogeneity of the diamond compared to the gyroid [70, 91, 167] (see Sec. 8.1 for a more in-depth discussion). In the diamond phase, the system has to fill more domain space compared to a gyroid phase with a similar degree of Gaussian curvature and arranges this by placing the additional material – more water and proteins, respectively – within the water channels. By further adding water to the water-protein-lipid system, the phase eventually transitions into a P-surface configuration [168].

Biological bicontinuous membranes

Biological membranes of lipids with TPMS morphology, known as *cubic membranes* [62, 171, 172], have been reported in various lifeforms. Among these systems are, for example, chloroplasts which form prolamellar bodies under lack of light [63, 173], endoplasmatic reticula in response to heightened concentration levels of specific proteins [62, 169] (see Fig. 1.11a) or mitochondria of amoebae under starvation [60, 170] as shown in Fig. 1.11b. Also the mitochondria in the retina of tree shrews exhibit membranes with gyroid morphology [174]. Even though it has been noticed [62, 175] that these membranes in vivo transition into cubic phases exceptionally often when subject to cellular stresses like starvation [60], viral infections [176, 177] or hypoxia [178] and although it has been conjectured that these transitions are part of an antioxidant defence mechanism of the cells [179] the exact biological functions and fundamental formation processes are still unknown.

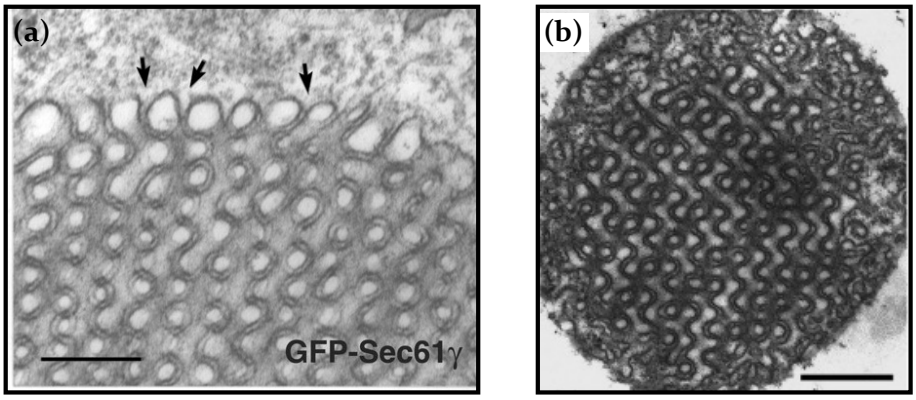

Figure 1.11: (a) A TEM image of endoplasmatic reticulum forming a cubic membrane structure with the same morphology as the diamond surface. The image is adopted with permission from Ref. [169]. (b) A TEM image of a diamond-like cubic membrane found in mitochondria of starving amoeba. The image is adopted with permission from Ref. [170].

Moreover, it is conjectured that in an intermediate stage of the wing development of the butterfly in Fig. 1.4, the molecules form bilayers with the same morphology as the gyroid minimal surface [180, 181], which act as a membrane separating space into two percolating channels. It has been argued that this bilayer arrangement functions as a cast, which templates externally extruded chitinous cuticle, resulting in the final chiral single gyroid structure. This method has inspired scientists to develop a similar templating technique to generate inorganic gyroid structures from the butterfly nanostructure [182, 183, 184] or other self-assembled templates [185, 186, 187]. Thus, the use of *biotemplates* can be understood as an indirect self-assembly approach.

Block copolymers

The second important group of molecules that adopt double gyroids are copolymeric melts [68, 69, 70, 71, 72, 73, 188], in particular, di-block copolymers (note also the review about copolymeric self-assembly in Ref. [189]). Di-block copolymers consist of two different chains, each built up of single monomer "beads" A and B, which are linked to generate one single molecule. Both end chains energetically favour coming closer to chains of the same kind and, therefore, also establish some kind of amphiphilic behaviour. Depending on the relative volume fractions of the two monomers, the di-block copolymers arrange in similar phases to those of lipid system,

namely lamellar, columnar and micellar phases [68, 188]. At a volume fraction of 33% the melt can also adopt a gyroid geometry (see Fig. 1.10d). Here the majority component fills the channels separated by a matrix formed by the minority moiety. A transition to the diamond and primitive phase has been theoretically and computationally examined by adding A-homopolymers [71, 190] and experimentally stabilised upon addition of inorganic components [191]. Even more complex, polycontinuous TPMS, where space is subdivided into more than two domains, have been studied by adding more monomer types to the molecule [192].

There are other lyotropic and thermotropic liquid crystals [74, 75, 76] and also dry monovalent soaps [77], dendrimers [78], mesoporous silica [79] and germanium oxides [80] which form bicontinuous phases as well.

Although self-assembly shows great potential for recreating the formation processes of TPMS in nature, bottom-up strategies still face some issues, especially concerning limits in orientation and scalability. Until now, only very small self-assembled gyroid structures (with the largest having periods of about 258 nm [193]) have been synthesised with periodicities below the ones found in nature. Hence, those systems mainly interact with UV light instead of light in the visible region and cannot yet be used as color creating devices. Even though there have been some advances to shift self-assembled nanostructures into the visible light range [194, 195, 196], which are potentially applicable to gyroid assemblies, and to the synthesis of systems with controlled orientation [197], this open question is still unresolved. Therefore, we investigate a self-assembly approach which stands out with a certain uniqueness and is based on the interaction between hard colloidal nanoparticles.

1.3.3 Colloids

In this thesis, we mainly focus on a specific class of lyotropic liquid crystals, namely colloidal lyotropic liquid crystals [198]. *Colloids* are non-mixing suspensions of nano- or microsized particles of a certain state (gas/liquid/solid) in another substance of the same or different state. This includes, for example, foams (gas bubbles in a liquid), fog (water droplets in air), milk (liquid fat droplets in water) or blood (solid blood cells in liquid blood plasma). Due to the small size and low mass of the colloidal particles, their dynamics are mainly dominated by the interactions between themselves and

the Brownian motion caused by the surrounding solvent. External forces like gravitation, however, do not affect the colloidal system on the time scale for which they are usually studied in experiments. For large colloids on the micron-scale, gravity is certainly relevant, but we are not interested in these particular systems. This negligible influence of gravity distinguishes colloidal systems greatly from granular materials and makes them easier to study using computational techniques like simulations. Nevertheless, most colloids are also large enough to be seen using light microscopy. This makes them interesting for experiments.

Lipids and di-block copolymers are great examples of systems which feature complex electrostatic interactions between the LCs or the LC and the solvent and mainly self-assemble into ordered structures due to a dominant enthalpic component. In general the mesophases, however, arise as a result of minimizing the Helmholtz free energy F of the system, which has an energetic part U and an entropic part S, given by

$$F = U - T \cdot S. \tag{1.6}$$

The influence of entropy is often, in particular in popular science writing and even thermodynamic or statistical mechanics textbooks, misinterpreted and its part in creating ordered phases is not properly acknowledged. This is based on the flawed notion that entropy is often falsely, or overly simplistically, associated with an increase in disorder [199, 200, 201] rather than with the proper definition of the Boltzmann entropy as a measure for the configuration space Ω of the particles [202]

$$S = k_B \ln \Omega \tag{1.7}$$

with the Boltzmann constant k_B. Already 70 years ago, however, Onsager contradicted this misconception of equating entropy with randomness. By calculating and minimizing the free energy, Onsager predicted the orientational order of infinitely long hard spherocylinders satisfying $\frac{L}{D} \to \infty$ with length L and width D at high densities [203]. Hard colloidal particles only interact via volume exclusion, that is short-ranged, repulsive and infinitely steep interactions. To put it in other words the only restriction which prevents particles from roaming freely is that they are not allowed to overlap. For the purpose of this thesis, we define a colloid to primarily interact as such hard particles.

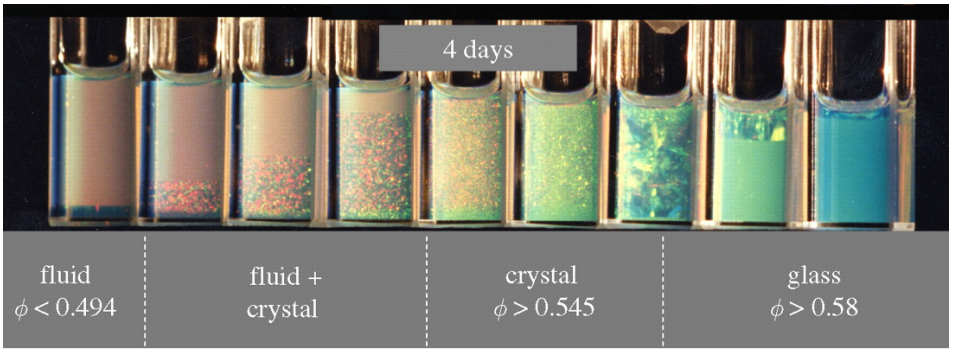

Figure 1.12: A colloid experiment showing crystallisation of hard spheres performed by Pusey and van Megen, which displays entropically driven order. This experiment shows that hard colloidal sphere systems way below the random close packing fraction ($\Phi = 0.634$ [204]) equilibrate into crystalline arrangements. This can be explained by maximizing the entropy of the system (reproduced with permission form [205]).

Onsager's spherocylinders are quintessentially entropy-driven. The mere interactions via collision imply that all allowed microscopic states are associated with a constant internal energy U. Considering Eq. (1.6), only the entropic term contributes to the free energy minimization. It also becomes apparent that in this case T, usually constant in experiments, does not affect mesophase formations either and can be interpreted as a scaling factor for the time-scale in which colloidal systems equilibrate. Even though it seems counter-intuitive, at first glance, that a system with a preferred orientations is able to adopt more configurations than systems with randomly distributed particle orientation, the constraint in the rotational degrees of freedom increases the translational freedom at high densities. Consequently, the spherocylinders try to orient parallel to each other to adopt a wider range of positions and so obtain more space to "wiggle" around without hitting neighbouring particles. Later the first computational simulations on the simplest hard particle assemblies – hard spheres – also illustrated translationally ordered arrangements due to entropy. Alder and Wainwright [206] observed a phase transition into a colloidal crystal far below the later determined random close packing density of 0.636 [204]. It was only with the beautiful demonstration and illustration by Pusey and van Megen [205, 207] in the 1980s that these simulation predictions could be confirmed experimentally (see Fig. 1.12). Also the longstanding discussions to this day about the two-dimensional equivalent hard disc system have to be mentioned when talking about the importance of entropy in self-assembly [208, 209].

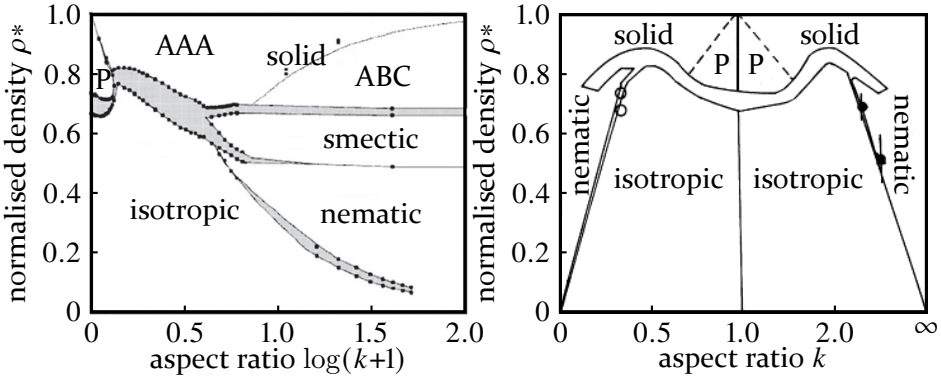

Figure 1.13: The phase diagrams of hard spherocylinders (left) and hard ellipsoids (right) in regards to density and aspect ratio of the particles. Despite their close similarity in shape, only the spherocylinders adopt a smectic phase. The figures are reproduced with permission from [237] (left) and [214] (right)

Since the simulations of Alder and Wainwright, a lot of theoretical [210, 211, 212] and computational [213, 214, 215, 216, 217, 218, 219, 220, 221, 222, 223] work has been done to predict the behaviour of several, differently shaped particles. Furthermore, the last decade has witnessed major improvements in our ability to synthesise a variety of colloids and nanoparticles with complex aspherical shapes in large numbers. These have revealed and confirmed that a great range of phases and behaviours (such as shear banding [224, 225]) are accessible to colloidal systems. Common shapes which can be prepared nowadays include multi-sphere particles [226, 227], ellipsoids [228, 229], rods [230, 231], polyhedra [232, 233], superballs [234] and even more elaborate particle shapes [235, 236].

It appears intuitive that, in hard particle assemblies, where excluded volume is the most important parameter, the particle shape is a crucial property of the system. The enormous influence of shape becomes apparent by comparing the phase behaviour of hard spherocylinders [213] and hard ellipsoids [214] obtained by simulations and displayed in Fig. 1.13. Even though the shapes of the individual particles seem rather similar the smectic phase is only assembled by spherocylinders and not by ellipses. Thus predicting the right phase behaviour of particles exclusively by looking at their shapes is a sheer impossible task[4], which makes the theoretical and computational colloidal studies of exceeding importance [236, 238]. By the same token, the

[4] Even though for some structures some necessary characteristics are suggested [221].

number of possible shapes promises a large variety of different obtainable structures [202]. Including other more complex interactions, obviously influences the phase behaviour of colloids [202, 239, 240]. Nevertheless, also for these systems, the entropic effect on the choice of the adopted phase has to be considered as the interaction terms are typically of the same order as the thermal energy k_BT. Often a concept of particle shape is held responsible for more complex nanostructures, rather than simply orientationally ordered nematic or smectic phases, for example TPMS.

Colloidal gyroid phases

Over ten years ago it was computationally asserted by Ellison and Cleaver that colloidal particles are able to adopt a gyroid structure [241]. For this they studied the phase behaviour of a purely repulsive hard pear-like particle system [241, 242, 243]. Even though the importance of entropy for the self-assembly of amphiphilic systems into the gyroid has long been recognised, and is implicit in both the molecular shape concept [50, 244] and the Helfrich formalism [245, 246], the pear-shaped colloid system is a particularly good system to widen our understanding of the entropic aspect in the formation of bicontinuous phases. Pear-shaped particles are tapered versions of ellipsoids, best thought of as prolate ellipsoids with a wider 'blunt' end and a narrower 'sharp' end. For appropriate parameter values, equilibrium ensembles of such pear-shaped particles adopt a curvy bilayer arrangement which was later identified as the double gyroid structure (see Fig. 1.10b). For a detailed description of this phase I refer to Chap. 4 and Fig. 4.1. Furthermore, they extracted the intertwined channel domains based on the positions of the blunt ends of the pears. Hence, the thin moiety of the pear-particles accumulates around the minimal surface. The pears adopt this liquid crystal phase in an arrangement that fills space fairly uniformly, at fluid-like densities. As these particles interact purely repulsively on a short range – using Gaussian hard overlap potentials – this system is purely entropy-driven.

The model based on Gaussian overlap potentials, however, is just an approximation of the pear-shape. Originally thought to be a sufficiently accurate representation of the hard pear-shape, it showcases small differences. In this connection, the question arises if these distinctions alter the phase behaviour like between ellipsoids and spherocylinders? Or is the phase stable in terms of minor shape changes? These questions are the context of this thesis and are explored in the subsequent eight chapters.

2 Computational models of pear-shaped liquid crystals

> *"The trouble with optimists is that they don't do well in a pear-shaped world."*
>
> – Lucy Kellaway

The realm of shapes and forms is vast and provides a virtually fathomless plethora of shapes for possible use as colloidal particles. Although the application of large-scale computer simulations in modern-day colloidal science fuels the hope to gain control over elaborate particle designs, the uncountable number of possible particle shapes seems overwhelming. Especially in morphological approaches, where it is assumed that the particle shape is a key determinant of the phase behaviour, the endeavour to find and conceive specific shapes, which are accompanied by interesting and complex mesophases, appears overwhelming. However, it is often assumed possible to make preliminary predictions about the distinctive collective behavioural patterns of molecules and to reduce the number of possible candidates significantly [221, 247]. Usually, this is done by capturing the morphological essence of the colloids and effectively encoding their shapes to a finite number of shape descriptors (real numbers). For example, some anisotropic ordered states, which occur in the equilibrium of thermal systems, are typically related to the existence of only a couple of morphological key features shared by the molecules forming those phases. For instance, it has been shown that close-packed structures, like those based on the γ-brass lattice, require particles with a high isoperimetric quotient, which indicates the ratio between the particle's volume and its surface area [221]. This concept of simplifying shape is common in other multi-particle based systems like granular materials [248, 249] or in non-equilibrium pattern formation [250, 251, 252], which, however, will not be covered in this thesis.

One of the most important properties which is crucial for the formation of globally orientationally ordered nematic or smectic phases, is the *aspect ratio* k. The aspect ratio is defined by the relation between length l and width d

of an object as $k = \frac{l}{d}$. In case of colloidal spherocylinders and ellipsoids it has been shown that a certain amount of elongation is needed to stabilise entropically driven nematic order without the support of attractive forces ($k > 3$ for ellipsoids [214] and $k > 4.7$ for spherocylinders [213, 237]). Also for disk-like ellipsoids, the particles have to be flat enough, so far enough from spherical to form columnar phases $k < 0.36$ [214]. Less aspherical ellipsoids or spherocylinders, but also the extensively studied globular platonic solids [253, 254] do not exhibit orientationally ordered mesophases in between the isotropic fluid and the crystalline solid. Only by stretching or flattening the latter into polyhedra/prisms and basically by increasing their aspect ratios to sufficiently high values, nematic and columnar phases can be obtained via self-assembly, respectively [219, 221, 222].

Nonetheless, even in this arguably simplest case of asphericity – namely elongated particles – it is still important to distinguish between the exact analytical shapes of ellipsoids and spherocylinders. This manifests in the lack of a smectic phase for ellipsoids [214], whereas spherocylinders, which only differ slightly, spontaneously form a smectic mesophase for $k > 4.1$ [213, 237]. Thus the inter-particle differences have to be considered to obtain the more specific details of the molecules' phase behaviours. This hints at a conceivable issue that for more complex mesophases than "simply" globally orientational ordered phases the exact shape plays an even more crucial role in self-assembly.

2.1 Definition of pear shape

In this thesis, we address the spontaneous behaviour of particles which feature another shape-defining property besides its elongation. The particle trait in question, called *pear-shapedness*, is a measure for the head-tail-asymmetry of elongated molecules without inversion symmetry. It can be described by an effective tapering of colloids (see Fig. 2.1), which is a promising candidate to form much more complex and symmetric phases than the "simple" global alignment of particles along a director. The interest in tapering is based on the already mentioned copolymers and lipids which adopt a cone-like shape (without inversion symmetry) to create TPMS structures (see in Sec. 1.3.2). In terms of colloids, the impact of tapering on self-assembled structures is best studied on axially symmetric pear-shaped particles, reminiscent of tapered prolate ellipsoids. Those particles have also shown their potential to form highly complex structures, like the Ia$\bar{3}$d double

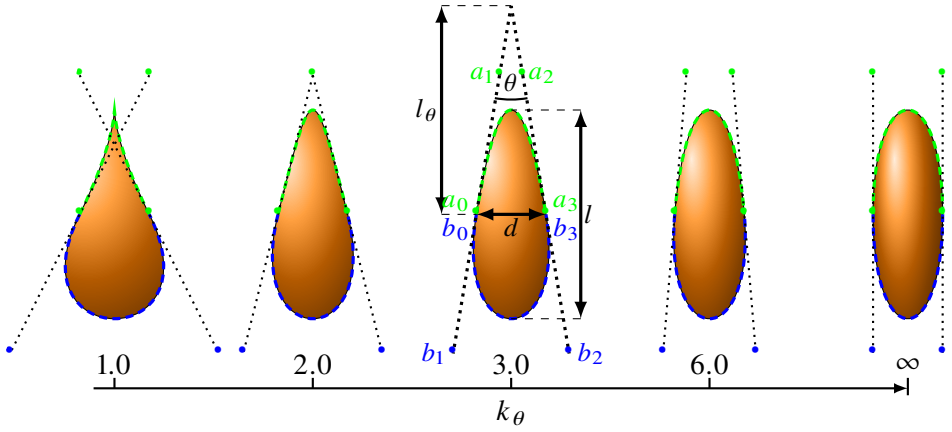

Figure 2.1: The contours of differently tapered pear-shaped particles with aspect ratio $k = 3$. The corresponding tapering parameter k_θ is indicated underneath the cross-sections. Each shape is generated by two Bézier-curves forming the bottom (blue) and the upper (green) half. The dots determine the positions of the anchor points. The tapering angle is spanned by the two tangents at both sides of the contours. Pear-shaped particles with $k_\theta < 2$ are concave (see very left pear).

gyroid phase [241], and hence, are an excellent model system to analyse further in more detail. Moreover, those particles can be naturally compared to ellipsoidal colloids which have been studied in great detail and can be used as a reference.[1]

The contour, from which the pear is generated as a body of revolution, is defined by a set of cubic Bézier-curves [243] in two-dimensional Euclidean space. In general, Bézier-curves are described in terms of their anchor points $\mathbf{a}_i$ by

$$\mathbf{B}(t) = (1-t)^3\mathbf{a}_0 + 3t(1-t)^2\mathbf{a}_1 + 3t^2(1-t)\mathbf{a}_2 + t^3\mathbf{a}_3. \tag{2.1}$$

To be more specific, the silhouettes are analytically described by two Bézier-curves forming the upper and bottom half of the pear-shape. The anchor points $\mathbf{a}_i$ of the upper half are chosen as

$$\mathbf{a}_0 = \begin{pmatrix} 0.5d \\ 0 \end{pmatrix} \quad \mathbf{a}_1 = \begin{pmatrix} 0.5d\frac{k_\theta - \frac{2}{3}k}{k_\theta} \\ \frac{2}{3}l \end{pmatrix} \quad \mathbf{a}_2 = \begin{pmatrix} -0.5d\frac{k_\theta - \frac{2}{3}k}{k_\theta} \\ \frac{2}{3}l \end{pmatrix} \quad \mathbf{a}_3 = \begin{pmatrix} -0.5d \\ 0 \end{pmatrix}. \tag{2.2}$$

[1] In fact, the ellipsoid is the limit $k_\theta \to \infty$ of the pear-shape defined below.

Analogously the anchor points $\mathbf{b}_i$ of the bottom half are selected as

$$\mathbf{b}_0 = \begin{pmatrix} 0.5d \\ 0 \end{pmatrix} \quad \mathbf{b}_1 = \begin{pmatrix} 0.5d\frac{k_\theta+\frac{2}{3}k}{k_\theta} \\ -\frac{2}{3}l \end{pmatrix} \quad \mathbf{b}_2 = \begin{pmatrix} -0.5d\frac{k_\theta+\frac{2}{3}k}{k_\theta} \\ -\frac{2}{3}l \end{pmatrix} \quad \mathbf{b}_3 = \begin{pmatrix} -0.5d \\ 0 \end{pmatrix}. \tag{2.3}$$

This choice of anchor points ensures a differentiable outline. The resulting contour is the basis from which we generate a three-dimensional object as a solid of revolution, henceforth referred as "pear-shape". In Fig. 2.1 the cross-sections of some exemplary pears are depicted with $k = 3$ and different values of k_θ described by two Bézier-curves. All of them exhibit thick or blunt bottom ends and thin pointy ends at the top and hence, feature an adjustable tapering.

For the analytical description of the pear-shape in Eq. (2.2) and Eq. (2.3), the degree of tapering is expressed by a *tapering parameter*

$$k_\theta = \frac{1}{2}\arctan\left(\frac{\theta_k}{2}\right) \tag{2.4}$$

with the tapering angle θ_k. For pears θ_k is spanned by the tangents at the central anchor points $\mathbf{a}_0/\mathbf{b}_0$ and $\mathbf{a}_3/\mathbf{b}_3$ on both sides of its contour. Alternatively $k_\theta = \frac{l_\theta}{d}$ can be described as the ratio between the distance of the center of the particle to the position where both of the tangents l_θ meet and d (see Fig. 2.1). This definition implies a very small tapering parameter for very cone-like molecules whereas for $k_\theta \to \infty$ the object turns more and more ellipsoidal and therefore symmetrical. It becomes apparent that the pears are separated into two types. For $k_\theta \geq \frac{2}{3}k$ the pears are convex. Otherwise for $k_\theta < \frac{2}{3}k$ the colloids are concave.

2.2 Pear-shaped particle models in simulations

2.2.1 Hard-core potentials

In order to perform numerical simulations, we have to translate the different pear-shapes into suitable potentials between the molecules. In computational physics, colloids are often identified as hard core particles which are solely interacting via their excluded volume. The hard potential U_{ij} between two objects B_i and B_j is defined by

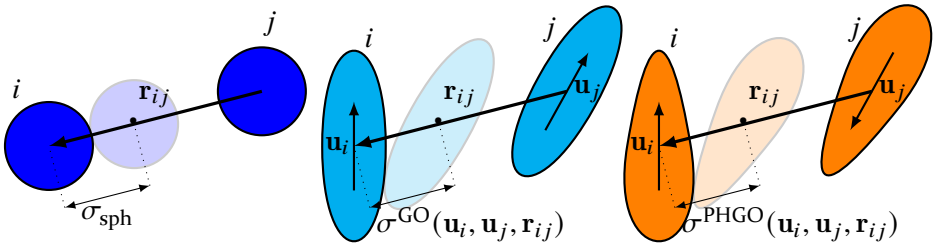

Figure 2.2: The concept of contact functions σ for spheres, ellipsoids and pear-shaped particles. For spheres σ_{sph} is constant and equal to the diameter of the spheres. For ellipsoids and pears the contact function is dependent on the relative arrangement of the particles to each other encoded within the distance vector $\mathbf{r}_{ij}$ and the orientation vectors $\mathbf{u}_i$ and $\mathbf{u}_j$.

$$U_{ij} := \begin{cases} 0, & \text{if } B_i \cap B_j = \emptyset \\ \infty, & \text{if } B_i \cap B_j \neq \emptyset. \end{cases} \tag{2.5}$$

Consequently, the particles only influence their nearest neighbours directly if they overlap. Thus, the interactions of particles with perfectly hard-core potentials can be interpreted as collision-like, where the force is only non-zero (and, in fact, infinite) when the particles touch.

The hard-core interactions of spheres can be controlled mathematically in a more practical way by a *contact distance* σ. Here, the decision if two spheres overlap is rephrased in terms of the Euclidean distance $r_{ij} = |\mathbf{r}_i - \mathbf{r}_j|$ between the centers $\mathbf{r}_i$ and $\mathbf{r}_j$ of the two molecules. Also the potential can be rewritten as

$$U_{ij} := \begin{cases} 0, & \text{if } r_{ij} \geq \sigma \\ \infty, & \text{if } r_{ij} < \sigma. \end{cases} \tag{2.6}$$

Therefore, r_{ij} has to be at least σ, where the colloids are exactly in contact, or greater to prevent intersections. For mono-disperse spherical particles it is easy to argue that the contact $\sigma_{\text{sph}} = 2r_{\text{sph}}$ is twice the sphere radius r_{sph} (see Fig. 2.2).

For aspherical particles the analytical description of σ often becomes non-trivial. On the one hand, σ does not stay constant for arbitrary shapes. On the other hand, σ in general is also defined as a *contact function* $\sigma(\mathbf{u}_i, \mathbf{u}_j, \hat{\mathbf{r}}_{ij})$ dependent on the orientation vectors of the particles $\mathbf{u}_i$ and $\mathbf{u}_j$ and the normalised distance vector $\hat{\mathbf{r}}_{ij} = \frac{\mathbf{r}_{ij}}{r_{ij}}$. These three vectors collectively encode the

exact arrangement of the particles relative to each other, since we assume uni-axial (rotationally symmetric) particles. One of the few examples for which the distances of closest approach has been determined analytically is for hard spherocylinders [203, 255]. Nevertheless, only small changes, like removing the caps at the end of the spherocylinders, can make the calculation of $\sigma(\mathbf{u}_i, \mathbf{u}_j, \hat{\mathbf{r}}_{ij})$ much more complicated (see collision detection of rigid cylinders [256]) or even analytically unpredictable. Despite the fact that in two dimensions ellipses can be treated analytically [257], the exact contact profile has to be calculated numerically for their three-dimensional ellipsoidal counterparts as its solution requires a sixth-order polynomial [258]. As the pear-shapes are even more complicated than ellipsoids it is rather unlikely that the exact analytical description of its contact function can be derived either.

Hard pears of revolution (HPR) contact function

A simple idea to model the pear-shape without its exact analytical contact function is to compose the particle out of multiple spherical fragments, which in total roughly follow the Bézier-curves. However, these "snowman" particles tend to crystallise or vitrify as they interlock due to the concave features of their non-smooth surfaces [220, 259, 260, 261] and do not form liquid crystal phases. Also for other multi-sphere approaches, issues in regards to degraded smoothness of the particle surface have been raised earlier [262, 263, 264]. For hard-core pears, we use an alternative (but computationally very slow) approach which is kept more closely to Eq. (2.5) and based on densely sampled triangulated meshes of the three-dimensional pear surface of revolution (see Fig. 2.3). Here, the particles are treated as multifaceted polyhedra such that the surface mesh T is composed out of $N_\triangle \approx 1000$ triangles $t_\alpha \in T$ with

$$\begin{aligned} \partial B &= \bigcup_{\alpha=1}^{N_\triangle} t_\alpha \qquad \text{and} \\ \emptyset &= t_\alpha \cap t_\beta \quad \text{if } \alpha \neq \beta. \end{aligned} \tag{2.7}$$

Two particle meshes T_i and T_j with distance $\mathbf{r}_{ij}$ and orientations $\mathbf{u}_i$ and $\mathbf{u}_j$ are considered as overlapping if one can find at least one pair of triangles $\{t^{(i)}, t^{(j)}\}$ which intersects:

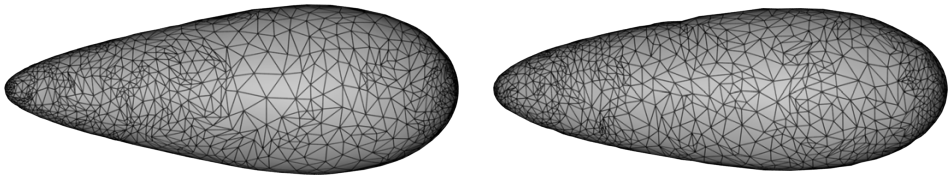

Figure 2.3: Exemplary triangulations of pear-shaped particle surfaces which are used to determine the contact of two objects in the HPR model. The meshes are represented by pear-shaped particles with $k = 3$ and $k_\theta = 2$ (left) and $k_\theta = 3.5$ (right).

$$U_{ij} := \begin{cases} \infty, & \text{if } \exists\{t^{(i)} \in T_i, t^{(j)} \in T_j\} : t^{(i)} \cap t^{(j)} \neq \emptyset \\ 0, & \text{else} \end{cases} \tag{2.8}$$

This model to determine the overlap of two particles will be called the hard pears of revolution (HPR) model. While giving the most accurate results for the contacts of pear-shaped particles the algorithm to detect collisions for polyhedra is very time-expensive if a large number of triangles are needed to catch all the pear details. Even by enhancing the performance by a hierarchical method based on oriented bounding boxes to find the potentially intersecting triangle quicker and the use of the separating axis theorem [265, 266, 267], the algorithm stays rather slow. As a result, only small simulations with a small number of particles ($\lesssim 2000$ particles) are performed.[2] Additionally, this approach is only suitable for Monte Carlo based simulations (see Sec. 3.2.2). Despite all these disadvantages, it is one of the most efficient methods to represent the exact contact function of pear-shaped particles in respect to the Bézier-curve representation and therefore, will be used in the following chapters. We will refer to this effective contact function as σ^{HPR}. It is also conceivable to apply other algorithms to represent pear-shaped particles which identify the exact contact distances for ellipsoids and might be possible to be derived for pears [270, 271]. Those are, however, de facto even more impractical than meshes in terms of computational time for simulation purposes.

Hard pear-sphere (HPS) contact function

For the interactions between a hard sphere and pear-shaped particle, a similar approach is implemented as the one between two hard pears of revolution.

[2] Often the triangulated mesh approach is used with even smaller particle numbers [268, 269]

However, the examination of the overlap reduces to a two-dimensional problem as we are dealing with a rotational symmetric pear and a rotational invariant sphere. This reduction in dimensionality is given by considering to projections of the colloids onto a plane which is spanned by the orientation of the pear $\mathbf{u}_i$ and the distance vector $\mathbf{r}_{ij}$. Consequently, we do not have to use a mesh of both particle species to determine their overlap but instead can check if the sphere cuts the contour line defined by the intersection of the projection plane and the pear-shaped particle. This decreases the complexity of the numerical calculations significantly.

To implement this overlap algorithm we first sample the Beziér curve, which defines the pear-shaped particle on the projection plane, by a set of points

$$c_\alpha = x_\alpha \cdot \frac{\hat{\mathbf{r}}_{\mathbf{ij}} - (\mathbf{u}_i \cdot \hat{\mathbf{r}}_{ij})\mathbf{u}_i}{\sqrt{\hat{\mathbf{r}}_{\mathbf{ij}}\hat{\mathbf{r}}_{\mathbf{ij}} - (\mathbf{u}_i \cdot \hat{\mathbf{r}}_{ij})^2}} + y_\alpha \cdot \mathbf{u}_i \in C(\mathbf{u}_i, \hat{\mathbf{r}}_{ij}) \tag{2.9}$$

with the coordinates x_α and y_α in the projection plane coordinate system (see Fig. 2.4). The contour $C(\mathbf{u}_i, \hat{\mathbf{r}}_{ij})$ of a pear-shaped particle with orientation $\mathbf{u}_i$ intersects a sphere with radius r_{sph} and distance $\mathbf{r}_{ij}$ if one can find at least one point $c_i \in C(\mathbf{u}_i, \hat{r}_{ij})$ which is closer to the center of the sphere than its radius:

$$U_{ij} := \begin{cases} \infty, & \text{if } \exists c_i \in C(\mathbf{u}_i, \hat{\mathbf{r}}_{ij}) : \text{dist}(c_i, \mathbf{r}_{ij}) < r_{\text{sph}} \\ 0, & \text{else} \end{cases} \tag{2.10}$$

This determination criterion can also be translated to a contact function σ^{HPS}. To do so, the closest point on the pear contour c_α to the neighbouring sphere is determined. Based on this point, the contact function is given by:

$$\sigma^{\text{HPS}}(\mathbf{u}_i, \hat{\mathbf{r}}_{ij}) = \begin{cases} A(\mathbf{u}_i, \hat{\mathbf{r}}_{ij}), & \text{if } r_s < |y_\alpha \sqrt{1 - (\mathbf{u}_i \cdot \hat{\mathbf{r}}_{ij})^2} - x_\alpha (\mathbf{u}_i \cdot \hat{\mathbf{r}}_{ij})| \\ A(\mathbf{u}_i, \hat{\mathbf{r}}_{ij}) + B(\mathbf{u}_i, \hat{\mathbf{r}}_{ij}), & \text{else} \end{cases} \tag{2.11}$$

Here we use an abbreviation for the first and second term of the contact function

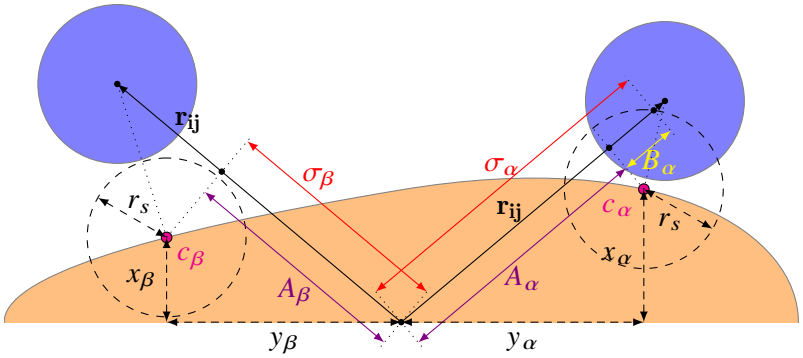

Figure 2.4: Determination the contact distance σ between a hard pear-shaped particle and a hard sphere with radius r_s according to Eq. (2.11). The overlap is based on a point set on the pear contour with c_α is the closets point to the sphere. The contact distance is composed of a first term A_α and a second term B_αi defined in Eq. (2.12).

$$\begin{aligned} A(\mathbf{u}_i, \hat{\mathbf{r}}_{ij}) &= x_\alpha \sqrt{1 - (\mathbf{u}_i \cdot \hat{\mathbf{r}}_{ij})^2} + y_\alpha (\mathbf{u}_i \cdot \hat{\mathbf{r}}_{ij}) \\ B(\mathbf{u}_i, \hat{\mathbf{r}}_{ij}) &= \sqrt{r_s^2 - (y_\alpha \sqrt{1 - (\mathbf{u}_i \cdot \hat{\mathbf{r}}_{ij})^2} - x_\alpha (\mathbf{u}_i \cdot \hat{\mathbf{r}}_{ij}))^2}, \end{aligned} \tag{2.12}$$

based on simple geometric arguments which are explained in the sketch of Fig. 2.4. Note here, that the first case in Eq. (2.11) never identifies an overlap of the particles and is usually outside the cut-off range explained below. Therefore, only the second case has to be considered for the numerical calculations.

Hard Gaussian overlap (HGO) contact function

For simulations of large systems, an approximation to the hard-core contact function, based on the so-called *Gaussian overlap* model (GO), has been proposed which still has hard core interactions but a slight "non-additivity". The GO model was originally introduced by Berne and Pechukas [272] where they derived an approximation of $\sigma(\mathbf{u}_i, \mathbf{u}_j, \hat{\mathbf{r}}_{ij})$ from ellipsoidal Gaussian distributions for identical uniaxial ellipsoids of length d of the small axis and length l of the large axis. It yields

$$\sigma^{\mathrm{GO}}(\mathbf{u}_i, \mathbf{u}_j, \hat{\mathbf{r}}_{ij}) = \sigma_0 \left(1 - \frac{\chi}{2}\left[\frac{(\mathbf{u}_i \cdot \hat{\mathbf{r}}_{ij} + \mathbf{u}_j \cdot \hat{\mathbf{r}}_{ij})^2}{1 + \chi(\mathbf{u}_i \cdot \mathbf{u}_j)} + \frac{(\mathbf{u}_i \cdot \hat{\mathbf{r}}_{ij} - \mathbf{u}_j \cdot \hat{\mathbf{r}}_{ij})^2}{1 - \chi(\mathbf{u}_i \cdot \mathbf{u}_j)}\right]\right)^{-\frac{1}{2}}, \tag{2.13}$$

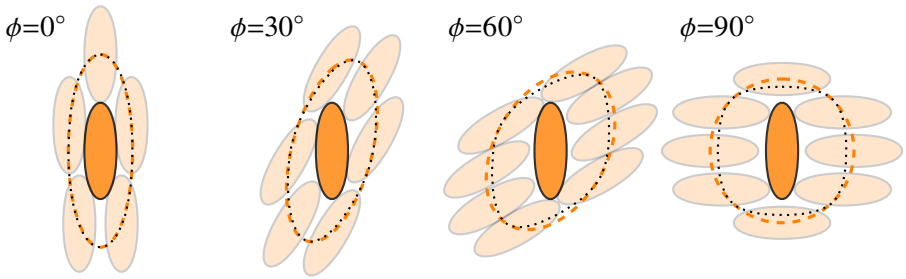

Figure 2.5: The contact profiles according to the HGO model (- - -) and the HPR model with $k_\theta = \infty$ (·····) for identical ellipsoids with $k = 3$ at different angles between the molecules $\phi = \arccos(\mathbf{u}_i \cdot \mathbf{u}_j)$ in the xz-plane. The surrounding ellipsoids are positioned in contact according to the HGO model.

where $\sigma_0 = \sqrt{2}d$ is the length parameter and $\chi = \frac{l^2-d^2}{l^2+d^2}$ defines the shape anisotropy parameter. Based on this expression, the approximation can be extended to the generalised hard Gaussian overlap (HGO) function for mixtures of ellipsoids

$$\sigma^{\mathrm{HGO}}(\mathbf{u}_i, \mathbf{u}_j, \hat{\mathbf{r}}_{ij}) = \sigma_0^{\mathrm{HGO}} \times \left(1 - \chi_{\mathrm{HGO}} \left[\frac{(\alpha^2_{\mathrm{HGO}}(\mathbf{u}_i \cdot \hat{\mathbf{r}}_{ij})^2 + \alpha^{-2}_{\mathrm{HGO}}(\mathbf{u}_j \cdot \hat{\mathbf{r}}_{ij})^2 - 2\chi_{\mathrm{HGO}}(\mathbf{u}_i \cdot \hat{\mathbf{r}}_{ij})(\mathbf{u}_j \cdot \hat{\mathbf{r}}_{ij})(\mathbf{u}_i \cdot \mathbf{u}_j)}{1 - \chi^2_{\mathrm{HGO}}(\mathbf{u}_i \cdot \mathbf{u}_j)^2}\right]\right)^{-\frac{1}{2}} \tag{2.14}$$

by deriving it from dissimilar Gaussian distributions [273]. Here σ^{HGO} and χ_{HGO} are generalisations of the parameters in Eq. (2.13). Additionally, there is a second shape anisotropy parameter α. For a pair of ellipsoidal molecules (i, j) with small axis lengths (d_i, d_j) and long axis lengths (l_i, l_j) the parameter are defined as

$$\begin{aligned} \sigma_0^{\mathrm{HGO}} &= (d_i^2 + d_j^2)^{\frac{1}{2}}, \\ \chi_{\mathrm{HGO}} &= \sqrt{\left(\frac{(l_i^2 - d_i^2)(l_j^2 - d_j^2)}{(l_j^2 + d_i^2)(l_i^2 + d_j^2)}\right)} \quad \text{and} \\ \alpha^2_{\mathrm{HGO}} &= \sqrt{\left(\frac{(l_i^2 - d_i^2)(l_j^2 + d_i^2)}{(l_j^2 - d_j^2)(l_i^2 + d_j^2)}\right)}. \end{aligned} \tag{2.15}$$

The HGO contact profile is depicted in Fig. 2.5, which shows that it represents the true ellipsoid shape for aligned particles satisfactorily but overestimates the overlap for particles perpendicular to each other slightly.

Pear-shaped hard Gaussian overlap (PHGO) contact function

To extend Eq. (2.14) even further and to give a formula for an approximated contact function of pears, we can substitute d and l by $d(\mathbf{u}, \hat{\mathbf{r}})$ and $l(\mathbf{u}, \hat{\mathbf{r}})$, respectively. In doing so, the widths and lengths of the ellipsoids do not stay constant but depend on their relative arrangement to each other. This technique gives us the opportunity to mould convex shapes out of a multitude of ellipsoids, which locally coincide with the associated morphology. Due to the close resemblance of pears and ellipsoids, this method has been adapted to pear-shaped particles [243]. Here, each colloid does not interact with the pear directly but with a "virtual" ellipsoid which describes the pear in this specific constellation of particles best (see Fig. 2.6). For uni-axial rotationally symmetric molecules the width and length, in general, are written as polynomials in terms of the scalar product $(\mathbf{u}\cdot\hat{\mathbf{r}})$

$$\begin{aligned} d(\mathbf{u}, \hat{\mathbf{r}}) &= \sum_{n=0}^{N_d} k_d^{(n)} (\mathbf{u}\cdot\hat{\mathbf{r}}) \\ l(\mathbf{u}, \hat{\mathbf{r}}) &= \sum_{n=0}^{N_l} k_l^{(n)} (\mathbf{u}\cdot\hat{\mathbf{r}}) \end{aligned} \tag{2.16}$$

with the polynomial amplitudes $k_d^{(n)}$ and $k_d^{(n)}$ of order n. Putting theses expressions into Eq. (2.14) gives us a contact function for pear-shaped particles

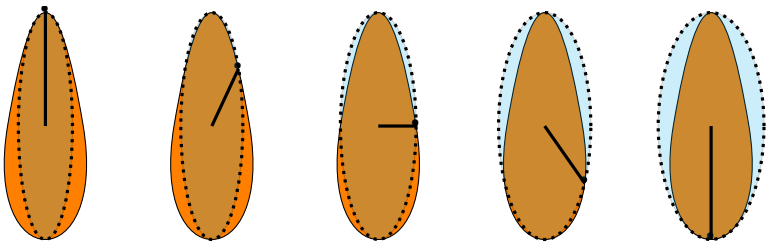

Figure 2.6: The schematics of the PHGO potential describing a pear particle with $k = 3$ and $k_\theta = 3$ are shown. Depending on the direction of the other object, the morphology is locally described by different "virtual" ellipsoids. These ellipsoids are determined by expressing their length and width by polynomials (see Eq. (2.16)) and by fitting them such that the virtual ellipsoids describe the Bézier-curves best.

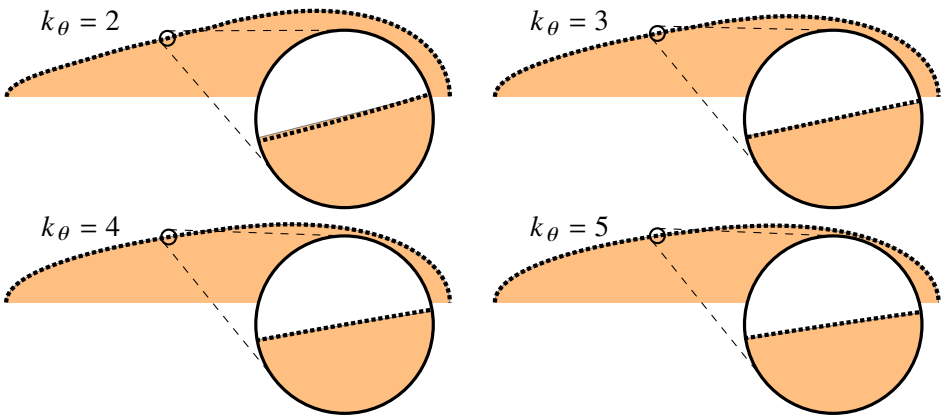

Figure 2.7: The effective pear shape modelled by the virtual ellipsoid after fitting them to the Bézier-curves. The orange object shows half of the cross-sections of different pear-shapes generated with the Bézier approach. The black dotted lines, obtained by the virtual ellipsoids after fitting, coincide nicely with the outline of the desired shape.

$$\sigma^{\mathrm{PHGO}}(\mathbf{u}_i,\mathbf{u}_j,\hat{\mathbf{r}}_{ij}) = \sigma_0^{\mathrm{PHGO}} \times \left(1- \chi_{\mathrm{PHGO}} \left[\frac{(\alpha_{\mathrm{PHGO}}^2(\mathbf{u}_i\cdot\hat{\mathbf{r}}_{ij})^2+\alpha_{\mathrm{PHGO}}^{-2}(\mathbf{u}_j\cdot\hat{\mathbf{r}}_{ij})^2-2\chi_{\mathrm{PHGO}}(\mathbf{u}_i\cdot\hat{\mathbf{r}}_{ij})(\mathbf{u}_j\cdot\hat{\mathbf{r}}_{ij})(\mathbf{u}_i\cdot\mathbf{u}_j)}{1-\chi_{\mathrm{PHGO}}^2(\mathbf{u}_i\cdot\mathbf{u}_j)^2} \right] \right)^{-\frac{1}{2}} \tag{2.17}$$

with

$$\sigma_0^{\mathrm{PHGO}}(\mathbf{u}_i,\mathbf{u}_j,\hat{\mathbf{r}}_{ij}) = (d_i(\mathbf{u}_i,\hat{\mathbf{r}}_{ij})^2 + d_j(\mathbf{u}_j,\hat{\mathbf{r}}_{ij})^2)^{\frac{1}{2}}, \tag{2.18}$$

$$\chi_{\mathrm{PHGO}}(\mathbf{u}_i,\mathbf{u}_j,\hat{\mathbf{r}}_{ij}) = \sqrt{\left(\frac{(l_i(\mathbf{u}_i,\hat{\mathbf{r}}_{ij})^2 - d_i(\mathbf{u}_i,\hat{\mathbf{r}}_{ij})^2)(l_j(\mathbf{u}_j,\hat{\mathbf{r}}_{ij})^2 - d_j(\mathbf{u}_j,\hat{\mathbf{r}}_{ij})^2)}{(l_j(\mathbf{u}_j,\hat{\mathbf{r}}_{ij})^2 + d_i(\mathbf{u}_i,\hat{\mathbf{r}}_{ij})^2)(l_i(\mathbf{u}_i,\hat{\mathbf{r}}_{ij})^2 + d_j(\mathbf{u}_j,\hat{\mathbf{r}}_{ij})^2)} \right)}$$

and

$$\alpha_{\mathrm{PHGO}}(\mathbf{u}_i,\mathbf{u}_j,\hat{\mathbf{r}}_{ij})^2 = \sqrt{\left(\frac{(l_i(\mathbf{u}_i,\hat{\mathbf{r}}_{ij})^2 - d_i(\mathbf{u}_i,\hat{\mathbf{r}}_{ij})^2)(l_j(\mathbf{u}_j,\hat{\mathbf{r}}_{ij})^2 + d_i(\mathbf{u}_i,\hat{\mathbf{r}}_{ij})^2)}{(l_j(\mathbf{u}_j,\hat{\mathbf{r}}_{ij})^2 - d_j(\mathbf{u}_j,\hat{\mathbf{r}}_{ij})^2)(l_i(\mathbf{u}_i,\hat{\mathbf{r}}_{ij})^2 + d_j(\mathbf{u}_j,\hat{\mathbf{r}}_{ij})^2)} \right)}.$$

Even though there is no particular rule how to choose the degrees N_d and N_l of the polynomials, it has been shown that for $N_d = 10$ and $N_l = 1$ the pear-shape can be modeled in good agreement with the Bézier-curves and

therefore, can be represented by the virtual ellipsoids accurately [243]. Here, $k_d^{(n)}$ and $k_d^{(n)}$ are fitted via a least squares method to its contour according to the particle-point contact function

$$\sigma(\mathbf{u}_i, \hat{\mathbf{r}}_{ij}) = \frac{d_i(\mathbf{u}_i, \hat{\mathbf{r}}) \cdot l_i(\mathbf{u}_i, \hat{\mathbf{r}})}{\sqrt{l_i^2(\mathbf{u}_i, \hat{\mathbf{r}}) - (l_i^2(\mathbf{u}_i, \hat{\mathbf{r}}) - d_i^2(\mathbf{u}_i, \hat{\mathbf{r}})) \cdot (\mathbf{u}_i \cdot \hat{\mathbf{r}}_{ij})^2}}, \tag{2.19}$$

where we used Eq. (2.17) with $d_j = 0$, $l_j = 0$ and $\mathbf{u}_j = 0$. Fig. 2.7 shows that the profiles match the Bézier curves closely. In the following we will refer to this model as the *pear-shaped hard Gaussian overlap* (PHGO) model and denote the associated contact function by σ^{PHGO}.

Self-non-additive properties of the PHGO model

In Fig. 2.8 the contact profiles of σ^{PHGO} and σ^{HPR} are compared. It becomes apparent that the two models show for angles between 50° and 130° considerable differences. In this regime the PHGO profile often overestimates the overlap, which leads to gaps between the particles. This, however, is inherited from a similar error between the HGO and HER (hard ellipsoids of revolution) potential of the ellipsoid as seen in Fig. 2.5. The HGO model is designed to imitate the hard potential for parallel configurations closely. This is important to represent the orientationally ordered phases, like nematic, as precise as possible. Here large angles between neighbouring particles hardly occur such that poor representation of those angles does not preponderate. We can make the same argument for pears as we do not expect angles close to 90° for dense systems. For parallel or anti-parallel configurations, the different models coincide well. Note here, however, that for small angles an additional effect occurs. At around 30° the PHGO profile also occasionally underestimates the contact distance such that the pears overlap with their blunt ends.

In the following, we will use the term *self-non-additivity* to describe this combination between over- and underestimation of the contact distance. Conventionally, hard-core interactions are labelled non-additive, if in an athermal mixture the distance of closest approach σ_{AB} between species A and B is not restricted by additive constraints of the contact distance between particles of the same type: $\sigma_{AB} \neq 0.5(\sigma_{AA} + \sigma_{BB})$ [274, 275, 276, 277, 278]. A similar effect, however, also occurs in the mono-disperse PHGO particle system. This becomes apparent by explaining the choice of the prefix

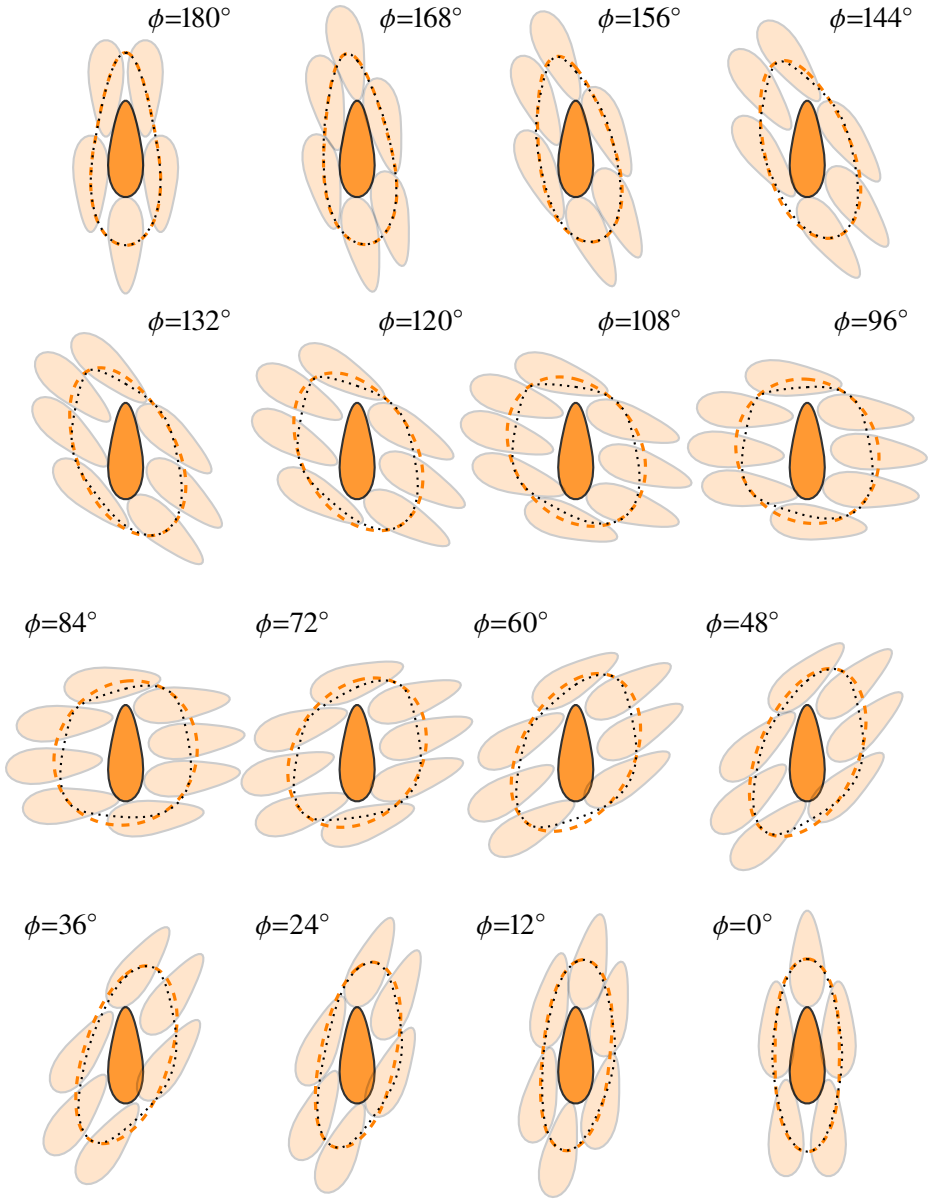

Figure 2.8: The contact profiles according to the PHGO model (- - -) and the HPR model (·····) for identical pear-shaped particles with $k = 3$ and $k_\theta = 3$ at different angles between the molecules $\phi = \arccos(\mathbf{u}_i \cdot \mathbf{u}_j)$ in the xz-plane. The surrounding pears are positioned in contact according to the PHGO model.

"self" in self-non-additivity which is illustrated by analysing the contact distance between the blunt ends of the pear-shaped particles in Fig. 2.8. For certain relative angles, the blunt ends overlap ($\phi = 36°$), whereas for other angles their contact coincides with the Bézier description ($\phi = 144°$). Similar behaviour is observed for the contact between the thin ends (gaps at $\phi = 108°$ and no gap at $\phi = 156°$). Hence, differently orientated pears can be interpreted as two distinct hard particle species with non-additive interactions. Moreover, the described angular dependency of the contact function implies that a true physical hard shape cannot copy the PHGO model.[3] Instead, the Bézier pear-shape has to be seen as the closest realisation of a real physical hard PHGO body.

In conclusion, the PHGO model does not perfectly mimic the pear-shape but is closely related and also inherits the most important features like the tapering towards one end and the aspect ratio. Additionally, the PHGO approximation is computationally very effective and moreover the only feasible way to analyse pear-shaped particles in large assemblies ($\gtrsim$2000 particles). However, even though the discrepancies between the HPR and PHGO model seem negligible, we will show that these distinctions have to be considered very well throughout this thesis (see Chap. 5 and specifically Chap. 6).

2.2.2 Soft-core Weeks-Chandler-Andersen (WCA) potential

In Molecular Dynamics simulations, soft approximations of hard potentials can be simulated much more efficiently than hard-core potentials as stated in Eq. (2.5) . We, therefore, now introduce a soft version of the pear-particle model, called PHGO-WCA, which 'softens' the non-additive PHGO potential into a slightly soft potential that can be used for MD simulations.

Additionally, hard-core particle potentials are only idealised versions of the observed steric interactions in many nanoparticle and colloidal systems in experiments [207, 279, 280, 281]. These interactions cause short range, strongly repulsive forces between the colloidal particles and are imitateted in a more realistic way by the *Weeks-Chandler-Andersen potential* (WCA) [282].

[3] Additional overlap rules (like adding non-additive features to the blunt ends see Sec. 6.4) are required to imitate the interactions between PHGO particles with physical hard shapes.

For identical spheres with diameter σ_{sph}, the WCA potential is a truncated and shifted Lennard-Jones potential

$$V_{ij}^{\text{WCA}} = \begin{cases} 4\epsilon_0 \left[\left(\frac{\sigma_{\text{sph}}}{r_{ij}} \right)^{12} - \left(\frac{\sigma_{\text{sph}}}{r_{ij}} \right)^{6} \right] + \epsilon_0, & \text{if } r_{ij} < 2^{\frac{1}{6}} \sigma_{\text{sph}} \\ 0, & \text{if } r_{ij} \geq 2^{\frac{1}{6}} \sigma_{\text{sph}}, \end{cases} \tag{2.20}$$

such that the potential energy rapidly increases if the particles are closer than the cut-off distance $r_{\text{cut}} = 2^{\frac{1}{6}} \sigma_{\text{sph}}$. This choice of r_{cut} at the minimum of the Lennard-Jones-potential ensures that the particles interact purely repulsively. The additional shift ϵ_0 sets the potential at $V_{ij}^{\text{WCA}}(r_{\text{cut}}) = 0$ and makes it simultaneously also differentiable. The parameter ϵ_0 also dictates how quickly the potential increases. The larger ϵ_0 the closer is the WCA potential to a hard-core potential. In the following we set ϵ_0 to 1. The difference to the hard-core is depicted in Fig. 2.9. To adapt the WCA potential to ellipsoids two suggestions have been made. The first application was originally introduced by Berne and Pechukas [272], where they simply replaced the sphere contact function with the contact function of ellipsoids in Eq. (2.13). The same can be done by using the contact function of pears σ^{PHGO}. This is equivalent to stretching the potential to fit the desired contact profiles. As a result the potential does not increase at the same rate for every possible two-particle configuration in contact and thus varies in softness by a great margin. If the cut-off distance r_{cut} is small, for example for pears placed side-to-side, the potential energy grows more steeply than for configurations with larger r_{cut} where the particles touch with their ends (see Fig. 2.9).

To remove this configurational dependency, a revised version was suggested a couple of years later [283] where the interface according to the contact functions is altered, not by stretching using the Lennard-Jones model, but by shifting the potential according to the Gay-Berne model. Here the WCA potential is written by

$$V_{ij}^{\text{PHGO}} = \begin{cases} 4\epsilon_0 (R^{12} - R^6) + \epsilon_0, & \text{if } r_{ij} < r_{\text{cut}}, \\ 0, & \text{if } r_{ij} \geq r_{\text{cut}}, \end{cases} \tag{2.21}$$

with the distance parameter

$$R = \frac{\sigma_w}{r_{ij} - \sigma^{\text{PHGO}}(\mathbf{u}_i, \mathbf{u}_j, \hat{\mathbf{r}}_{ij}) + \sigma_w}. \tag{2.22}$$

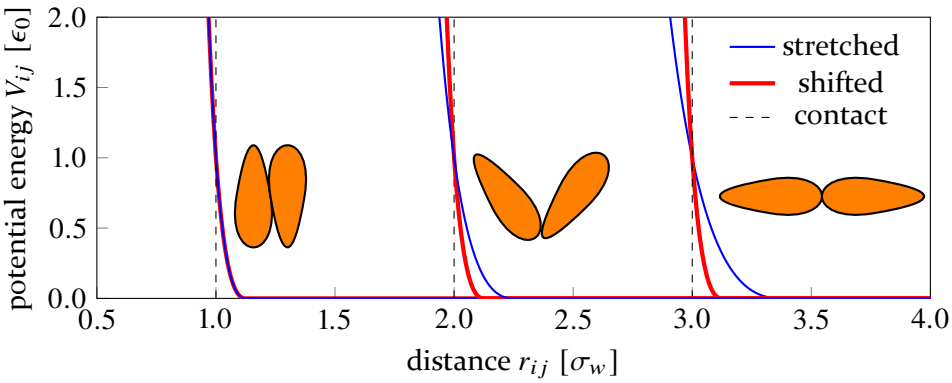

Figure 2.9: The Weeks-Chandler-Andersen potential, mimicking the steric interactions of pear-shaped particles for three different pear configurations. In the Lennard-Jones approach (see Eq. (2.20)), the potential is stretched to fit the contact function of the pear which leads to different softness for different configurations. This is resolved by the Gay-Berne model (see Eq. (2.21)) where the potential is shifted rather than stretched.

The factor $\sigma_w = \sqrt{0.5}$ is a necessary and arbitrarily chosen parameter, which sets up a unit of length as the pre-factor σ_0 in Eq. (2.18) is not constant for pear-shaped particles but is also dependent on the thickness of the virtual ellipsoids $d_i(\mathbf{u}_i, \mathbf{r})$ and $d_j(\mathbf{u}_j, \mathbf{r})$. Additionally, σ_w defines the effective width of the pear-shaped particle as well. To make the potential again overall purely repulsive, it is truncated at

$$r_{\text{cut}} = \sigma^{\text{PHGO}}(\mathbf{u}_i, \mathbf{u}_j, \hat{\mathbf{r}}_{ij}) + (2^{\frac{1}{6}} - 1)\sigma_w \,. \tag{2.23}$$

In the following we will mostly study pear-shaped particles with steric interactions by implementing the second version of the WCA potential based on the formulations by Gay and Berne. However, we will also compare it with perfect hard particle interactions according to σ^{HPR} to determine the major influence of minor changes in shape on the self-assembly in greater detail.

3 Simulation methods and structure analysis tools

> *"Since we cannot change reality, let us change the eyes which see reality."*
>
> – Nikos Kazantzakis

Computational methods, and in particular simulation methods, play a major role in canvassing the phase behaviour for families of experimentally available and (yet) unavailable particle shapes and are key tools for guiding the development of new particle synthesis techniques. Those methods have become very cost-effective and less time-consuming compared to experiments and allow scientists to implement delicate features of the particles more easily. Pear-shaped particles have not been synthesised as colloidal objects yet. Thus, in the case of this thesis, our simulation methods and theoretical descriptions of the collective properties of pears are regarded as preliminary studies of a hopefully upcoming experimental realisation of the system, even though the pear-shaped particles were originally investigated as a generic model for molecules [272].

In this thesis, our interest is in thermodynamically equilibrated phases of pear-shaped particles. In general, multi-particle systems in equilibrium are thermodynamically defined by a small number of parameters like their temperature T, pressure P or the number of particles N. Usually, this macroscopic view of thermodynamics and the study of the behaviour of these quantities is much more efficient to characterise physical phenomena than to deal with the dynamics of each particle on its own. Nevertheless, techniques which try to describe systems on this detailed microscopic level, like computational simulations, are essential tools to derive and predict macroscopic quantities. Even though we are by far not capable of analysing naturally-occurring microscopic systems with $O(10^{23})$ molecules with modern day computers, it is usually already enough to consider only a fraction of these systems for analysing multi-particle phenomena, like the self-assembly

of bicontinuous structures.[1] Thus, computational methods, which enable systems of sizes of "only" up to $O(10^6)$ to be studied [209, 285], are generally more than suitable and additionally less time consuming and more cost-effective than experiments. Hence, they were used to successfully predict multiple physical effects in colloidal and liquid crystal science and, therefore, play an inherent and integral part in soft matter physics today.

3.1 Statistical ensembles

In the following, we will briefly discuss the basic principles of statistical physics needed for the simulations of pear-shaped particles presented in this thesis. For a more detailed introduction, we refer to Ref. [286, 287] on which this section is loosely based.

3.1.1 Sampling

Time average

In the microscopic approach, systems in statistical physics are described by the positions $\mathbf{q}$ and momenta $\mathbf{p}$ of all atoms within the configuration. As we will deal mostly with anisotropic pear-shaped particles, also their orientational state in terms of an angular vector $\mathbf{\Theta}$ and angular momentum $\mathbf{L}$ is needed for a complete description. For N atoms this means that they collectively span a $2N_F \cdot N$-dimensional space, the so-called phase space Ω, where N_f is the number of degrees of freedom for each particle. Here $N_f = 5$ is composed of three translational and – for axially symmetric objects – two rotational degrees of freedom. A single point or microstate in this phase space is defined as $\Gamma^N = (\mathbf{q}^N, \mathbf{\Theta}^N, \mathbf{p}^N, \mathbf{L}^N) \in \Omega$ and contains the information of all positions, orientations, momenta and angular momenta of all particles. The value of a certain property $\mathcal{A}$ at this phase point Γ^N can be written as $\mathcal{A}(\Gamma^N)$.

In equilibrium, all microscopic realisations are uniformly distributed. Hence, the system tends towards a macrostate with macroscopic properties A which has the most microstates under given constraints (see Sec. 3.1.2 for the different possible constraints). As the equilibrated system evolves in time t, also $\Gamma^N(t)$ changes constantly by following its trajectory in the phase

[1] In experimental single chain lipid systems, for example, the gyroid structure contains roughly 90 lipids per unit cell [284].

space. Therefore, $\mathcal{A}$ cannot be directly related to the property of the equilibrated system that is measured in experiments but as an "instantaneous" value of the microscopic state which is exposed to fluctuations. By assuming that in equilibrium the phase space trajectory will visit all points in the phase space after a certain time t, known as the principle of ergodicity [288, 289], we obtain the macroscopic property A by calculating the *time average* of $\mathcal{A}(\Gamma^N)$ ideally over an infinite amount of time t_{obs}:

$$A = \langle \mathcal{A}(\Gamma^N) \rangle_{t_{\text{obs}}} = \lim_{t_{\text{obs}} \to \infty} \frac{1}{t_{\text{obs}}} \int_0^{t_{\text{obs}}} \mathcal{A}(\Gamma^N(t)) \mathrm{d}t. \tag{3.1}$$

Even though the time evolution can be easily carried out, for example by solving Newton's equation of motion (see Sec. 3.2.1), the infinite time frame for measuring observables as stated in Eq. (3.1) can obviously not be reached. However, if the simulation is averaged over a sufficiently long interval of time and assuming that the trajectory is, loosely speaking, a "representative equilibrium trajectory", it can be argued that our results coincide with real-world observations. In our computational studies, time is quantised such that the system is evolved in small time steps Δt over a large finite number of time steps τ_{obs} with $t_{\text{obs}} = \tau_{\text{obs}} \cdot \Delta t$ generating an array of dynamically obtained snapshots. Consequently, the equation can be rewritten as

$$A = \langle \mathcal{A}(\Gamma^N) \rangle_{t_{\text{obs}}} \approx \frac{1}{t_{\text{obs}}} \sum_{\tau=0}^{\tau_{\text{obs}}} \mathcal{A}(\Gamma^N(\tau \Delta t)) \Delta t = \frac{1}{\tau_{\text{obs}}} \sum_{\tau=0}^{\tau_{\text{obs}}} \mathcal{A}(\Gamma^N(\tau \Delta t)) \tag{3.2}$$

Here, again, we have to be careful to choose a sufficiently long t_{obs} such that the system is able to sample a satisfactory amount of the physically relevant part of the phase space with this finite time evolution. This includes setting smartly chosen initial conditions for the starting values of the particles to ensure a high degree of accuracy and to sample the phase space correctly. Additionally, an intelligently selected starting configuration can lead to shorter τ_{obs}. In general, this average calculation corresponds to an average of certain time frames of the system. The computational technique which uses this ansatz is called Molecular Dynamics and is explained in more detail in Sec. 3.2.1.

One advantage of Eq. (3.2) is that the sequence of time frames does not have to be necessarily in the right order or even from the same simulation run. This guarantees the reproducibility of the simulations and that the

average can be obtained over multiple measurements. The series in Eq. (3.2) could entice into the false assumption that non-physical sets, which are not collected by a technique simulating the passage of time of pear-shaped particle systems, are appropriate to be used. However, here we have to be careful as in these cases some conditions have to be met. To determine these conditions we have to address the alternative way to sample the system which leads to Gibbs-ensemble averaging.

Ensemble average

Besides the time average, the macroscopic properties of a system in thermal equilibrium can also be calculated by the *ensemble average*, also known as the statistical average, which was introduced by Gibbs [290]. An ensemble is defined as a collection of points in the phase space which share the same fixed thermodynamic parameters and which, consequently, are in the same thermodynamic state. The points Γ^N are distributed according to the phase-space density $f(\Gamma^N)$. Each point can be thought of as one copy of the same system following different trajectories measured at the same time rather than as one system with the same trajectory measured at different time steps. As each replica evolves in time, in principle the density distribution can change in time as well. However, as we are only interested in equilibrated states of the systems, we can assume that $f(\Gamma^N)$ stays constant $\frac{\partial f}{\partial t} = 0$ and, therefore, that the trajectories are stationary. Hence, it is reasonable to argue that if one trajectory is visiting all points in the phase space, each trajectory will also pass all phase points at some moment in time. Consequently, after a long enough time period, the obtained states are independent of the initial states. As a consequence, it does not matter if we follow one single pear-shaped particle system and average its property in time or if the average is integrated over a bundle of replicas of the ensemble all frozen in time. The time average in Eq. (3.1) can be replaced by the ensemble average

$$A = \langle \mathcal{A}(\Gamma^N) \rangle_{\text{ensemble}} = \int \mathcal{A}(\Gamma^N) f(\Gamma^N) \mathrm{d}\Gamma^N. \tag{3.3}$$

Similar to the time average approach, we cannot hope to reach the number of microscopic copies, related to an ensemble for our numerical calculations, and therefore perfect ergodicity.

In section 3.2.2, however, we will show a method, the so-called Metropolis Monte Carlo method, in generating a sequence of n states of the phase space $(\Gamma_i^N)_{i=0}^n = (\Gamma_0^N, \Gamma_1^N, \ldots, \Gamma_n^N)$ out of one single initial state Γ_0^N. Here, it is important that the set is also correctly weighted by $f(\Gamma^N)$. With this approach, the different states are not correlated in time and even unphysical steps between two states, where successive states are not connected through the system's time evolution, are allowed. Thus, observables which describe the dynamics of the system like diffusion cannot be calculated with this approach.

Finally, we have to make the same argument as for the time average that the initial state has to be chosen wisely to assure an accurate sampling of the phase space and counteract the fact that we are not able to cover all possible microstates. This can be countered, for example, by multiple simulations with different initial conditions. Additionally, the set of visited states has to be sufficiently large to ensure accurate results. By using a sequence of n states Γ_i^N, which correctly represents the phase-space density $f(\Gamma^N)$, Eq. (3.3) can be approximated by

$$A = \langle \mathcal{A}(\Gamma^N) \rangle_{\text{ensemble}} \approx \sum_{\Gamma^N} \mathcal{A}(\Gamma^N) f(\Gamma^N) \overset{\text{MC}}{=} \frac{1}{n} \sum_{i=0}^{n} \mathcal{A}(\Gamma_i^N) \tag{3.4}$$

The resemblance of Eq. (3.2) and Eq. (3.4) again highlights the connection between both approaches of sampling the phase space.

3.1.2 Common ensembles

The probability density distribution $f(\Gamma^N)$ depends on the ensemble and, therefore, the fixed thermodynamic parameters of the configuration. One of the simplest, but also most important ensembles is the *microcanonical ensemble*. In systems described by this ensemble, the number of particles N, the volume of the space V which particles are allowed to occupy, and the overall energy of the system E which ensures the conservation of energy, are set to constant values (see the sketch in Fig. 3.1). This ensemble is also known as the NVE-ensemble.

In general, the total energy of a multi-particle system is given by the Hamiltonian

$$\mathcal{H}(\Gamma^N) = \mathcal{K}(\mathbf{p}^N, \mathbf{L}^N) + \mathcal{V}(\mathbf{q}^N, \boldsymbol{\Theta}^N), \tag{3.5}$$

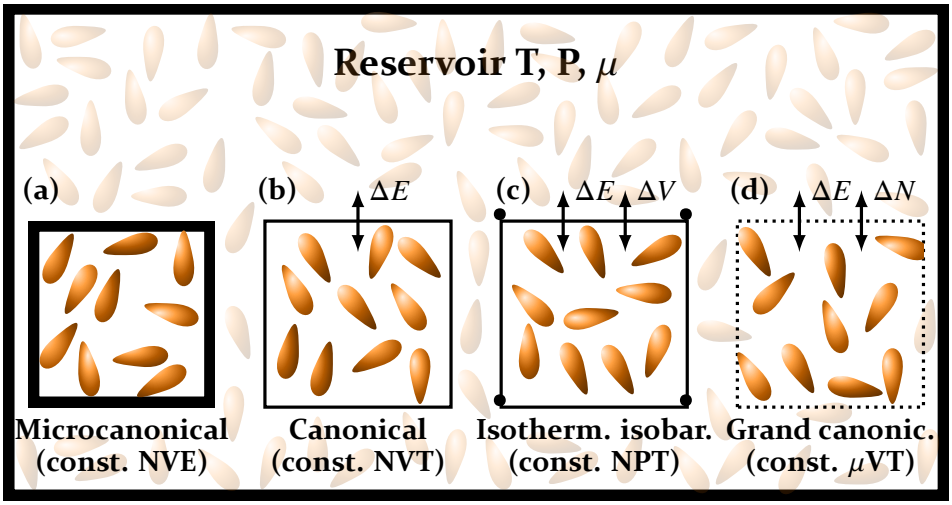

Figure 3.1: The four most important statistical ensembles and their relation to an external reservoir are sketched. In the microcanonical ensemble (constant N, V, and E) the particles are within an isolated space. Canonical ensembles (constant N, V, and T) are coupled with a heat bath to interchange energy. In the isothermal-isobaric ensemble (constant N, P, and T) the systems interact with the reservoir thermally but can also adjust to the reservoir's pressure by changing its volume. Lastly, in the grand canonical ensemble (constant μ, V, and T) the systems exchange energy and particles with their environment.

which is split into a kinetic and an interaction potential term. The kinetic energy

$$\mathcal{K}(\mathbf{p}^N, \mathbf{L}^N) = \mathcal{K}_{\text{trans}}(\mathbf{p}^N) + \mathcal{K}_{\text{rot}}(\mathbf{L}^N) = \sum_{i=0}^{N} \left(\frac{\mathbf{p}_i^2}{2m_i} \right) + \sum_{i=0}^{N} \left(\frac{L_{i,x}^2}{2I_{i,xx}} + \frac{L_{i,y}^2}{2I_{i,yy}} + \frac{L_{i,z}^2}{2I_{i,zz}} \right) \tag{3.6}$$

itself consists of two parts – the translational kinetic energy $\mathcal{K}_{\text{trans}}(\mathbf{p}^N)$ and the rotational kinetic energy $\mathcal{K}_{\text{rot}}(\mathbf{L}^N)$ – and is a function of just the momenta $\mathbf{p}$ and angular momenta $\mathbf{L} = (L_x, L_y, L_z)^T$ of all particles with their masses m_i and the diagonal elements $I_{i,\alpha\alpha}$ of the inertia tensor $\mathbf{I}$ in a principal axis frame (x, y, z). The interaction potential $\mathcal{V}(\mathbf{q}^N, \mathbf{\Theta}^N) = \mathcal{U}(\mathbf{q}^N, \mathbf{\Theta}^N) + \mathcal{V}_{\text{ext}}(\mathbf{q}^N, \mathbf{\Theta}^N)$ consists of the internal interaction potential $\mathcal{U}$ and an external potential $\mathcal{V}_{\text{ext}}$. In the following we will mostly neglect the external potential term as we will investigate self-assembly processes, where external forces are not required. Therefore, we will set $\mathcal{V}(\mathbf{q}^N, \mathbf{\Theta}^N) = \mathcal{U}(\mathbf{q}^N, \mathbf{\Theta}^N)$, unless like in Chap. 7 explicitly stated otherwise.

To single out only specific space points Γ^N which are assigned to the chosen energy, the Hamiltonian of the system is restricted to $\mathcal{H}(\Gamma^N) = E$. Thus, the probability density has to be proportional to the delta distribution $\delta(E - \mathcal{H}(\Gamma^N))$. This yields

$$f_{\mathrm{NVE}}(\Gamma^N) := \frac{1}{N!\, h^{3N}} \frac{\delta(E - \mathcal{H}(\Gamma^N))}{W(E)}. \tag{3.7}$$

The Gibbs factor $\frac{1}{N!}$ corrects over-counting due to indistinguishable pear-shaped particles, whereas the Planck constant $h \approx 6.63 \cdot 10^{-34}$ Js ensures the microcanonical partition function

$$W(E) := \frac{1}{N! h^{3N}} \int \delta(E - \mathcal{H}(\Gamma^N)) \mathrm{d}\Gamma^N \tag{3.8}$$

is dimensionless. The partition function determines the space of all microstates for a given set of N, V and E and acts as a normalisation factor. $W(E)$ also determines the entropy of the system according to Eq. (1.7).

Even though in principle the microcanonical ensemble is able to describe all systems in the thermodynamic limit of infinite system size, the fixed thermodynamic parameters of this ensemble do not match the typical experimental conditions, particularly for finite systems. Consequently, other descriptions have proven to be more convenient choices. Keeping the volume, energy and number of molecules constant, the NVE-ensemble resembles ideal isolated systems best. By examining the protocols of many colloidal experiments, however, it becomes apparent that a great number of particle systems are not isolated and have to be recognised as subsystems embedded within their environment (see Fig. 3.1). Especially in terms of energy the environment is often coupled with the particle system and serves as an energy reservoir to keep the mean temperature T rather than the energy of the system constant. Therefore, the subsystem is in the NVT-ensemble also referred to as the *canonical* ensemble. Nevertheless, the condition of energy, conservation is again met by including the energy reservoir to the observation space. Thus, the whole system (our subsystem + the environment) can be treated microcanonically again

$$\mathcal{H}(\Gamma^N) + \mathcal{H}(\Gamma^N_{\mathrm{res}}) = E. \tag{3.9}$$

We retain in this microcanonical approach too much unnecessary information about the environment and an overall system which is heavily dominated by the reservoir such that no predictions about the subsystem can be

made. To extract only the information about the subsystem, the density distribution within this confined phase space has to be calculated. This can be derived from the whole system using Eq. (3.7) and Eq. (3.9) with

$$\begin{aligned} f_{\mathrm{NVT}}(\Gamma^N) &= \int f_{\mathrm{NVE}}(\Gamma^N, \Gamma^N_{\mathrm{res}}) \mathrm{d}\omega_{\mathrm{res}} \\ &\propto \int \delta(E - \mathcal{H}(\Gamma^N) - \mathcal{H}(\Gamma^N_{\mathrm{res}})) \mathrm{d}\omega_{\mathrm{res}} \propto W(E - \mathcal{H}(\Gamma^N)). \end{aligned} \tag{3.10}$$

Using Eq. (1.7) and the argument that the number of particles in the reservoir is much larger than in our subsystem $N_{\mathrm{res}} \ggg N$ it can be shown that the density distribution of the canonical ensemble is given by

$$f_{\mathrm{NVT}}(\Gamma^N) = \frac{1}{N! h^{3N}} \frac{\exp(-\beta \mathcal{H}(\Gamma^N))}{Z_{\mathrm{NVT}}(T)} \tag{3.11}$$

with the inverse temperature $\beta^{-1} = k_B T$ and the canonical partition function

$$Z_{\mathrm{NVT}}(T) = \frac{1}{N! h^{3N}} \int \exp\left(-\beta \mathcal{H}(\Gamma^N)\right) \mathrm{d}\Gamma^N. \tag{3.12}$$

The canonical partition function defines the Helmholtz free energy F of the system

$$F(T, V, N) = -\beta^{-1} \ln Z_{\mathrm{NVT}}(T) \tag{3.13}$$

which the particle system minimises in equilibrium. With the distribution function we now have the necessary equipment to sample the phase space in the NVT-ensemble. The canonical ensemble average is given by

$$A = \langle \mathcal{A}(\Gamma^N) \rangle_{\mathrm{NVT}} = \frac{\int \mathcal{A}(\Gamma^N) \exp(-\beta \mathcal{H}(\Gamma^N)) \mathrm{d}\Gamma^N}{N! h^{3N} \cdot Z_{\mathrm{NVT}}(T)}. \tag{3.14}$$

To calculate this formula Eq. (3.4) and Eq. (3.11) are used.

There also exist other ensembles, like the *isothermal isobaric* ensemble (NPT) with constant number of particles N, pressure P and temperature T or the *grand canonical* ensemble (μVT), where the particle system is in chemical and thermal thermodynamic equilibrium with the reservoir and can exchange energy (constant T) and particles (constant chemical potential μ). The latter is important for the theoretical part of my thesis in Chap. 7. The density distribution is given by

$$f_{\mu\mathrm{VT}}(\Gamma^N) = \frac{1}{N!h^{3N}} \frac{\exp(-\beta(\mathcal{H}(\Gamma^N) - \mu N))}{Z_{\mu\mathrm{VT}}(\mu, T)} \tag{3.15}$$

with the grand canonical partition function

$$Z_{\mu\mathrm{VT}}(\mu, T) = \mathrm{Tr}_{\mathrm{cl}} \exp(-\beta(\mathcal{H}(\Gamma^N) - \mu N)). \tag{3.16}$$

Here we used the classical trace

$$\mathrm{Tr}_{\mathrm{cl}} \cdots = \sum_N \frac{1}{N!h^{3N}} \int \cdots \mathrm{d}\Gamma^N \tag{3.17}$$

as a shorthand notation. The grand canonical potential Ω of this system is written as

$$\Omega(T, V, \mu) = -\beta^{-1} \ln Z_{\mu\mathrm{VT}}(\mu, N). \tag{3.18}$$

In the following, computational studies of pear-shaped particle systems, we will use the canonical ensemble to imitate experimental conditions. Even though other ensembles are occasionally a better fit to experiments, the canonical point of view with some modifications (specifically the floppy-box mechanism explained below) seems to be suitable to predict physical phenomena like the self-assembly of pear-shaped particles[2] and is also more time efficient in terms of computational algorithms.

3.2 Simulation techniques

Now that the fundamental statistical methods and ensembles have been established, we describe two algorithms to generate sequences of microscopic states to sample the phase space of canonical pear-shaped particle ensembles accurately. The first technique is a dynamical approach called Molecular Dynamics. Secondly, an alternative stochastic method, namely Metropolis Monte Carlo, is introduced. See Ref. [292, 293] for more information.

Note here that throughout this thesis all observables and parameters are dimensionless. This is achieved by expressing them in terms of a fundamental set of units – mass m_0, energy ϵ_0 and length σ_0. Often, quantities in reduced

[2]We performed some sample checks which do not indicate qualitative changes between NVT (with wall moves) and NPT. The floppy-box mechanism has to be implemented to avoid the development of (incorrect) pressure anisotropy in fluid phases [291].

energy	U^*	$= (\epsilon_0^{-1})U$
temperature	T^*	$= (k_B\epsilon_0^{-1})T$
volume	V^*	$= (\sigma_w^{-3})V$
number density	ρ_N^*	$= (\sigma_w^3)\rho_N$
pressure	P^*	$= (\sigma_w^3\epsilon_0^{-1})P$
time	t^*	$= (\frac{\epsilon_0}{\sigma_w^2 m_0})^{\frac{1}{2}}t$
mass	m^*	$= (m_0^{-1})m$
distance	$\mathbf{r}^*$	$= (\sigma_w^{-1})\mathbf{r}$
velocity	$\mathbf{v}^*$	$= (m_0\epsilon_0^{-1})^{\frac{1}{2}}\mathbf{v}$
momentum	$\mathbf{p}^*$	$= (m_0\epsilon_0)^{-\frac{1}{2}}\mathbf{p}$
force	$\mathbf{F}^*$	$= (\sigma_w\epsilon_0^{-1})\mathbf{F}$
acceleration	$\mathbf{a}^*$	$= (\sigma_w m_0\epsilon_0^{-1})\mathbf{a}$
moment of inertia	I^*	$= (m_0\sigma_w^2)^{-1}$
angular velocity	ω^*	$= (\frac{m_0}{\sigma_w^2\epsilon_0})^{\frac{1}{2}}\omega$
angular momentum	$\mathbf{L}^*$	$= (\frac{\sigma_w^2}{m_0\epsilon_0})^{\frac{1}{2}}\mathbf{L}$
torque	τ^*	$= (\epsilon_0^{-1})\tau$
angular acceleration	α^*	$= (\frac{\sigma_w^2 m_0}{\epsilon_0})\alpha$

Table 3.1: The relation between observables and parameters in reduced units and their equivalents in SI units.

units are marked by an asterisk *; however, as all calculations are performed in reduced units, we refrain from using this marker in the following. The relation between reduced properties and their equivalents in SI units is given in Table 3.1.

3.2.1 Molecular Dynamics simulations

The main idea of *Molecular Dynamics* (MD) simulations is to computationally replicate an experimental study on multi-particle systems. Starting from some initial configuration the trajectories of all particles, which only depend

on the inter-particle interactions, are numerically predicted by integrating Newton's equations of motion. Based on this, the given system is propagated in time to generate a time sequence of microstates which is used in Eq. (3.2) to calculate time averages. Considering a system of N aspherical pear-shaped particles, the Newton equation of motion of all N particles can be derived from the Hamiltonian shown in Eq. (3.9). We obtain the translational motion of every particle

$$\begin{aligned} \dot{\mathbf{q}}_i &= \frac{\partial \mathcal{H}}{\partial \mathbf{p}_i} = \frac{\mathbf{p}_i}{m_i} \\ \dot{\mathbf{p}}_i &= -\frac{\partial \mathcal{H}}{\partial \mathbf{q}_i} = -\nabla_i \mathcal{V} = \mathbf{f}_i \end{aligned} \tag{3.19}$$

with the total force $\mathbf{f}_i = \sum_j^N \mathbf{f}_{ij}$ acting on particle i summed over all pair-particle interactions calculated from Eq. (2.21). The rotational equations of motion are derived similarly

$$\begin{aligned} \dot{\mathbf{\Theta}}_i &= \frac{\partial \mathcal{H}}{\partial \mathbf{L}_i} = \frac{\mathbf{L}_i}{I_i} \\ \dot{\mathbf{L}}_i &= -\frac{\partial \mathcal{H}}{\partial \mathbf{\Theta}_i} = -\nabla_{\mathbf{\Theta}_i} \mathcal{V} = \tau_i . \end{aligned} \tag{3.20}$$

with the total torque τ_i acting on particle i. For rigid, elongated, and rotationally symmetric particles like pear-shaped particles it is often more convenient to describe their orientations by normalized orientation vectors $\mathbf{u}_i$ rather than the associated angle vectors $\mathbf{\Theta}_i$. Also, in case of the PHGO-model of pear-shaped particles, the contact function between two pears in Eq. (2.17) is expressed in terms of their orientation vectors. As the pear only has two rotational degrees of freedom, due to the fact that it is invariant under rotations around the symmetry axis, and, as the rotation is always perpendicular to $\mathbf{u}_i$, τ_i can be reduced to

$$\tau_i = \mathbf{u}_i \times \mathbf{g}_i \tag{3.21}$$

in terms of the gorque $\mathbf{g}_i$ which functions as a force causing the particles to turn. Similarly to the force, the gorque is a derivative of the particle potential $\mathbf{g}_i = -\nabla_{\mathbf{u}_i} \mathcal{V}$. It has been shown [294] that the dynamics of the orientation vector can be expressed by

$$I_i \ddot{\mathbf{u}}_i = \mathbf{g}_{\perp i} + \lambda \mathbf{u}_i . \tag{3.22}$$

Here $\mathbf{g}_{\perp i}$ is the component of the gorque perpendicular to $\mathbf{u}_\mathbf{i}$. The factor λ is a Lagrange multiplier to conserve the unity of the orientation vector.

To integrate the equations of motion in Eq. (3.19) and Eq. (3.22), a version of the Velocity-Verlet algorithm for rotationally symmetric particles is implemented [293, 295]. The Velocity-Verlet scheme is chosen because it advantageously combines energy conservation on large time scales and, furthermore, time reversibility. The integration is performed in small finite time steps Δt such that the time progression of the translational quantities (position $\mathbf{q}_i$ and linear velocity $\mathbf{v}_i$) is attained in an iterative fashion as

$$\begin{aligned}
\mathbf{v}_i(t{+}0.5{\cdot}\Delta t) &= \mathbf{v}_i(t) + \frac{\Delta t}{2m_i}\mathbf{f}_i(t) \\
\mathbf{q}_i(t{+}\Delta t) &= \mathbf{q}_i(t) + \Delta t \cdot \mathbf{v}_i(t{+}0.5{\cdot}\Delta t) \\
\mathbf{v}_i(t{+}\Delta t) &= \mathbf{v}_i(t{+}0.5{\cdot}\Delta t) + \frac{\Delta t}{2m_i}\mathbf{f}_i(t{+}\Delta t).
\end{aligned} \tag{3.23}$$

To set up the initial configuration, the absolute values of the linear velocities of the particles are arbitrarily chosen according to the Maxwell-Boltzmann distribution

$$f_v(T) = \left(\frac{m}{2\pi k_B T}\right)^{\frac{3}{2}} \exp\left(\frac{-mv^2}{2k_B T}\right). \tag{3.24}$$

The directions of velocity, however, are assigned to each particle randomly.

The Velocity-Verlet algorithm for the rotations is applied similarly at which the restriction $|\mathbf{u}_i| = 1$ has to be considered with additional terms

$$\begin{aligned}
\dot{\mathbf{u}}_i(t{+}0.5{\cdot}\Delta t) &= \dot{\mathbf{u}}_i(t) + \frac{\Delta t}{2I_i}\mathbf{g}_{\perp i}(t) + \lambda \mathbf{u}_i(t) \\
\mathbf{u}_i(t{+}\Delta t) &= \mathbf{u}_i(t) + \Delta t \cdot \dot{\mathbf{u}}_i(t{+}0.5{\cdot}\Delta t) \\
\dot{\mathbf{u}}_i(t{+}\Delta t) &= \dot{\mathbf{u}}_i(t{+}0.5{\cdot}\Delta t) + \frac{\Delta t}{2I_i}\mathbf{g}_{\perp i}(t{+}\Delta t) + (\dot{\mathbf{u}}_i(t{+}0.5{\cdot}\Delta t) \cdot \mathbf{u}_i(t{+}\Delta t))\mathbf{u}_i(t{+}\Delta t).
\end{aligned} \tag{3.25}$$

The Lagrangian correction multiplier λ is obtained by

$$\begin{aligned}
\lambda'' &= -\frac{\Delta t}{2}\left(\dot{\mathbf{u}}_i(t) \cdot \dot{\mathbf{u}}_i(t) + \frac{\Delta t}{2I_i}\mathbf{g}_{\perp i}(t) \cdot (2\dot{\mathbf{u}}_i(t) + \frac{\Delta t}{2I_i}\mathbf{g}_{\perp i}(t))\right) \\
\lambda' &= \lambda'' - \frac{(1+\lambda''\Delta t)^2(\mathbf{u}_i(t) \cdot \mathbf{u}_i(t)) - 1 - \lambda''\Delta t}{2\Delta t(1+\lambda''\Delta t)} \\
\lambda &= \lambda' - \frac{(1+\lambda'\Delta t)^2(\mathbf{u}_i(t) \cdot \mathbf{u}_i(t)) - 1 - \lambda''\Delta t}{2\Delta t(1+\lambda'\Delta t)}
\end{aligned} \tag{3.26}$$

where the last two steps can be thought of as refinement steps for the multiplier. Even though it is reasonable to also distribute the original rotational velocities according to the Maxwell-Boltzmann distribution, it is not necessarily needed. The equipartition of energy over all degrees of freedom causes the adjustment to an accurate distribution of the angular velocities within a few time steps due to interparticle collisions except at very low densities which are not considered here. Therefore, we do not initiate rotations and set $\dot{\mathbf{u}}_i(0) = 0$ for all particles i.

So far the pear system is described in the microcanonical ensemble at constant energy. Therefore, a thermostat has to be introduced which enables us to perform MD canonically at constant temperature. In the formalism of Nosé and Hoover [292, 293, 296], the thermodynamic interaction with an external heat bath is achieved by extending the Hamiltonian of Eq. (3.5) as

$$\mathcal{H}_{Nose} = \sum_i^N \left(\frac{\mathbf{p_i}^2}{2m_i s^2} + \frac{\mathbf{L_i}^2}{2I_i s^2} \right) + \mathcal{V}(\mathbf{q}^N, \mathbf{u}^N) + \frac{p_s^2}{2Q} + N_f k_B T_0 \ln s. \tag{3.27}$$

The parameter s can be interpreted as an additional coordinate of the reservoir with an effective mass Q and effective momentum p_s. Using again the Hamilton equations, Eq. (3.19) and Eq. (3.20) are rewritten to

$$\begin{aligned}
\dot{\mathbf{q}}_i &= \frac{\mathbf{p}_i}{m_i} \\
\dot{\mathbf{p}}_i &= -\frac{\partial \mathcal{V}(\mathbf{q}^N, \mathbf{\Theta}^N)}{\partial \mathbf{q}_i} - \xi \mathbf{p}_i \\
\dot{\mathbf{\Theta}}_i &= \frac{\mathbf{L}_i}{I_i} \\
\dot{\mathbf{L}}_i &= -\frac{\partial \mathcal{V}(\mathbf{q}^N, \mathbf{\Theta}^N)}{\partial \mathbf{\Theta}_i} - \xi \mathbf{L}_i \\
\dot{\xi} &= \frac{1}{Q} \left(\sum_i^N \frac{\mathbf{p_i}^2}{m_i} + \sum_i^N \frac{\mathbf{L_i}^2}{I_i} - N_f k_B T_0 \right).
\end{aligned} \tag{3.28}$$

To simplify the equations we here introduce the thermodynamic friction coefficient $\xi = \frac{p_s}{Q}$. Based on these dynamics a similar Velocity-Verlet algorithm can be implemented as described by Smith [297].

Simulation box

The computational simulations are performed on the flat 3-torus using periodic boundary conditions to imitate systems in bulk. Here, it is assumed that the cuboidal simulation box is surrounded by replicas of the system in the x-, y- and z-directions, which image the original box. In our simulations, this implies that every pear-shaped particle has a counterpart in every periodic box, which moves the same. When a pear-shaped particle crosses the boundary and leaves the simulation domain, it is replaced by an image pear which enters the simulation box on the opposite side. Due to the periodic boundary conditions, the pear-shaped particles only interact with the closest image of neighbouring particles, known as the minimum image convention [292, 293].

The systems are initially set up within a floppy tetragonal simulation box, which is able to move its walls without changing the overall volume to relax the particle arrangements. The initial shape is a cubic simulation box. The wall moves are implemented by first randomly choosing one of the simulation box edges l_1, l_2 or l_3. Afterwards, the chosen edge is rescaled by a factor Λ (stretch) or $\frac{1}{\Lambda}$ (compression) with $\Lambda = 1.005$, whereas the other two edges are rescaled by $\frac{1}{\sqrt{\Lambda}}$ and $\sqrt{\Lambda}$, respectively, to keep the volume constant. This can lead to cuboidal simulation boxes decreasing the possibility of the occurrence of phases which are imposed by the boundary conditions. The wall moves are performed every 100 steps.

As we have shown, MD usually relies on the calculation of the interparticle forces. In hard-core particle models as introduced in Eq. (2.5), however, the potential is by definition non-differentiable. Thus, a direct implementation of the hard-core potential into the algorithm above is often unfeasible. Even though event-driven approaches can be considered [292, 298], where the time step Δt is not constant and analytically determined between two collisions, such a method is rather complex and, especially for aspherical particles, highly non-trivial. Additionally, for very dense systems, like those covered in this thesis, the time steps between two collisions become very small and, consequently, make the event-driven algorithm inefficient. To still analyse the dynamical behaviour of pear-particle systems, the hard core-potential is approximated. We use the short range, purely repulsive, sharply increasing potential which mimics the exclusive volume interactions according to the PHGO-contact function (see Eq. (2.17)) of the

pear-shaped particle as close as possible. To be more precise, we use the Weeks-Chandler-Anderson potential, introduced in Eq. (2.21). Even though it does not match the description of a hard-core particle perfectly, it probably resembles more realistic slightly soft interaction profiles like those observed in experimental colloidal systems [207, 279, 280, 281]. The MD approach described here is applied in Chap. 4 and Chap. 5 to single-component pear-shaped particle systems and in Chap. 8 to pear-sphere mixtures.

3.2.2 Monte Carlo simulations

Another type of algorithms to computationally study the phase behaviour of pear-shaped liquid crystals is *Monte Carlo* (MC) simulations. Especially, for hard particles systems, MC has been an important tool to predict mesophases [206, 213, 214, 215, 216, 217, 218, 219, 220, 221]. In contrast to the MD simulations, where the initial state at time zero determines the states at all other times t, MC is non-deterministic. Its main idea is to generate a probabilistic set of samples of the phase space, called a Markov chain [299], using an iteration process of stochastic trial moves of particles. This means that the simulation does not follow the time-evolution trajectory of a specific system, but sweeps the configuration space according to the density distribution f_{NVT}. At every trial move, the algorithm attempts to map the current particle configuration Γ_c^N to an arbitrarily chosen new configuration Γ_n^N, by relocating particles. The probability density to obtain the new state is given by $\text{prob}(\Gamma_c^N \to \Gamma_n^N) = \alpha(\Gamma_c^N \to \Gamma_n^N) \times \text{acc}(\Gamma_c^N \to \Gamma_n^N)$ and contains the probability to choose the step from Γ_c^N to Γ_n^N $\alpha(\Gamma_c^N \to \Gamma_n^N)$ and the probability to accept this transition $\text{acc}(\Gamma_c^N \to \Gamma_n^N)$ afterwards.

In an equilibrated system the density distribution is static $\frac{\partial \text{prob}}{\partial t} = 0$. Accordingly, the average number of accepted transitions from the current state has to equal the average number of transitions into the current state. This condition is called global balance

$$\int \mathrm{d}\Gamma'^N f(\Gamma_i^N) \cdot \text{prob}(\Gamma_i^N \to \Gamma'^N) = f(\Gamma_i^N) = \int \mathrm{d}\Gamma'^N f(\Gamma'^N) \cdot \text{prob}(\Gamma'^N \to \Gamma_i^N). \tag{3.29}$$

One property of an algorithm, which complies with global balance by imposing a much stricter requirement, is *detailed balance*. Here the outgoing flux from Γ_c^N to Γ_n^N is set equal to the reversed incoming flux from Γ_n^N to Γ_c^N. Given that additionally $\alpha(\Gamma_c^N \to \Gamma_n^N) = \alpha(\Gamma_n^N \to \Gamma_c^N)$ is chosen to be

symmetric, so that the probability to choose a trial move from Γ_c^N to Γ_n^N is equal to the probability to choose a move the other way around, detailed balance is written as

$$f(\Gamma_c^N) \cdot \mathrm{acc}(\Gamma_c^N \to \Gamma_n^N) = f(\Gamma_n^N) \cdot \mathrm{acc}(\Gamma_n^N \to \Gamma_c^N). \tag{3.30}$$

In principle, detailed balance is not necessary to guarantee an accurate sampling as other algorithms show [300, 301]. Nevertheless, for non-spherical particles like pears, the implementation of detailed balance is still the most convenient approach. Combining Eq. (3.30) and Eq. (3.11) we find

$$\frac{\mathrm{acc}(\Gamma_c^N \to \Gamma_n^N)}{\mathrm{acc}(\Gamma_n^N \to \Gamma_c^N)} = \frac{f_{\mathrm{NVT}}(\Gamma_n^N)}{f_{\mathrm{NVT}}(\Gamma_c^N)} = \exp(-\frac{\mathcal{V}(\Gamma_n^N) - \mathcal{V}(\Gamma_c^N)}{k_B T}). \tag{3.31}$$

Even though there are uncountable options for $\mathrm{acc}(\Gamma_c^N \to \Gamma_n^N)$ to validate detailed balance, Metropolis *et al.* [292, 293, 302] introduced an efficient choice for the acceptance probability between two states

$$\mathrm{acc}(\Gamma_c^N \to \Gamma_n^N) := \begin{cases} \exp(-\frac{\mathcal{V}(\Gamma_n^N) - \mathcal{V}(\Gamma_o^N)}{k_B T}), & \text{if } \mathcal{V}(\Gamma_n^N) \geq \mathcal{V}(\Gamma_c^N) \\ 1, & \text{if } \mathcal{V}(\Gamma_n^N) < \mathcal{V}(\Gamma_c^N) \end{cases} \tag{3.32}$$

which is still widely used and known as the *Metropolis algorithm*. In terms of hard-particle interactions the use of Metropolis' approach proves particularly beneficial. According to Eq. (2.6) the acceptance matrix $\mathrm{acc}(\Gamma_c^N \to \Gamma_n^N)$ in Eq. (3.32) becomes binary. As all permissible configurations feature equal potential energy, a trial step is only rejected if particles overlap. In terms of pear-shaped particles the overlap occurs according to its contact functions (see Sec. 2.2.1 for the different contact function models). We can, thus, change Eq. (3.32) to

$$\mathrm{acc}(\Gamma_c^N \to \Gamma_n^N) := \begin{cases} 1, & \text{if particles do not overlap} \\ 0, & \text{if particles overlap.} \end{cases} \tag{3.33}$$

Computationally, this leads to the advantage that the algorithm is accelerated significantly. On the one hand, the acceptance step does not have to be randomized anymore. On the other hand, a trial step attempt can be rejected as soon as one overlapping pair of molecules has been identified.

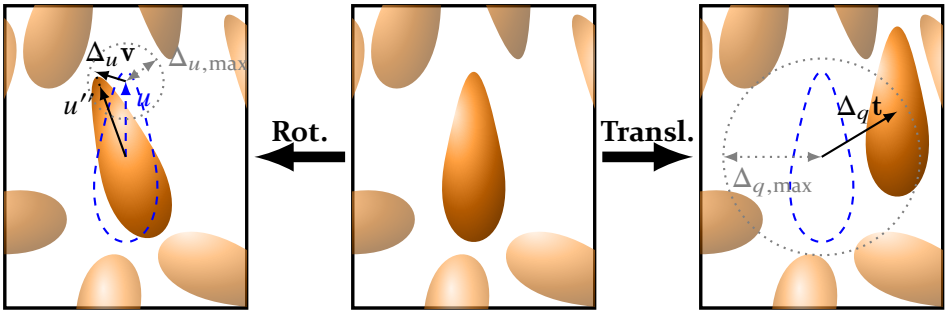

Figure 3.2: The two possible move sequences in the Monte Carlo simulation of hard-core pear-shaped particle. Left: A random pear is rotated by adding a vector $\mathbf{v}$ with random direction and length Δ_u to its orientation vector $\mathbf{u}$ which is normalised afterwards. Right: A random pear is translated by a vector $\mathbf{t}$ with random direction and length Δ_q. If the moving particle does not overlap with another particle the step is accepted. Otherwise, the move is reversed again.

Like in MD, the Metropolis algorithm is applied to a system of N hard-core molecules within a floppy cuboidal simulation box with periodic boundary conditions. For every trial move, an arbitrary particle is chosen and displaced by a small margin. For pear-shaped particles, this is realised either by a minor translation or by a rotation of the orientation vector around a small angle (see Fig. 3.2). To ensure detailed balance and the symmetry of $\alpha(\Gamma_c^N \to \Gamma_n^N)$, the direction of translation is given by a random unit vector $\mathbf{t}$ and a randomly chosen factor $\Delta_q \in [0, \Delta_{q,\max}]$

$$\mathbf{q}' \to \mathbf{q} + \Delta_q \mathbf{t}. \tag{3.34}$$

For MC, no velocities are assigned to the particles demonstrating once more that this algorithm is purely statistical in its nature.

Analogous to the linear translations, also the rotation is performed by adding a random unit vector $\mathbf{v}$ multiplied by a randomly chosen factor $\Delta_u \in [0, \Delta_{u,\max}]$. Afterwards the orientation vector is normalized

$$\begin{aligned} \mathbf{u}' &\to \mathbf{u} + \Delta_u \mathbf{v} \\ \mathbf{u}'' &\to \frac{\mathbf{u}'}{|\mathbf{u}|}. \end{aligned} \tag{3.35}$$

One MC step is completed after N trial move attempts. The maximal translational $\Delta_{q,\max}$ and the maximal orientational displacement $\Delta_{u,\max}$ are selected such that both trial move variants are accepted with a probability of 50 % on average. Hence, in every MC-run a preparation stage, where $\Delta_{q,\max}$

and $\Delta_{q,\max}$ are determined, precedes the production stage, where the phase space is sampled.

The advantage of MC over MD simulations is that we can directly use the hard-core potentials. More specifically, the MC approach is applied in Chap. 4–8 with the PHGO contact function and in Chap. 5–7 using the HPR model. Secondly, the MC algorithm tends to reach equilibrated states after a smaller number of simulation steps, as it does not have to follow physical trajectories and, hence, forgives poorly initiated starting conditions, where the particle system is very far from equilibrium, more easily. However, this also implies that no predictions about kinetic features of the system can be obtained with this method.

Additionally, the Metropolis Monte Carlo scheme is hard to parallelise for highly efficient and fast simulation runs. Even though parallel codes have been developed for spherical particles [285] where the simulation box is subdivided into multiple subdomains like a checkerboard, those algorithms are mostly expensive for elongated, aspherical particles, like ellipsoids or pears. This means that despite the theoretically faster equilibration of the system, MD simulations are often faster if the initial condition is chosen conveniently, so close to the equilibrium state. Therefore, we use both the MC and MD approach to analyse pear-shaped particle self-assembly to cover a wide range of quantifiable observables.

3.3 Thermodynamic observables

In the following, the most important observables in dynamic computational simulations are established. The first type of observables we introduce here are of thermodynamic nature. Note that some of these variables cannot be determined by the ensemble average method and are only retrieved from the Molecular Dynamics technique of Sec. 3.2.1.

3.3.1 Temperature

The temperature T, for example, is a constant predetermined parameter in MC-simulations due to the non-dynamical nature of the MC algorithm and cannot be calculated. In our hard pear-shaped particle systems, the temperature does not even contribute to the Metropolis step (see Eq. (3.33)) and, therefore, has to be interpreted rather as an adjustable parameter which

governs the time-scale. Also in MD-simulations with a thermostat, the average temperature is determinate beforehand. Yet, T can be obtained from the Hamiltonian $\mathcal{H}$ to review the accuracy of the algorithm or to assess equilibrium. In particular, the equipartition theorem, which states that the energy has to be equally distributed among all degrees of freedom, relates T with $\mathcal{H}$ and all variables x_i assigned to one degree of freedom of the $(2N_F \cdot N)$-dimensional phase space Ω as

$$\left\langle x_\alpha \frac{\partial \mathcal{H}}{\partial x_\beta} \right\rangle = \delta_{\alpha\beta} k_B T. \tag{3.36}$$

Here $\delta_{\alpha,\beta}$ symbolises the Kronecker delta. Focussing only on the momentum of each particle $\mathbf{p}$, the temperature can be directly derived from the average translational kinetic energy per degree of freedom with Eq. (3.6) by

$$\left\langle p_\alpha \frac{\partial \mathcal{H}}{\partial p_\alpha} \right\rangle = \left\langle p_\alpha \frac{\partial \mathcal{K}_{\text{trans}}}{\partial p_\alpha} \right\rangle = \left\langle \frac{p_\alpha^2}{m} \right\rangle = k_B T. \tag{3.37}$$

Thus, for every step of the computational simulations, the instantaneous temperature $\mathcal{T}$

$$\mathcal{T} = \sum_i^N \frac{m_i \mathbf{v}_i^2}{k_B \cdot (3N - 3)} \tag{3.38}$$

is averaged over all particles by calculating the translational kinetic energy of the whole system and dividing it by the total number of translational degrees of freedom $3N$. In this way we can prevent high fluctuations and enhance our statistics. The formula is given in terms of the molecules' velocities $\mathbf{v}_i$ rather than its momenta as it is more convenient to save the velocities in Molecular Dynamics.

Alternatively, $\mathcal{T}$ can be procured by calculating the rotational kinetic energy in the same way. However, here we have to be careful that there are only $2N$ rotational degrees of freedom in total so

$$\mathcal{T} = \sum_i^N \frac{\omega_i^T \mathbf{I}_i \omega_i}{k_B \cdot 2N}. \tag{3.39}$$

The equilibrium temperature T is the time average of $\langle \mathcal{T} \rangle$. In general, T does not affect the phase behaviour of soft-core particle systems like the WCA in Sec. 2.2.2. According to Eq. (1.6), the temperature can be seen as a scaling factor of the system. The higher the temperature is set, the faster the

system equilibrates. However, high temperatures and, therefore, fast particles, are also accompanied by the possibility of large overlaps of particles between two finite time steps during the discrete time integration of the MD algorithm. Those overlaps result in extremely high potential energies and can break the simulation. To resolve this issue, we choose the time step size Δt sufficiently small which increases computational time considerably. Thus, a compromise between a sufficiently high temperature and time step for a fast equilibration has to be found.

3.3.2 Pressure

The pressure P is also a result of the equipartition theorem. Instead of the relation between temperature and momenta, the position coordinates q_α of each particle are inserted in Eq. (3.36)

$$\left\langle q_\alpha \frac{\partial \mathcal{H}}{\partial q_\alpha} \right\rangle = \left\langle q_\alpha \frac{\partial \mathcal{V}}{\partial q_\alpha} \right\rangle = \langle -q_\alpha \cdot F_\alpha \rangle = k_B T. \tag{3.40}$$

Here we used that only the interaction potential term is dependent on q_α (see Eq. (3.5)) and the identity $\Delta_i \mathcal{V} = -F_i$ between the potential and the force F_i which is acting on particle i. This directly gives us the virial theorem

$$\sum_i^N \langle \mathbf{q}_i \cdot \mathbf{F}_i \rangle = -3N \cdot k_B T = -2 \langle E_{\text{kin}}^{(\text{trans})} \rangle \tag{3.41}$$

with the average translational kinetic energy $\langle E_{\text{kin}}^{(\text{trans})} \rangle$. In the canonical ensemble the particles are assumed to be contained within a closed box. Therefore, the forces which impact single molecules are composed of the internal forces between different particles $\mathbf{F}_{ij}$ with $\mathbf{F}_{ii} = 0$ and an external force between the wall and a particle $F_i^{(\text{wall})}$. The internal term can be outlined as

$$\langle \sum_{i=1}^N \sum_{j=1}^N \mathbf{q}_i \cdot \mathbf{F}_{ij} \rangle = \langle \sum_{i=1}^{N-1} \sum_{j=i+1}^N (\mathbf{q}_i \cdot \mathbf{F}_{ij} - \mathbf{q}_j \cdot \mathbf{F}_{ij}) \rangle = \langle \sum_{i=1}^{N-1} \sum_{j=i+1}^N \mathbf{r}_{ij} \cdot \mathbf{F}_{ij} \rangle \tag{3.42}$$

with the distance vector $\mathbf{r}_{ij}$ between two pears. The pressure of the system is defined as the force of the particle system imposed on the wall of the confining volume V divided by its surface ∂V. Simultaneously an infinitesimally small patch of the wall $\mathrm{d}S \subset \partial V$ acts on particles at position $\mathbf{q} \in \mathrm{d}S$ on the boundary based on the action-reaction principle with a force $\mathbf{F}^{(\text{wall})} = -\mathbf{n} P \mathrm{d}S$.

The vector $\mathbf{n}$ is the normal direction of the surface patch $\mathrm{d}S$. By means of the divergence theorem the external term can be written as

$$\langle \sum_i^N \mathbf{q}_i \cdot \mathbf{F}_i^{(\mathrm{wall})} \rangle = -P \oint_{\partial V} \mathbf{q} \cdot \mathbf{n} \mathrm{d}S = -P \int_V \nabla \cdot \mathbf{q} \mathrm{d}V = -3PV. \tag{3.43}$$

Implementing Eq. (3.42) and Eq. (3.43) into Eq. (3.41) leads to

$$P = k_B T \frac{N}{V} + \frac{2}{3V} \left\langle \sum_{i<j}^N \mathbf{F}_{ij} \cdot \mathbf{r}_{ij} \right\rangle. \tag{3.44}$$

The excess pressure

$$P_{\mathrm{ex}} = \frac{2}{3V} \left\langle \sum_{i<j}^N \mathbf{F}_{ij} \cdot \mathbf{r}_{ij} \right\rangle. \tag{3.45}$$

however, has to be treated with caution, as we deal with a soft potential close to the hard core limit. For perfectly hard particles the forces diverge. However, the duration of the collisions also vanishes such that the momentum exchange $\Delta\mathbf{p}$ is finite. The Eq. (3.44) can be replaced by

$$P = k_B T \frac{N}{V} + \frac{2}{3V\tau} \left\langle \sum_c \Delta\mathbf{p}_{ij} \cdot \mathbf{r}_{ij} \right\rangle \tag{3.46}$$

where the symbol c entails all collisions during the time interval τ. The momentum exchange $\Delta\mathbf{p}_{ij}$ is calculated from the velocities of the particle i right before and after the contact with particle j. Usually, it is not as informative as for systems interacting via soft-core interactions. Nevertheless, as we will see it still contains enough information to identify phase transitions in Sec. 5.1.

3.3.3 Diffusion

The last important thermodynamic observable that has to be introduced is diffusion. Diffusion is defined as a measure of the mean distance a particle travels in time t. In simulations, the diffusion coefficient D is usually obtained by using the mean squared displacement

$$\langle \mathbf{r}_i^2(t) \rangle_i = \langle (\mathbf{q}_i(t) - \mathbf{q}_i(0))^2 \rangle_i = \frac{1}{N} \sum_i^N (\mathbf{q}_i(t) - \mathbf{q}_i(0))^2 \tag{3.47}$$

and describes the development of the mean squared distance between the original positions of the particles at time $t_i = 0$ and their current position at time $t_c = t$. Here the dynamics of each individual particle is tracked. Consequently, the mean squared displacement only contains physically meaningful information about diffusive behaviour by using MD and time averaging (but not for MC methods) . In three dimensions the relation between the mean squared displacement and diffusion coefficient is given by

$$\langle \mathbf{r}_i^2(t) \rangle_i = 6 \cdot D \cdot t^{\alpha} \text{ in the limit } t \to \infty. \tag{3.48}$$

The parameter D is the long-time diffusion coefficient. Mostly the mean squared displacement is linearly dependent on time $\alpha = 1$ and in the diffusive state which is a result of Brownian motion. For $0 < \alpha < 1$ the system is called subdiffusive, whereas for $\alpha > 1$ it is characterised as superdiffusive. For all systems described in this thesis, the behaviour corresponds to either normal diffusion ($\alpha = 1$) or the non-diffusive state ($\alpha = 0$).

3.4 Structural observables

The second important set of observables are structural observables. These are metrics and properties used to detect structural correlations between different molecules in the systems at a certain time. Hence, structural observables are static measures and not dependent on the dynamics of the whole system. Consequently, their values can be obtained using both a Molecular Dynamics and Monte Carlo simulation approach. However, it is argued that the Monte Carlo sampling is a much more efficient way as it is not restricted to the "dynamical" path to form the equilibrated configuration and excuses poorly chosen initial conditions more easily.

3.4.1 Nematic and polar order parameter

The concept to characterise global orientational order in the form of a nematic or smectic phase by a prominent direction called nematic director $\mathbf{n}$ has already been introduced in Sec. 1.3.2. This normalised director defines a preferred orientation of anisotropic particles within the system. As in the nematic phase, there is no distinction between parallel and anti-parallel alignment; so the sign of the director can be chosen arbitrarily $\mathbf{n} \equiv -\mathbf{n}$. This also holds even though the investigated pear-shaped particles covered in this thesis possess a pronounced head-tail-asymmetry and a distinct orientation thereto. It is equally likely to find pears facing up as pears facing down in

the particle system. Due to thermodynamic fluctuations, molecules are not perfectly aligned with the director. Therefore, to quantify nematic order the nematic order parameter P_2 is introduced [157, 303].

After expressing the directions $\mathbf{u}(\theta, \phi)$ of the long axis of a rod-like molecule in terms of polar coordinates with a polar angle θ and azimuthal angle ϕ, we can define the probability to find a particle which is oriented within a small angular element $\mathrm{d}\Omega = \sin\theta \mathrm{d}\theta\mathrm{d}\phi$ as $f(\theta, \phi)\mathrm{d}\Omega$. The angular distribution function $f(\theta, \phi)$ defines the molecular orientational distribution of the system. As we consider only uniaxial particles, which only have one marked long axis, the whole system has to be axially symmetric around $\mathbf{n}$ as well. Thus, the distribution function does not depend on ϕ when the coordinate system is placed such that the z-direction coincides with $\mathbf{n}$: $f(\theta, \phi) = \frac{f(\theta)}{2\pi}$. The angle θ can now be recognized as the angle between the molecule and the director. To reduce the density function to a sequence of scalars, which will be the measure of particle alignment, $f(\theta)$ is expanded to a sum of Legendre polynomials $P_n(\mathbf{n} \cdot \mathbf{u})$

$$f(\theta) = \sum_{n=0}^{\infty} f_n P_n(\mathbf{n} \cdot \mathbf{u}) = \sum_{n=0}^{\infty} f_n P_n(\cos\theta) \tag{3.49}$$

with

$$f_n = \frac{2n+1}{2} \int_{-1}^{1} f(\theta) P_n(\cos\theta) \mathrm{d}(\cos\theta). \tag{3.50}$$

The coefficients f_n include all the information of the angular density distribution and are, therefore, the best candidates for the nematic order parameter.

The first term with $f_0 = \frac{1}{2}$ is useless to measure nematic order as it is a constant for all distributions. $f_n = f_0\delta_{n0}$ resembles the angular distribution function of an isotropic configuration without any orientational order. Also the second amplitude f_1 has to be excluded. As the director and its antiparallel equivalent are interchangeable to describe a global alignment of particles, the angular distribution is symmetric around $\theta = \frac{\pi}{2}$. We obtain $f(\theta) = f(\pi - \theta)$. Calculating Eq. (3.50) it is shown that the second dipolar term vanishes $f_1 = 0$.

Hence, the nematic order parameter P_2 is defined by the first non-trivial multipole: the quadrupole f_2. Furthermore, we can identify the nematic order parameter

$$P_2 = \frac{2}{5} f_2 = \int_{-1}^{1} f(\theta) \frac{1}{2} (3\cos^2\theta - 1) \mathrm{d}(\cos\theta) = \langle P_2(\cos\theta) \rangle \tag{3.51}$$

using Eq. (3.50) as the average second Legendre polynomial of the angle between the director and the particle orientations. The factor $\frac{2}{5}$ ensures that P_2 lies within the interval $[-\frac{1}{2}, 1]$. If the distribution is peaked around $\theta = 0$ and $\theta = \pi$, which is tantamount to a near perfectly aligned system, P_2 approaches 1. The lower boundary $-\frac{1}{2}$ corresponds to a perfectly perpendicular arrangement of molecules to $\mathbf{n}$, which is not observed in the absence of external fields. For a constant $f(\theta)$ and an isotropic system, P_2 equals 0.

However, computational simulations face a problem as the director is not known a priori and P_2 cannot be identified by the particle orientations directly. One strategy of determining $\mathbf{n}$ is choosing a random direction $\mathbf{n}_0$ and calculating an order parameter using Eq. (3.51). Then an iterative algorithm is used to maximise $P_2(\mathbf{n})$ by calculating the gradient of the imminent $\mathbf{n}_k$ numerically. The nematic director $\mathbf{n}$ can be sufficiently closely approached after a finite number of iterative steps k: $\mathbf{n}_k \approx \mathbf{n}$. Nevertheless, this procedure is computationally very demanding and inefficient.

Luckily, P_2 can be calculated alternatively in a much more direct way using the nematic order tensor

$$\mathbf{Q} = \frac{1}{2N} \sum_{i}^{N} (3\mathbf{u}_i \otimes \mathbf{u}_i - 1). \tag{3.52}$$

The matrix $\mathbf{Q}$ depends on the orientational configurations of the whole system. Additionally, it is traceless and symmetric and, hence, can be represented by a diagonalised matrix $\mathbf{D}$ with an orthogonal matrix $\mathbf{S}$: $\mathbf{Q}$=$\mathbf{S}\mathbf{D}\mathbf{S}^T$.

The nematic order parameter can be written in terms of the order tensor with [157, 304]

$$\begin{aligned} P_2 = \langle P_2(\cos\theta) \rangle &= \left\langle \frac{1}{2} \left(3(\mathbf{n}^T \mathbf{u_i})^2 - 1 \right) \right\rangle = \left\langle \frac{1}{2} \left(3(\mathbf{n}^T \mathbf{u_i})^2 - 1 \right) \right\rangle = \\ &= \left\langle \frac{1}{2} \left(3(\mathbf{n}^T \mathbf{u_i})(\mathbf{u_i}^T \mathbf{n}) - 1 \right) \right\rangle = \mathbf{n}^T \left\langle \frac{1}{2} (3\mathbf{u_i} \otimes \mathbf{u_i} - 1) \right\rangle \mathbf{n} = \\ &= \mathbf{n}^T \mathbf{Q} \mathbf{n} = \mathbf{n}^T \mathbf{S}\mathbf{D}\mathbf{S}^T \mathbf{n} = \hat{\mathbf{n}}^T \mathbf{D} \hat{\mathbf{n}} = \lambda_1 \hat{n}_1^2 + \lambda_2 \hat{n}_2^2 + \lambda_3 \hat{n}_3^2 \end{aligned} \tag{3.53}$$

where $\lambda_1 > \lambda_2 > \lambda_3$ are the eigenvalues of $\mathbf{Q}$. It is apparent that P_2 is maximised if the director in the eigenbasis of $\mathbf{Q}$ is $\hat{\mathbf{n}} = (1, 0, 0)^T$. Consequently, P_2 can be identified as the largest eigenvalue of the nematic order matrix λ_1. The corresponding eigenvalue is the nematic director $\mathbf{n} = \mathbf{S}\hat{\mathbf{n}}$. Using this definition of P_2, even though a good measure for nematic or ordered phases, will lead to small positive values in the isotropic phase as a finite size effect. Therefore, we will talk about an orientationally ordered phase in the rest of this thesis if $P_2 > 0.2$.

As pears are polar particles, also a global polar order parameter P_1 according to a polar director $\mathbf{n}_{P_1}$ can be determined. The polar director is defined as the average normalized orientation over all particles in the system

$$\mathbf{n}_{P_1} = \frac{\sum_i^N \mathbf{u}_i}{|\sum_i^N \mathbf{u}_i|}. \tag{3.54}$$

To calculate P_1 the polar director is coupled with the particles orientations by

$$P_1 = \frac{1}{N}\left\langle \sum_i^N \mathbf{n}_{P_1}\mathbf{u}_i \right\rangle = \frac{1}{N}\left\langle \frac{\sum_i^N \mathbf{u}_i \sum_i^N \mathbf{u}_i}{|\sum_i^N \mathbf{u}_i|} \right\rangle = \frac{1}{N}\left|\left\langle \sum_i^N \mathbf{u}_i \right\rangle\right|. \tag{3.55}$$

This definition of the polar order corresponds to the first coefficient of the Legendre polynomial extension f_1 (see Eq. (3.50)). Here, we already argued that in general f_1 vanishes. Consequently, it does not make sense to calculate polar order globally. Nonetheless, the polar order and also the nematic order parameter can be coupled with the pair correlation function (defined in the very next section) which gives a measure for local polar and nematic order, respectively.

3.4.2 Pair correlation functions

One of the most powerful observables to characterise the translational order of particle systems are the *pair correlation function* $g(r)$, also known as the *radial distribution function*. The radial distribution function represents the probability, given that particle i is placed at the origin, to find another molecule j at a radial distance r. Thus $g(r)$ bears valuable information about the positional correlations between the particles. Based on the number density distribution function

$$\rho_N(\mathbf{r}) = \langle \sum_i \delta(\mathbf{r} - \mathbf{r}_i) \rangle \tag{3.56}$$

the radial distribution function is written as

$$g(r) = \frac{1}{N\rho_N} \left\langle \sum_i \sum_{j \neq i} \delta(r - r_{ij}) \right\rangle \tag{3.57}$$

with the global number density

$$\rho_N = \frac{N}{V}. \tag{3.58}$$

To calculate $g(r)$ numerically in our simulations, Eq. (3.57) has to be discretized and rewritten. Based on the definition of $g(r)$, the mean number of particles $\delta N(r)$ found within a small distance interval $[r, r+\delta r]$ from another particle is given by

$$\delta N(r) = \rho_N g(r) V_{\text{shell}}(r) \tag{3.59}$$

with $V_{\text{shell}}(r)$ being the volume of the thin spherical shell of thickness δr whose inner boundary is a sphere of radius r. By approximating $V_{\text{shell}}(r) = V_{\text{sph}}(r+\delta r) - V_{\text{sph}}(r) \approx 4\pi r^2 \delta r + O(\delta r^2)$ and rearranging Eq. (3.59), we obtain

$$g(r) = \frac{1}{\rho_N} \frac{\delta N(r)}{4\pi r^2 \delta r}. \tag{3.60}$$

This can be interpreted as a formula to generate the radial distribution function by a normalized histogram. The histogram is computed by counting all pair separations, corresponding to the domain $m\delta r < r_{ij} < (m+1)\delta r$ and normalize them according to Eq. (3.60). Note that the "normalisation" factor in this case indicates that $g(r)$ converges towards 1 for large distances: $\lim_{r\to\infty} g(r) = 1$. This indicates that a pair of particles at large distance from one another is uncorrelated. Additionally, to prevent boundary effects only pairs with $r_{ij} < \frac{L}{2}$ are considered. The concept is pictured in Fig. 3.3a.

In the analysis of liquid crystals it is often advantageous not to determine the radial distribution of a system, but to separate the distance between two molecules into a longitudinal and a lateral part. This is vividly illustrated by particles forming a smectic phase. Due to their anisotropic features, the order parallel to the director is different from perpendicular to the director. The radial distribution function, thus, superimposes the signatures along

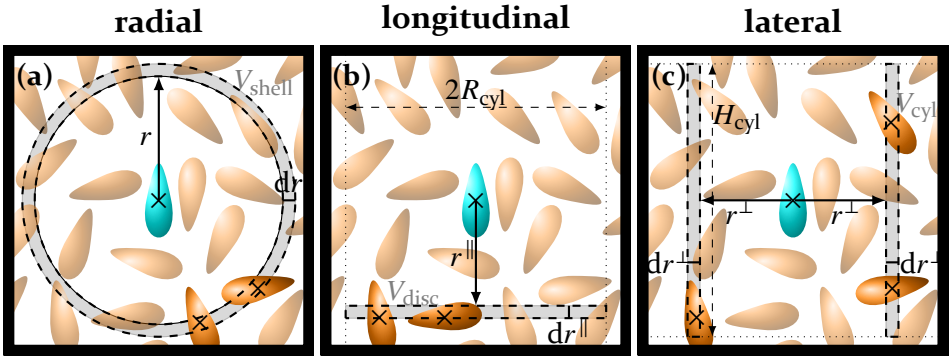

Figure 3.3: Schematics of the radial (a), longitudinal (b) and lateral distribution function (c). The figures show cross sections through the sampling space. The gray areas represent shells which bin the space around the center pear-shaped particle and are used to create the corresponding histogram. The shells are spherical (a), discal (b) and cylindrical (c).

both directions. By calculating $g^{\parallel}(\mathbf{n}\cdot\mathbf{r})$ and $g^{\perp}(\sqrt{r^2-(\mathbf{n}\cdot\mathbf{r})^2})$ the superimposition can be decoupled. The former characterises the smectic layering of the system, whereas the latter is a measure of translational order within the layers. However, this approach has the disadvantage that global orientational order is needed. Lipid systems adopting a bicontinuous surface geometry, exhibit no overall global orientational order as they form pronouncedly curved bilayers. Nevertheless, locally neighbouring lipids are clearly orientationally correlated such that a lateral and longitudinal distribution function on a local scale seems to be more effective. Thus, we replace the director with the orientation of the liquid crystal at the origin $\mathbf{u}_i$. In this way, we can guarantee to detect both curved bilayer ordering but also smectic layering as $\mathbf{u}_i \approx \mathbf{n}$.[3] The longitudinal and lateral distance are defined by $r^{\parallel} = \mathbf{u}_i \cdot \mathbf{r}$ and $r^{\perp} = \sqrt{r^2 - r^{\parallel 2}}$, respectively. Note here, that $r^{\parallel}$ can become negative. For pear-shaped particles, positive longitudinal distances correspond to a distance in the direction of the thin narrow end while negative distances have to be assigned to particles which are placed in the direction of the thick blunt end.

To compute the longitudinal distribution function $g^{\parallel}(r^{\parallel})$ and lateral distribution function $g^{\perp}(r^{\perp})$ we use a similar histogram approach like in Eq. (3.60). For simplifying the normalisation of the histograms they are calculated within

[3] This only applies to the smectic-A phase. For other smectic phases it is still more convenient to use the director as a reference.

a cylinder. This implies that only particles which lie within a cylinder with radius R_{cyl} and height H_{cyl} centered at the position of particle i are considered. The cylinder, furthermore, shares the same rotational symmetry axis as the very particle i (see Fig. 3.3b). The dimensions of the encapsulating cylinder have to be chosen such that the periodic boundaries of the simulation box are not trespassed

$$\begin{aligned} H_{\mathrm{cyl}} &< L \sin\alpha \\ R_{\mathrm{cyl}} &< \frac{L}{2} \sin\alpha. \end{aligned} \tag{3.61}$$

Here α encodes the aspect ratio of the cylinder $\tan\alpha$. The probability to find a particle at longitudinal distance $r^{\parallel}$ within a circular disk of thickness $\delta r^{\parallel}$ and volume $V_{\mathrm{disc}} = \pi R_{\mathrm{cyl}}^2 \delta r^{\parallel}$ bounded by the cylinder is given by

$$g^{\parallel}(r^{\parallel}) = \frac{1}{\rho_N} \frac{\delta N^{\parallel}(r^{\parallel})}{\pi R_{\mathrm{cyl}}^2 \delta r^{\parallel}}. \tag{3.62}$$

$\delta N^{\parallel}(r^{\parallel})$ is the mean number of particles within the disc. Analogously, probability to find a particle at lateral distance $r^{\perp}$ within a cylindrical shell of thickness $\delta r^{\perp}$ and volume $V_{\mathrm{disc}} \approx 2\pi r \delta r^{\parallel} H_{\mathrm{cyl}}$ is defined as

$$g^{\perp}(r^{\perp}) = \frac{1}{\rho_N} \frac{\delta N^{\perp}(r^{\perp})}{2\pi H_{\mathrm{cyl}} r^{\perp} \delta r^{\perp}}. \tag{3.63}$$

Here $\delta N^{\perp}(r^{\perp})$ is the mean number of particles within the cylindrical shell. The notion of both distribution functions is depicted in Fig. 3.3b+c.

The different distribution functions provide the possibility to study the local orientational ordering in a much more detailed way as well. Here, the number density in Eq. (3.56) can be weighted by a factor which includes the relative orientations of the pear particles. With this take on $g(r)$ we can define a polar radial distribution function g_{P1} weighted by the first Legendre polynomial $P_1(\mathbf{u}_i \cdot \mathbf{u}_j) = \cos(\mathbf{u}_i \cdot \mathbf{u}_j)$

$$g_{P_1}(r) = \frac{1}{N \delta N(r)} \left\langle \sum_i \sum_{j \neq i} \cos(\mathbf{u}_i \cdot \mathbf{u}_j) \delta(r - r_{ij}) \right\rangle. \tag{3.64}$$

For the nematic radial distribution function g_{P2} the second Legendre polynom $P_2(\mathbf{u}_i \cdot \mathbf{u}_j) = \frac{1}{2}(3\cos^2(\mathbf{u}_i \cdot \mathbf{u}_j) - 1)$ is used as weighting factor, such that

$$g_{P_2}(r) = \frac{1}{N\delta N(r)} \left\langle \sum_i \sum_{j \neq i} \frac{1}{2}(3\cos^2(\mathbf{u}_i \cdot \mathbf{u}_j) - 1)\delta(r - r_{ij}) \right\rangle. \tag{3.65}$$

Both the polar and nematic distribution function are scaled by the mean number of particles at distance r to easier relate the values to the polar and nematic order parameters (see Eq. (3.51) and Eq. (3.55)). This means that $g_{P_1}(r)$ and $g_{P_2}(r)$ determine how strongly two particles separated by a distance r are orientationally correlated. However, the functions do not contain information about the likeliness of such configurations occurring. In a similar vein also lateral and longitudinal variants of the distributions are defined.

3.4.3 Structure factor and scattering pattern

In a homogenous, equilibrated and infinitely large liquid system, the radial distribution function $g(r)$ is related to the structure factor $S(\mathbf{k})$ by a Fourier transformation [287]

$$S(\mathbf{k}) = 1 + \rho_N \int \exp(-\mathrm{i}\mathbf{kr})(g(\mathbf{r}) - 1)\mathrm{d}\mathbf{r}. \tag{3.66}$$

In experiments, the structure factor is usually obtained by measuring the diffraction or scattering patterns of a crystalline sample. The relative intensity $I(\mathbf{k})$ of the pattern is equivalent to the structure factor $S(\mathbf{k})$.[4] The structure factor contains information about the crystallographic symmetry of the analysed configuration which is a decisive step to identify the exact morphology. By plotting the intensity in terms of the absolute value of the scattering vector $\mathbf{k}$, the pattern displays characteristic peaks. These peaks can be assigned to reflection planes for corresponding ordered structures individually, but collectively specify the three-dimensional space group. Experimental scattering techniques, like small angle X-ray scattering, have shown to be the most reliable methods to identify elaborate and highly symmetric structures like the double gyroid [180, 305, 306, 307, 308, 309, 310].

[4] More precisely $I(\mathbf{k}) = f(\mathbf{k})S(\mathbf{k})$ with $f(\mathbf{k})$ is the form factor of the considered point cloud.

In computational physics, "scattering" is modelled by calculating the Fourier transform of the three-dimensional point density $\rho_N(\mathbf{r})$ which represents the multi-particle system[5] [287]

$$S(\mathbf{k}) = \frac{1}{N}\left|\int \rho_N(\mathbf{r})\exp(-\mathrm{i}\mathbf{k}\cdot\mathbf{r})\,\mathrm{d}\mathbf{r}\right|^2. \tag{3.67}$$

In particular, the scattering pattern is obtained by discretising the density into ρ_{ijk} with $0 \leq i,j,k < M-1$ representing the density amplitude at $\mathbf{r} = \frac{l_{\max}}{M}(i,j,k)^{\mathrm{T}}$ with box size l_{max}. Performing Fast Fourier transformation gives us the amplitude

$$\Psi_{\mathrm{lmn}} = \sum_{ijk}^{M-1} \rho_{ijk}\exp\left(-\mathrm{i}\frac{2\pi}{M}(l\cdot i + m\cdot j + n\cdot k)\right). \tag{3.68}$$

The scattering pattern $S(\mathbf{k})$ at $\mathbf{k} = \frac{2\pi}{l_{\max}}(l,m,n)^{\mathrm{T}}$ is roughly proportional to $|\Psi_{\mathrm{lmn}}|^2$. Moreover, using this computational tool, the structure factor cannot only be resolved radially in one dimension or as a projection in two dimensions but can also be unravelled easily in three dimensions such that we gain even more structural information than with state-of-the-art scattering experiments, where only 2D diffraction patterns can be realised.

3.4.4 Cluster algorithm

Another structural analysis tool we use in this thesis is a clustering algorithm which is tailored specifically to pear-shaped particle systems forming bicontinuous phases. The primary goal of this algorithm is to identify the two channel domains of triply-periodic minimal surface structures by separating the pear-shaped particles into two distinct subsets. Moreover, the clustering tool is performed to enable structural characterisation of phases.

To assign a pear-shaped particle to one of the channel domains we consider the position of its blunt end. Ellison *et al.* has shown that in the gyroid phase these ends are situated close to the skeletal backbone of the channel networks [241]. Based on this information the algorithm is partitioned into the following three steps which are also illustrated pictorially in Fig. 3.4:

[5]Note that Eq. (3.66) and Eq. (3.67) are equivalent up to a delta function term.

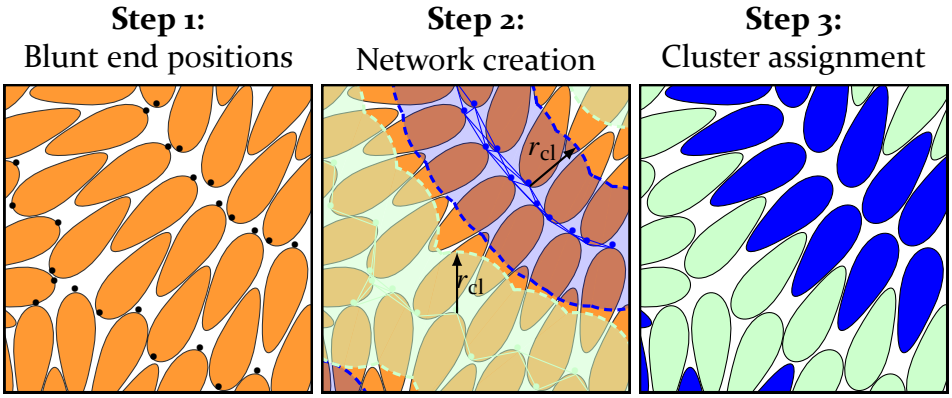

Figure 3.4: A pictorial illustration of the three major steps of the clustering algorithm. In the first step (left) nodes are assigned to the blunt ends of the pears. In the second step (centre) all nodes with a relative distance smaller than r_{cl} are linked which results in multiple connected graphs. In the third step (right) all pears, which belong to the same network are grouped to a cluster and coloured accordingly.

1. In the first step, nodes n are placed at the position of the blunt end of each particle as in the gyroid phase these ends ocularly group together.

2. Afterwards, we define two nodes n and $\tilde{n}$ as connected if their Euclidean distance $\mathrm{dist}(n, \tilde{n})$ is smaller than a certain threshold distance r_{cl} or in other words if $\tilde{n}$ is within the r_{cl}-neigbourhood $N_{r_{cl}}$ of n:

$$\tilde{n} \in N_{r_{cl}}(n) = \{p \in \mathbb{E} \mid \mathrm{dist}(n, p) < r_{cl}\}. \tag{3.69}$$

   This leads to a complex graph effectively linking different pears.

3. Nodes n and m, and subsequently the associated pears, are assigned to the same cluster in the last step if a path $n_1, n_2, .., n_{N-1}, n_N$ with $n_1 = n$ and $n_N = m$ between them can be found where

$$\forall 0 < i < N \quad n_i \in N_{r_{cl}}(n_{i+1}). \tag{3.70}$$

   Thus, the clusters are defined as the connected components of this graph.

3.4.5 Set-Voronoi tessellation

The structural analysis of the proximity of particles on the microscopic scale is a significant aspect in soft matter and related fields of physics. In particular,

the local geometric properties around the particles can give valuable insight into the stability of systems and reveal certain mechanisms about formation processes of particle configurations.

One important tool in this regard is the description of occupied space by *Voronoi cells* along with the pair correlation functions. The idea to tessellate space according to this method has found a wide range of useful applications, not only in many particle-based fields of science like granular materials [12, 311, 312, 313], colloidal systems [221, 314, 315, 316], biophysics [317, 318, 319, 320, 321] and other systems of statistical physics [322, 323, 324, 325, 326], but has also proven to be beneficial in other fields like cosmology [327, 328], solid state physics [329, 330], engineering [331, 332] or even outside science in city planing [333]. The original idea of *Voronoi tessellation*, also known as *point Voronoi tessellation*, which assigns each particle a certain volume which is closer to the centre of this particle than to any other particle is accredited to Dirichlet and Voronoi [334] but can be traced back even further to Descartes [335]. The process leads to individual non-overlapping cells which partition the whole system (see Fig. 3.5 left).

The Voronoi cell V_i^{cell} of particle i is defined mathematically in three-dimensional Euclidean space $\mathbb{E}^3$ by

$$V_i^{\text{cell}} = \{\mathbf{x} \in \mathbb{E}^3 \mid \text{dist}(\mathbf{x}, \mathbf{q}_i) \leq \text{dist}(\mathbf{x}, \mathbf{q}_j)\ \forall j \neq i\} \tag{3.71}$$

with $\text{dist}(\mathbf{x}, \mathbf{q_i})$ being the Euclidean distance between point $\mathbf{x}$ and the central point $\mathbf{q}_i$ of particle i. The combination of all cells is referred to as the *Voronoi diagram* and fills space completely as

$$\bigcup_i V_i^{\text{cell}} = \mathbb{E}^3. \tag{3.72}$$

This definition can be generalised, in the obvious way, to lower and higher dimensions but also to other metric spaces besides $\mathbb{E}$.

This basic version of the Voronoi diagram is a well-established method to study points sets. By inference, it is only applicable to non-overlapping mono-disperse sphere configurations. Already for polydisperse spheres but also for objects with much more intricate shapes, like pear-shaped particles, the Voronoi cells which are constructed with the concept above based on centre points alone, cannot be interpreted as the vicinity of the particles any more [335]. This can be seen especially in aspherical particle systems at

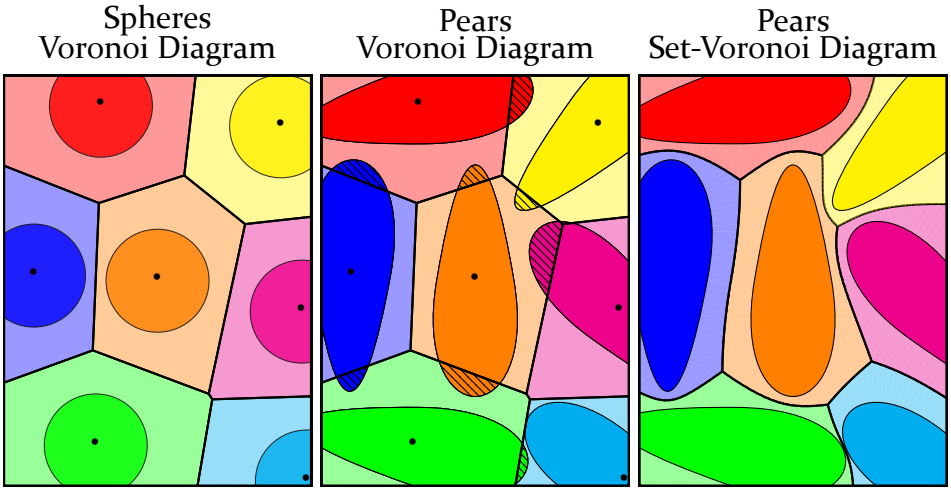

Figure 3.5: Left: The Voronoi diagram in a system of monodisperse spheres. The cells are constructed such that each point within a domain is closer to the centre of a sphere than to any other sphere. Center: The Voronoi diagram of the centre points of pear-shaped particles fails to describe a tessellation of particle environments for polydisperse and aspherical systems. Right: For complicated shapes, like pear-shaped particles, the Set-Voronoi diagram is used to divide space according to particle domains. This is done by relating the distance of the point to the surface of the particles rather than its centre.

high densities like those occurring in the gyroid phase of pear-shaped particle systems. Here the particles are often not entirely encapsulated by the Voronoi cell, but parts of the particle reach into the cell domain of a neighbouring particle (see Fig. 3.5 centre). This contradicts the intuitive notion of the environment of an object. The method breaks down because arbitrary features of shape often cannot be captured by just a single point in space like for example the centre of the particle. Additionally, the term "centre" point of a particle is not uniquely defined for most complex shapes.[6]

Another more advanced version of the point Voronoi diagram is the *Laguerre tessellation* [325, 336], otherwise referred to as the *Power diagram* [337] or *Voronoi S-net* [338]. This improvement, however, is tailored specifically to polydisperse sphere systems and yet fails for aspherical particles as well. The most suitable generalisation of the Voronoi diagram for pears, but also aspherical particles in general, is the *Set-Voronoi tessellation* [339], which

[6]There exist a magnitude of different definitions for the "centre" of an object like the centre of mass, Steiner point, centre of the maximal inscribed sphere and centre of the minimal circumscribed sphere

is also known as *tessellation by zone of influence* [340] or *navigational map* [312]. In this approach, the cells are related to the surface of the objects and thus the bodies themselves rather than only their centre point. The resulting cells are still space filling and non-overlapping, but also exhibit in contrast to point Voronoi tessellations curved faces and are not necessarily purely convex as indicated on the right-hand side of Fig. 3.5. Moreover, this method can cover a wide range of particle morphologies from simple monodisperse sphere systems to mixtures of nearly arbitrary shapes.

The mathematical definition of the Set-Voronoi cells of an object i is

$$V_i^{\text{cell}} = \{\mathbf{x} \in \mathbb{E}^3 \mid \text{dist}(\mathbf{x}, \mathcal{B}_i) \leq \text{dist}(\mathbf{x}, \mathcal{B}_j)\ \forall j \neq i\}. \tag{3.73}$$

Here the distance $\text{dist}(\mathbf{x}, \mathcal{B}_i)$ between the point $\mathbf{x}$ and the interior $\mathcal{B}_i$ of the object is given by the minimal Euclidean distance of the $\text{dist}(\mathbf{x}, \mathcal{B}_i) = \min_{\mathbf{p}\in\mathcal{B}_i} \text{dist}(\mathbf{x}, \mathbf{p})$. With this definition we are able to prevent particles to extend into multiple cells as $\text{dist}(\mathbf{x}, \mathcal{B}_i) = 0\ \forall x \in \mathcal{B}_i$. Note that the point $\mathbf{p}$ in the definition of $\text{dist}(\mathbf{x}, \mathcal{B})$ always lies on the surface of the particle $\partial\mathcal{B}$.

3.4.6 POMELO: A generic Set-Voronoi tool

Even though we can describe the surface of the pear-shaped particles by Bézier-curves, the curved interfaces between neighbouring Set-Voronoi cells cannot be calculated directly from this parametrisation. Therefore, we apply a computational construction algorithm, which was introduced in Ref. [339], in order to extract the Set-Voronoi tessellations of pear-shaped particle systems in this thesis. This algorithm is based on the computation of the conventional point Voronoi tessellation paired with a triangulation of the particles' bounding surfaces and consists of three major steps:

1. In the first step, the surface of all pear-shaped particles is sampled. This is done by generating a point-cloud which represents the surface.

2. Afterwards, the point Voronoi tessellation based on these surface-points is calculated numerically.

3. Subsequently, all cells which belong to surface points of the same pear-shaped particle are merged. The resulting collection of regions corresponds to the Set-Voronoi diagram of the pear system.

The steps are also illustrated in Fig. 3.6.

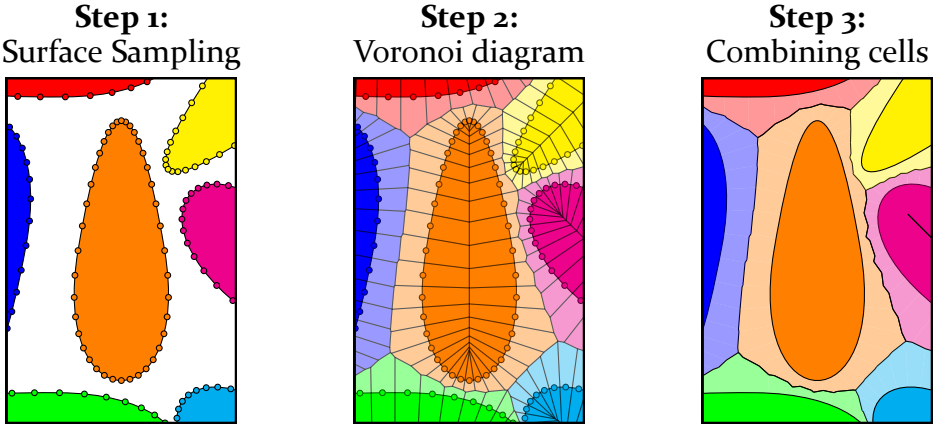

Figure 3.6: A pictorial illustration of the three major steps of the Set-Voronoi tessellation algorithm executed by POMELO. In the first step (left) the surfaces of the particles are sampled by point clouds. In the second step (centre) the point Voronoi cells of the surface point distribution are calculated. In the third step (right) all cells which belonging to surface points of the same particle are merged. The resulting tessellation corresponds to the Set-Voronoi diagram.

To calculate all the Set-Voronoi tessellations in the following we used a new software tool called *POMELO*, which was developed as a side project in the course of this thesis in collaboration with Simon Weis [341, 342]. In general, POMELO is designed to calculate Set-Voronoi tessellations of arbitrarily shaped particle packings. Beside systems of pear-shaped particles (see especially Chap. 4.3 and Ref. [343]), POMELO has also been applied to sphere [344, 345], ellipsoid [346] and tetrahedra [347] packings. Moreover, it has been successfully used to analyse systems of amino-acid molecules [348]. Additionally, modes to calculate the Set-Voronoi diagrams of spherocylinders, coarse-grained copolymers and point clouds are implemented.

To highlight the versatility of POMELO and how it can be applied in soft-matter physics in addition to particle packings like the pear-shaped particle system presented in this thesis, we want to briefly discuss another two fields of applications, which we were significantly involved with. In particular, we briefly focus on a project about creating amorphous cellular geometries with a hidden hyperuniform order which has been published in Ref. [349][7]

[7] My contribution to this work was the implementation of the Voronoi diagram computations, as well as technical and scientific advice on the computer-geometric analysis of shape metrics for Voronoi structures.

and secondly a still ongoing study of disordered minimal surface structures. Note that these two examples are mostly decoupled from the topic of the rest of this thesis and, hence, can be interpreted as a small intermezzo. In order to continue with the main project of this PhD project, the following two subsections can be skipped.

Interlude I: Hyperuniform structures

To find space tessellation with extremal geometrical properties is a fundamental mathematical and physical problem. One example is the Kelvin problem [350], asking the question about the ideal space partition which minimises the interface-area between the cells.[8] Another one is the Kepler problem [352] searching for the sphere packing with the highest overall packing fraction.[9] The trinity of such extremal tilling questions is completed by the Quantizer problem [354], where the cells of the space filling tessellation are sought to be as "spherical" as possible. Naturally, the cells cannot obtain perfect spherical shape without creating voids. It is conjectured that a Voronoi-tessellation based on a body-centred cubic lattice is the closest attempt to realise such packing of sphere-like cells [355].

A way to measure the sphericity a the Voronoi cells C_i with generator points $\mathbf{z_i}$ within a tessellation is the sum of their Quantizer energies $E(C_i)$

$$\sum_i E(C_i) = \sum_i \int_{C_i} ||\mathbf{x} - \mathbf{z}_i||^2 d\mathbf{x} \tag{3.74}$$

which favours centroidal Voronoi tessellations (CVT) [356] where the centres of mass coincides with the generating points. This energy is reminiscent of the chain stretching free energy of copolymers in the strong segregation limit [357]. A gradient descent algorithm, known as Lloyd algorithm [358] has shown to dynamically generate CVT point patterns [359]. Here the generating points of the Voronoi diagram are shifted to the centres of mass, consequently iteratively decreasing the Quantizer energy of Eq. (3.74).

Starting from different disordered point distributions and applying POMELO for the Voronoi cell calculations, we could show that the point pattern converges towards a universal amorphous state rather than a more

[8] So far the best known optimum is the Weaire-Phelan foam structure [351].
[9] It has been proven that the face-centered cubic is the perfect packing [353].

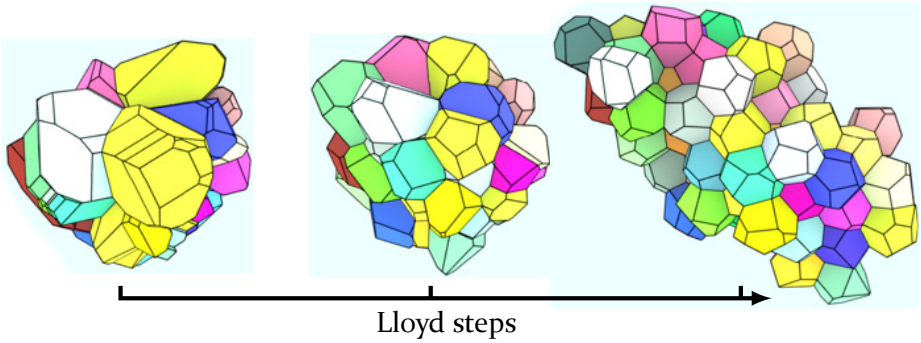

Figure 3.7: Convergence of Lloyd's algorithm in three dimensions. A subset of a three-dimensional system before, during (5 steps), and after (12202 steps) applying Lloyd's algorithm. The distributions $f(v)$ of cell volumes v demonstrate the high degree of uniformity in cell volumes in the final states. The total energy converges to a value slightly above the value of the optimal BCC lattice. The image is taken with permission from Ref. [349].

expected ordered structure like the "ideal" BCC lattice (see Fig. 3.7). The final states are all both energetically slightly less beneficial than the BCC lattice and hyperuniform. Hyperuniformity [360] is defined as an anomalous suppression of density fluctuations on large length scales which is indicated by a vanishing structure factor $S(k)$ for small wavevectors $k \to 0$. This behaviour suggests a hidden order on the macroscopic scale even though the point pattern showcases amorphous properties otherwise and has been observed and applied in various fields of science [361, 362, 363, 364, 365, 366, 367]. The stability of this energetically non-ideal hyperuniform state could be related to local configurations with lower energies than the global ground state. These local domains frustrate the system geometrically and prevent it from reaching the optimal state. Similar observations have also been made in two dimensions.

The observed universal hyperuniform point patterns are closely related to the geometrically frustrated equivalents in the Kepler (random close packing limit [368]) and Kelvin problem (disordered structures in sheared soap froth [325]). Hence there is a reasonable chance that also the hyperuniform patterns resulting from Lloyd's algorithm are present in physics and biology, but have not been identified yet. To identify this possibility we, however, have to analyse the stability of the anomalous state further by for example applying a modified algorithm where we introduce a temperature similar to the Metropolis Monte Carlo technique.

Interlude II: Disordered minimal surfaces

A further geometrically frustrated minimisation problem is the problem of minimal surfaces itself. Similar to the Quantizer problem, where a space tessellation of perfectly spherical cells is impossible, there is no "physical", or in other terms non-self-intersecting, embedding of a minimal surface with constant negative Gaussian curvature in Euclidean space [369, 370][10]. It is argued that the gyroid is the minimal surface with the least variation in constant Gaussian curvature and thus the closest approach to a negative constant-Gaussian-curvature surface [91, 167] (for a more in-depth discussion about the homogeneity of TPMS we refer to a later chapter, in particular Sec. 8.1).

Due to the resemblance between the Quantizer and negative constant-Gaussian-curvature surface problem, the question arises if for the latter similar amorphous surface structures exist which are locally stable but energetically not ideal. Here, very promising candidates are the lipidic L_3 phases known as sponge phases in soft matter physics [371]. The sponge phase can be interpreted as a disordered cubic phase where a lipid bilayer separates a bicontinuous aqueous channel network. Even though the sponge is well studied, it is not yet clarified if this bilayer arrangement is fully disordered or is indeed based on a pattern with some hidden order [372].

Consequently, we are interested if a connection between L_3 phases and the point patterns obtained by Lloyd's algorithm can be found. This hypothesis is strengthened by the symmetry of the conjectured ideal solutions of both minimisation problems. As we mentioned above the Quantizer problem is minimised by a Voronoi tessellation of a BCC lattice. The assumed global minimum of the negative constant-Gaussian-curvature problem, the $Ia\bar{3}d$ gyroid, also displays body centred symmetry. Hence, we try to create disordered sponge surfaces and suggest an algorithm to obtain them from hyperuniform point patterns by the following:

1. In the first stage, we generate the three-dimensional hyperuniform point pattern by performing Lloyd's algorithm from a random initial configuration of 100 points within a cubic simulation box with periodic boundary conditions.

[10] Hilbert even proved in Ref. [369] that there exists no complete regular surface of constant negative Gaussian curvature immersed in $\mathbb{R}^3$ at all.

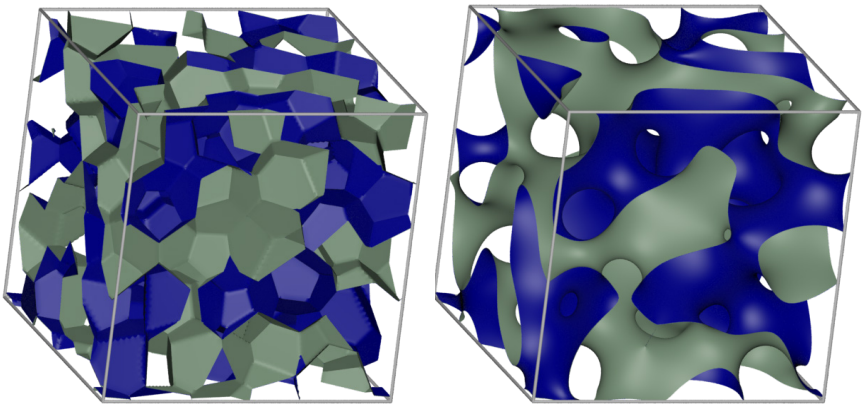

Figure 3.8: The disordered minimal surface structures obtained from the hyperuniform point pattern which is generated by Lloyd's algorithm. Left: The polygon interface between the points of the different subgroups is calculated by POMELO. Right: The same surface after the minimisation algorithm is applied by using Surface Evolver.

2. Afterwards the points are randomly assigned into two groups.

3. The Voronoi cell tessellation is calculated by applying POMELO on the point distribution. All cells which belong to points of the same subgroup are merged. The resulting volumes can be interpreted as a bicontinuous network domain which is divided by a polygon interface with surface area A.

4. A random point of one subgroup is interchanged with a random point of the opposite subgroup.

5. Step 3 is repeated and the surface area A is compared with the area A' of the previous subgroup composition.

6. If $A > A'$ the two points are switched back. Otherwise, the switch is accepted.

7. The algorithm is iterated from step 4 until the partition with the minimal A has been found (see Fig. 3.8 left).

8. The interface is converted to a minimal surface without changing the topology by minimising the surface area further by the software tool Surface Evolver [97, 98]. The volume fraction between both channels is set 50:50.

The resulting surface is a disordered bicontinuous minimal surface which is highly reminiscent of sponge phase structures (see Fig. 3.8 right). Note that these surfaces have to be studied more before we can draw a final conclusion. For example, it would be interesting to compare the variation in Gaussian curvature with sponges in lipid systems. Another indication might be given by the channel sizes of the labyrinths. In general, the sponges are created by diluting and swelling the water channels. Also our surfaces reveal some large regions can be found. However, there is also a good chance that the algorithm has some need for improvement. For once, it sometimes occurs that channel necks shrink down to single lines during the minimisation protocol of the Surface Evolver. This might be prevented by coupling the area with the curvature of the surface and using this new property as the minimisation parameter. Secondly, we are dealing with the steepest descent method until now, which might be improved by some Markov chain implementation.

4 The gyroid phase in PHGO pear-shaped particle systems

"Only entropy comes easy!"

– Anton Chekhov

This chapter addresses the entropic self-assembly of the bicontinuous $Ia\bar{3}d$ double gyroid phase in PHGO pear-shaped particle systems. It significantly extends previous studies on this phase by Ellison et al. [241, 373]. We determine reliable estimates for the unit cell size by determining the structure factor of the gyroid network and test the hypothesis that this phase is analogous to a "local smectic phase" with cubic symmetry. Moreover, we probe the mechanism by which interdigitating sheets of pears in these systems create surfaces with negative Gaussian curvature. This is achieved by the use of a Voronoi tessellation, whereby both the shape and volume of Voronoi cells can be assessed in regards to the local Gaussian curvature of the gyroid minimal surface. This analysis shows that the mechanisms prevalent in this entropy-driven system differ from those found in systems which form gyroid structures in nature (lipid bilayers) and from synthesised materials (di-block copolymers), systems in which the formation of the gyroid is enthalpically driven.[1]

[1]This chapter is based, in parts, on the article P.W.A. Schönhöfer, L.J. Ellison, M. Marechal, D.J. Cleaver, and G.E. Schröder-Turk, "Purely entropic self-assembly of the bicontinuous $Ia\bar{3}d$ gyroid phase in equilibrium hard-pear systems", *Interface Focus* **7**:20160161, 2017. All simulation methods, numerical procedures and data analyses of this paper were implemented and executed by me (with the MD code based on earlier code by Laurence Ellison). Alongside the senior authors, I was a major contributor to the conceptual questions and research methods addressed in the article, and the interpretations presented as results. I created all 13 illustrations and graphs in the article and have written the manuscript, with help and comments from Gerd Schröder-Turk, Matthieu Marechal and Douglas Cleaver. In addition, parts of the Set-Voronoi analysis have been published in S. Weis, P.W.A. Schönhöfer, F.M. Schaller, M. Schröter and G.E. Schröder-Turk, "Pomelo, a tool for computing generic Set-Voronoi diagrams of aspherical particles of arbitrary shape", *Europhys. J.*, **140**:06007, 2017. Pomelo was developed by me and fellow PhD student Dr Simon Weis. My substantial contribution is reflected in the 'equal contribution' statement in the author list. I created 5 of the 9 illustrations and graphs in the article, and have written the manuscript together with the other authors. Verbatim quotes from these papers may have been used without explicit citations.

Microscopically, the pear-shaped particle conveys a more or less plain and unremarkable impression. Like many other basic colloidal shapes, however, the simplicity of the pear hides the fact that assemblies of these particles can display a high degree of complexity on the macroscopic level. In particular, earlier computational research on the PHGO pear-shaped particle model (see Eq. (2.17) for the definition of the PHGO contact function) showcased an interesting and, in terms of dominantly entropically driven systems, exotic phase behaviour, worthwhile to undergo an in-depth analysis. Pear-shaped particle systems have the capability to globally align which is revealed by a nematic and smectic phase (for an analysis of these phases see Sec. 5.1). They stand out, however, through the more complex collective behaviour, namely through the spontaneous formation of the bicontinuous double gyroid structure, as first observed by Ellison *et al.* in Ref. [241].

Ellison *et al.* have shown that the PHGO particles adopt this liquid crystal phase in a warped "bilayer"-arrangement that fills space fairly uniformly, at fluid-like densities (see Fig. 4.1a). More specifically the blunt ends of the pears point into the labyrinthine domains of the double gyroid structure. Furthermore, it was conjectured that the pear positions adopt a distribution of distances from the (hypothetical) minimal surface and that the pear orientations create characteristic angles around the minimal surface normal directions. The blunt ends, hence, can straightforwardly be subdivided into two subsets, each occupying one or the other of the labyrinthine domains, whereas the locations of the sharp ends are staggered near the minimal surface, see Fig. 4.1b.

In this chapter, we are particularly interested in deeper scrutiny of this gyroid phase formed by pears interacting according to the PHGO contact function to get a greater understanding of the relations between the pear-shaped particles arrangements and the geometry of the gyroid minimal surface. This presents the prospect to assess the hypotheses about the microscopic behaviour of pear-shaped particles within the gyroid and to learn more about the collective mechanisms which result in the self-assembly of one of nature's most complex, most ordered, and most symmetric structures.

We already mentioned in Sec. 1.3.2 that in various forms, the double gyroid is a regularly observed structure in a variety of self-assembled soft matter systems [50, 374, 375]. Also the importance of entropy for the self-assembly of amphiphilic molecules – with energetic terms that favour local segregation –

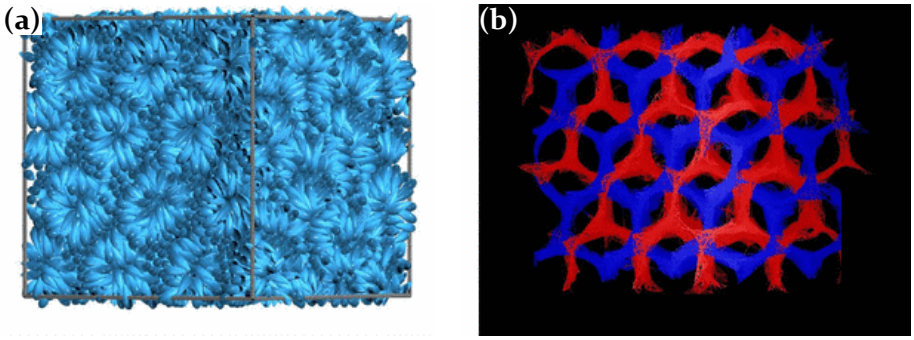

Figure 4.1: (a) The PHGO pear-shaped particles form a curved bilayer phase as observed by Ellison [241, 373]. (b) This phase can be identified as the Ia$\bar{3}$d gyroid phase by extracting the channel domains on the basis of the positions of the pear blunt ends. The figures have been obtained with permission from Ref. [241].

has been mentioned, implicit in both the molecular shape concept [50, 244] and the Helfrich formalism [245, 246]. Indeed, soft matter physics is generally concerned with systems in which entropy plays a significant role, that is, where the relevant interaction terms are typically of the same order as the thermal energy k_BT [376]. This is undoubtedly the regime in which the bicontinuous double gyroid phase is formed by amphiphilic molecules.[2]

However, all of these "conventional" gyroid-forming systems in soft matter also have a clear enthalpic component, evident in the amphiphilic (segregating) nature of their constituent molecules. For instance, lipids (in water) form minimal surface structures by facing the solvent with their solvophilic moiety and, hence, create a head-tail disparity enthalpically. This induces a type of tapering, indicated by the shape parameter, necessary to stack the molecules on the minimal surface effectively. Also the di-block copolymers, which are easier to compare with the pear-shaped particle system because they also fill space completely as a melt, break the symmetry due to the different potentials between distinct pairings of monomers. This is a significant difference from the purely-repulsive pear-shaped particles studied here, which interact via excluded volume only, albeit the excluded volume cannot be reduced to an exact additive hard shape.

[2]The hydrophobic (tail-tail) interactions are typically larger than $\approx k_BT$, but these are concealed by other tails. Hence, their contribution can be seen as irrelevant.

The proclaimed uniqueness of the double gyroid phase in this particular system lies in its existence despite the lack of any attractive or modulated forces, which give specific particle configurations energetic benefits. One could indeed raise the argument that, based on its description in earlier chapters (see Fig. 2.8), the self-non-additivity of the PHGO contact function can be interpreted as an effective, attractive potential term or as "entropic amphiphilic" (the extent to which the non-additivity of the interaction can be interpreted as a polarity is discussed in Chap. 6). However, even though it might be a possible route to copy the non-additivity of the PHGO contact function in experiments by introducing attractive forces, in our simulations, we do not explicitly include attraction but enforce merely repulsive forces and even hard-core interactions between particles. This, however, means that the conditions of the PHGO system are of similar nature to hard sphere, rod or the latter discussed HPR systems, as in all these models the particles only interact via collision governed by a contact function. Moreover, the high degree of complex long-ranged order contained within the gyroid morphology of the PHGO system emerges by the same mechanism as the crystallisation transition in the hard sphere equilibrium fluid [206, 207] or the nematic and smectic order in simple liquid crystal models like spherocylinders [213, 377, 378]: merely by maximising entropy!

This chapter is structured as followed. First in Sec. 4.1 we reproduce the simulations of Ref. [241] to obtain the gyroid phase in PHGO particle systems. In Sec. 4.2, we undertake a detailed structural analysis, where we determine the mesoscopic length-scale/unit cell size of the gyroid structure by calculating the structure factor for large systems of 10000 pear-shaped particles. Moreover, simulations of only a single unit cell are performed in Sec. 4.3, through which we gain insight into the nature of the pear gyroid and how it differs from those exhibited by different classes of experimental systems. Those investigations include the use of Set-Voronoi diagrams to explain the mechanism behind stabilising the minimal surface structure. Note that this chapter addresses only particle systems with the PHGO contact function. Hard pears of revolution do not form the gyroid phase (see detailed discussion in chapter Chap. 5).

4.1 Creating the gyroid phase in PHGO pear-shaped particle systems

As an initial step, we reproduce the self-assembly of the gyroid in systems of 10000 monodisperse PHGO pear-shaped particles as observed by Ellison

[241, 373]. As already mentioned not all pear-shaped particles form the desired mesostructure, such that we use the same parameter set as in that study. In Ref. [241] Ellison obtained distinct gyroid phases for 10000 pears with an aspect ratio $k = 3$ and tapering parameter $3.0 < k_\theta < 4.6$. Therefore, we perform multiple simulations within the particle interval $k_\theta \in \{3.2, 3.3, \ldots, 4.5, 4.6\}$ and $k = 3$ to both cover a wide range of pears which are able to assemble into the gyroid sufficiently and to compare their differences and similarities. In terms of the tapering angle, the interval lies between $12.4° < \theta_k < 18.9°$.

We here use Molecular Dynamics and Monte Carlo simulation techniques, as discussed in Sec. 3.2, to generate the gyroid configurations of all different pears by compression. In this thesis, we will, in general, describe the density as the *global volume density* of the system

$$\rho_g = \frac{N \cdot V_{\text{pear}}}{V_{\text{box}}}, \tag{4.1}$$

which corresponds to the packing fraction. Here, the pear volume V_{pear} is calculated numerically using a mesh of the particle's surface and the volume V_{box} describes the dimensions of the simulation box.

The interaction potential, which is used to represent the hard-core interaction of pears in the MD simulations, is the modified version of the purely repulsive WCA potential, see Eq. (2.21). Full simulation sets are performed in the canonical NVT-ensemble, where the simulation box is set up such that it can adapt its three edge lengths independently while maintaining fixed total volume. The time step and the temperature are set to $\Delta t = 0.0015$ and $T = 1$ like for the simulations to determine the phase diagram to keep consistency.

Additionally, MC simulations using the same parameters are performed for $k_\theta = 3.8$. Here, the hard-core PHGO contact function was used as a criterion for particle overlap (see Eq. (2.6) and Eq. (2.17)). The MC translation step and the rotation step are again initially set to $\Delta_{q,\max} = 0.015\sigma_w$ and $\Delta_{u,\max} = 0.015\sigma_w$, respectively, but have been adjusted during the compression to make certain that always roughly 50% of the displacement attempts are accepted successfully. The results of these two simulation techniques show no significant differences.

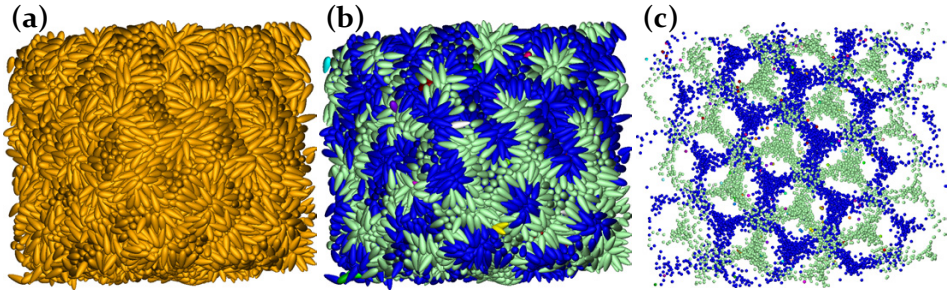

Figure 4.2: (a) An assembly of 10000 pear-shaped particles forming the gyroid structure (k_θ = 3.8, ρ_g = 0.57). (b) The same gyroid configuration after the cluster determination process (see Sec. 3.4.4). The colors indicate the cluster assignment of the pear-shaped particles. (c) Only the positions of the blunt ends of the pears are illustrated by spheres. The colors again comply with distinct clusters.

For each set, the pears are initially placed for simplicity at the positions of a large simple cubic lattice at a low density (ρ_g = 0.2) and developed for 500, 000 simulation steps to erase all configurational memory before being slowly compressed to a density of ρ_g = 0.555. Afterwards, the simulations undergo an equilibration run of $1.5{\cdot}10^6$ steps before the final sequence of $2.0{\cdot}10^7$ steps is performed where the data is sampled. For an additional set of simulation runs we also start from an artificial smectic phase at the target density ρ_g = 0.555, where all particles are perfectly aligned. For both initial conditions we eventually obtain double gyroid structures like those depicted in Fig. 4.2 for k_θ = 3.8.

At first glance, the structures again do not differ substantially from a disordered isotropic phase (see Fig. 4.2a) . In particular, the nematic order parameter stays close to P_2 = 0 for the whole compression process which indicates that there is no global orientational order present. Also, with the artificial smectic starting configuration, all systems quickly lose the global nematic order already in the equilibration phase of the first $2.5{\cdot}10^6$ steps (see Fig. 4.3). It is striking that more ellipsoidal particles keep the nematic order longer than the more tapered pear-shaped particles. After the equilibration P_2 only fluctuates slightly around o which indicates the fluid-like behaviour of the gyroid phase.

For all simulated configurations, the gyroid networks are identified by cluster analysis as described in Sec. 3.4.4. This is displayed in Fig. 4.2b+c. Despite all the strong indications and the fact that we already called this

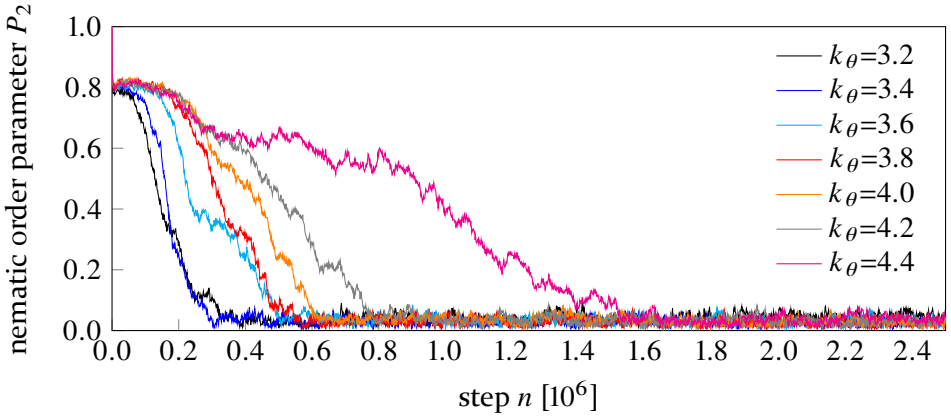

Figure 4.3: The nematic order parameter P_2 during the equilibration phase of different PHGO pear-shaped particle systems with $N = 10000$ and $k = 3$ at a density $\rho = 0.555$. Perfectly aligned artificial smectic configurations are used as initial structures.

phase as a gyroid, we can technically not yet conclusively confirm that the emerging channel domains are, indeed, coincident with the skeletal network of the gyroid. However, without knowing the periodicity of the gyroid, this is a difficult task to undertake. Fortunately, we can kill two birds with one stone by taking the crystallographic route and calculating the structure factor of the arrangement of the blunt ends. On the one hand, we are able to obtain the symmetry of the structure from its scattering pattern and eventually pinpoint the structure exactly. On the other hand, this approach comes with the benefit of additionally providing information about the unit cell size of the mesostructure, which is crucial for a detailed computational analysis of this phase.

4.2 Crystallographic analysis of the gyroid structure

The triply-periodic feature of the gyroid phase indicates that its structure is governed by its periodicity. Like all simulations of periodic phases, all the simulations of the gyroid phase presented in this thesis are subject to commensurability issues (between the lattice parameter, spontaneously adopted by the phase, and the simulation box size). In experiments, the systems of molecules are in the thermodynamic limit, such that the number N_{PUC} of particles within a translational unit cell and the lattice parameter a stem from thermodynamic equilibration. Resultant fluctuations in the number

of particles within a unit cell or the dimensions of that cell can then be adjusted since the total number of unit cells, and the total number of molecules is effectively infinite. By contrast, only a finite system volume can be modelled using simulation techniques. In the hypothetical case where a and N_{PUC} are known *a priori*, it comes quite natural to arrange the edge lengths of the simulation box such that they coincide with integer multiples of the translational unit cell size. An alternative choice would be to impose a box, which represents a larger, differently oriented translational periodicity of the crystal structure (such as the one based on both {001} and {110} directions described later). However, for simulation boxes, which are not both correctly oriented and commensurate with N_{PUC} and a, the mesostructure would be distorted compared to the infinite system. The system might accommodate the poorly chosen simulation box dimensions by forming defects, adopting a geometric structure that is not thermodynamically stable (but stabilised by the imposed simulation box), or attaining a modified version of the true equilibrium structure.

In practice, a and N_{PUC} are not known *a priori*. The challenge lies in detecting rigorous estimates for these parameters from simulations of finite systems – and indeed determining beyond a reasonable doubt that an observed geometric phase corresponds to the equilibrium (i.e., infinite) structure, rather than being stabilised by the finite simulation box. Even when the geometry is known, determining a and N_{PUC} from simulations is not straightforward. This problem has been considered in the context of cluster crystals [379] and a low-density low-temperature gyroid phase [380]; however, the methodology, similar to an μVT ensemble (see Sec. 3.1.2), applied therein is not transferrable to our hard-core PHGO pear systems at high densities.[3]

In our case, we have to determine the periodicity by a sufficiently large simulation where the boundary-condition effects are as small as possible such that no major defects are created. It turns out that our simulations of 10000 pear-shaped particles are already large enough and a suitable candidate to identify the unit cell size of the gyroid structure[4]. Admittedly, the channel domain illustration in Fig. 4.2c suggests that also here the adopted

[3]The method of Mladek *et al.* [379] relies on Widom's test particle insertion method [381, 382] to determine the chemical potential, but sampling efficiency for this approach is very poor for short-ranged repulsive potentials, particularly at the packing fractions of interest in this work.

[4]For $k_\theta = 3.8$ simulations with $N = 12000$ and $N = 15000$ give similar results.

gyroid configuration is slightly affected by the incompatibility of the simulation box and unit cell dimensions as the crystallographic {100}-direction of the gyroids formed with particles $3.2 < k_\theta < 4.6$ are generally not aligned to the {100}-direction of the simulation box. Nevertheless, we can make the argument that the adjustable boundary walls successfully counteract the induction of substantive deformations. All systems exhibit a multitude of unit cells which showcase only minor stretches and small distortions from the ideal cubic symmetry.

4.2.1 Determination of the space group

To obtain the unit cell size and to confirm the Ia$\bar{3}$d cubic symmetry group, we calculate the three-dimensional structure factor $S(\mathbf{k})$ of large systems. For our analysis, we perform the Fast Fourier Transform of the density profile of both identifiable network domains. Therefore, the three-dimensional point density distribution of the blunt ends, which constitute the backbone of the two labyrinthine channels, is voxelised and used as an input to calculate the mean peaks of the resultant three-dimensional scattering pattern. The method to obtain the scattering pattern is discussed in Sec. 3.4.3.

In Fig. 4.4 projections of a representative scattering profile of 10000 pear-shaped particles with $k_\theta = 3.8$ are shown. Note here that for all the other considered k_θ the same behaviour has been observed as well. Already these projections indicate that the pear structure is indeed the double gyroid. The projections exhibit 6-fold rotational symmetry in the {111}-direction (plane orbifold group: $*632$), 4-fold rotational symmetry in the {100}-direction (plane orbifold group: $*442$) and 2-fold rotational symmetry in the {110}-direction (plane orbifold group: $2*22$). To describe the two-dimensional space groups of the projections we here use the orbifold notation. Orbifolds or "orbit-manifolds" characterise symmetric patterns by encoding isometries into manifold singularities or topological features [383].[5] A pictorial description is shown in Fig. 4.4 to give a better understanding of the orbifold notation in relation to the scattering patterns. Even though there are

[5] Conway has introduced orbifold symbols to signify these orbifolds and the underlying transformations by a simple coding [384]. Integers i left of the asterisk indicate cone-points which lead to i-fold-rotations around a gyration point. Integers i right of the asterisk describe corner singularities of the manifold or rotations of i-th order around a kaleidoscopic point, where in addition i-mirror lines meet. For the sake of completeness, there are also two other symbols which encode linear translations ($\circ$) and glide reflections ($\times$). However, those are not needed to describe the symmetries of the 2D scattering patterns of the double gyroid.

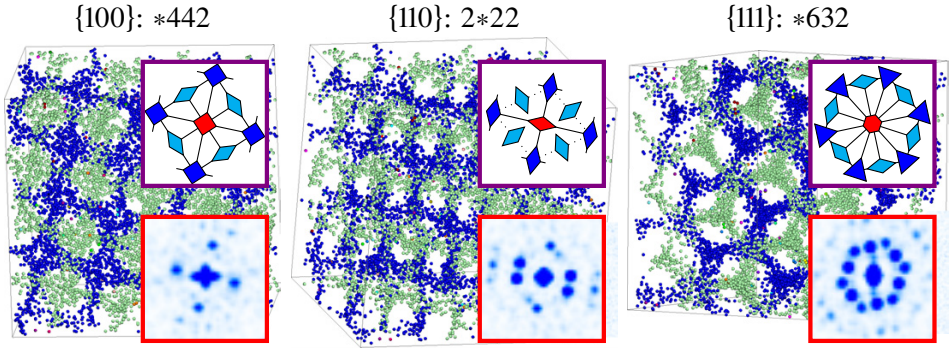

Figure 4.4: Representative scattering patterns of the density distribution of the channel domains (only the positions of the blunt ends are considered) in the gyroid phase ($\rho_g = 0.555$). The cuboidal system contains 10000 pears with $k = 3$ and $k_\theta = 3.8$. The high-symmetry projections of the three-dimensional scattering patterns are depicted in the red boxes. They reveal a 4-fold symmetry in the {100}-direction, a 2-fold symmetry in the {110}-direction and a 6-fold symmetry in the {111}-direction characteristic for the Ia$\bar{3}$d double gyroid. In the violet boxes are the corresponding cell structures of the symmetry groups. Hexagons represent 6-fold rotations, squares 4-fold rotations, triangles 3-fold rotations and rhombi 2-fold rotations. The black lines describe mirror lines. Dotted lines are just a guide to the eye.

also other space groups that are consistent with these high-symmetry projections, like the Fm$\bar{3}$m [305] corresponding to an F-RD minimal surface structure [87], the Ia$\bar{3}$d is the most applicable candidate, especially once the other previously made observations are adduced.

The structure assignment as a body-centered structure (specifically Ia$\bar{3}$d) is further supported by analysing the corresponding three-dimensional scattering pattern directly. While they show that most of the analysed cells are compensating the incommensurability of mesoscale and boundary conditions by slightly elongating towards the {111}-direction and becoming non-cubic, it proves possible to reliably determine the appropriate reciprocal lattice vectors of an FCC lattice in Fourier-space, which is the reciprocal lattice of a BCC real space structure. Thus, the lattice vectors of the channel struc-ture in the pear-shaped particle system describe a BCC lattice and again match the underlying lattice of the Ia3d double gyroid.

4.2.2 Unit cell size and density

From the length of the lattice vectors in real space, the average unit cell dimensions $\langle a \rangle$ are obtained. Also the average number of particles within each

unit cell N_{PUC} are calculated. To this end we simply extract the number of particles with volume V_{pear} within a unit cell volume $\langle a \rangle^3$ at density ρ_g by

$$N_{PUC} = \frac{\rho_g \cdot \langle a \rangle^3}{V_{\text{pear}}}. \tag{4.2}$$

In general it is shown that the tapering parameter has a relatively small influence on the gyroid unit cell as all systems yielding a mean cell size $\langle a \rangle = 10.4\sigma_w \pm 0.2\sigma_w$ and mean particle number of roughly $N_{PUC} = 380 \pm 11$ (see Fig. 4.5). For pear-shaped particles with $k = 3$ and $k_\theta = 3.8$ the same procedure was repeated for larger system sizes $N = 12000$ and $N = 15000$ giving similar results.

Taking the mean number $N_{PUC} = 380$ of particles within the unit cell of all generated gyroid structures, we can create simulations which fit the periodicity of the gyroid phases better. Therefore, we perform MD simulations with $N = 380$ using the same protocol as for $N = 10000$. A representative structure for $k = 3$ and $k_\theta = 3.8$ is depicted in Fig. 4.10. Cluster analysis shows that the system also assembles into the double gyroid structure. Here, the $N = 380$ system can be identified as a single unit cell structure. In the context of the results summarized in Fig. 5.1, we also note that, for $N = 3040$ particles with $k_\theta = 3.8$, a cubic simulation box with edge length $20.84\sigma_w$ with the pear's width σ_w was required to form eight unit cells of the gyroid in a 2×2×2 arrangement. This can be illustrated by comparing

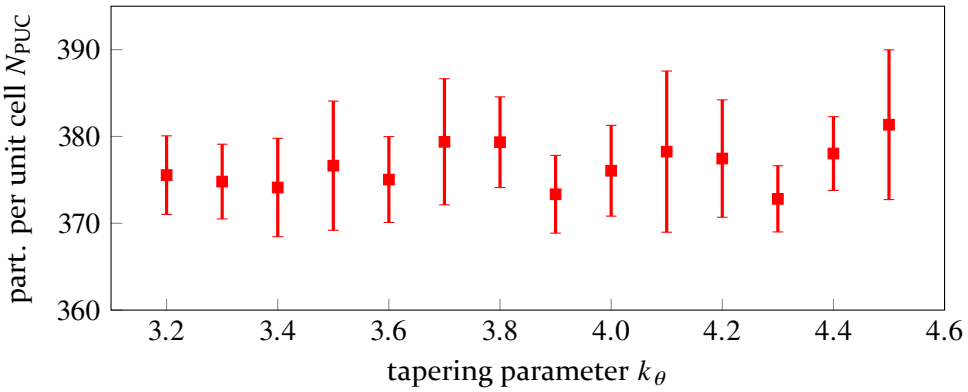

Figure 4.5: The number of particles within a unit cell, which is obtained from the three-dimensional scattering profile of PHGO particle systems with different tapering parameters k_θ forming the double gyroid structure, are plotted. The cuboidal systems contain 10000 pears with $k = 3$ at a global density $\rho_g = 0.555$.

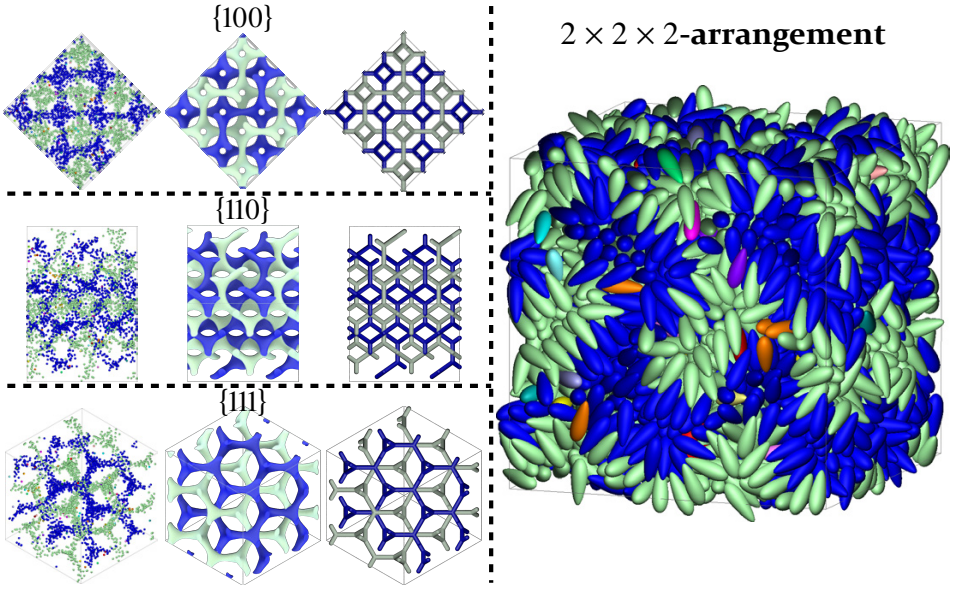

Figure 4.6: An assembly of 3040 pear-shaped particles forming the $2 \times 2 \times 2$ unit cell of the double gyroid structure ($k = 3$, $k_\theta = 3.8$, $\rho_g = 0.57$) on the right. The colours indicate the algorithmic cluster assignment (see Sec. 3.4.4) of the pear-shaped particles. On the left, only the positions of the blunt ends are depicted as spheres to showcase the labyrinth-like channels (first column). The system is shown in the {100}-, {110}- and {111}-direction and compared with the channel domain (second column) and the skeletal-graph (third column) of the double gyroid structure. The former is generated using the nodal approximation of the double gyroid.

the point clusters of the blunt ends of the pears with the skeletal network or channel domain representation of the gyroid arrangements as shown in Fig. 4.6.

We find that equivalent behaviour is obtained from repeated compression sequences performed on a series of simulated systems in a range of between 3000 and 3200 particles within the simulation box at the same number density ($\rho_g = 0.55$). Cluster analysis (see Sec. 3.4.4) also shows that for $N = 3200$ the particles are distributed slightly more uniformly between both gyroid clusters than for N =3040. This might be a hint that the actual number of particles within a unit cell is a bit larger than obtained from the scattering function. However, the phase seems rather robust such that we will set $N_{PUC} = 380$ in the following. Finally, we also generate systems with $N = 2N_{PUC} = 760$ pears within a cuboidal simulation box which would correspond to a $\sqrt{2} \times \sqrt{2} \times 1$ unit-cell system. In Fig. 4.7 the self-assembled

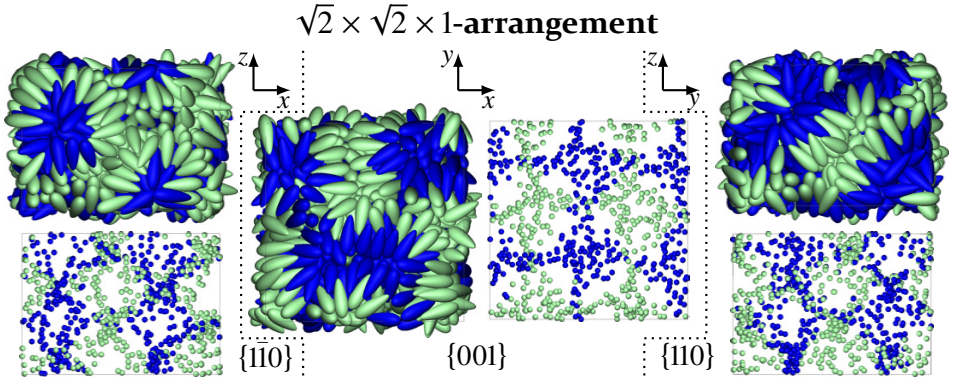

Figure 4.7: An assembly of $N = 760$ pear-shaped particles forming a double gyroid configuration. The positions of the blunt ends of the pears are depicted by spheres which are colour coded to denote clusters calculated based on the proximity of pear blunt ends. The edge lengths of the simulation box are set to a ratio $\sqrt{2} \times \sqrt{2} \times 1$ to enforce the gyroid in a certain orientation. The x-axis points into the crystallographic {110}-, y into the {1̄10}- and z into the {001}-direction.

structure displays both channel domains which are oriented differently, but as expected in the simulation box, namely with the {110} lattice vectors along the two lateral directions of the simulation box (of length ratio $\sqrt{2}$) and the {001} direction corresponding to the vertical direction of the simulation box (of length ratio 1).

Estimating the number of particles within the unit cell as $N_{PUC} = 380$ within the gyroid phase at a density $\rho_g = 0.555$, the cubic lattice parameter is $a = 10.4\sigma_w$ in units of the width of the pears σ_w. It is instructive to compare the number N_{PUC} to that found in gyroid-forming lipid systems. Considering the fact that the surface area of the gyroid minimal surface is $S = 3.0915 \cdot a^2$ and the average area of a single chain lipid such as monoolein is 37Å^2 (at 25°C, [385]), we can estimate the number of lipid molecules in an Ia$\bar{3}$d cubic gyroid phase with lattice parameter $a = 140$Å to be $N = 2(3.0915 \cdot 140^2/37^2) \approx 9$ [284]. Accordingly, the crystallographic order of pear-shaped particle systems is present on a smaller length scale and embraces a considerably greater number of particles than in lipid systems.

4.3 Geometric analysis of the PHGO gyroid structure

4.3.1 The gyroid minimal surface

To draw further comparisons between the lipid/water and copolymer systems on the one hand and our pear-shaped system on the other, we now interrogate the microstructure of its underlying minimal surface and perform Voronoi analysis to examine its correlations. Having determined the unit cell size and having shown, in Fig. 4.2, Fig. 4.6 and Fig. 4.7, that pear-shaped particles can be attributed to a channel system by cluster analysis of their blunt ends, we now take another important aspect of the observed gyroid phase into account – the characterization and analysis of its minimal surface on the microscopic level. In binary lipid/water systems, lipids produce sheets of bilayers such that the surfactant-water interfaces are draped onto the gyroid minimal surface. The pears form *bilayers* as well, where two opposite arrays or *leaflets* of aligned particles interdigitate (see Fig. 4.8c) and which have the same topology as the gyroid. However, unlike the lipids in a mixture with water, the pear bilayers have to homogeneously occupy space as great density fluctuations are generally entropically penalised in hard-core colloidal systems. The distance between the interpenetrating bilayers sheets has to be able to accommodate variable pore radii as the channel domains of the gyroid are not uniformly wide. As a result, the bilayer thickness cannot be assumed to be constant, and the distance between each pear centre and the hypothetical interface which optimally bisects that bilayer has to be determined.

Hence, we define a local particle-particle distance measure, called the bilayer staggering length Δ, as the distance between the particle centers of the two interpenetrating sheets. This length is used to quantify by how much the pears interdigitate on average. For this calculation, we consider restricted longitudinal distribution functions $g^{\parallel}_{r_c^{\perp}}(r^{\parallel})$ of the double unit cell systems at a density of $\rho_g = 0.555$ to avoid possible errors caused by the minorly deformed gyroid in the 10000 particles system (see Eq. (3.62) for comparison)

$$g^{\parallel}_{r_c^{\perp}}(r^{\parallel}) = \frac{1}{\rho_N} \frac{\delta N^{\parallel}_{r_c^{\perp}}(r^{\parallel})}{\pi\, r_c^{\perp\,2}\, \delta r^{\parallel}}. \tag{4.3}$$

The calculation of $g^{\parallel}_{r_c^{\perp}}$ is restricted in such a way that only pears within a cylinder of radius $r_c^{\perp} = 0.9\sigma_w$ around that axis are taken into account (see Fig. 4.8c). The number of particles $\delta N^{\parallel}_{r_c^{\perp}}$ therefore corresponds to the

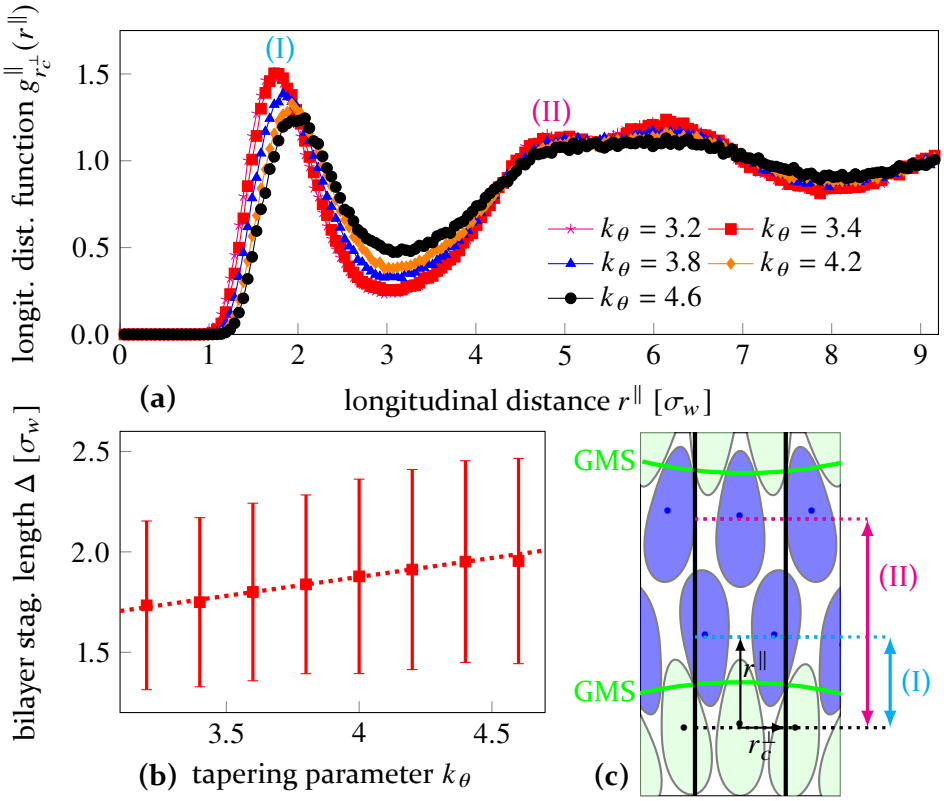

Figure 4.8: (a) The longitudinal distribution function of pear-shaped particle systems with 10000 particles at a density $\rho_g = 0.555$. (b) The mean distance between the centre of the particles and the gyroid minimal surface for different tapering parameters. The error bars indicate the full width at half maximum of the first peak. Moreover, the dotted line is a linear fit of the presented data. Note that the systems with $k_\theta = 4.6$ do not generate gyroid but nematic structures. Nevertheless, these structures are regarded as representatives since they reflect the corresponding changes in bilayer thickness and pear locations. (c) A sketch of the calculation of the longitudinal distribution function. Only particles within a cylinder around the reference pear (black lines) are considered. The radius $r_c^{\perp}$ is chosen such that particles of the same leaflet of the bilayer are outside the cylinder.

number of particles within a disk of radius $r_c^{\perp}$ at longitudinal distance $r^{\parallel}$ from the centre of the pear. This limiting radius is applied to ensure that pears from the same layer are excluded from the calculation. Otherwise the histogram would be dominated by the major peak contributed by those pears which complicates the determination of Δ. The resultant profiles are given in Fig. 4.8a.

We extract the bilayer staggering length from the first peak attributed to the mean relative distance of two next neighbouring pears of interpenetrating sheets, measured along their rotational symmetry axes

$$\Delta := \sup\{g^{\parallel}_{r_c^{\perp}}(r^{\parallel}) : r^{\parallel} \in \mathbb{R}^{+}\}. \tag{4.4}$$

We only take positive distances in directions of the pointy end of the pears into account as we are interested in neighbour particles of the same bilayer.

The location of this first peak shifts to larger $r^{\parallel}$ with increase in k_θ (the error bars in Fig. 4.8b indicate the full width at half maximum of the first peak in $g^{\parallel}_{r_c^{\perp}}(r^{\parallel})$ rather than the measurement error). This shift suggests that particles with a smaller tapering parameter, and consequently a higher tapering angle, interdigitate more deeply, hence implying a shorter distance between these leaflets. The width of the first peak shows for all considered systems that Δ is not constant within the gyroid. This is analysed in further detail in Sec. 4.3.3. The $g^{\parallel}_{r_c^{\perp}}(r^{\parallel})$ curves could be terminated before their second peak which roughly corresponds to the distance between two bilayers. The curvature of the sheets introduces unacceptable levels of uncertainty in the data at this range of $r^{\parallel}$. This is substantiated by the occurrence of partly two distinct peaks, where the longitudinal distance of the bilayer-pairing of particles can be estimated, and partly one broad single peak, where the information of the longitudinal distance to the neighbouring bilayer is completely blurred. The other noteworthy trend in Fig. 4.8a is that the peak heights drop and the tail at intermediate $r^{\parallel}$ grows with an increase in k_θ. This behaviour indicates that reducing the pear tapering angle widens the distribution of observed stagger distances. Finally, we recall that these observations are made in the context that, as noted in Sec. 4.2.2, the overall unit cell size does not change with the tapering parameter.

4.3.2 Local density distribution

For the next stage of this analysis, we take one step further and switch our perspective on the gyroid to a more microscopic level. Therefore, we study the structural properties of each particle in the gyroid configuration individually by calculating the Set-Voronoi diagram of the assembly. The Set-Voronoi diagram consists of a partition of space which is based on the position and shape of the particles. The idea behind the mathematical concept and the construction algorithm of Set-Voronoi tessellations is described in

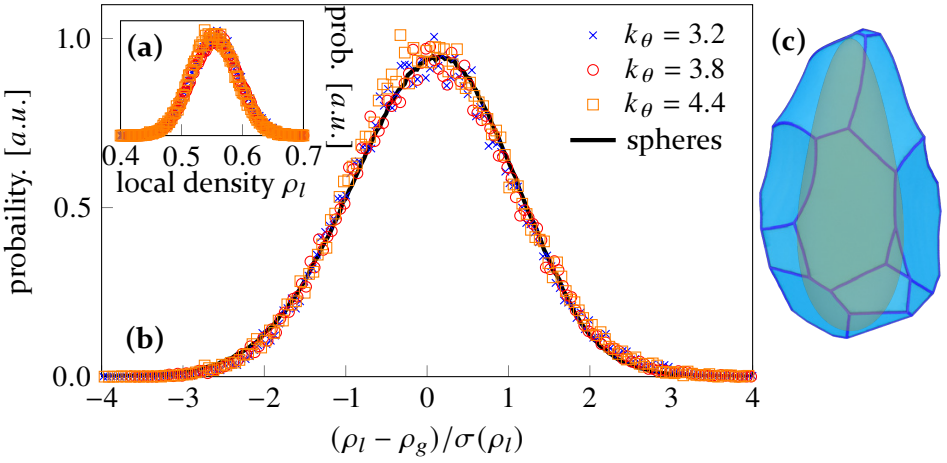

Figure 4.9: (a) The local density distribution for pear-shaped particle systems with $k = 3$ and different tapering angles in the gyroid phase at a global density $\rho_g = 0.555$. (b) The same data plotted in terms of $\frac{\rho_l - \rho_g}{\sigma(\rho_l)}$ with the standard deviation of the local density $\sigma(\rho_l)$. The distributions collabse on the same line as Voronoi cell distributions of spherical and ellipsoidal granulate packings. The sphere data with $\rho_g = 0.64$ was provided by Sebastian Kapfer. (c) The Voronoi cell of a single pear-shaped particle with $k = 3$ and $k_\theta = 3.8$ within the gyroid phase at a global density $\rho_g = 0.555$.

Sec. 4.3.2. The emerging Voronoi cells, which envelope the single particles, relate to the local free-volumes or vicinities of the pears and hence, give valuable information about the local geometric properties of the system.

For this analysis, we apply the Set-Voronoi analysis on systems with $N = 380$ at density $\rho_g = 0.555$ to only obtain the single unit cell structure of the gyroid. A typical Set-Voronoi cell of a single pear within such a unit cell system is depicted in Fig. 4.9c. As the Set-Voronoi cells V_i^{cell} represent the spaces of influence of the pear-shaped particles with volume V_{pear} we can define a local density

$$(\rho_l)_i = \frac{V_{\text{pear}}}{V_i^{\text{cell}}} \tag{4.5}$$

around each pear which is proportional to the inverse volume of the Set-Voronoi cell of particle i.

In Fig. 4.9a the volume distribution of the local densities in the gyroid phase is plotted. It becomes apparent that the local density follows a

bell-shaped distribution around a mean value $\overline{\rho_l} \approx 0.553$ for all studied k_θ. Also the width of the bell shape distribution, determined from the full width at half maximum ≈ 0.086, seems to be unaffected by the particle's taper. Moreover, we can assume that the distributions indicate a different amount of available space in different parts of the gyroid structure, which can be occupied by the pear-shaped particles. To investigate this further, we relate the Set-Voronoi cells to the gyroid structure in the following sections.

The distributions of Voronoi cells have been already studied extensively for spherical particles in regards to granular materials [11, 313, 386, 387, 388] and super cooled liquids [324]. During their studies on random jammed, spherical granulate packings below the random closed packing limit, Aste *et al.* [11] determined a universality which was also shown for the super cooled liquids [324]. The universal behaviour appears in both cases by plotting the local density distribution in the context of the Voronoi cells as a function of $\frac{\rho_l - \rho_g}{\sigma(\rho_l)}$ with the standard deviation of the local densities $\sigma(\rho_l)$. Independent of the global packing fraction ρ_g the distributions all fall on a single curve. Later those studies have been extended by Schaller *et al.* [12, 249, 389] who showed that this collapse also holds for granular ellipsoid packings. Interestingly, the very same curve also roughly describes the local density distribution of pear-shaped particles in the gyroid configuration (see Fig. 4.9b). This suggests that the universality not only covers global density and aspect ratio but also the degree of tapering.

4.3.3 Local arrangement within interdigitated bilayers

As we have seen, the pear gyroid phase can be understood as pears occupying the two labyrinthine domains defined by the gyroid surface. In this section, we will analyse the arrangement of pears relative to the gyroid TPMS, in terms of the relative orientation of pear-directors to the surface normal vectors and the relationship of local density to surface curvature.

Algorithmic best-fit identification of the minimal gyroid interface for given pear configurations

The position of a pear-shaped particle within the gyroid configuration can be specified in terms of the local measures of the gyroid minimal surface in close vicinity. A suitable approach is to designate a certain point p on the gyroid minimal surface and assign the corresponding Gaussian curvature

$K(p)$ and distance $d(p)$ to the pear. Our attempt to successfully encode the pear position by p, however, raises two issues on how to place the minimal surface into the system correctly first.

1. Even though we have already determined in Sec. 4.3.1 that the pears have to cut the surface with their tips such that the two channel domains occupied by the blunt ends are divided adequately, it is highly non-trivial to embed the minimal surface in space accurately. The bilayer staggering length Δ, which was determined in the very same section, does not compensate defects and fluctuations, caused by the fluid nature of the gyroid mesophase, well, so construction of the surface from the pears based on Δ seems hardly feasible.

2. The difficulties are aggravated by the particles being diffusive in the gyroid phase. Therefore, it is very likely that the dividing surface is not stationary in the course of the simulations and rather translates along with the particle system. Therefore, the placement of the gyroid surface has to be determined for each snapshot separately.

As we only consider simulations of one unit cell ($N = 380$), where the simulation box fits exactly the periodicity of the gyroid we do not have to worry about rotations of the minimal surface.

To solve this algorithmic problem we take a reversed route and rather fit the pear assembly to a fixed embedding of the gyroid surface than the surface to the fluid-like system. Hence, we create multiple pear configurations, which we will refer to as the "constraint" gyroid, by artificially restricting the particles close to the minimal surface during the MC simulations. Those system will act as reference configurations to fit the imposed surface embedding accurately. The constraint is implemented in such a way that the pears are only allowed to be located within a range $\epsilon = 0.5$ which is determined by the nodal approximation of the gyroid surface (see Eq. (1.5)):

$$f(x,y,z) := \left| \sin(\frac{2\pi x}{a}) \cos(\frac{2\pi y}{a}) + \sin(\frac{2\pi y}{a}) \cos(\frac{2\pi z}{a}) + \sin(\frac{2\pi z}{a}) \cos(\frac{2\pi x}{a}) \right| < \epsilon, \tag{4.6}$$

with (x, y, z) is the position of the pear and a is the unit cell length of the gyroid surface. Here the function $f(x, y, z)$ will serves roughly as a distance measure, even though $f(x, y, z) = \epsilon$ does not strictly coincide with an envelope of the gyroid surface.

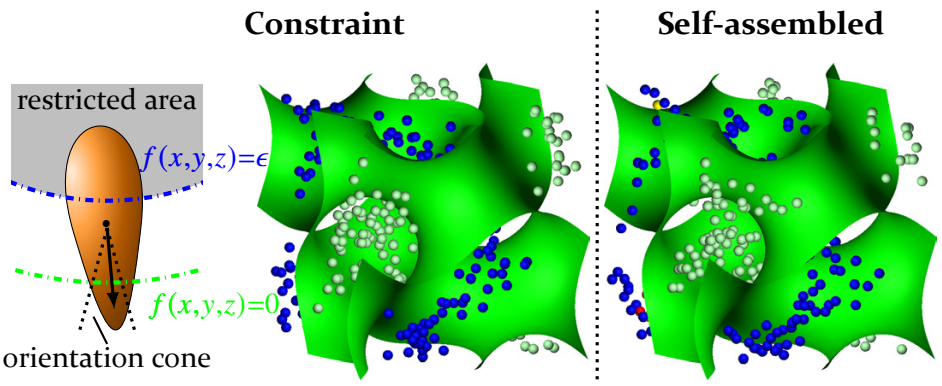

Figure 4.10: The channel domains of the gyroid unit cell using $N = 380$ hard PHGO particles with $k = 3$ and $k_\theta = 3.8$ ($\rho_g = 0.555$). The channel domains are obtained by only visualising the positions of the blunt ends of the pear-shaped particles represented by spheres. On the left the gyroid phase is created artificially by Monte Carlo simulation with particles restricted to the nodal approximation (see Eq. (4.6)) in such a way that the particles cut the gyroid surface within the range of ϵ at the distance determined in Sec. 4.3.1 and Fig. 4.8. Also their orientations are constrained to lie close to the nodal surface normal at all Monte Carlo steps as indicated in the sketch. On the right, the equivalent unit cell surface generated by unrestricted self-assembly is shown. The blunt end density distribution of the restricted and the unrestricted self-assembled unit cells can both nicely be separated by the gyroid minimal surface (green) and can be compared by using an MC algorithm to maximise their correlation concerning simulation box translation.

Computationally, the contiguity to the surface is ensured by rejecting a translational step attempt if the particle would leave the ϵ-domain (see sketch in Fig. 4.10). The parameter $\epsilon = 0.5$ is chosen such that the particles are both sufficiently bounded by the predefined macrostructure but also theoretically capable of being placed at the distance $\frac{\Delta}{2}$ to the minimal surface. Additionally, their orientations are constrained to lie within a cone in regards to the nodal surface normal (in the range of $\pm 15°$) at all Monte Carlo steps as indicated in the sketch of Fig. 4.10. An exemplary constraint configuration is depicted in Fig. 4.10. Afterwards, the positions of the blunt ends of all constraint gyroid configurations are combined to a point set $G_{(\mathrm{con})}$ and compared to the density distributions of the blunt ends of the pears in the self-assembled gyroid systems for different simulation box translations. Here, the sum of all Euclidean distances between the position q_i of the blunt ends of all pears i within the self-assembled system and the coordinate $\tilde{q} \in G_{(\mathrm{con})}$, which is closest to q_i, is minimised:

$$D := \sum_i \mathrm{dist}(q_i, G_{(\mathrm{con})}) = \sum_i \min_{\forall \tilde{q} \in G_{(\mathrm{con})}} \mathrm{dist}(q_i, \tilde{q}). \tag{4.7}$$

The translation vector which maps the self-assembled to the constraint gyroid best is used as an initial guess for a steepest descent method to maximise their correlation and minimise D further. In Fig. 4.10 the channel systems of both the constraint and the translated, but self-assembled – and consequently unconstraint – unit cell are separated by the gyroid minimal surface parametrised by the Enneper-Weierstrass representation [48, 85]. Whilst for the unrestricted unit cell the placement of the gyroid surface has to be seen as the best estimate we note that the two systems are qualitatively indistinguishable (see also the movie in supplementary materials or in Ref. [390]).[6]

Local smectic order on the gyroid surface

As the first measure of the correlation between the local structure of the pears and the geometry of the gyroid, the orientational arrangement of the particles relative to the minimal surface is determined. Therefore, we define the point p on the minimal surface, which determines the position of the pear-shaped particle, as the intersection of the rotation symmetry axis of the particle and the minimal surface (see the sketch in Fig. 4.11a). The relative direction is specified by the scalar product $\cos(\tau) \coloneqq \hat{\mathbf{n}}(p) \cdot \mathbf{u}_i$ of the orientation vector $\mathbf{u}_i$ of pear i and the normal vector $\hat{\mathbf{n}}(p)$ of point p which encodes the angle τ between $\hat{\mathbf{n}}(p)$ and $\mathbf{u}_i$ and also the position of the particle in terms of the gyroid surface. The angle distribution is illustrated in Fig. 4.11a. Here, the plots exhibit distinct peaks at $\tau = 0$ across the whole range of considered tapering parameters k_θ. This corresponds to an alignment of the particle directions and the surface normals.

An even more striking observation is that the distributions are very narrow. This can be clarified by the full width at half maximum values of the distributions. In the gyroid configuration half of the PHGO pears generate an angle with the minimal surface normal which falls within $\tau \lesssim 19.5°$ for all considered k_θ (see Table 4.1). Even by considering 90 % of the pear-shaped particles and by determining the full width at tenth of maximum the range of adopted angles is still very tight $\tau \lesssim 36.3°$ for all k_θ (see Table 4.1). Thus, we can conclude that the pears tend to orientate perpendicular to the minimal surface and that the gyroid phase, as already conjectured earlier, can

[6] We have also tested other approaches like to find the best translation which minimises $\sum[f(x, y, z)]^2$. However, the approach with constraint reference structures provided the most reliable results.

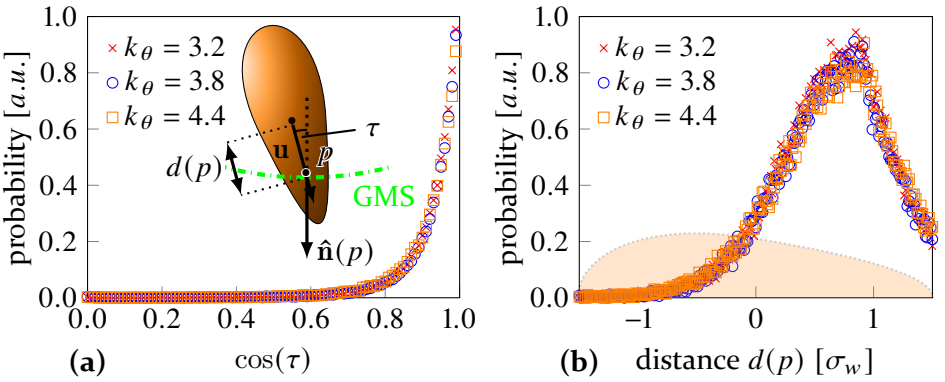

Figure 4.11: (a) The relative orientation distribution between the pear direction $\mathbf{u}_i$ and the normal direction $\hat{\mathbf{n}}(p)$ of the gyroid minimal surface at point p where the pear crosses the surface for pear systems with different tapering angles in the gyroid phase at a global density $\rho_g = 0.555$. The data is plotted in dependence of the angle τ between the two vectors $\cos(\tau) = \mathbf{u}_i \cdot \hat{\mathbf{n}}(p)$ as indicated in the sketch. (b) The distribution of the lateral distance $d(p)$ between the center of the pear and the minimal surface is depicted for the same systems (see sketch). The orange outline of a particle with $k_\theta = 3.2$ serves to relate $d(p)$ relative to the pears.

indeed be interpreted as a curved smectic phase with a director which is predetermined by the normal vector of a gyroid surface. Note related work on possible nematic ordering in block copolymers [391].

The smectic order perpendicular to the minimal surface is reminiscent of the cubic phases observed in X-shaped bolapolyphiles [392, 393, 394]. The cores of these molecules can be interpreted as sticky rods with side chains, which link neighbouring particles via π-conjugations, and are stacked in the normal direction on the minimal surface. However, in contrast to the pear-shaped particles, the bolapolyphiles form monolayers instead of interdigitated bilayers. The similar order poses the question, nevertheless, if it is possible to assimilate both systems further by shifting the bolapolyphile from an X-shape to a more inversion asymmetric †-shape.

Another observable, which supports the conclusion of local smectic order in the pear gyroid phase, is the distances $d(p)$ from the centre of the pear to the corresponding point p on the minimal surface. The distance distribution of Fig. 4.11b displays the bilayer formation as most pears intersect the minimal surface with their narrow parts. Also the bilayer staggering parameter $\frac{\Delta}{2} \approx 0.85$ can be determined by the pronounced peak. However, the interdigitation depth which is associated with $d(p)$ is rather flexible and

tapering	relative orientation distribution Fig. 4.11a	
k_θ	full width at half of maximum	full width at tenth of maximum
3.2	$\tau \in [0°, 19.3°]$	$\tau \in [0°, 35.7°]$
3.8	$\tau \in [0°, 19.4°]$	$\tau \in [0°, 36.2°]$
4.4	$\tau \in [0°, 20.0°]$	$\tau \in [0°, 37.2°]$

Table 4.1: The full width at half and tenth of maximum of the relative orientation distribution between the gyroid minimal surface and the pear-shaped particle orientation are listed for different tapering parameter k_θ. The data is obtained from Fig. 4.11a.

varies by a greater margin. This might be a hint that locally Δ is not constant throughout the unit cell and that for example at high curvature points the particles are more interdigitated, whereas at the flat curvature points the leaflets within a bilayer are more separated. To quantify this, however, we have to relate the Gaussian curvature $K(p)$ and the distances $d(p)$ which is the subject of the following section.

We can, furthermore, claim that both observations regarding $d(p)$ and $\mathbf{u}_i$ are qualitatively independent of the tapering angle of the pear-shaped particles. The two distributions, hence, provide a quality measure for the presented surface fit algorithm and indicate that the surfaces are satisfactorily placed within the system for further analysis.

4.3.4 Mechanism to generate negative Gaussian curvature

Now that we have established the local smectic nature of the pear gyroid phase, we need to argue where the predisposition for negatively curved interfaces stems from. To do so, we first correlate the particle/Voronoi cell properties to the Gaussian curvature of the penetrated section on the minimal surface. Afterwards, we thematise why the pear-assembly ostensibly contradicts the shape of space tilings based on parallel surfaces, which are required to generate homogeneous packings on negatively curved surfaces. Yet, we also give a solution to how this packing law is fulfilled collectively by a combination of particle arrangement and pear-shape.

Creating curvature via bilayer-thickness modulation

In order to relate curvature and interdigitation depth, the minimal surfaces which are shown in Fig. 4.10 are triangulated and tessellated according to their intersections with the configuration-derived Voronoi diagrams. As a result, characteristics of the Voronoi diagram and the gyroid are assigned to every point/triangle p_t on the minimal surface such that p_t shares the same quantities with a pear if it lies within the particle's domain according to the Set-Voronoi diagram. This method to obtain the correlations is more meaningful than considering the point p to average over a wider range of Gaussian curvatures and it suppresses fluctuations more effectively.

In Fig. 4.12 the local Gaussian curvature and the mean (from 1000 configurations) volume of intersecting Voronoi cells are, respectively, depicted on two gyroid minimal surfaces. From this, it is apparent that highly curved regions at the necks of the gyroid tend to be intersected by cells with higher volume, whereas more tightly packed particles reside in lower curvature zones (particularly the nodes). This can be interpreted as meaning that higher curvature requires lower particle density since this avoids the restrictions otherwise associated with leaflet interdigitation and induces flexibility to create curvature. To achieve a more quantitative measure of this effect, the area A_0 occupied by each Voronoi cell V^{cell} is summarised in a plot of $\langle \frac{V^{\text{cell}}}{A_0} \rangle$ against $|K|$ - an anti-correlation is observed (see Fig. 4.13a).

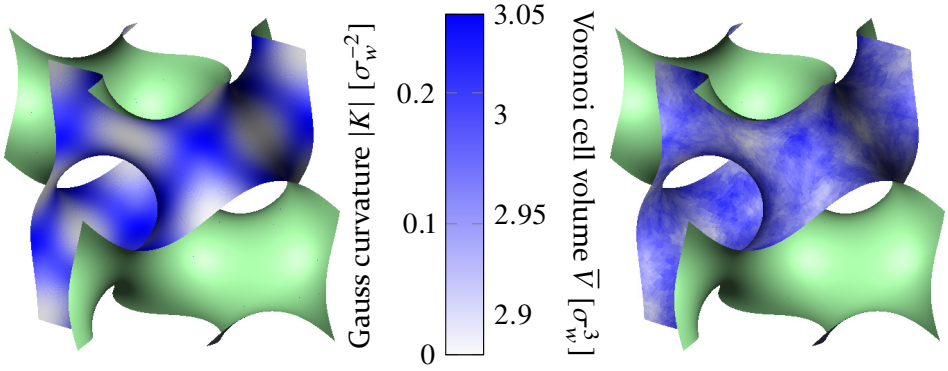

Figure 4.12: Left: The gyroid surface coloured by Gaussian curvature. More curved areas are blue, less curved areas are white. Right: By comparison, the gyroid is coloured in respect of the mean volume of intersecting Set-Voronoi cells. Blue sections are intersected by cells with high volume whereas white sections are intersected by cells with low volume. For the calculation 1000 systems of $N = 380$ pear-shaped particles with $k = 3$ and k_θ are used.

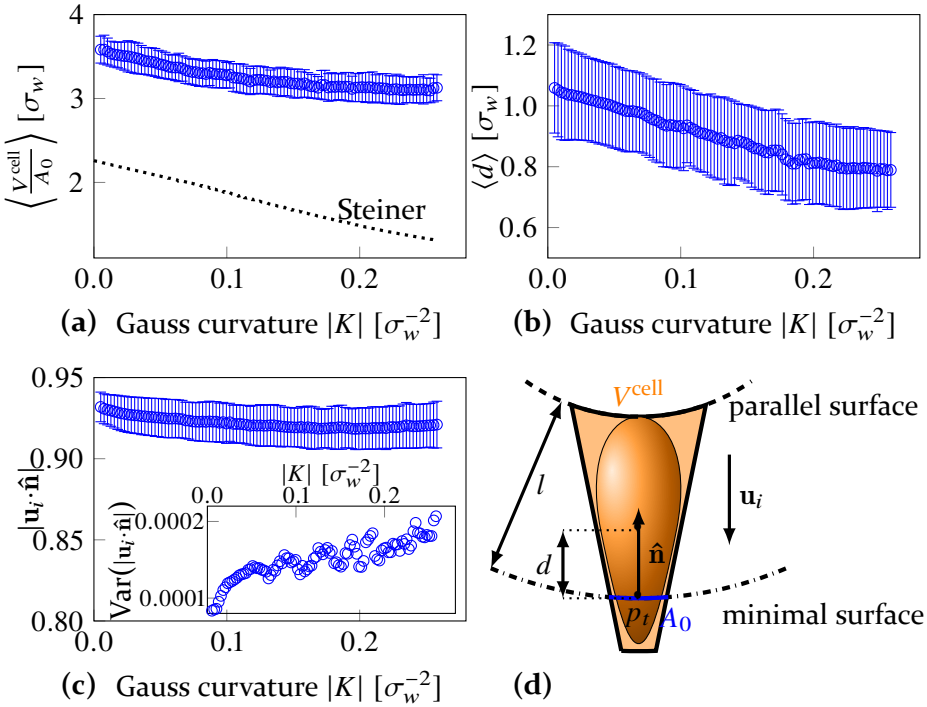

Figure 4.13: Gaussian curvature of the gyroid minimal surface plotted against the mean volume of intersecting Set-Voronoi cells (a), against the mean distance between the center of the pear and the gyroid surface $\langle d \rangle$ (b) and against the relative orientation between the particle and the gyroid surface $\hat{\mathbf{n}} \cdot \mathbf{u}_i$ and its variance (c) using pears with $k_\theta = 3.8$. Every point represents a triangle p_t of the triangulated gyroid surface (d). For the calculation 1000 systems are used. The dotted line in (a) indicates Steiner's theorem (Eq. (4.8)), where $l = d_{\text{MS}}(p_t)$ is the distance between p_t on the gyroid surface and its corresponding point on the medial surface (see Sec. 1.2). The Gaussian curvature $K(p_t)$, $d(p_t)$ and $\hat{\mathbf{n}}(p_t)$ are calculated numerically using the gyroid minimal surface parametrised by the Enneper-Weierstrass representation [48, 85]. The mean curvature $H(p_t)$ is 0 at every point p_t on a minimal surface.

Similarly, another anti-correlation is found when the mean distance between the points p_t on the gyroid surface and the pear positions was plotted against the Gaussian curvature (see Fig. 4.13b). This means that the pears remain further away from the minimal surface at the nodes than at the necks. This is both expected and intuitive. It is expected as the pears have to fill more space in the channel domain with their blunt ends at the nodes and, therefore, are not able to interdigitate as deeply without leaving unphysical void space around the medial axis (see the definition for the medial surface in Sec. 1.2).

Furthermore, both anti-correlations (the one between Voronoi cell volume and Gaussian curvature, and the one between the distance to minimal surface and Gaussian curvature) are mutually consistent since low curvature is compatible with high interpenetration. For the intuitive explanation that greater interdigitation leads to more curvature, we take a closer look at the particles within the bilayer. By reaching further into the opposite leaflet of the bilayer, the pears act as wedges, which occupy more space and creates larger angles between direct neighbouring particles. This, in turn, introduces more curvature into an otherwise flat bilayer. The penetration depth, thus, acts as a mechanism to control the local Gaussian curvature of the membrane. Here we also want to refer to mixtures in Sec. 8 where a similar mechanism is observed.

Lastly, we demonstrate that the nematic order on the gyroid surface is present and independent of the position of the particle and the corresponding local Gaussian curvature (see Fig. 4.13c). The only observable difference can be seen by plotting the variance of the tilt between the normal vector of the gyroid surface and the pear orientation (see the smaller plot in Fig. 4.13c). It shows that the fluctuations of the tilt increase with growing $|K|$. However, this trend is explained by the heightened susceptibility of the relative pear orientation to translational fluctuations at surfaces of high curvature. By slightly translating the pears in flat regions of the gyroid, the relative tilt angle stays roughly constant and is not affected by the displacement. In contrast, small changes in the particle's position within highly curved areas lead to more considerable variations of the tilt.

The regulation of Gaussian curvature via interdigitation and the simultaneous nematic order on the minimal surface might also explain the existence of the smectic/nematic phases on either side of the gyroid phase, which we just addressed briefly at the beginning of this chapter and which will be discussed in great detail in the next chapter Chap. 5 (note especially Fig. 5.1):

- If k_θ is too large, the particles are in principle able to generate the full range of K needed for the gyroid formation. However, the particle shape itself shows a lack of head-tail-asymmetry which mostly prevents the arrangement into bilayers and leads to nematic global order and a planar interface.
- On the other hand if k_θ is too small, the particles cannot interdigitate deeply enough to both introduce the maximum amount of curvature

and simultaneously keep the internal bilayer structure of two antiparallel particle arrays intact, so again, the planar nematic and smectic phases form.

In between the taper of the particles[7] just allows for a compromise between the ability to form bilayers and to create enough curvature via interdigitation such that stabilisation of curved surfaces (aka the gyroid minimal surface) is facilitated.

The difference between Voronoi and Steiner cell in PHGO particle systems

Comparing these findings for our pear system with those for lipids and polymers, differences are apparent. The molecular geometry of lipids and diblock copolymers is often described by the "surfactant parameter" $\frac{v}{A_0 \cdot l}$ where v is the effective surfactant chain volume and l is the chain length [50]. By invoking the relationship between molecular shape and resulting interface curvatures, one can then express the so-called Steiner's formula [395] as:

$$v(l) = A_0(l + H \cdot l^2 + \frac{1}{3}K \cdot l^3). \tag{4.8}$$

The volume cell $v(l)$ is defined by the space which is spanned between the surface patch $\mathrm{d}S$ with area A_0 on the surface S and its counterpart $\mathrm{d}S'_l$ on the parallel surface S'_l at distance l. The parallel surface patch $\mathrm{d}S'_l$ is the mapping of $\mathrm{d}S$ by the function $f_{\parallel,l}$ which translates all points $p_t \in S$ by a distance l on a surface in normal direction $\hat{\mathbf{n}}(p_t)$:

$$\begin{aligned} f_{\parallel,l} &: S \rightarrow S'_l \\ f_{\parallel,l}(p_t) &= p_t + l \cdot \hat{\mathbf{n}}(p_t). \end{aligned} \tag{4.9}$$

If $l = d_{\mathrm{MS}}(p_t)$, such that the v is defined between the minimal surface and its medial surface, we call the volume *Steiner cell* (see Fig. 4.14g).

According to Steiner's formula the surface patch $A(l)$ increases or decreases with l depending on the mean and Gaussian curvatures H and K. The gyroid surface is characterised by its mean curvature $H = 0$ and negative Gaussian curvature $K \leq 0$ at every point $\mathbf{p}_t$. Therefore, lipids and copolymers which form the gyroid surface are conventionally sketched as cones

[7] We will show in Chap. 5 that for $k = 3$ the tapering parameter to form gyroid phases ranges between $2.5 < k_\theta < 4.5$.

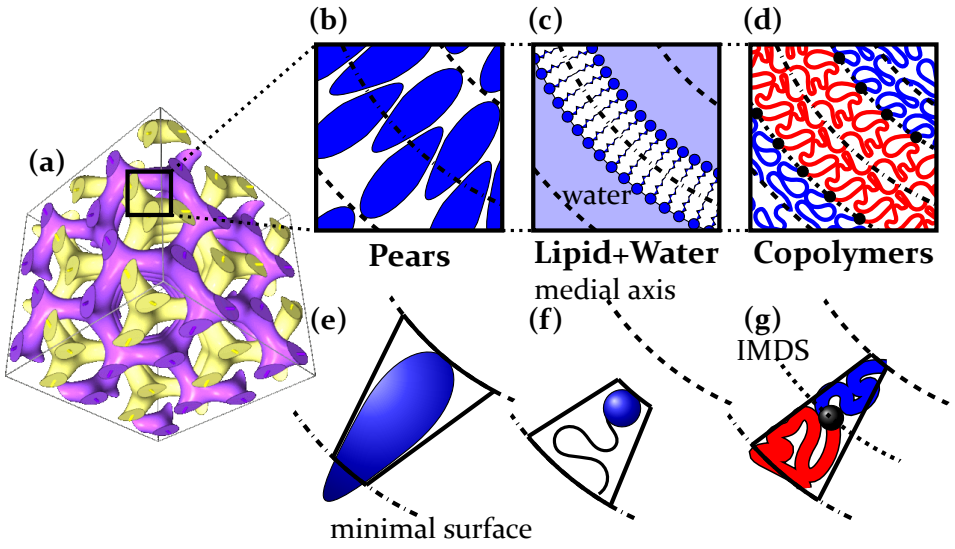

Figure 4.14: The three different arrangements within the gyroid phase (a) generated by tapered liquid crystalline pears, (b) lipids in a mixture with water, (c) and di-block copolymers (d). The lipids and copolymers follow Steiner's theorem and taper towards the medial axis (f+g) and the inter-material dividing surface (IMDS) (g). In contrast, the pears form interpenetrating bilayers and, consequently, get wider as they approach the medial axis (e).

($\frac{v}{A_0 \cdot l} < 1$) tapered towards the medial axis, whereas in the lamella phase the molecules are considered as cylinders ($\frac{v}{A_0 \cdot l} = 1$) [50, 244]. This is illustrated in Fig. 4.14f+g. Plotting Steiner's formula in Fig. 4.13a and analysing the shape of the tapered Voronoi cell of a single pear (see Fig. 4.9c), shows that the pear-shaped particles have a surfactant parameter greater than 1 which usually corresponds to positively curved surface phases like micelles.

However, while molecular flexibility means that it is often feasible for lipids and copolymers to have differing surfactant parameters in opposing leaflets, this is patently *not* the case in the systems studied here. Here the difference in obtainable space is directed by the interdigitation mechanism. Due to this interdigitation and the fixed particle shape in our pear-shaped particle systems (see Fig. 4.14b+e), it is necessary for pear blunt ends to point into the opposing channels. This means, however, that the pear system appears to violate Steiner's theorem based on the volume occupied by single particles, leading to the poor agreement between simulation data and Eq. (4.8). The interlocking bilayer arrangement rather suggests that multiple particles have to be considered collectively. This is because, in contrast

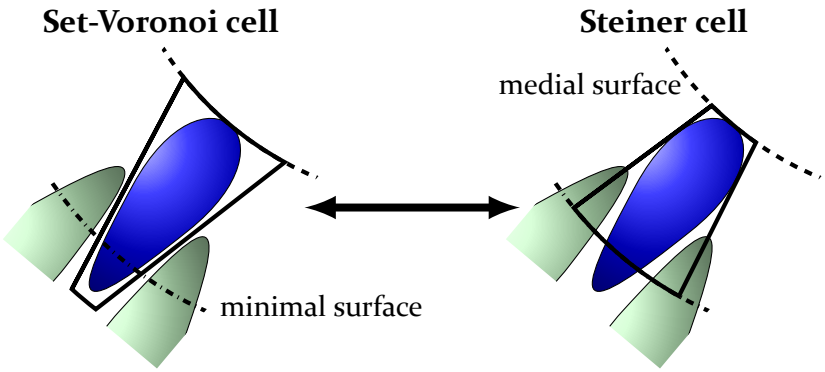

Figure 4.15: A possible way how pears collectively fulfil Steiner's theorem in gyroid phases. As the pears do not occupy space exclusively in one channel domain, the tips of the neighbouring particles might contribute to the local surfactant parameter s and turns it from $s > 1$ for a single pear to $s < 1$. Hence, the Voronoi cell does not coincide with the Steiner cell.

to the lipid and copolymer systems, where the molecules are only within one channel domain, the pear-shaped particles occupy space on both sides of the separating membrane. Hence, the Voronoi cell of a single particle can not be equated with the Steiner cell in the pear-shaped particle systems. It is more than plausible that the surfactant parameter becomes smaller than 1 by taking the blunt end of one pear and the tips of the surrounding antiparallel pears into account and joining the Steiner cell from multiple particles (see Fig. 4.15). This is hardly feasible to quantify as it is highly nontrivial to predict which exact collection of pears complies with Steiner's theorem. Even though we cannot prove this conjecture, the behaviour of pear-shaped particles within the gyroid structure leads us to the conclusion that the mechanisms behind the formation of the gyroid by lipids/copolymers and pear-shaped colloids are fundamentally different from one another.

4.4 Conclusion and outlook

In this chapter, we have performed a crystallographic and geometric analysis to determine key characteristics of the gyroid phase in PHGO particle systems, such as the unit cell size, number of particles per unit cell and the bilayer staggering length. Moreover, we could confirm earlier observations and also substantiate hypotheses which were made in Ref. [241]. In particular, we were able to identify a multitude of different gyroid configuration with different protocols (see Table 4.2) indicating the robustness of the gyroid phase

Orientation			N_{pear}	Gyroid observed		Unit cell	Ref.
x	y	z		Init Iso	Init Sm		
{100}	{010}	{001}	370-400	✓	✓	1×1×1	Fig. 4.10
			3000-3200	✓	✓	2×2×2	Fig. 4.6
{110}	$\{1\bar{1}0\}$	{001}	760	✓	–	$\sqrt{2}\times\sqrt{2}\times1$	Fig. 4.7
–			10000	✓	✓	25-27	Fig. 4.2 Fig. 4.4

Table 4.2: The different PHGO particle systems where the gyroid structure has been identified. This table holds for both Molecular dynamics (with a WCA potential) and Monte Carlo (with a hard-core potential) simulations of pear-shaped particle systems with $k = 3$, $3 < k_\theta < 4.5$ and $\rho_g = 0.555$. The simulations to generate the gyroid structures either include a compression sequence form the isotropic phase (Init Iso) or start to form a pre-prepared smectic configuration at the targeted global density (Init Sm).

(in Chap. 5 the robustness of the PHGO gyroid phase will be further tested in terms of the particle shape). The main results of the gyroid phase formed by PHGO particle systems are listed below:

- We analysed the scattering patterns of the density distribution of the pear's blunt ends to ascertain the symmetry and reciprocal lattice vectors of the $Ia\bar{3}d$ double gyroid.
- The PHGO particles arrange in space filling (no solvent needed) interdigitated bilayers and orientate parallel to the normal of the dividing gyroid minimal surface. Hence the gyroid phase corresponds to a curved smectic in which the director is locally determined by the normal of the minimal surface.
- Correlations between the curvature of the gyroid surface and the Voronoi cells of the pears show that a more open structure is adopted in regions of higher curvature and that the gyroid's range of channel widths are accommodated by variation in leaflet interpenetration.
- We were able to identify a multitude of different gyroid configuration with different protocols (see Table 4.2) indicating the robustness of the gyroid phase (in Chap. 5 the robustness of the PHGO gyroid phase will be further tested in terms of the particle shape).

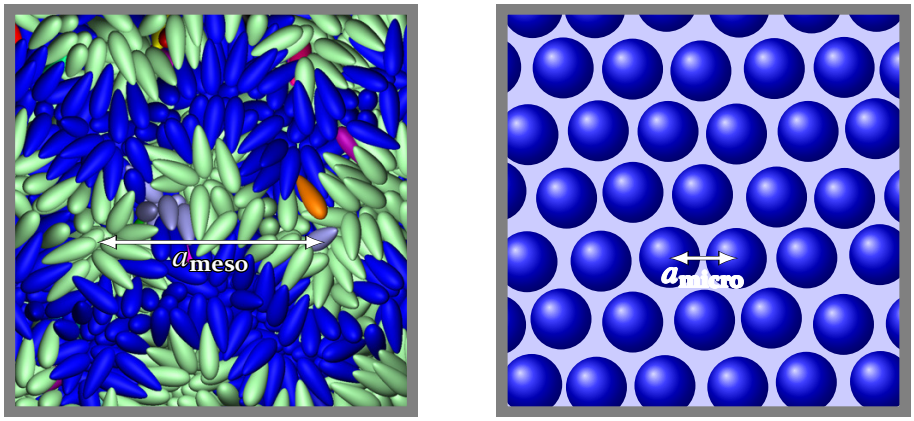

Figure 4.16: Left: The gyroid phase in a system of pear-shaped particles with $k = 3$, $k_\theta = 3.8$ and $\rho_g = 0.555$. The gyroid exhibits long-ranged order on a mesoscopic length-scale a_{meso} which is determined by the unit cell of the gyroid. Right: A sketch of the crystallisation in hard sphere systems. The periodicity of the crystalline order is on the microscopic level such that the determining length-scale a_{micro} is on the same order of magnitude as the particle size.

In general, we have confirmed that the gyroid structure can be obtained purely via entropic self-assembly of the PHGO particle systems. Even though the PHGO contact function features some non-additive properties, the observed gyroid phase stems from the same principles as the crystallisation of hard spherical colloids or the nematic phase in hard rod-like systems. However, there is one particular way in which the behaviour of these pear-shaped systems is distinguished from those of other entropy-driven ordering processes. The onset of the double gyroid phase creates crystallographic order over multiple particles and thus, introduces a larger length-scale than the particle or molecular scale. This "mesoscopic" length-scale a_{meso} is defined by the unit cell whose dimension is one or more orders of magnitude larger than the constituent's size. This contrasts with the ordered phases of hard spheres and liquid crystals where the crystallographic parameter matches the translation from one particle to its nearest neighbour and hence to the molecular scale a_{micro} itself. A sketch is provided in Fig. 4.16. While the formation of emergent meso-scale order by self-assembly is by now a well-established concept, a clear discrimination between the energetic and entropic contributions is an only partially understood question and one to which we hope to contribute with our results.

5 The phase diagrams of single-component pear systems

"Ordeeerrrrrr!!!"

– John Bercow

This chapter focuses on the self-assembly of pear-shaped particle systems on a broader aspect in which we both resume and significantly extend previous studies on entropic self-assembly by Barmes [243] and Ellison [241]. Specifically, we introduce the complete phase diagram of the mono-disperse system of hard-core pear-shaped particles using the pear hard Gaussian overlap (PHGO) model, with global density and particle shape as the two variable parameters. The phase diagram incorporates the bicontinuous double gyroid phase, which we started to analyse in detail already in Chap. 4 and which we put into more perspective here, as well as disordered isotropic, smectic and nematic phases. Furthermore, we also provide the phase diagram of the hard pears of revolution (HPR) particle system which can be used for comparison. Here we show that the entropic self-assembly of highly symmetric phases like the gyroid is sensitive to shape changes. In particular, we demonstrate that the small differences between the PHGO and the HPR model destabilise the formation of bilayer phases (including the gyroid) such that only isotropic and nematic phases remain.[1]

[1]This chapter is based, in parts, on the article P.W.A. Schönhöfer, L.J. Ellison, M. Marechal, D.J. Cleaver, and G.E. Schröder-Turk, "Purely entropic self-assembly of the bicontinuous Ia$\bar{3}$d gyroid phase in equilibrium hard-pear systems", *Interface Focus* **7**:20160161, 2017. All simulation methods, numerical procedures and data analyses of this paper were implemented and executed by me (with the MD code based on earlier code by Laurence Ellison). Alongside the senior authors, I was a major contributor to the conceptual questions and research methods addressed in the article, and the interpretations presented as results. I created all 13 illustrations and graphs in the article and have written the manuscript, with help and comments from Gerd Schröder-Turk, Matthieu Marechal and Douglas Cleaver. Verbatim quotes from that paper may have been used without explicit citations.

Even though different pear-shapes have been investigated since the PHGO model has been introduced, an in-depth study of the phase behaviour for a wide range of differently tapered PHGO pears has not yet been provided in full detail. To take an example, Barmes *et al.* [243] showed that, for long, tapered monodisperse particles with aspect ratio $k = 5$ and $k_\theta = 5$, the nematic, bilayer smectic and crystalline phases are formed. For shorter particles, however, this initial study only found a "domain ordered" arrangement on compression of systems of 1000 tapered particles, which could not be assigned successfully to an exact structure. Subsequently, by simulating 10000 particles with $k = 3$, Ellison *et al.* [241] showed for $k_\theta = 3.8$, and we confirmed for the range and $3.0 < k_\theta < 4.5$ in the last chapter that, on compression from the isotropic fluid and on decompression from an artificial smectic phase, the system was actually entering gyroid arrangement with long-range, three-dimensional periodicity like the one shown in Fig. 4.16. The pears adopt this liquid crystal phase in an arrangement that fills space fairly uniformly, at fluid-like densities (see Chap. 4 for an in detail analysis of the gyroid phase). Additionally, Ellison considered in his PhD thesis [373] a couple of other values of k_θ within an aspect ratio of $k = 3$ showing similar phase behaviour as the pear-shaped particles with $k = 3$ and $k_\theta = 3.8$, which was the initial attempt to determine the phase diagram thoroughly. Based on this, we will extend this phase diagram in Sec. 5.1.

Up to this point, also no comparison between the PHGO model and the HPR model has been undertaken, a fortiori, as for the ellipsoidal counterparts (the hard Gaussian overlap (HGO) ellipsoids and the hard ellipsoids of revolution (HER)) small differences between the two models are known [396]. The phase transitions between the isotropic and orientationally ordered liquid crystal phases do not match perfectly for both ellipsoid models as the HGO interaction profile (see Eq. (2.13)) promotes the alignment of particles by a greater margin. This can be seen by comparing the excluded volumes in Fig. 2.5, where the HGO model slightly overestimates the contact distance when the two ellipsoids are perpendicular to each other. Consequently, the phase transition of the HGO ellipsoids occurs for lower densities than for HER ellipsoids. Nevertheless, the distinct transition density does not change the characteristics of the observed phase behaviour significantly. Both models exhibit a similar nematic phase in between the isotropic and solid state without the HGO ellipsoids adding more complex phases. Thus, the two types of ellipsoids are qualitatively equivalent and their small differences in particle-shape are of only marginal consequences.

However, the double gyroid phase is a much more complex structure than the "simple" nematic.

It seems plausible that higher complexity goes along with increased response and that especially the self-assembly of configurations like the double gyroid is more sensitive to the interaction of the particles. Hence, we will provide a second phase diagram using the HPR model in Sec. 5.2. Here we will show that the gyroid phase, which can be interpreted as a warped bilayer phase, is not universal for tapered pear particles and that the special features of the PHGO contact function promote the formation of otherwise unfavourable bilayer-configurations.

Finally, as a conclusion in Sec. 5.3, the entropy-driven gyroid phase formed by the PHGO pear system is evaluated. Through this, a compelling argument is made that it is a realisation of a modulated splay-bend phase in which the conventional nematic has been predicted to be destabilised at the mesoscale due to a molecular-scale coupling of polar and orientational degrees of freedom as suggested by Selinger [397].

5.1 Phase diagram of the pear hard Gaussian overlap (PHGO) system

For the first part of the chapter, Molecular Dynamics and Monte Carlo simulations, as per the procedure described in Sec. 4.1, are performed on systems with $N = 3040$ and $N = 3200$ monodisperse PHGO particles, that is, particles of the same size and shape. For a description of the PHGO model see Sec. 2.2. The simulations are set up such that the particles are confined within a cubic box with three-dimensional periodic boundary conditions. The tapering parameter k_θ lies between 2.0 and 6.0 which corresponds to tapering angles between 28.1° and 9.5°. The lower boundary of $k_\theta = 2$ is set to ensure that there is no particle concavity. The interaction potential, which is used to approximate the hard-core interaction of pears in the MD simulations, is the modified version of the purely repulsive WCA potential which we introduced in Eq. (2.21). Here, full simulation sets are performed in the canonical NVT-ensemble, with the time step $\Delta t = 0.0015$ and the dimensionless temperature T set to 1.

Additionally, MC simulation sets using the same parameters and the same compression protocol are performed for $k_\theta = 2.2$, $k_\theta = 3.8$ and $k_\theta = 5.4$. In

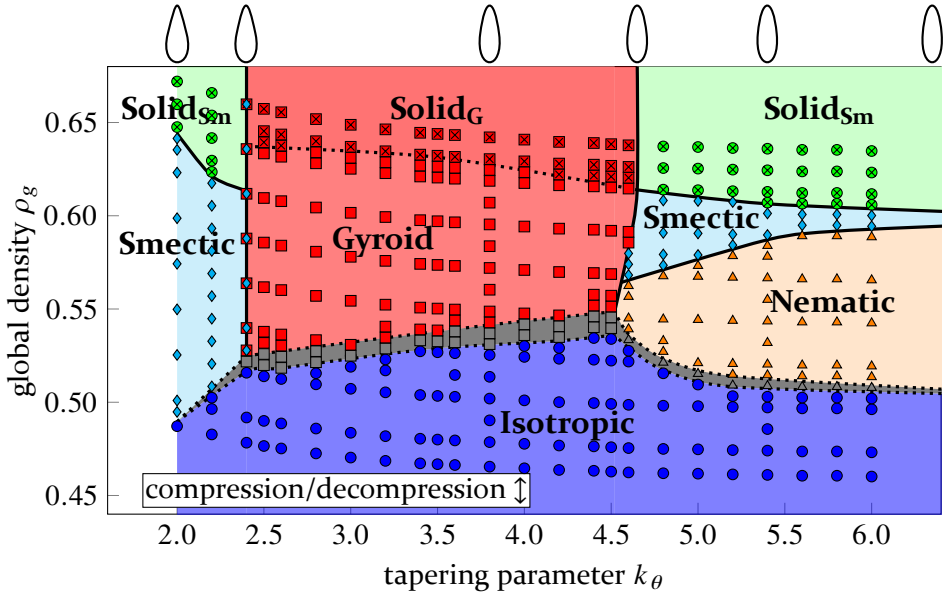

Figure 5.1: Phase diagram of hard PHGO pear-shaped particles with $k = 3.0$ obtained by compression (from isotropic) and decompression at fixed tapering parameter k_θ for systems of 3040 particles in a cubic simulation box. Grey regions between the isotropic and ordered phases indicate parameter values for which phase hysteresis is observed between compression and decompression sequences. The same phase diagram obtained by an alternative route of changing the particle shape is shown in Fig. 5.8. The schematics above the graph indicate the cross-sectional shape of the particles associated with each k_θ value.

this case we used the hard-core potential with the PHGO contact function instead of the WCA potential. The MC translation step and the rotation step are initially set as $\Delta_{q,\max} = 0.015\sigma_w$ and $\Delta_{u,\max} = 0.015\sigma_w$, respectively, but have been adjusted in an equilibration phase to guarantee an acceptance rate of roughly 50 % for the displacement attempts at every global density. The results of the MC and MD simulation sets show no significant differences.

For each value of k_θ, an initial, crystalline ordered configuration generated at low density ($\rho_g = 0.28$) is run to provide isotropic starting conditions before being compressed to the density $\rho_g = 0.44$. Subsequently, a sequence of small compression steps is imposed (see symbols in Figure 5.1) each of which entails an equilibration run of $1.5{\cdot}10^6\Delta t$ and a production run of $5.0{\cdot}10^6\Delta t$. Compressions are made up to $\rho_g = 0.67$, which is found to be a solid state for all k_θ. We perform expansion sequences in an equivalent, but reverse,

manner from each $\rho_g = 0.67$ state. The resultant phase diagram is shown in Fig. 5.1. To examine the sensitivity of the phase diagram in terms of used particles, additional simulations with different system sizes from $N \approx 1750$ to $N \approx 10000$ are performed. These simulations show only modest changes in the phase diagram concerning system size and box shape. We, therefore, come to the conclusion that the very small crystallographic moduli at play here mean that commensurability effects in terms of the simulation box dimensions, while undoubtedly present, are surprisingly weak [398].

Phase identification is based on four main observables, described in detail in Sec. 3.3 and shown in Fig. 5.2:

1. The first of these was the excess pressure P_{ex}, like described in Eq. (3.45), which is dependent on the distance r_{ij} of the center positions and the forces f_{ij} between particles i and j. All forces f_{ij} are repulsive, since the PHGO model is a soft-repulsive particle model [242, 243]. The excess pressure, however, has to be treated with caution, as we deal with a potential close to the hard-core limit (maximally 1.5 % overlap according to the PHGO-contact function), in which P_{ex} is much harder to determine computationally (see Sec. 3.3.2 for more information). Therefore, P_{ex} is only obtained by the Molecular Dynamics.

2. The second key observable is the nematic order parameter P_2 as described in Eq. (3.51).

3. The third measured quantity is the standard deviation of local orientations
$$\sigma(\alpha_i) = \sqrt{\frac{1}{N-1}\left[\left(\sum_{i=1}^{N}\alpha_i^2\right) - \frac{1}{N}\left(\sum_{i=1}^{N}\alpha_i\right)^2\right]}, \tag{5.1}$$
based on the scalar product $\alpha_i = \mathbf{u}_i \cdot \mathbf{u}_j$ of the orientation vectors of nearest neighbour particles i and j.

4. Lastly, the diffusion coefficient D is determined from the diffusive-regime slope of the mean squared displacement such as those shown in Fig. 5.3 and explained and defined in Eq. (3.48) in more detail.

These observables, except D, also serve to confirm system equilibration by using stationarity or constancy of these properties as an indication for how converged the configurations are.

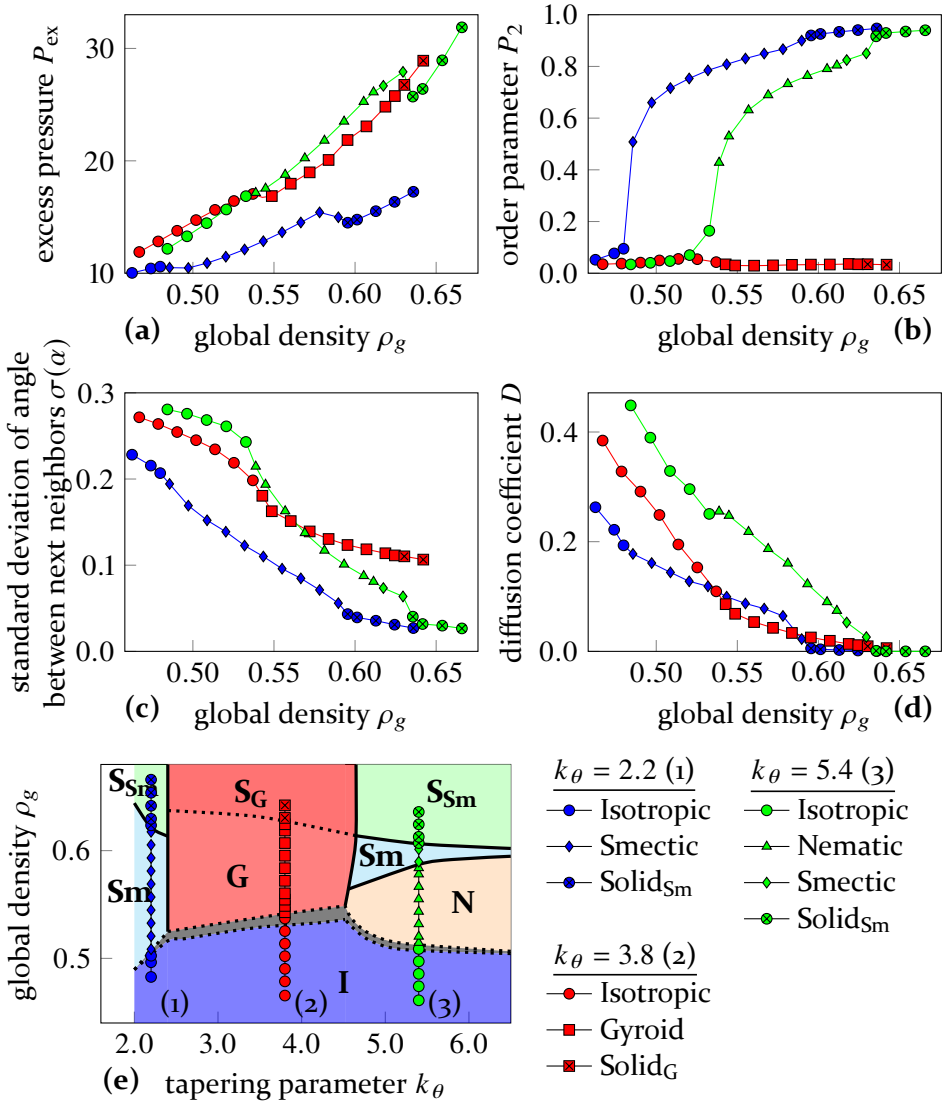

Figure 5.2: (a) The excess pressure P_{ex} (Eq. (3.45)), (b) nematic order parameter P_2 (Eq. (3.51)), (c) standard deviation of angles between nearest neighbour particles $\sigma(\alpha)$ (Eq. (5.1)) and (d) diffusion coefficient D obtained from the compression sequences of $k_\theta = 2.2$ (strong particle tapering), $k_\theta = 3.8$ (intermediate particle tapering) and $k_\theta = 5.4$ (weak particle tapering) PHGO particles, as depicted in (e). The diffusive character of the isotropic (I), nematic (N), smectic (Sm) and gyroid phase (G) and the non-diffusive character of both solid phases (S_{Sm} and S_G) are shown by the mean squared displacement in Fig. 5.3. All observables are obtained by both MD and MC simulation with the exception of D and P_{ex} (MD only), showing statistically no significant differences.

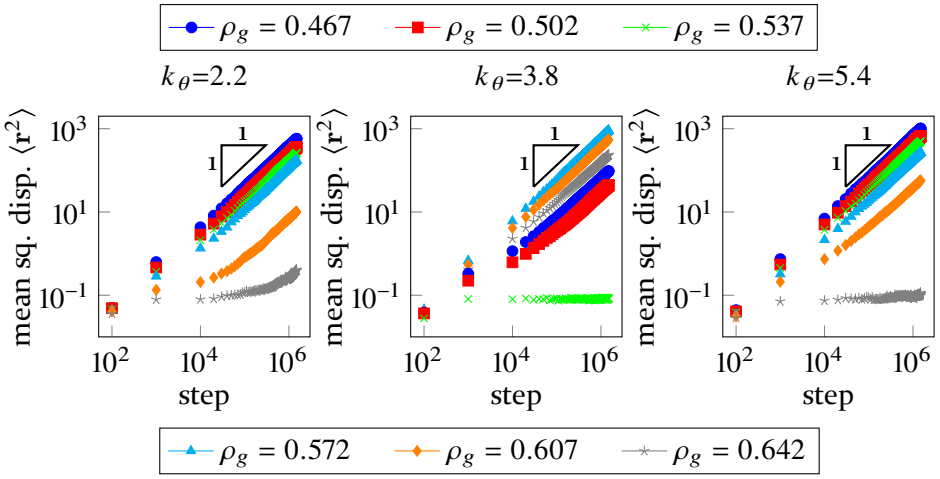

Figure 5.3: The mean squared displacement at different global densities for $k_\theta = 2.2$ (a), $k_\theta = 3.8$ (b) and $k_\theta = 5.4$ (c). A slope of 1 implies diffusive behaviour. At a density of $\rho_g = 0.546$ with $N = 3040$ particles, the mean squared displacement of $20.84\sigma_w$ corresponds to a displacement of the linear size of the simulation box. Depending on the phase parameters, such a displacement is achieved by a number of steps between $\approx$ 90000 steps (smectic, $k_\theta = 2.2$) to $\approx$ 160000 (gyroid, $k_\theta = 3.8$).

Additionally, systems are analysed by calculating the pair-correlation functions, which are defined in Eq. (3.62) and Eq. (3.63) (see Fig. 5.4) and using the cluster identification algorithm which was introduced in Sec. 3.4.4. For all following cluster constructions we use $r_{\text{cl}} = 1.35\sigma_w$ to later color the pears according to their cluster affiliation.

The scattering patterns of the blunt end density distributions are consulted especially to distinguish the gyroid and isotropic phase (see the more detailed analysis of the scattering pattern in Sec. 4.2.1). This is important as occasionally the clustering algorithm cannot perfectly separate the two network domains of the double gyroid and instead combines them to one large cluster due to defects. From this, six distinct phases are identified - isotropic, nematic, smectic (bilayer and monolayer), gyroid, solid smectic and solid gyroid - as well as narrow biphasic or hysteretic regions (marked in grey on Fig. 5.1) between isotropic and ordered fluid phases. Since the resultant phase diagram, Fig. 5.1, can readily be divided into three sections with regard to the particle tapering parameter k_θ, details of observable characterisation are now given in the three Sections 5.1.1–5.1.3 .

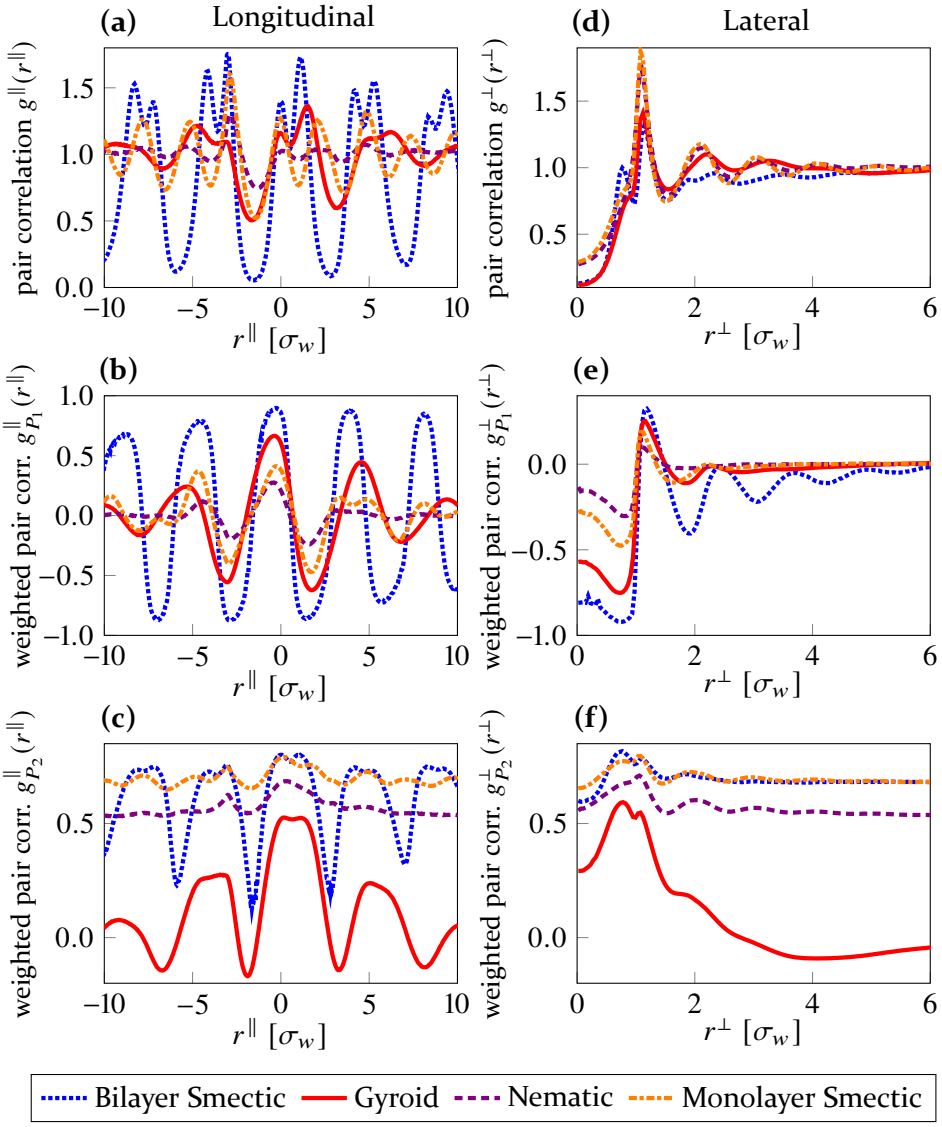

Figure 5.4: The longitudinal pair-correlation function $g^{\parallel}(r^{\parallel})$ (left column) and the lateral pair-correlation function $g^{\perp}(r^{\perp})$ (right column) of the smectic bilayer ($k_\theta = 2.2, \rho_g = 0.57$), the gyroid ($k_\theta = 3.8, \rho_g = 0.56$), the nematic ($k_\theta = 5.4, \rho_g = 0.56$) and the smectic monolayer phase ($k_\theta = 5.4, \rho_g = 0.585$). The pair-correlation functions are additionally weighted by the polar order parameter P_1 (second row) and the nematic order parameter P_2 (third row). The definitions of the different pair-correlation functions are decribed in Sec. 3.4.2 (see also sketch in Fig. 3.3).

5.1.1 Strong taper ($2.0 < \mathbf{k}_\theta < 2.4$: $\mathbf{I \rightarrow Sm_B \rightarrow S_{Sm}}$)

The first class of particles is composed of pears with small tapering parameters between $k_\theta = 2.0$ and $k_\theta = 2.4$, which correspond to tapering angles between $\theta_k = 28.1°$ and $\theta_k = 23.5°$. We will refer to these particles as strongly tapered. In this range, the pear particle systems undergo three different states: the isotropic, the bilayer smectic and the solid smectic phase. Characteristic structures for $k_\theta = 2.2$ are depicted in Fig. 5.5 to visualize the progression of structures.

For low densities below $\rho_g = 0.49$ ($k_\theta = 2.0$) and $\rho_g = 0.52$ ($k_\theta = 2.4$) the systems have low orientational order, and cluster algorithms cannot identify a global arrangement into lamella structures. The simulations do display short thread-like clusters of a few (around 8-12) intertwined particles, such as those appearing in Fig. 5.5 (especially in nematic representation), when the ordered phase is approached from below the isotropic phase. Those clusters are randomly oriented within the systems and unjoined such that they do not form long-ranged structures. Nevertheless, their existence can be interpreted as a precursor to the formation of interdigitated bilayers. Similar pre-order has been obtained, for example, at the isotropic-nematic phase transition of disk-shaped particles [399, 400].

On compression from the isotropic, the system exhibits bilayer smectic and solid-smectic phase behaviours. Whilst the excess pressure is an effective indicator of the transition from isotropic to smectic lamellar (Fig. 5.2), the main signal of this transition is the adoption of high orientational order parameter (see Fig. 5.2b or Fig. 5.5 right). As depicted in Fig. 5.5 (left), in the smectic phase, flat layers of interdigitating bilayer leaflets are formed in which all particles are orientationally aligned either parallel or antiparallel to one another.

The formation of bilayers becomes apparent also in the signature of the different longitudinal pair-correlation functions $g^{\parallel}(z)$ (see Fig. 5.4 left). All three plot indicate multiple distinct peaks suggesting both long ranged transitional, polar and nematic order in the longitudinal direction but also a piling of multiple sheets of pear-shaped particles. Moreover, the bifurcation of peaks in Fig. 5.4a implies an organisation into stacks of interdigitated bilayers rather than monolayers. Here, the arrangement into parallel leaflets (left peak), where the polar order parameter P_1 locally exhibits positive values, and antiparallel leaflets of the bilayers (right peak), where P_1 changes sign,

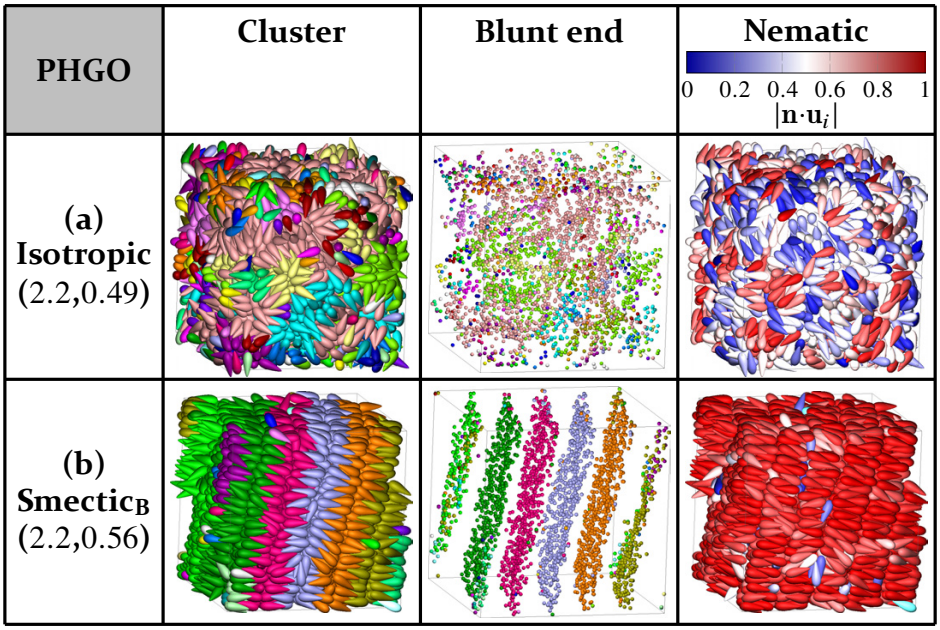

Figure 5.5: Representative configurations of 3040 pear-shaped particles with $k = 3$ and $k_\theta = 2.2$ forming the isotropic (first row: $\rho_g = 0.49$) and bilayer smectic (second row: $\rho_g = 0.56$) phases. The structures are illustrated in the cluster representation (first column) and the blunt end representation (second column) where the colors indicate the cluster affiliation. In the third column the particles are additionally colored according to their relative orientation to the director $\mathbf{n}$.

can be identified. The leaflets are also affirmed by the $g^{\parallel}_{P_2}(z)$ profile of this phase in the form of small dips at each maximum.

Also the lateral pair-correlations indicate the smectic bilayer phase (see Fig. 5.4 right). Firstly, the weighted functions show that the particles are aligned for large lateral distances suggesting that the layers are flat. Secondly, a small peak before the main peak is observable in Fig. 5.4d+f, which can be assigned to the immediate antiparallel and parallel neighbours of the reference pears in the same bilayer, respectively.

Lastly, mobility remains diffusive at intermediate densities, whereas the particle motion is dominated by in-leaflet diffusion but also involves occasional 'flips' of pear-shaped particles from one into another neighbouring sheet. A second transition, between smectic and solid-smectic, is characterised by a steep drop in mobility (see Fig. 5.2d) as well as features in the excess pressure and order parameter characteristics.

5.1.2 Weak taper ($k_\theta > 4.6$: I→N→Sm_M→S_{Sm})

On the other end of the phase diagram, for pear-shaped particle systems with $k_\theta > 4.6$, the simulations exhibit four different phases over the density range $0.46 < \rho_g < 0.65$. From compression of the isotropic phase these weakly tapered pears adopt nematic order between the isotropic and smectic regions (see Fig. 5.2b and representative structures for $k_\theta = 5.4$ in Fig. 5.6). Here, the clustering algorithm fails to highlight any transitional order indicating a nematic phase. This window of nematic phase stability integrates straightforwardly into the phase diagram, as can be seen from the excess pressure and diffusion characteristics in Fig. 5.2a+d, neither of which distinguish between the nematic and the gyroid. Also the pair-correlation functions in Fig. 5.4 clearly suggest a nematic phase as the positional correlations quickly decay both in parallel (a) and perpendicular (d) direction to the pears. However, the orientational correlations (c+f) remain large also for larger distances. Other more intricate signatures, like the bifurcation observed in the bilayer smectic phase, are not obtained.

On the upper bound of the nematic phase, the weakly tapered pears form a smectic phase. A representative structure of this phase is shown in Fig. 5.6. Even though the cluster analysis also shows the formation of sheets like for highly tapered particles, the algorithm identifies twice as many clusters in terms of the position of the blunt ends as for highly tapered particles (see Fig. 5.5). The pair-correlation functions confirm that the particles are not arranged within a bilayer formation and rather create separate monolayers. Although both translational and orientational order is still present, the correlations are weaker than for bilayer arrangements. Furthermore, the plots not only differ quantitatively but also qualitatively. On the one hand, the division into two maxima per peak for $g^{\parallel}(r^{\parallel})$ in Fig. 5.4a vanishes. On the other hand, the small secondary peak which was contributed to the opposite leaflet of a bilayer also disappears for small $r^{\perp}$ in $g^{\perp}(r^{\perp})$ (see Fig. 5.4d). Both of these phenomena can be explained by the lack of inversion asymmetry. In this regime, the particles are not tapered enough to interdigitate into a neighbouring sheet and rather form a separate monolayer. Moreover, the weak taper causes the polarity within a sheet to be less pronounced (indicated by P_1) as in the bilayer smectic phase, such that antiparallel particles can be found within the same leaflet more often.

We note from the phase diagram that the density range of smectic phase stability narrows as k_θ increases. This behaviour is expected since there is

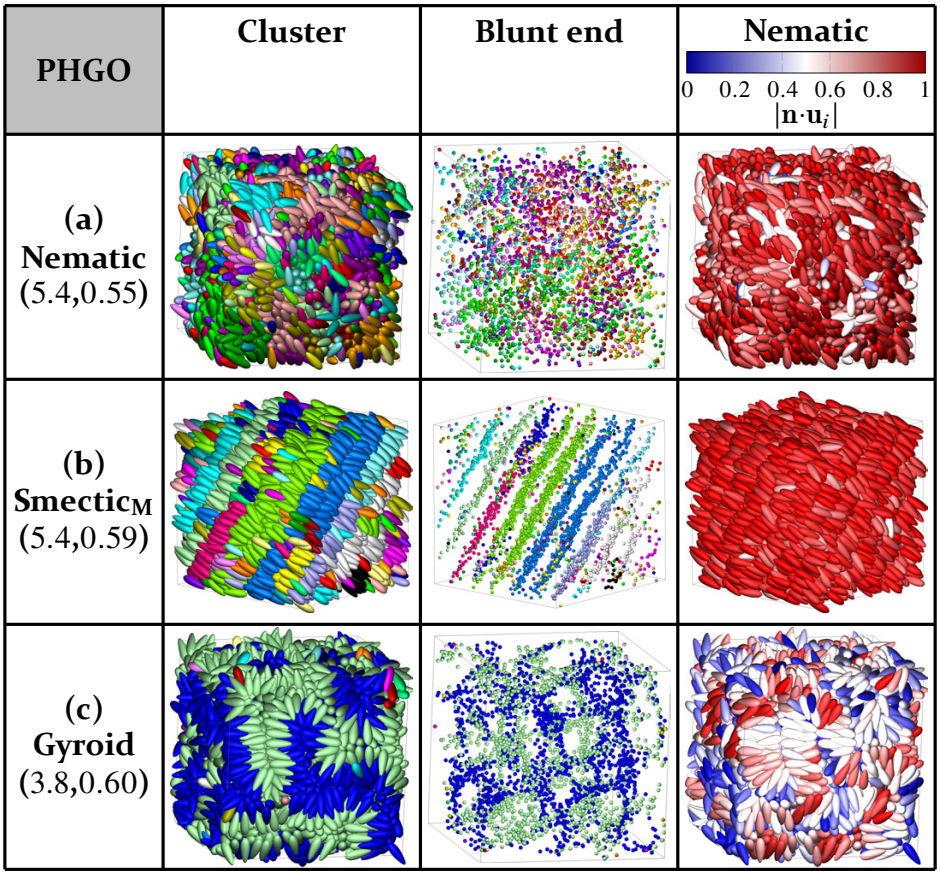

Figure 5.6: Representative configurations of 3040 PHGO pear-shaped particles forming the nematic (first row: $k_\theta = 5.4$, $\rho_g = 0.55$), monolayer smectic (second row: $k_\theta = 5.4$, $\rho_g = 0.59$) and gyroid (third row: $k_\theta = 3.8$, $\rho_g = 0.60$) phases. The structures are illustrated in the cluster representation (first column) and the blunt end representation (second column) where the colors indicate the cluster affiliation. In the third column the particles are additionally colored according to their relative orientation to the director $\mathbf{n}$.

no smectic phase for particles with $k_\theta \to \infty$, which represent ellipsoids, and systems exhibit transitions directly from the solid to the nematic phase [214]. Also the transition density for the most ellipsoidal pears from the isotropic to the nematic phase is in good agreement with the values that have been obtained for the HGO model of ellipsoids: The nematic transition lies between $\rho_g = 0.4785$ and $\rho_g = 0.4860$, accordingly [401, 402].

5.1.3 Intermediate taper ($2.4 < k_\theta < 4.5$: I→G→S_G)

In between the two globally orientationally ordered regimes of the phase diagram, the pears are classified as intermediately tapered. This regime ranges from $2.4 < k_\theta < 4.5$ and $23.5° > \theta > 12.7°$ respectively. For small values of ρ_g, they form an isotropic fluid which also features short bilayer-like threads. As the density is increased for these disordered systems, the gyroid arrangement is adopted rather than the nematic or bilayer smectic phase. The isotropic-gyroid transition occurs at densities of between $\rho_g = 0.52$ ($k_\theta = 2.4$) and $\rho_g = 0.55$ ($k_\theta = 4.5$); see Fig. 5.1. For a full identification and analysis of the gyroid phase, we refer to Chap. 4. Therefore we here just briefly repeat the most important properties of this phase and focus on the new insight gained by the observables in Fig. 5.2 and Fig. 5.4.

At the phase boundary from the isotropic to the gyroid phase, the orientational order parameters of these intermediate particle tapering systems remain low during both compression and decompression (Fig. 5.2b) in sharp contrast to what is seen for strong and weak particle tapering. This is quite surprising as this type of orientational order is typical for elongated particles. However, the associated drop in the standard deviation of local orientations $\sigma(\alpha)$ (Fig. 5.2c) suggests that the systems have adopted short-range orientational order. The transition from isotropic to gyroid phase is also indicated by a feature in the excess pressure (Fig. 5.2a), which coincides with the point of inflection of $\sigma(\alpha)$. Entering the gyroid phase is also associated with a decrease in the gradient of the diffusion coefficient concerning density (Fig. 5.2d).

Also the pair correlation functions prove that the arrangement of single particles within the interdigitating curved bilayers is locally similar to those observed in the flat bilayer-smectic phase of strongly tapered pears. The bifurcation of peaks (a) and the clear bump at the location of the secondary minor maximum for small $r^\perp$ in the bilayer smectic phase (d) coincide with the architecture of interdigitated bilayers. Yet, both of these plots also point to considerable differences on a larger length scale. The correlations are less distinct and diminish faster in the longitudinal and lateral direction which can be explained by the inherent curvature of the minimal surface structure. The influence of the warped bilayers is reflected even more in the characteristics of the weighted pair correlation functions. Firstly, the polar order vanishes in (b+e) for large distances and is less periodic (see especially the double peak at $r^\parallel = 4$ in Fig. 5.4b). Secondly the nematic order

in (c) oscillates around 0 and, like the plot in (f), eventually approaches this very value for $r^{\parallel}$. This means that the stacks of bilayers do not lie parallel to each other anymore and also that largely separated particles within the same leaflet are likely to be differently oriented.

Especially by using cluster analysis (see Sec. 3.4.4), the configurations can be identified as interdigitating curved bilayer super-structures characterised by two interpenetrating, triply-periodic channel networks (see Fig. 5.5), where the thick ends are situated. In addition to being bicontinuous and triply-periodic, the labyrinth-like networks also feature nodes with three branch junctions, as is characteristic for the double gyroid. This is displayed in the second column of Fig. 5.5, where only the blunt ends of the pears are depicted by spheres rather than the pears themselves. These clusters are, indeed, readily identifiable with the network domain of the gyroid and close to the 2×2×2. In this phase, the pear-shaped particles can traverse the simulation box in all directions, through both in-leaflet diffusion and leaflet to leaflet flip-flop. All these results confirm the observation which was already made in Sec. 4.3.3 that the PHGO particles obtain a smectic order on the gyroid minimal surface.

Above a density of $\rho_g = 0.62$, a change in the diffusion characteristic is seen a second time. In this density range, the pear particles no longer traverse the simulation box in the course of a simulation run, such that we characterise the system as solid. Due to the kinetic character of this method to ascertain solidification, the transition between the diffusive and solid state is not defined distinctly and, consequently, is indicated as a dotted line in the phase diagram.

Compared to the solidification of the smectic bilayers, where the particles eventually obtain crystalline ordered domains, the gyroid systems remains diffusive for higher densities. This leads to an apparent discontinuity of the solidification line at the transition $k_\theta = 2.4$ between the smectic and gyroid phase. This may be an indication that the solid gyroid phase is an arrested glassy state of the system caused by an extended relaxation time for high densities. Therefore, a solid lamellar arrangement, which is kinetically inaccessible for MD and entropically barely differentiable for MC, might be the true stable phase at these high densities. Another explanation might be the differences in the diffusion of the particles in the gyroid phase (mostly 3D) and the smectic phase (mostly 2D).

A potential method to clarify the equilibrated state at high densities and hone the phase diagram, in general, is using simulations to measure the free energy of the structures. Even though different techniques to obtain the relative free energy between two structures exist [381, 382, 403, 404, 405, 406], they are not readily adaptable to compare the stability between the gyroid and bilayer smectic phase. For example, the Widom's test particle insertion method [381, 382] is impractical for short-ranged repulsive potentials, particularly at the packing fractions of interest in this work. We also face some challenges in integration methods, like Einstein [403] or thermodynamic [404] integration schemes, where the free energy difference is determined by a continuous transition between phases via a perturbative external potential. For instance, accurate parametrisations of the bilayer phases are needed.[2] A common approach is also density functional theory [405, 406]. Here, however, we refer to Chap. 7 where we will introduce density functional theory and its applications to hard pear-shaped particles in great detail.

5.1.4 Phase boundary between bilayer smectic/gyroid (k_θ=2.4)

Additionally, systems of pears simulated at this phase boundary (or as close to it as numerically possible) between the bilayer smectic and gyroid phases, i.e. those with $k_\theta = 2.4$, cannot be unambiguously assigned to either phase since both phase transition cycles (isotropic–smectic–solid and isotropic–gyroid) are observed for different compression and decompression sequences. At this apparent transition region in terms of k_θ between the smectic and gyroid phases, some configurations even show long-lived coexistence between regions of parallel and curved bilayers. Here, however, we have to consider that commensurability with the periodic boundary conditions might be a subtle issue.

The coexistence structures of the lamellar and gyroid phase (see Fig. 5.7) are reminiscent of the intermediate structures during the rearrangement from an artificial bilayer smectic to the gyroid structure, which was investigated in Ref. [241]. Here, the pears form interconnected layers, such that two leaflets are connecting each other by perforating through an intermediate bilayer and thus, form a channel between the two leaflets. The structures can

[2] One idea is to use the nodal approximation of the gyroid (see Eq. (4.6)) as a parametrisation. However, as the nodal approximation is not perfectly exact and the bilayer interdigitation depth varies in terms of the Gaussian curvature (see Sec. 4.3.4), it is nontrivial to apply the nodal approximation accurately. However, this approach might help not only to determine the equilibrated state but can also lead to more accurate results for the gyroid unit cell size.

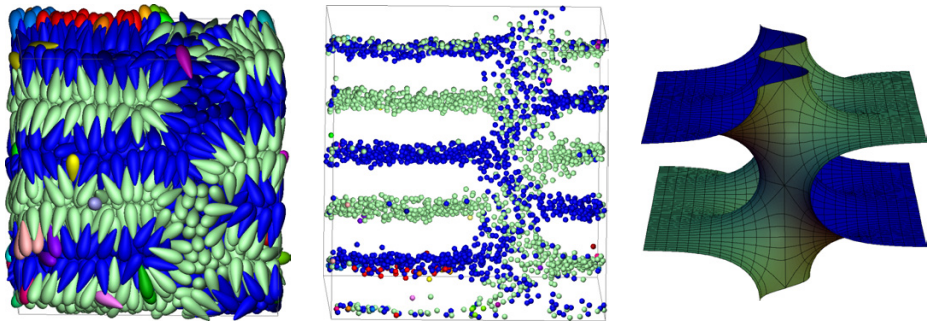

Figure 5.7: Left: Representative configurations of 3040 pear-shaped particles forming a perforated smectic macrostructure at the phase transition between smectic and gyroid phase at $k_\theta = 2.4$ and $\rho_g = 0.56$. Center: Only the position of the blunt ends are depicted by spheres. Colour coding of particles is used to indicate clusters calculated based on the proximity of the pear's blunt ends. Right: The Scherk minimal surface which might be a good model for this configuration.

also be compared to so-called perforated lamella phases in di-block copolymer systems [407, 408, 409]. Here different layers of the same monomer type are linked by hexagonally arranged channels which create holes in the domain of the opposite monomer type.

In mathematical terms, the coexistence structure is also reminiscent of another bicontinuous minimal surface, the so-called double Scherk surface [410]. A variation of this surface, which has been introduced by Karcher [411], the Scherk saddle tower has the same morphological features and might be a good mathematical model to describe the pear-shaped particle structure. This hypothesis can be reinforced as large twist angle grain boundaries between layered structures, causing similar perforations, are often described by a Scherk surface in di-block copolymers and smectic liquid crystals [412, 413, 414, 415, 416, 417, 418]. For comparison, the pear-system and the Scherk saddle tower are depicted in Fig. 5.7.

5.1.5 Phase behaviour upon changes of particle shape

To investigate this co-existence behaviour further and to investigate if the Scherk-like structure is indeed subject to commensurability effects, a second phase diagram is generated by performing simulation sequences with changing k_θ and constant ρ_g (see Fig. 5.8). Even though this procedure of changing the shape of particles is hardly possible for experiments on hard

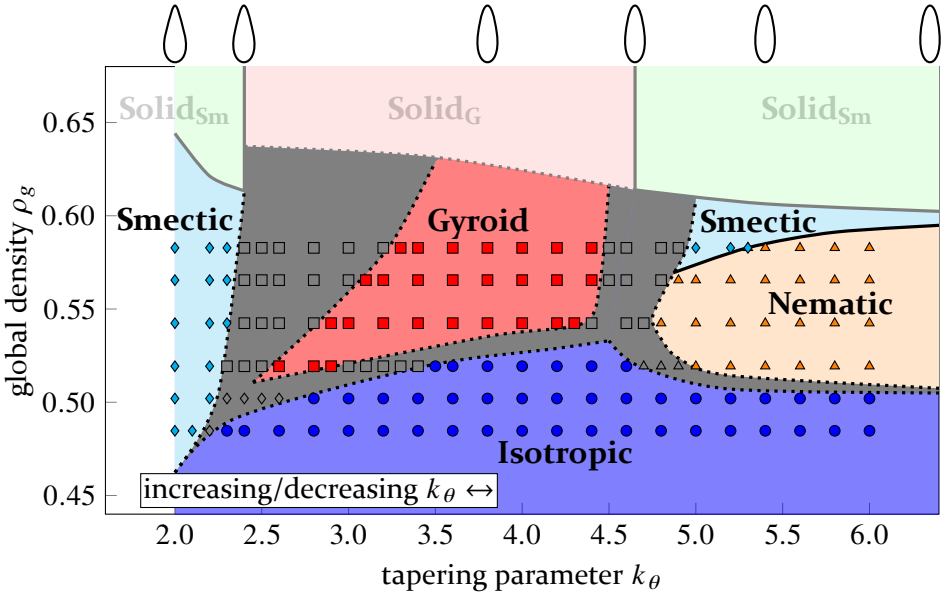

Figure 5.8: Phase diagram of hard pear-shaped particles with $k = 3.0$ obtained by increasing (from smectic) and decreasing k_θ at fixed global density ρ_g for systems of 3040 particles in a cubic simulation box. Grey regions between phases indicate parameter values for which phase hysteresis is observed between the increasing and decreasing sequences of k_θ. The schematics above the graph indicate the cross-sectional shape of the particles associated with each k_θ value. For the solid (dense) phases in Fig. 5.1 it is not possible to dynamically adapt the particle shape.

particles, we follow this idea which is inspired by the "molecular shape concept" in lipid self-assembly [419, 420]. In binary lipid-water mixtures, many facets of the phase diagram can be understood simply by the recognition that changes in pressure, pH, salt concentration or temperature translate to changes of the shape of the individual molecules. Recently also colloids have been synthesised which can shift their shape by introducing different chemical or light stimuli [421, 422].

Starting from smectic configurations with $k_\theta = 2.0$ the tapering parameter is increased by $\Delta k_\theta = 0.1$ steps until $k_\theta = 6.0$. In the MD simulations, the tapering angle of the PHGO particles is simply switched to the new value due to the soft-core WCA potential. In case of the MC simulation and the hard-core particle interactions, the transition from particles with lower k_θ to higher k'_θ is only accepted if no particles overlap according to the PHGO contact function. Otherwise, the simulations are continued for 1000 simulation

steps with k_θ, before the change to k'_θ is attempted again. After $k_\theta = 6.0$ is reached, the tapering parameter is decreased again with the same transition rules until the particles take their original shape. Note here that the particles also change volume during the shape change such that the simulation box has to be adjusted accordingly to keep the global density constant.

The disposition of the phases is similar compared to the phase diagram in Fig 5.1. This indicates that the gyroid phase is a robust liquid crystal state within the PHGO particle system and not an artifect of the simulation method. However, the grey area indicates major hysteresis effects between the smectic/nematic and gyroid phase, which mainly reduce the parameter space where the gyroid phase forms. The hysteresis effect is more dominant for higher densities, which suggests again that for these high densities lamellar structures are similarly stable as the gyroid.

5.1.6 Comparison to phase behaviour of amphiphilic systems

Given that geometric theories exist for bicontinuous phase formation in lipid/water [244, 423] and copolymer systems (strong segregation limit) [424], we summarise our findings about the PHGO phase behaviour by comparing the phase diagrams of lyotropic [50, 419], AB di-block copolymer [188] and PHGO particle systems (see Fig. 5.1, Fig. 5.8 and Fig. 5.9). It is apparent that the phase diagrams exhibit both similarities and differences. As we already mentioned in Sec. 4.3.4 the effective shape of amphiphilic particles can be quantified by a shape parameter of the particles Steiner cell (see Sec. 4.3.4 and Eq. (4.8))

$$s = \frac{v}{A_0 l}. \tag{5.2}$$

The parameter v, A_0 and l denote the volume, base area and height of the Steiner cell, respectively, which encapsulates the molecule (see Fig. 5.9 where we used the example of lipids). The shape parameter can be varied for example by controlling the volume fraction of the solvophilic and solvophobic parts, like the length fraction between the monomer chains in di-block copolymers.

For $s = 1$ amphiphiles obtain a cylindrical shape and typically form lamella phases similar to weakly tapered hard pear-shaped particles. By decreasing s and k_θ, respectively, and making the particles more and more cone-shaped,

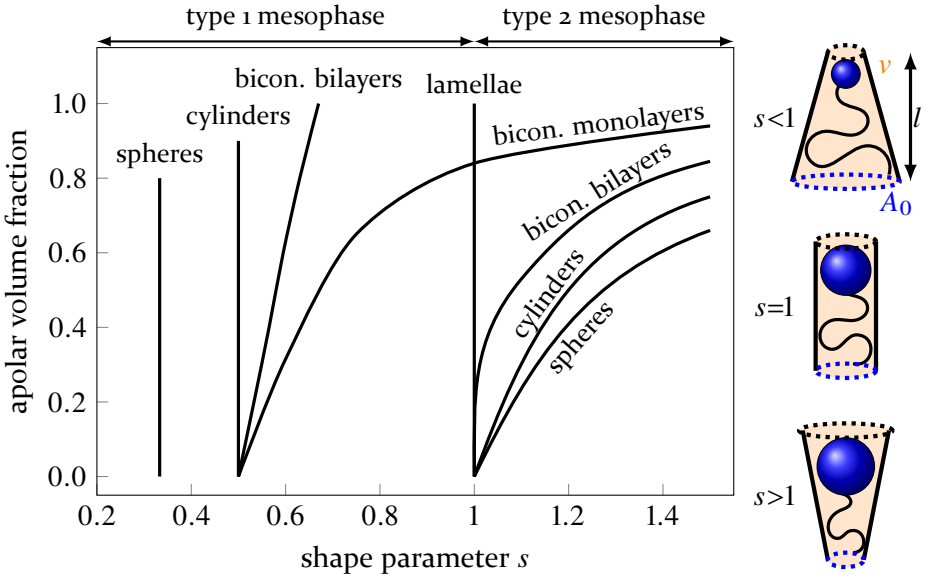

Figure 5.9: Left: The diagram of the typical phase behaviour of amphiphilic particles. The diagram is plotted in terms of the shape parameter s (see Eq. (5.2)) and the apolar volume fraction of the molecules and recreated from Ref. [50]. Right: The concept of the shape parameter is portrayed by the example of lipids.

all three systems first transition into the bicontinuous gyroid phase. Close to $s = 0$, lipid/water and copolymer systems form cylindrical hexagonal phase structures and eventually spherical micelles, whereas hard pear-shaped particles with small k_θ generate smectic structures again, which are, as already mentioned, characteristic for cylindrically shaped lipids and copolymers with $s = 1$ and $f = 0.5$. Note here, however, that the molecular shape for the hexagonal columnar phase is wedge-like rather than cone-like as for the cubic phases. Thus it is just impossible for hard particles to make this "shape-transition".

The major differences for small shape parameters can be explained by the interdigitation mechanism of the pear-shaped particles which we discussed in Sec. 4.3.4. In this chapter, we identified that in the gyroid phase the Steiner cells of the pear-shaped particles, which lead to curved surface structures, do not coincide with the Set-Voronoi cells as the pears occupy space in both channel domains. This is in contrast to lipid and di-block copolymer assemblies where this equivalence between the two cells is valid. Hence, the shape parameter of pear-shaped particle arrangements cannot

be directly related to the shape of single particles but instead has to be expanded to an array of neighbouring pear colloids (see Fig. 4.15). This leads us to the conclusion that also in the bilayer smectic phase the strongly tapered pear-shaped particles within a bilayer collectively form Steiner cells with a cylindrical outline. For weakly tapered pears, on the other hand, the interdigitation breaks such that the Set-Voronoi cells become a sufficient estimate for s again and the phase behaviour is consistent with Fig. 5.9. Consequently, the gyroid phase, where interdigitation introduces tapered Steiner cells, is framed in Fig. 5.1 by smectic phases with collective (bilayer smectic) and singular (monolayer smectic) cylindrical Steiner cells.

5.2 Phase diagram of the hard pear of revolutions (HPR) system

After we created the phase diagram of the PHGO particle model, we put the obtained phase diagram of Fig. 5.1 into perspective. In the following, we want to highlight especially the sensitivity of the special collective behaviour of PHGO pears in terms of particle shape. On that account we perform further simulations where the second approach to represent pear-shaped particles is applied, namely the HPR model. Here the contact criteria of the pears are based on the overlap of triangulated surface meshes (see Sec. 2.2.1 for the exact methodology). Thus a second reference phase diagram is determined (see Fig. 5.10) next to the phase diagram of amphiphilic particles in Fig. 5.9.

The phase diagram is based on Monte Carlo simulations with $N = 400$ and $N = 1600$ monodisperse HPR particles interacting via a hard-core potential. The simulation runs follow roughly the compression and decompression protocol of Sec. 5.1. Hence, the boundary conditions of the cuboidal simulation box are set as periodic in all three directions. The tapering parameter k_θ lies between 2.0 and 5.0 which corresponds to tapering angles between 28.1° and 11.4°. The MC translation step and the rotation step are like for the PHGO particles initially set as $\Delta_{q,\max} = 0.015\sigma_w$ and $\Delta_{u,\max} = 0.015\sigma_w$, respectively, but have been adjusted in an equilibration phase to guarantee an acceptance rate of roughly 50% for the displacement attempts.

We cannot use Molecular Dynamics to simulate the HPR systems as this method is rather impractical. The contact of particles is determined numerically rather than analytically such that it turns out unfeasible to construct

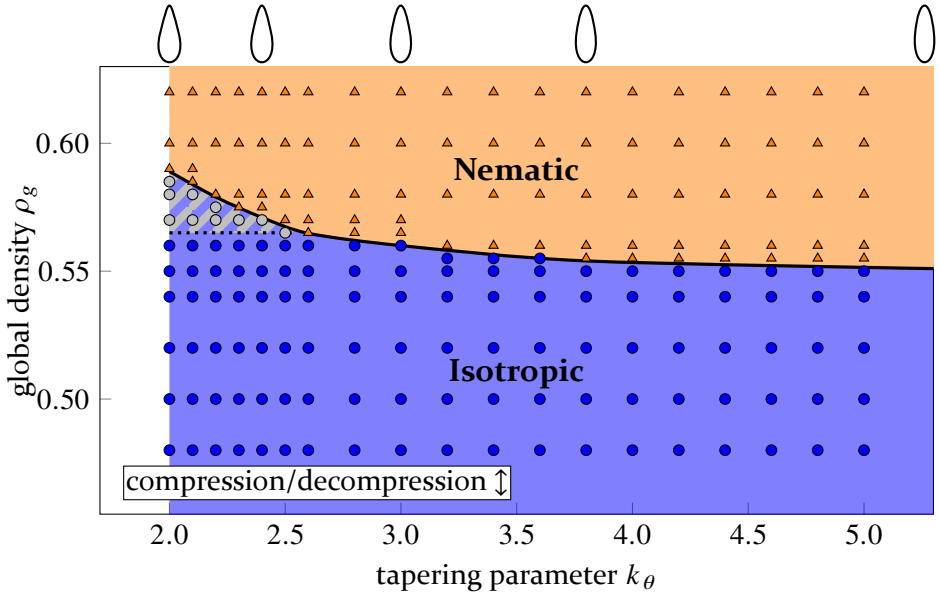

Figure 5.10: Phase diagram of hard HPR particles with $k = 3.0$ obtained by compression (from isotropic) and decompression at fixed tapering parameter k_θ for systems of 400 and 1600 particles in a cubic simulation box. Grey shaded regions indicate configurations which showcase a high degree of local orientational order and basic features, which could lead to bilayer formations according to their pair-correlation functions (see Fig. 5.13). However, this should not be seen as a separate phase from the isotropic state. The schematics above the graph indicate the cross-sectional shape of the particles associated with each k_θ value. The definitions of the different pair-correlation functions are decribed in Sec. 3.4.2 (see also sketch in Fig. 3.3).

a WCA soft-shell potential and calculate inter-particle forces. As a result, some of the observables which were used to identify phases of the PHGO pears are either not or hardly obtainable by MC simulations. On the one hand, the hard-core potential complicates the calculation of the excess pressure P_{ex}. On the other hand, the diffusion D cannot be extracted due to the non-dynamic nature of the MC sampling method. Therefore, we confine ourselves to the nematic order parameter P_2, the longitudinal and lateral pair-correlation functions and the clustering algorithm to determine possible bilayer structures.

Every simulation starts from an initially crystalline arrangement of particles at very low density, which is then slowly compressed to the $\rho_g = 0.44$. Subsequently, the systems are slowly compressed (see symbols in Fig. 5.10). For each step of the sequence, the assembly is equilibrated for $2{\cdot}10^6$ steps and

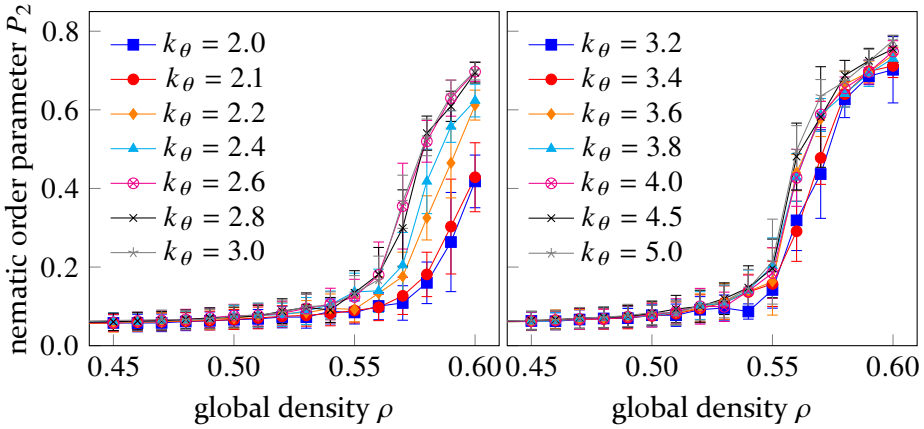

Figure 5.11: The nematic order parameter P_2 during the compression of HPR particle systems with $N = 400$ for different tapering parameters k_θ.

afterwards analysed for $1.8{\cdot}10^7$ steps. We chose the upper limit of $\rho_g = 0.63$ for all compressions due to equilibration issues. At those high densities, the mean square displacement of the individual pears indicates trapped particles. Those particles hardly "travel" (diffuse) within the simulation box during simulation runs. However, we avoid the claim that this phenomenon is an indicator of a solid state as we lack information about its diffusion. Thus, solid phases are not drawn in the phase diagram. Afterwards, expansion sequences are performed in an equivalent, but reverse, manner from each $\rho_g = 0.63$ state. The resultant phase diagram is shown in Fig. 5.10.

Already at first sight, the phase diagram differs starkly from the phase diagram of Fig. 5.1. It becomes apparent that the remarkable division into three different regimes in terms of shape is absent. Independent of shape all particles feature a similar phase behaviour. For low densities, the particles adopt the expected isotropic phase. However, during the compression, the pear-shaped particles begin to globally align with the director of the system and eventually transition into a nematic state (see nematic order parameter in Fig. 5.11). A characteristic configuration of a nematic HPR assembly is pictured in Fig. 5.12. The influence of the tapering parameter k_θ is manifested in a shift of the transition density from the isotropic to the nematic phase. A greater head-tail asymmetry of the pear shape induces stabilisation of the nematic order such that the transition occurs for larger densities. Also note that the hysteresis effects are marginal compared to those observed in the

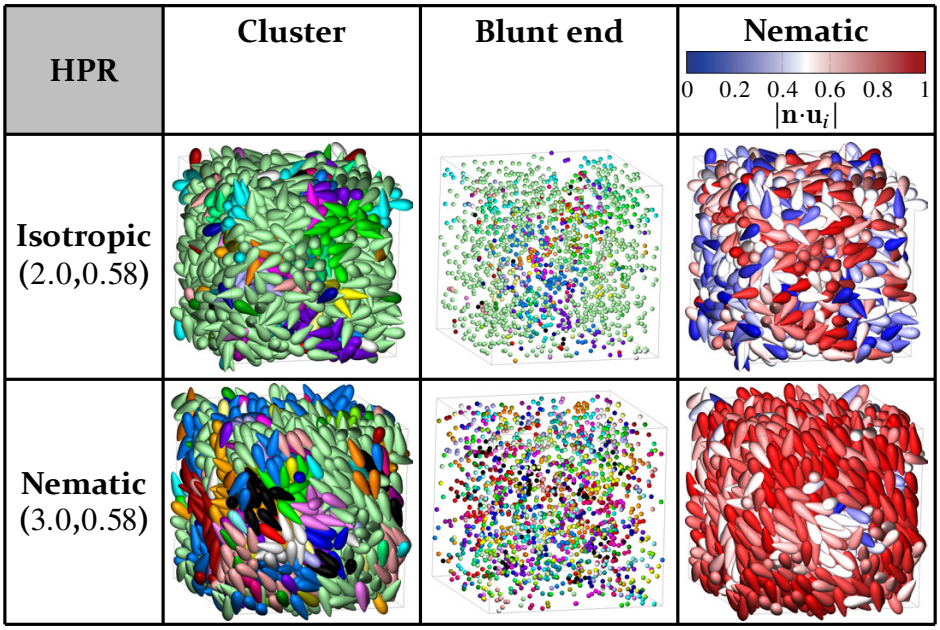

Figure 5.12: Representative configurations of 1600 HPR particles forming the locally ordered isotropic (first row: $k_\theta = 2.0$, $\rho_g = 0.58$) and nematic (second row: $k_\theta = 3.0$, $\rho_g = 0.58$) phases. The structures are illustrated in the cluster representation (first column) and the blunt end representation (second column) where the colors indicate the cluster affiliation. In the third column the particles are additionally colored according to their relative orientation to the director $\mathbf{n}$.

process of constructing Fig. 5.1. The hysteresis is not drawn in this phase diagram consequently. Moreover, the transition line nicely coincides with previous observations of the isotropic-nematic transition for prolate ellipsoids with $k = 3$ and $k_\theta \to \infty$ ($\rho_{in} = 0.541$ [214, 425]).

As the nematic phase arches over all values of k_θ it becomes evident that HPR pears seem to be unable to form bilayer-structures via self-assembly: Neither a plane bilayer smectic phase nor a warped bilayer gyroid phase is not observed during any of the compression runs.

Even when the systems are initially prepared as an artificial smectic or gyroid arrangement, the stabilisation of those phases turned out to be unsuccessful in obtaining an equilibrated bilayer configuration. Here the preconstructed structures destabilise and transition into nematic configurations upon equilibration.

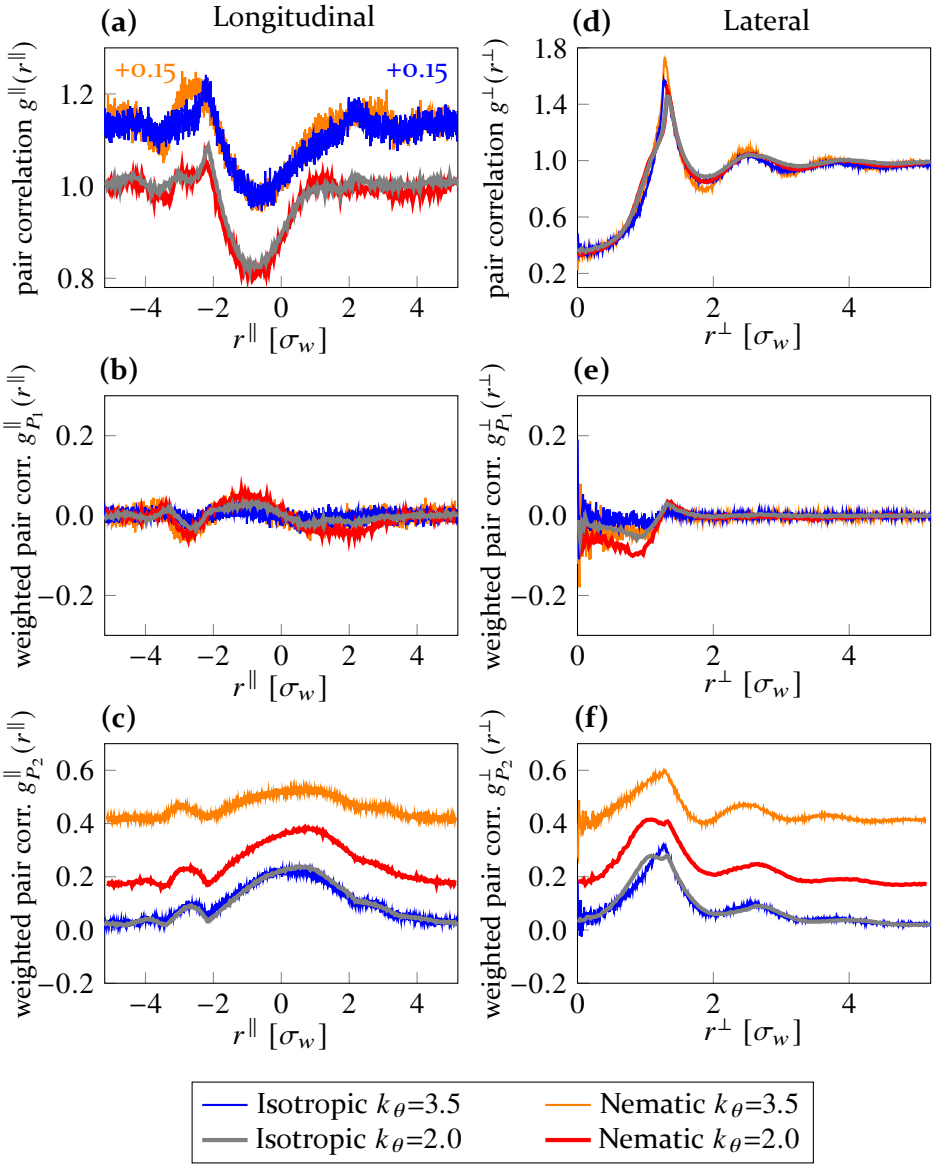

Figure 5.13: The longitudinal pair-correlation function $g^{\parallel}(r^{\parallel})$ (left column) and the lateral pair-correlation function $g^{\perp}(r^{\perp})$ (right column) of the isotropic ($k_\theta = 2.0$:$\rho_g = 0.58$ and $k_\theta = 3.5$:$\rho_g = 0.55$) and nematic ($k_\theta = 2.0$:$\rho_g = 0.6$ and $k_\theta = 3.5$:$\rho_g = 0.58$) in systems of $N = 400$ HPR particle. The pair-correlation functions are additionally weighted by the polar order parameter P_1 (second row) and the nematic order parameter P_2 (third row).

To analyse this nematic phase further, we look at the pair correlation functions shown in Fig. 5.13. The profiles of the nematic and the isotropic phase close to the transition line exhibit both similarities and differences to the liquid crystal phases of the PHGO pear systems in Fig. 5.4. The lateral pair-correlation functions $g^{\perp}(r^{\perp})$ of the nematic phases of both pear models, for example, produce similar plots, also comparable to the monolayer smectic of the PHGO model. The characteristic minor peak before the first major peak, however, which have been attributed to interdigitating bilayer arrangements, is not present. Only for pears close to $k_\theta = 2.0$ this peak is implied by a bump. Also the profiles of $g^{\perp}_{P_2}(r^{\perp})$ are akin (even if the alignment is not as strong) to the not-bilayer forming liquid crystal phases of the weakly tapered PHGO pears.

The most significant difference in terms of lateral correlation, however, is in the polarity of the neighbouring particles. For HPR pears the nearest neighbours show basically no preference of parallel or anti-parallel orientation. The high degree of local polar order for PHGO pears is at best vaguely reflected and largest for $k_\theta < 2.5$.

The plots of the longitudinal pair correlations $g^{\parallel}(r^{\parallel})$ in Fig. 5.13 give some additional indications why no bilayer structures are obtained. The most noticeable one is the missing peak at $r^{\parallel} = 0$. This signifies that this particular correlation is crucial for the formation of bilayer phases as it corresponds to particles sitting side by side to another. All other peaks can be attributed to their counterparts in the $g^{\parallel}(r^{\parallel})$-signature of the nematic/smectic phases of the PHGO pears, but seem to be closer together. Furthermore, the weighted functions indicate that the reference pears barely influence the polar preference of their neighbour's orientation, not even longitudinal direction. On a similar note, the local nematic order indicated by the minor peaks, even though obviously present, is not as pronounced and long ranged in this model, not to mention the double peaks, which can be observed for all liquid crystal phases in Fig. 5.4, but are not noticeable here.

Despite these distinctions, similarities can be determined as well. For once, the pears tend to aggregate preferentially at the blunt ends ($r^{\parallel} < 0$) rather than the pointy end ($r^{\parallel} > 0$) of other particles. This leads to the assumption that in principle the mechanism which brings the pears together with their blunt ends to form clusters also exists in the HPR model. Unfortunately, the impact of this mechanism is not strong enough to indeed induce

the self-assembly of bigger clusters (see cluster representation in Fig. 5.12). More intriguing, however, is the observation that for highly tapered particles $k_\theta < 2.5$ the peaks of $g^{\parallel}(r^{\parallel})$ and $g^{\perp}_{P_2}(r^{\perp})$ split into two. This can be already observed in the isotropic phase close to the phase transition. The area within the system which showcases this bifurcation is shaded in the phase diagram. Thus, some of the basic conditions for bilayer formation are also met at least for highly tapered HPR particles. Nevertheless, without additional features to the contact function, those effects are too weak to produce a more complex phase behaviour than nematic.

5.3 Conclusion and outlook

In this chapter, we have described the phase behaviour of two pear-shaped particle systems (PHGO and HPR). Even though the underlying potentials are very similar in shape and closely related the resulting phase diagrams exhibit big differences.

First, we simulated and analysed systems of PHGO pear-shaped particles capable of forming the Ia$\bar{3}$d gyroid phase. We have reproduced in various ways the spontaneous formation of the gyroid phase and, consequently, confirmed that attractive interactions are not necessary for the formation of this structure and that the gyroid can be stabilised by purely entropic effects. The phase diagram obtained here indicates that particles with a range of tapering parameters, corresponding to tapering angles of between 12.4° and 23.5°, are able to form the gyroid phase in various ways, which are summarised in Table 5.1. However, here we only restricted ourself to pears with aspect ratio $k = 3$, such that the parameter space is not fully exhausted. Hence, it is certainly interesting to expand the phase diagram further by controlling the aspect ratio. Some preliminary simulations have shown, for example, that the gyroid phase can still be assembled for PHGO particles between $k = 2.75$ (with $k_\theta = 3$) and $k = 3.5$ (with $k_\theta = 3$). Globally orientationally ordered phases have been obtained for PHGO pears as far as $k = 2.5$ ($k_\theta = 3$). Nevertheless, those systems should be investigated in more detail in the future.

The discussion of Sec. 4.3.4 has been continued as we could show that the phase behaviour of the PHGO pear systems differs from those of lipids and copolymers in terms of the shape parameters appropriate to particles in a bilayer. In particular, we note that also the phase boundaries found here for the gyroid are fundamentally different from those seen in many

Pear model		Potential	Sim.	Protocol	Gyr	Ref.
full-name	abbrev.					
Pear hard Gaussian overlap	PHGO Eq. (2.17)	hard-core Eq. (2.6)	MC	compression	✓	Fig. 5.1
				initial smectic	✓	Fig. 4.3
				shape-change	✓	Fig. 5.8
		WCA Eq. (2.20)	MD	compression	✓	Fig. 5.1
				initial smectic	✓	Fig. 4.3
				shape-change	✓	Fig. 5.8
Hard pear of revolution	HPR Eq. (2.8)	hard-core Eq. (2.5)	MC	compression	$\text{✗}^{?}$	Fig. 5.10
				initial smectic	✗	
				initial gyroid	$\text{✗}^{?}$	

Table 5.1: Summary of the ability of different pear potentials to form double gyroid phases. The sign $\text{✗}^{?}$ indicates that in this case no equilibrated gyroid has formed, but features which are characteristic to bilayers have been found.

experimental systems. Conventionally, the gyroid is sandwiched between planar lamellar and hexagonal phases, and its stability is argued in terms of curvature elasticities. This, though, is difficult to reconcile with the phase diagram of Fig. 5.1, in which the gyroid borders isotropic and nematic fluids for which there is no curvature elasticity. A possible explanation for this is offered by recent arguments from the Selinger group [397] that sufficiently strong bulk splay-bend coupling between polar and orientational degrees of freedom can destabilise the nematic concerning supra-molecular modulations (i.e. periodic structures). These arguments, in turn, hark back to the classic paper of Dozov [426] in which the central ideas of the twist-bend nematic were set out. Given that our hard pear systems clearly possess steric coupling between molecular-scale splay and bend, there appears to be a strong argument that the gyroid region observed here is indeed a realisation of a modulated splay-bend phase predicted by Dozov and Selinger.

Moreover, we generated a second phase diagram based on particles interacting according to strict hard-core interactions. Here we observed only a rudimentary phase behaviour in comparison to the PHGO particles. For all particle shapes analysed (i.e. all k_θ) the systems form nematic liquid crystal phases, where more highly tapered particles visibly destabilise the nematic

order and push the transition to higher densities. Both the gyroid and the bilayer smectic phase vanish (see Table 5.1). According to these observations the small differences in the contact function, which can easily, but mistakenly, be considered negligible, have a major impact on the self-assembly of pear-shaped particles. Even though most features of a pear (like aspect ratio and tapering parameter) are present in both models, the PHGO particles have to offer additional morphological properties, to which the stability of the gyroid phase is ascribed. This is also supported by the fact that only the nematic phase is obtained which also have been found for PHGO pears with small tapering angles. In this regime of large k_θ the two pear models differ the least in terms of contact functions (see Fig. 2.8). Hence, their collective behaviours are very similar. All these results lead to the assumption that the formation of bilayer structures, including the double gyroid phase, is due to the special orientation dependency of the PHGO contact function. Especially the self-non-additive features in reference to the pear shape (see Sec. 2.2.1) seem to magnify the spontaneous placement of pears side to side. This mechanism would naturally lead to sheets, which then interdigitate due to the pointy ends of the individual particles. However, to confirm this hypothesis, we have to examine the next-neighbour interactions of the two pear-shaped particle models, which will be the main topic of Chap. 6.

Despite the differences in phase behaviour, the self-assembly of some HPR particles with small k_θ close to the phase transition showcases also interesting properties, which were attributed as necessary precursors to the formation of bilayers. Therefore, it is conceivable that the HPR particles might be able to form similar phases like the PHGO pears, if we, for instance, add suitable changes to the pear-shape or introduce non-additivity to the HPR contact function. These particle modifications also have the potential to be utilised as a regulating mechanism to control the coupling strength between the blunt ends. This might allow us to create a model for pear-shaped particles, based on those indicated by the grey area in Fig. 5.10, with an intermediate degree of blunt end aggregation. These particles could potentially form phases with a short-range order, sufficient to display a bicontinuous network, but also displays with disorder over larger length scales. Those disordered cubic phases are known as L_3 sponge phases [371] and are formed typically in lipid-water mixtures by swelling the cubic phases due to the presence of additives [165, 427, 428, 429, 430, 431, 432, 433, 434].

As a closing note, we want to mention here that it is difficult to judge which of the two pear models represents the interactions of pear-shaped particles, which might be synthesised in the future, better. For example, it is well established that colloids in experimental systems are never truly hard and the interparticle potential always inherits some degree of softness [207, 279, 280, 281]. Therefore, the potentials we used here – both the PHGO *and* the HPR potentials – have to be considered as approximations of a real pear-shaped colloid. Additionally, pear-shaped particles have not been synthesised yet. In principle, many different strategies to produce nanoparticles with aspherical shapes have been developed like methods via templates [435, 436, 437], particle swelling and phase separation [226, 438, 439], seeded emulsion polymerisation [440, 441, 442, 443], controlled deformation of spherical colloids [235, 444, 445], particle confinement [446] or lithography [447, 448, 449]. However, many of these techniques are still limited in either their customizability of the particle shape, rely on colloids as a basic shape or cannot be mass-produced easily. These difficulties seem to be exacerbated by the big contrast of the two phase diagrams in Fig. 5.1 and Fig. 5.10, which highlights that in both experiments and simulations even small nuances of the interaction profiles of molecules have to be taken into account to predict the right phase behaviour. Also the composite sphere method, where complexly shaped particles are modelled from multiple sphere constituents, are known to faces issues with inaccuracies due to the degraded smoothness of the particle surface [262, 263, 264].

6 Depletion interactions between pears in a hard sphere fluid

"Entropy is the price of structure."

– Ilya Prigogine

This chapter analyses depletion effects that enable further contrast between the two pear-shaped particle models – the PHGO and HPR pear-shaped particles. After a brief introduction to depletion mechanisms and excluded volume computations for colloidal systems, we investigate the depletion attraction for both pear models. Furthermore, we compare the favourable two pear-shaped particle arrangements in terms of excluded volume, which are determined by MC simulations of PHGO and HPR particles in a pool of a hard spherical solvent, with the numerically obtained and, according to the Bézier-curv-curvee representation of the pear-shape, ideal configurations. While the HPR model behaves as expected from the analysis of excluded volumes, the PHGO model showcases a preference for splay between neighbouring particles which can be attributed to the non-additive characteristics of the PHGO contact function. Lastly, we propose a third pear-shaped particle model, the non-additive hard pear of revolution (NAHPR) model, which is based on the HPR model but also features non-additive traits to copy the depletion behaviour of the PHGO particles.

The previous chapter showed that minor discrepancies between contact profiles of the PHGO and the HPR particles lead to significant differences in the appearance of mesophases, most notably the presence of bilayer and gyroid phases in PHGO pears and their absence in the HPR model (see Chap. 5). However, until now only single-component configurations have been considered. The distinct mannerisms in the self-assembly of one-component systems is a clear indicator that the two pear-shaped particle models have to be distinguished. Nevertheless, the exact nature of the difference on a microscopical level and a specific reason why the phase diagrams differ for the two contact functions is not yet clear, and is the subject of this chapter.

In all liquid crystal phases, obtained both for the PHGO and the HPR particle model, the arrangement of each pear is highly affected by a multitude of next nearest neighbours. This elaborate interplay of particles coupled with the aspherical pear-shape, which features a significant degree of complexity, makes a more detailed analysis of the direct influence between adjacent particles impracticable. Hence, we reduce the complexity of our simulations in the following and shift our focus to systems which encapsulate the fundamental features of pure two particle interactions. In particular, we are interested in the specific depletion interactions of the pear-shaped particles. Within a sea of hard sphere particles acting as a solvent, depletion causes an effective attraction between two objects. Moreover, this can be seen as an initial step to add a second "solvent" component to the pure-pear liquid crystal phases in order to mimic lipid-water systems in Chap. 8.

This chapter is structured as follows: We first discuss the physics of depletion phenomena and the historical background of depletion interactions in Sec. 6.1. Here, however, we focus mainly on the central physical concepts. For a more detailed description of depletion, we refer to Ref. [450]. Then in Sec. 6.2 the optimal arrangement of pears in terms of their excluded volume is identified using numerical tools. Next (Sec. 6.3) we perform MC simulations of two large pear-shaped particles within a solution of smaller hard spheres; This is done for both the PHGO and HPR particle models to compare the computational results with the previous predictions of the ideal excluded volume, obtained by the numerical technique. These allow us to pinpoint the specific differences between the two models more efficiently and to make better assumptions why the PHGO particle favours the formation of bilayer phases like the bilayer smectic or gyroid phase in contrast to the HPR particle. Finally in Sec. 6.4, we will give a short outlook, how bilayer phases could possibly be stabilised in monodisperse systems based on the HPR interactions by introducing non-additivity to the contact function.

6.1 Basic concept of entropic forces

6.1.1 Depletion interaction of spherical colloids

Depletion describes the effect of small solvent particles, like polymers or small hard spheres, on the self-assembly of larger colloids. Already in the 1950s Asakura and Oosawa [451, 452] predicted an effective attraction between two plates and between two hard-core spheres within a diluted system

of smaller polymers, which was later also revisited by Vrij [453]. Moreover, they were able to relate this attractive force to a purely entropically driven effect similar to the entropic self-assembly of colloids into liquid crystal phases. In their calculations, the polymer depletants are modelled as an ideal gas of spheres, which, however, interact via a hard-core potential with the larger colloids. This model of the solvent is also referred to as the penetrable hard spheres model [450, 454]. Applying these approximations, the main physical process behind depletion can be simplified.

The free energy F of the system is predominantly governed by the degrees of freedom of the polymer particles. If the number of colloids N_{coll} is much smaller than the number of solvent particles N_{depl}, that is $N_{\text{coll}} \ll N_{\text{depl}}$, the total free energy can be approximated purely by the ideal gas free energy of the depletant (see Eq. (3.13)) [451, 455]

$$F_{\text{depl}} = N_{\text{depl}} \ln\left(\frac{N_{\text{depl}}\lambda^3}{V'}\right) - N_{\text{depl}}. \tag{6.1}$$

with the thermal de Broglie wavelength $\lambda = \sqrt{\frac{h^2\beta}{2\pi m}}$ of particles with mass m. Furthermore, V' is the volume which is available to the ideal gas. As the solvent cannot penetrate the large colloids we can identify $V' = V - V_{\text{excl}}$, where V is the volume of the system and V_{excl} is the volume, from which the excluded to the solvent by the colloids. Inserting this into Eq. (6.1) we get

$$\begin{aligned} F_{\text{depl}} &= N_{\text{depl}} \ln\left(\frac{N_{\text{depl}}\lambda^3}{V - V_{\text{excl}}}\right) - N_{\text{depl}} \\ &= N_{\text{depl}} \cdot \left[\ln\left(\frac{N_{\text{depl}}\lambda^3}{V}\right) - 1\right] + \frac{N_{\text{depl}}}{V} V_{\text{excl}} + O\left(\frac{V_{\text{excl}}^2}{V^2}\right). \end{aligned} \tag{6.2}$$

To find the minimum of the global free energy, which is associated with its equilibrium, the system practically minimises F_{depl} as the contribution of the large colloids and, hence, their degrees of freedom can be neglected. The dominance of the solvent particles implies that the particle configuration tries to decrease V_{excl} as much as possible, which corresponds to maximising the available space for the solvent spheres. The excluded volume of a single sphere is composed of its volume plus the volume of a thin film or "envelope" around the particle with thickness r_{depl} (radius of depletants) as depicted in Fig. 6.1. When additional colloids are introduced, their collective excluded volume depends on the position of the colloidal particles. If the

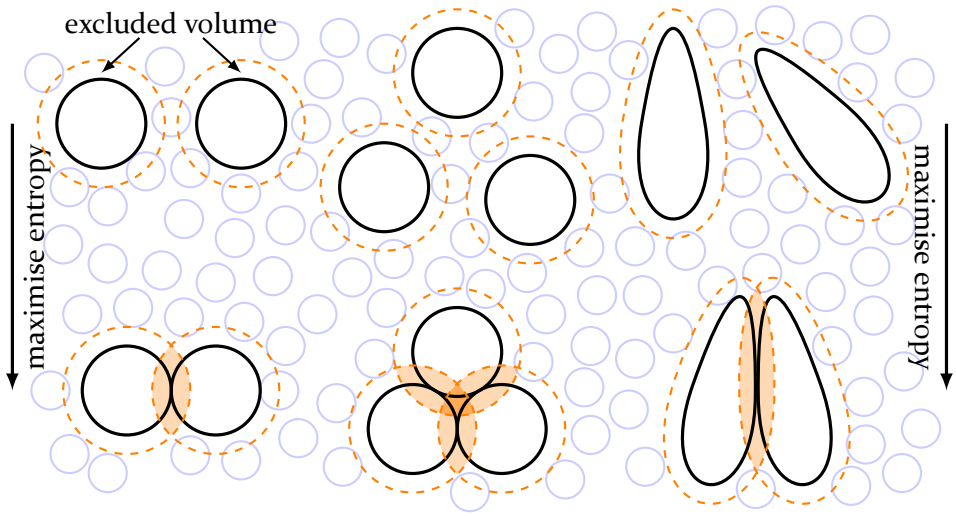

Figure 6.1: The concept of depletion is sketched by the example of two hard-core spherical colloids (left), three hard-core spherical colloids (centre) and two hard-core pear-shaped colloids (right) dissolved in a liquid of smaller hard spheres (indicated in light blue). The system is driven mainly by the entropy of the solvent particles and maximises the free energy by minimising the excluded volume of the bigger colloidal particles. The excluded volume cannot be penetrated by the depletant due to the presence of the colloid (indicated by the dashed line). Thus, the larger objects pack together such that their excluded volumes maximally overlap (indicated in orange) and more space is provided for the depletants. Overall this mechanism can be interpreted as an effective, entropically driven attraction between the colloids.

colloidal spheres are separated from each other by a distance greater than the solvent diameter the excluded volume is merely a multiple of the excluded volumes of the single spheres. However, if the colloids are within each other's vicinities, such that no solvent particle can be placed between them, the individual excluded volumes overlap and decrease the overall excluded volume. Hence, the entropy maximisation leads to the large colloids coming together as close as possible and form tight clusters (see Fig. 6.1).

This behaviour can be interpreted as an effective short-range attraction in addition to the hard-core potential also known as the Asakura-Oosawa potential [450, 451]. Note that the attraction results from a purely repulsive system and can then be categorised as an entropic force. The strength of the entropic force can be related to the osmotic pressure which is acting on the colloidal cluster by the depletant. Later the Asakura-Oosawa potential has been improved significantly by extending the theory to finite densities

[456, 457] and confirmed using computational simulations [458, 459]. In this improvements also an entropically driven repulsion was determined for high solvent packing fractions [457, 458, 459, 460]. In this regime, the solvent particles form shells around the colloid leading to effective repulsive forces. The higher order shells around the colloids even cause the depletion forces to oscillate [461, 462, 463].

Even though the initial depletion model by Asakura and Oosawa appears to reduce the problem to a very simplified system, the same entropic concept could be applied to other depletion theories which cover more realistic depletant models. Other theories approach polymers for example based on the ideal chain-model [464, 465], as hard-core spheres [456, 459, 462], as hard rods [466, 467, 468] or as hard disks [469, 470]. Note here, that depletion has been also predicted in classical density functional theory [462, 471, 472] (for more information about density functional theory see also Chap. 7).

The first successful attempt to measure depletion forces was made by Evans and Needham, who measured the strength of the attraction between two bilayer membranes in a solution of macromolecules [473]. Later also the second part of the Asakura-Oosawa theory was confirmed experimentally by directly determining the attractive forces between two large hard spheres [461]. However, already prior to the direct measurements, many phenomena in systems of hard spherical colloids have been successfully explained by depletion. For example, the ordering of spheres in a solution of polymers close to a hard wall could be attributed to depletion [474, 475, 476]. Also, the demixing of binary hard sphere mixtures into an ordered crystalline cluster of large spheres and a fluid of the small spherical solvent is a result of the excluded volume effects [477, 478, 479, 480, 481, 482, 483].

6.1.2 The effect of colloid shape on depletion

Similar to other self-assembly processes, the shape of the molecules/colloids naturally impacts how a pair of two colloidal particles in a solvent eventually arranges under the influence of depletion. By changing colloids from a simple sphere to objects with more complicated shapes, the excluded volume does not only depend on the separation but also the relative orientation of the particles (see Fig. 6.1). Consequently, depletion does not only induce convergence between colloids but also an orientational rearrangement of the particles. For instance, it has been shown that by adding dimples to one

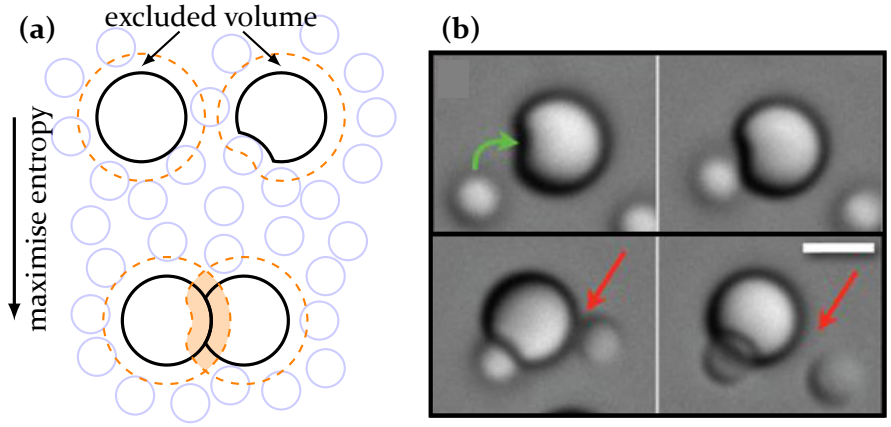

Figure 6.2: (a) The lock-and-key mechanism in colloidal systems is sketched for hard spheres with concavities within a hard sphere solvent (indicated in light blue). The depletion forces try to minimise the excluded volume (indicated by the dashed line) of the lock (colloids with concavities) and key (colloids without concavities) particles. Hence, depletion leads to the key objects anchoring at the fitting dimples of the lock particles. (b) The time sequence of an experimental system of spherical colloids with and without dimples. The green and red arrows indicate a successful and unsuccessful lock-key binding via depletion, respectively. Scale bar: 2 μm. (b) is adapted with permission from [484].

of the spheres the other colloid attaches at this concavity [484, 485]. This "lock-and-key" mechanism can be used as a tool to control the depletion of particles (see Fig. 6.2). Another sort of directionality can be introduced by creating elongated colloids. At a wall, hard prolate ellipsoids [486, 487] and spherocylinders [488] align with their long axis along the flat interface due to depletion. Moreover, it is known theoretically [489, 490] and from experiments [491, 492] that rod-like colloids self-assemble into clusters with nematic order when non-absorbing polymers are added. Excluded volume mechanisms provide access to rich phase behaviours for various mixtures of hard aspherical particles and depletant particles [489, 493, 494, 495, 496, 497, 498], including fascinating effects like depletion induced shape-selective separation in colloidal mixtures by the addition of non-adsorbing polymers [499, 500, 501, 502].

Depletion also takes a fundamental role in more complex biological or technological settings, like providing beneficial conditions for polymer crystallisation [503, 504] or describing the physics within the cytoplasm of cells. In the dense and crowded environments of cells [505, 506, 507] the molecular conformations of proteins and other macromolecules are not only influenced

by steric interactions but also partially driven by the excluded volume of the molecule [508, 509, 510]. In biology those effects are mostly known as "crowding" [508, 511, 512, 513, 514]. Prime examples are the influence of crowding agents on protein folding [513, 515, 516], the stabilisation of helicoidal structures due to excluded volume arguments [517, 518] or the bundling of fibres or microtubes by introducing polymers [519, 520]. The depletion interactions are known to affect biochemical reactions [521, 522, 523] and dynamical properties [524, 525, 526] within cell systems due to its impact on the molecular configurations. It is even argued that the interactions caused by crowding are strong enough to alter observations between in vivo and in vitro experiments, where for the latter the crowded environments tend to be neglected often [514, 527, 528, 529].

6.2 Excluded volume of two pear shaped particles

Here we perform numerical calculations to predict the ideal particle arrangement of two pear-shaped particles. For rotationally symmetric particles like pears defined by Bézier-curves, three degrees of freedom have to be considered in addition to the particle separation to define a specific constellation between two pears. Two of them can be dedicated to the relative orientations of the particles $\mathbf{u}$ and $\mathbf{v}$. The last one relates to the flexibility to select the contact point p_c on the surface of one colloid, in the case both particles are in touch and the separation is 0. The choices of $\mathbf{u}$, $\mathbf{v}$ and p_c, automatically determine the contact point on the surface of the other object. Theoretically, we are able to sweep the whole configurational space of the two-pear-depletion-problem and identify the configuration with the largest excluded volume overlap. The most important steps of the used sampling algorithm are both sketched in Fig. 6.3 and itemised below:

1. In the first step, an initial arrangement of two pear-shaped particles is chosen. We only consider arrangements where the two pears are in contact, as those configurations provide the minimal excluded volume for convex particles in terms of separation.

2. Afterwards, the surfaces of the particles are triangulated (B_1 and B_2). The same method is used for creating the meshes for the HPR model (see Sec. 2.2.1).

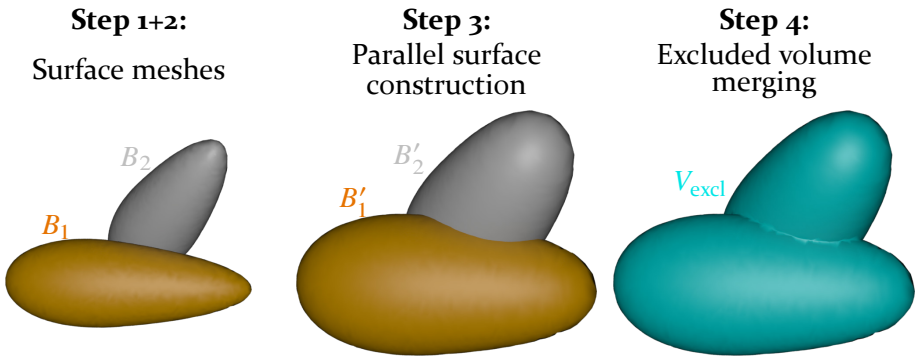

Figure 6.3: The main steps of the algorithm to predict the ideal two pear-shaped particle arrangement in terms of excluded volume. In the first and second step (left) a configuration is chosen, and the surface meshes B_1 and B_2 of the pear-shaped particles are created. In the third step (centre) the individual excluded volumes of the pears B'_1 and B'_2 are created by constructing the parallel surface of B_1 and B_2. Afterwards, (right) the two meshes are merged and the total excluded volume V_{excl} is computed. The steps are repeated until enough configurations are sampled.

3. In the next step, the parallel surfaces of the triangulations are generated. The construction of the parallel surface was already introduced in Sec. 4.3.4 (more specifically Eq. (4.9)), where the vertices of the triangulation are translated in normal direction by r_{depl}. The resulting new meshes $B'_1(r_{\text{depl}})$ and $B'_2(r_{\text{depl}})$ correspond to the interface separating the impenetrable and available space of virtual hard spheres with radius r_{depl} caused by the first and second pear, respectively.

4. Subsequently, $B'_1(r_{\text{depl}})$ and $B'_2(r_{\text{depl}})$ are merged to calculate the collective excluded volume defined by $V_{\text{excl}}(r_{\text{depl}}) = B'_1(r_{\text{depl}}) \cup B'_2(r_{\text{depl}})$.

5. Another configuration, which has not been observed yet, is chosen and the algorithm returns to step 2. This procedure is repeated until the configuration space is sampled sufficiently densely.

In the following this algorithm is applied to pears with aspect ratio $k = 3$ and tapering parameter $k_\theta = 3.8$, which, as we showed earlier, lie well within the gyroid phase for the PHGO model (see Fig. 5.1) but does not form cubic phases for the HPR-model as indicated in Fig. 5.10. Moreover, we use $r_{\text{depl}} = 0.31\sigma_w$, which corresponds to spheres with $V_{\text{sph}} = 0.08 \cdot V_{\text{pear}}$. The computations are performed with the 3D animation software tool Houdini [530].

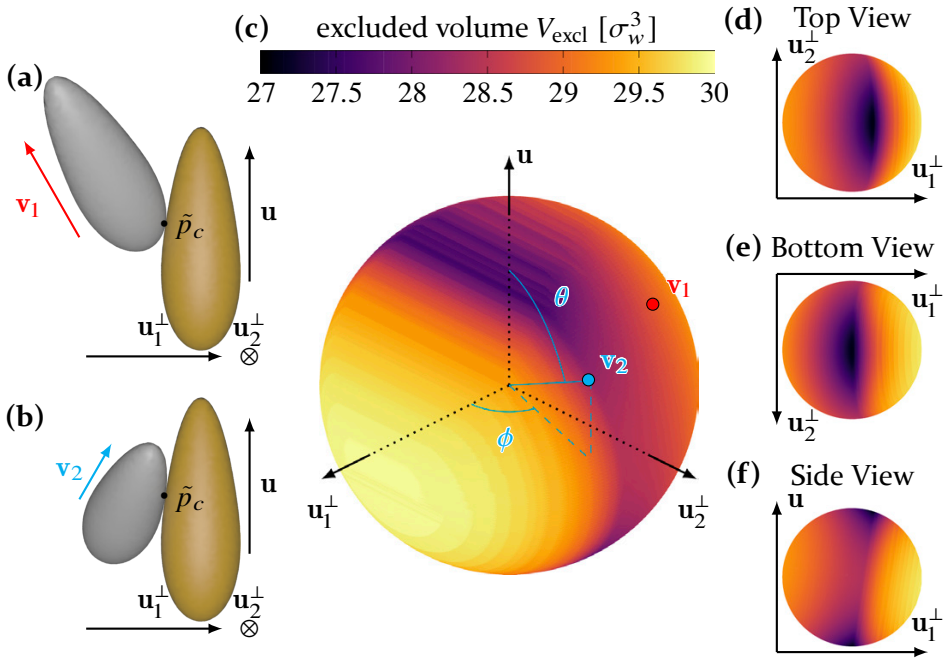

Figure 6.4: The excluded volume of two pear-shaped particles with $k = 3$, $k_\theta = 3.8$ and $r_{\text{depl}} = 0.3 l \sigma_w$ in relation to the relative orientation of the pears on the unit sphere. The contact point p_c is fixed for the reference pear and chosen such that the configuration with the global minimum can be adopted. In the centre (c), the orientation of the free pear $\mathbf{v}$ is given in spherical coordinates dependent on the orientation of the reference pear $\mathbf{u}$ and the direction towards p_c $\mathbf{u}_1^\perp$. On the right, the unit sphere is viewed from the top (d), bottom (e) and side (f) perspective. On the left (a)+(b) two exemplary configurations are shown. The locations of their corresponding orientations $\mathbf{v}_1$ and $\mathbf{v}_2$ on the unit sphere are indicated.

We first show that the three-dimensional excluded volume problem can be narrowed down to its two-dimensional counterpart to sample the configuration space as efficiently as possible. In more mathematical terms, we only consider arrangements of pears where the orientation vectors of the two pears $\mathbf{u}$ and $\mathbf{v}$ and their relative position vector $\mathbf{R}$ are linearly dependent. Only those positions are in line to find the ideal placement of pears. It is somewhat intuitive that, due to the pear's rotational symmetry, the configuration which occupies the least amount of space falls into the category of those linearly dependent arrangements rather than of asymmetric configurations. Moreover, any expansions of the excluded volume in the form of dilatations into the third dimension (like those indicated in Fig. 6.3) can be prevented by restricting the particles to a plane. This guess is confirmed by computing the excluded volume for different relative orientations with a

fixed contact point p_c of one of the pears as plotted in Fig. 6.4c. Here the pear with constant p_c acts as a reference (see Fig. 6.4a+b) such that $\mathbf{v}$ can be written in spherical coordinates with respect to the frame defined by $\mathbf{u}$ and p_c. The azimuthal angle $\phi = 0$ of the spherical coordinate system is defined by the direction from the contact point p_c to the centre of the reference pear. For all the tested values of p_c, the extremal values in V_{excl}, and hence both its global maximum and minimum, are attained by linearly dependent configurations, that is where the polar angle of $\mathbf{v}$ is either $\phi = 0$ or $\phi = \pi$.

To reduce the configuration domain even further, we can utilise another argument about the symmetry of the system. Specifically, the contact, which leads to the maximal or minimal excluded volume, has to be at the same point on both pear surfaces as the choice of the reference pear is arbitrary. Otherwise, the system would have two solutions with the same relative orientations, which is not possible for convex particles. Overall this leaves us with a sampling domain which practically only depends on one degree of freedom, namely on the shared p_c. By adding the constraint of linearly dependent orientations with $\phi = 0/\phi = \pi$ the polar angle, θ is restricted to maximally two possible orientations. The excluded volume calculations for the "roll" and "slide" sampling of the different contact points p_c are plotted in Fig. 6.5.

- **Roll route**: The particles start from an antiparallel configuration, when the pears touch with their blunt ends, pass through a parallel alignment next to each other and eventually end up antiparallel again where their pointy ends meet. This sampling can be interpreted as one pear is rolled over the other.
- **Slide route**: During the "slide" sampling the pears are perfectly antiparallel for all p_c which resembles a slide of one pear along the surface of the other.

Hence, the duality of θ is covered by those two computational pathways. The contact p_c is given by the angle β between $\mathbf{u}$ and the normal vector into the pear at p_c.

Interestingly, the different paths reveal two distinguishable relative positions at the same contact point $p_c = \tilde{p}_c$, which both can be associated with the global minimum of the excluded volume V_{excl}. In one solution the pears are placed side-by-side and oriented perfectly antiparallel towards one another: $\mathbf{u} \cdot \mathbf{v} = -1$ (see Fig. 6.5). The minimum, however, does not occur for

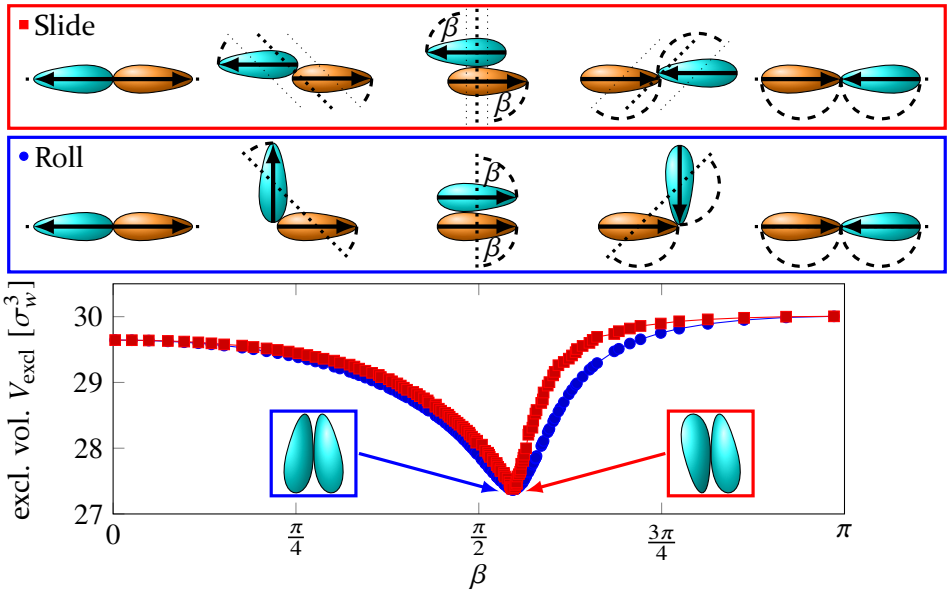

Figure 6.5: The excluded volume of two pear-shaped particles with $k = 3$, $k_\theta = 3.8$ and $r_{\text{depl}} = 0.3 1\sigma_w$ along the "roll" (blue) and "slide" (red) route, where the particles share the same contact point p_c, in terms of the angle β between the orientation of the pears and the normal direction into the pear at p_c. Both sampling pathways are sketched above. The plots show a minimum of the same value which can be identified as the global minimum of the system. The corresponding optimal configurations are highlighted in the small coloured boxes.

$\beta = \frac{\pi}{2}$ when the pears are at the same height. The particles are rather shifted towards their blunt ends by a small distance. The second ideal configuration exists due to the broken inversion symmetry of the pear-shape and is found when the two pears point roughly in the same general direction (see Fig. 6.5). However, here the colloids are not perfectly aligned but slightly tilted towards each other. This tilt also becomes apparent by looking at the excluded volume plot of different orientations at $\tilde{p}_c$ in Fig. 6.4d–f. The top, bottom and especially side view of the unit-sphere clearly show that the minimum at the northern hemisphere is shifted away from the north pole. The tilt can be related directly to the pear-shape. In particular, the angle between the pear-shaped solids is identified as their tapering angle of $\theta_k = 15°$. Hence, θ_k also defines the shift in the antiparallel domain, as both optimal configurations are attained for $\tilde{p}_c$.

Furthermore, the computations show that configurations, where the blunt ends touch ($\beta < \frac{\pi}{2}$ in Fig. 6.5), tend to be often more favourable than arrangements where the pears come together with their pointy ends ($\beta > \frac{\pi}{2}$). Also in Fig. 6.4c a similar observation can be made. If the particle is oriented away from the reference pear and comes in contact with the blunt end, the excluded volume is smaller than if the pear points directly towards $\tilde{p}_c$. This general behaviour indicates that during the rearrangement of inversion asymmetric particles from a separated state due to depletion interactions the colloids are likely to first approach each other with their bigger ends before eventually equilibrating into the most compact formation. This effective blunt end attraction suggests that even the hard HPR pears should have a tendency to cluster with their blunt ends. However, for HPR particles the mechanism seems to be weaker than the tendency in the PHGO model, and not strong enough to lead to equilibrated blunt-end-clustering as we showed in Sec. 5.2.

6.3 Monte Carlo simulations of depletion effects of pear-shaped particles

Having determined the most favourable conformations of pairs of pear-shaped particles in regards to their excluded volume, we compare the computational predictions to results obtained by computer simulations. Our goal, in particular, to replicate the behaviour of pear-shaped colloids due to depletion and, moreover, to study if the pears indeed prefer the states calculated in Sec. 6.2.

One very successful theoretical approach to describe depletion is density functional theory (DFT) which is discussed in more detail in Chap. 7. Roth introduced a so-called "insertion approach" [462, 531] within DFT, where the depletion potential is calculated from the solvent density distribution close to one fixed colloid by insertion of a second colloidal particle and use of the potential distribution theorem [532]. The interactions in a mixture of hard spheres [462], a system of a spherocylinder close to a hard wall [488], and a mixture of aspherical, but inversion symmetric particles [531] have been derived with this ansatz. Also, other theories have been applied to calculate depletion interactions [458, 459, 533] but have shown to be less efficient as every single configuration has to be treated individually. However, all those theoretical approaches only cover a set of particles with simple shapes and have not been applied to pear-shaped particles prior to this thesis. This

difficulty is enhanced even more as we would have to develop a functional of orientational-dependent contact functions like for PHGO particles. We will derive a density functional for hard pear-shaped particles later in Sec. 7.2, such that we might be able to implement a theoretical description of the pear-shaped particle depletion based on DFT in the future.

Alternatively, depletion interactions have been obtained with Monte Carlo simulation techniques. A typical procedure to calculate the depletion forces between various particles is the "acceptance" approach where the free energies between two different configuration states are compared. During these simulations, the positions and orientations of both colloids are fixed, and only the hard sphere solvent is displaced in the process of the Monte Carlo step. Finally, the free energy difference between two states can be related to the acceptance rate to jump from one colloid particle's relative position to the other and vice versa without causing particles to overlap [292, 487, 534, 535]. This procedure has been advanced using Wang-Landau Monte Carlo approaches [536, 537, 538, 539]. Also, a hybrid of simulation and DFT has been suggested [540]. Those approaches are, however, very complicated for the pear shape (in case of the hybrid approach) or very time inefficient, as for every configuration state a separate MC run has to be performed in the acceptance approach. Combining these issues with the already computationally demanding overlap check between two meshes for the HPR particles and hard spheres (see Sec. 2.2.1), the mentioned techniques are all impracticable. However, in general, we are not necessarily interested in the specific free energy-calculations of the different states but merely want to clarify the distinctions between the HPR and PHGO model. Therefore, the question of depletion is tackled by applying Monte-Carlo simulations in the following and more straightforward fashion.

6.3.1 Depletion interactions between HPR particles

Monte Carlo simulations are performed on systems with $N_{\text{pear}} = 2$ hard-core pear-shaped particles within a solvent, which is approximated by a large number $N_{\text{sph}} = 1498$ of surrounding smaller hard spheres, within a cubic box with periodic boundary conditions in all three dimensions. The aspect ratio $k = 3$ and tapering parameter $k_\theta = 3.8$ of the pear-shaped particles are chosen to easily compare the simulation results with the calculations of Fig. 6.4. For the same reason the sphere radii of the solvent r_{depl} is set to $0.31\sigma_w$, which corresponds to the volume ratio between the spheres and

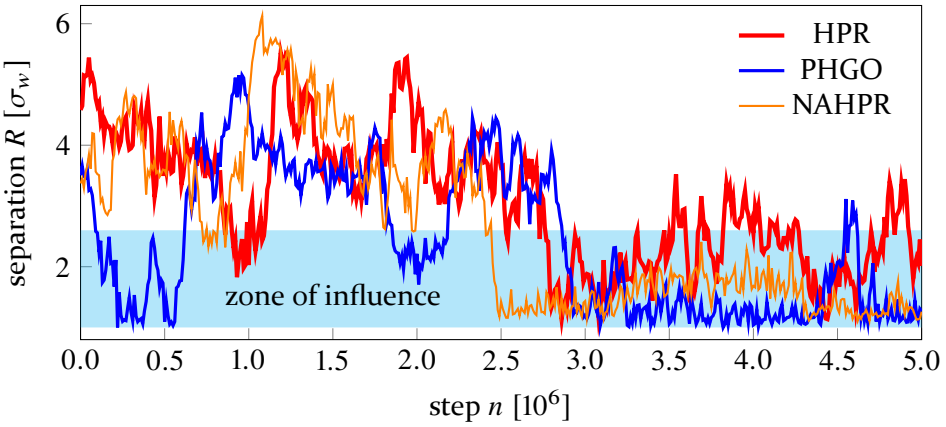

Figure 6.6: Representative progressions of the separation R of two pear-shaped particles (red: HPR, blue: PHGO, orange: NAHPR.) in a sea of 1498 hard spheres, acting as a solvent during the Monte-Carlo simulations. The simulations are performed at a global density of $\rho_g = 0.45$. All models show an effective attraction into the zone of influence induced by depletion effects. The shaded area approximates this zone of influence where the particles can be considered in contact.

pears $v = \frac{V_{\text{depl}}}{V_{\text{pear}}} = 0.08$. An acceptance rate of roughly 50 % has been achieved by setting the maximal translation $\Delta_{q,\max} = 0.085\sigma_w$ and the maximal orientational displacement $\Delta_{u,\max} = 0.085\sigma_w$ per step. The greater number of depletants assures that the simulations are not affected by the boundary conditions and the system can indeed be interpreted as two pear colloids within a sea of a hard sphere solvent. Furthermore, the sphere size is small enough to see depletion interactions between the particles occurring at higher densities. All sets are performed in the NVT-ensemble starting from different diluted initial states at

$$\rho_g = \frac{N_{\text{pear}} \cdot V_{\text{pear}} + N_{\text{sph}} \cdot V_{\text{sph}}}{V_{\text{box}}} = 0.1. \tag{6.3}$$

After a sequence of compressions to the final density $\rho_g = 0.45$ the system is studied for $5.0 \cdot 10^6$ steps.

We first simulate HPR pears in a hard sphere fluid. As we perform MC simulations, we can use the hard sphere-pear interactions based on the sampled Bézier-contour as described in Sec. 2.1. For every simulation run, the entropic depletion attraction between the pear-particles can be noticed when the colloids are in each other's vicinity, which means that their excluded

volumes overlap. More precisely, the particles stay together for a considerable number of MC steps (see Fig. 6.6), which leads to the conclusion that the system indeed favours the particles coming in contact. However, the entropic attraction seems to be short range and rather weak. This can be seen in Fig. 6.6, where the particles often separate again from a nearby configuration after some MC steps before they typically approach their zone of influence again. Here, we have to mention once more that this "approach" is not dynamic. Nevertheless, the preferred sampling of close pear arrangements is a strong indication for depletion interactions.

Even though the particles are affected by the presence of the second colloid, the determination of the relative arrangements of the colloid pair faces some difficulties. The main issue which has to be overcome is poor statistics. As we are studying a two-particle problem, it is hardly feasible to gather enough data for a detailed combined analysis of the possible states due to computational time constraints. Therefore, we decouple the degrees of freedom and only investigate one relative parameter at a time. In Fig. 6.7a the relative polar angle between two close HPR particles is plotted. For these plots, only configurations are considered if the excluded volumes overlap. This ensures that the sampled relative orientations are actually influenced by the close distance between the particles. The relative angle α between the orientation vectors of the pears $\mathbf{u}$ and $\mathbf{v}$ is split into two domains to characterise the orientational states further. For positive angles, the pears point away from each other such that their blunt ends are in contact. A negative angle indicates that the pears face towards one another and that their pointy ends are closer together. In the following we will refer to these two domains "V"-configurations ($\alpha > 0$) and "A"-configuration ($\alpha < 0$).

The histogram of the relative pear orientations shows three distinct peaks which match perfectly with the ideal configurations predicted in Fig. 6.4c and Fig. 6.5. The first preferred orientation is measured at $\alpha = -0.26 = -15°$, and hence categorised as an A-configuration. This relative angle corresponds directly to the parallel solution for minimal excluded volume as it coincides with the tapering angle $\theta_k = 15°$. The configuration can also be extracted from the simulations directly (see a snapshot in Fig. 6.7c). The second and third peak at $\alpha = \pm\pi = \pm 180°$ can be combined into a single characteristic orientation due to the duality of the A- and V-configuration for $\cos(\alpha) = -1$. Moreover, this orientation also coincides with the predictions as it fits the second solution of the excluded volume calculations, where the particles are

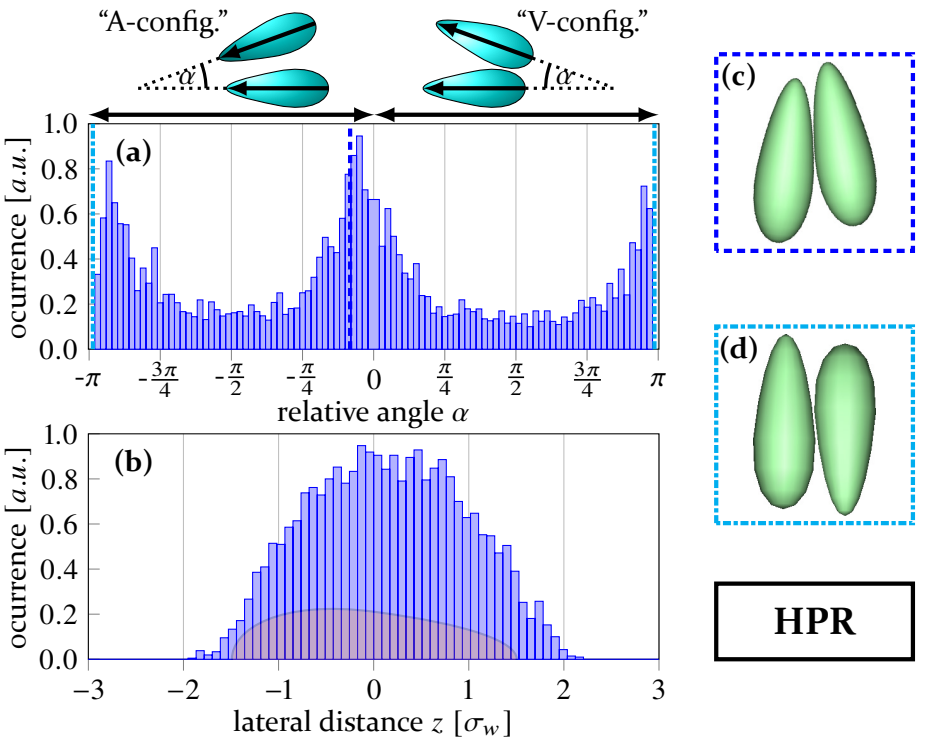

Figure 6.7: The relative orientation (a) and lateral distance distribution (b) of two HPR particles in a sea of 1498 hard spheres, acting as a solvent at global density $\rho_g = 0.45$, on the left. The particle parameters are set to $k = 3$, $k_\theta = 3.8$ and $r_{\text{depl}} = 0.31\sigma_w$ ($\frac{V_{\text{depl}}}{V_{\text{pear}}} = 0.08$). Only pair-configurations are considered if the pear-shaped particles are close to each other such that the excluded volumes overlap. Positive angles α indicate V-configurations (blunt ends together), whereas negative α values describe A-configurations (pointy ends together). On the right, two typical arrangements, extracted from the simulations, are shown. The top snapshot (dashed line, (c)) corresponds to the indicated peak and coincides with the parallel solution for maximal excluded volume overlap. The bottom configuration (dash-dotted line, (d)) contributes to the second peak and matches the anti-parallel solution in terms of minimised excluded volume.

aligned anti-parallelly next to each other. A snapshot from the MC simulation of this particular configuration is depicted in Fig. 6.7d.

The observations are corroborated by the lateral distance distribution between two particles when in contact. Fig. 6.7b highlights that the neighbouring pears are not distributed around the centre point of the reference particles. The distribution is rather slightly shifted towards the pointy end. The inversion asymmetric shape of the HPR particle consequently introduces a

move of the optimal contact point above the centre-point. Hence, the HPR particles behave precisely as expected according to Sec. 6.2 and according to the solutions of the ideal configurations to maximise the available space for the hard spheres.

6.3.2 Depletion interactions between PHGO particles

We established that the HPR particle model describes the imposed pear-shape very well in terms of depletion and reproduces the analytical predictions. Therefore, it acts perfectly as a reference for other models which describe pear-shaped particles like the PHGO model. This gives us an excellent opportunity to study the ramifications to describe a pear using a hard Gaussian overlap approach. Thus, the depletion MC simulations are repeated. The same parameters are applied except that the HPR contact function is replaced with the PHGO contact function to approximate the particle overlap.

The first distinction between the PHGO and HPR system becomes apparent during the MC sampling already. By tracking the distances between both particles for every MC step in Fig. 6.6 the depletion attraction between two PHGO pears seems to be stronger than in the equivalent HPR case. This can be explained by the development of the separation once the two PHGO pears are close together. After the pears pass a sequence of arbitrary displacements and eventually approach each other, the touching configuration stays stable for a significantly longer time. This is in contrast to the split-ups of the HPR particles where very short periods of configurations close together alternate with stages of separation and subsequent recombination. This means the depletion attraction is of the order of $k_B T$ or less for HPR and considerably more for PHGO particles. The increased strength of the entropic force, however, can be related to the contact function of the PHGO pear. Presuming the particles are in the optimal state, an attempted translational step and especially an attempted rotational step is much more strongly penalised for PHGO than for HPR particles. This is manifested in the contact profile of roughly perpendicular arrangements. Here, the pear size is overestimated, and a particle pair is accounted as overlapping even though they are not in contact according to the Bézier-curve depiction (see Fig. 2.8 for a comparison of the contact profiles between PHGO and HPR model). The effect is comparable to the PHGO pears and HGO ellipsoids entering

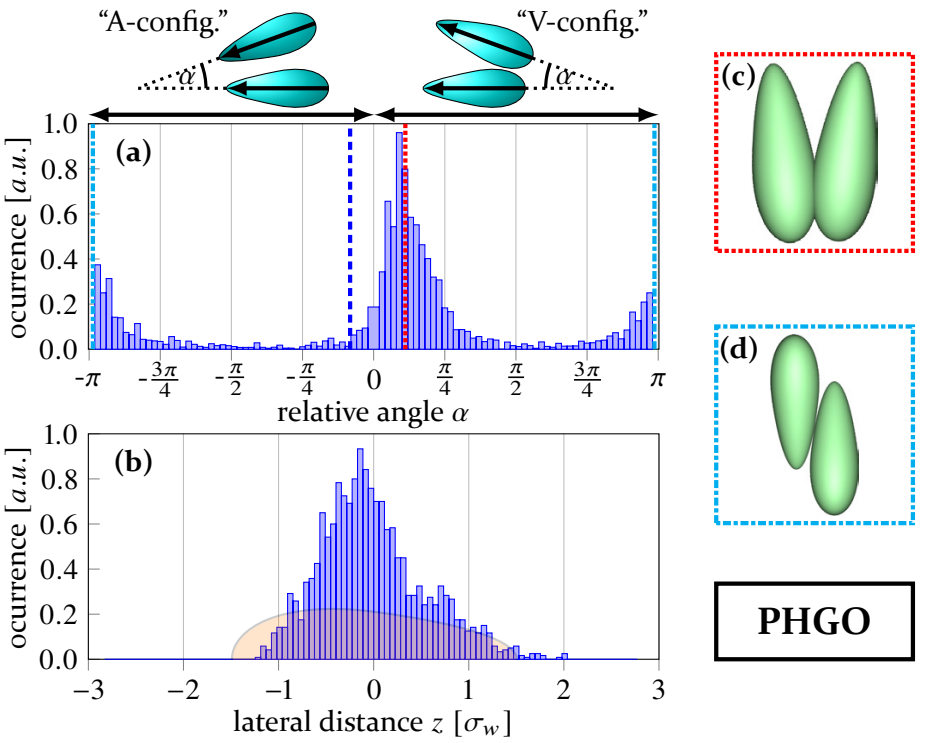

Figure 6.8: The relative orientation (a) and lateral distance distribution (b) of two PHGO particles in a sea of 1498 hard spheres, acting as a solvent at global density $\rho_g = 0.45$, on the left. The particle parameters are set to $k = 3$, $k_\theta = 3.8$ and $r_{\text{depl}} = 0.31\sigma_w$ ($\frac{V_{\text{depl}}}{V_{\text{pear}}} = 0.08$). Only pair-configurations are considered if the pear-shaped particles are close to each other and the excluded volumes overlap. Positive angles α indicate V-configurations (blunt ends together). Negative α values describe A-configurations (pointy ends together). This is also indicated above the plot. On the right two typical arrangements, extracted from the simulations, are shown. The top snapshot (dotted line, (c)) shows a V-configuration, which corresponds to the indicated peak. This configuration does not coincide with the parallel solution for maximal excluded volume overlap of Bézier pears. The bottom configuration (dash-dotted line, (d)) contributes to the second peak and matches the anti-parallel solution in terms of minimised excluded volume.[1]

orientationally ordered phases already for low densities [396]. The depth of the effective potential does not necessarily indicate that the two models

[1]Note here a slight difference to the data in the version of this thesis originally submitted for examination. In the original version, a small error (a missing prefactor) occurred in the PHGO overlap determination. This increased the observed depletion effects. However, the main conclusion from this data has not changed. What has changed is the relative height of the peaks. In particular, the probability of finding pears in the V-arrangement is, after the correction, higher than that of finding two pears positioned in anti-parallel orientation. Apart from this, the central message of this chapter has not changed.

differ qualitatively, but suggests that the depletion is more guided towards the equilibrium states.

The relative orientation distribution between two PHGO particles in close contact is plotted in Fig. 6.8a. Two distinct peaks are perceivable similar to the equivalent HPR system. The smaller peak is found at $\alpha = \pm\pi$ which again corresponds to an antiparallel configuration. Therefore, the orientation distribution suggests that the PHGO pear model reproduces the antiparallel solution sufficiently. In this domain, the HPR and PHGO differ the least from each other, such that it is quite intuitive that in the antiparallel case both models share the same solution. Additionally, we can find many configurations as depicted in Fig. 6.8d, which contribute to this smaller peak at $\alpha = \pm\pi$ and coincide with the ideal solution to a sufficient degree. By focusing on the second major peak, however, we observe two major differences compared to the HPR system. Firstly the peak is significantly more intense. This indicates that for PHGO particles the parallel configuration is more beneficial than the antiparallel solution. This is explained by the PHGO particles coming closer together than HPR particles when parallelly aligned. By changing the relative angle between the pear-shaped particles, the overlap tends to be underestimated by the PHGO model which consequently leads to a lower excluded volume. Thus, the duality of the ideal configuration is broken by the particular angle dependence of the PHGO contact function and weighted to the benefit of parallel arrangements.

The second difference is the position of the peak, which is shifted from $\alpha = -15°$ to a positive value close to $\alpha = 20°$. Hence, the particles form V-configurations rather than the expected A-configurations. To clarify the reason behind this transition we take a closer look at those V-configurations which can be obtained from the simulations directly. A representative pair is portrayed in Fig. 6.8c. It becomes apparent that the pears slightly overlap. Here, the term "overlap" might be misleading as the particles do not technically overlap in terms of their PHGO contact function but according to the best possible illustration using the Bézier representation. However, it also has to be mentioned that the spheres interact with the pear according to this Bézier shape. Thus, the solvent particles effectively experience the pear shape differently than another PHGO particle. Furthermore, the underlying underestimation of the PHGO-contact function enables the pear-shaped particles to occupy space, which by design cannot be reached by hard spheres and would also be prohibited for HPR particles. This effect is

known as pairwise non-additivity and is well studied for hard binary sphere mixtures [274, 275, 276, 277, 278], which successfully model the behaviour of binary alloys [541, 542] or organic mixtures [543, 544]. It is known that non-additivity leads to repelling and attracting effects [276, 545], which open the door for exotic crystalline phases [544, 546] and also shift the critical demixing density to lower values [547, 548]. Already Asakura and Oosawa studied a non-additive system to describe the depletion interactions where the large colloids "see" the polymers as hard spheres with finite radius whereas the polymers act as point particles among themselves [451].

The V-configurations can also be associated to the second type of non-additivity effects which are present between two PHGO pears, namely the self-non-additive features discussed in Sec. 2.2.1. Here the excluded volume is decreased instead of simple alignment by an alternative route, namely by increasing the overlap of the two particles due to self-non-additivity. For pears with $k = 3$ and $k_\theta = 3.8$ the maximal overlap occurs roughly at an angle of $\alpha_{\text{overlap}} \approx 30°$. This is considerably higher than the measured angle between the pears in the V-configuration observed in the simulations. However, we can argue that the adopted angle results from the intricate interplay of reducing excluded volume via overlap and alignment and the sphere radius of the solvent. For small volume ratios the overlap is more dominant and the V-arrangement more favourable, whereas for large ratios the contribution of the overlap becomes negligible and the aligned A-configuration will be adopted.

To complete the comparison between the HPR and PHGO particles, we investigate the lateral distance of the PHGO pears to its fellow pear in close contact in Fig. 6.8b. Compared to Fig. 6.7b the distribution is narrower and shifted towards the blunt end which leads the impression that the HPR particles are more flexible to obtain the equilibrium state whereas the PHGO pears are more restricted in terms of fluctuations from the ideal configuration. The emergence of the shifted peaks can again be attributed to the non-additive characteristics of the PHGO model. Furthermore, the two maxima at lateral distance $z = -0.17$ and $z = 0.70$ indicate the existence of two different contact points. One is associated with the V position ($z < 0$), the other peak can be identified as the contact for the antiparallel solution $z > 0$.

6.4 Conclusion and outlook

In this chapter, we studied depletion effects on pear-shaped particles due to a solvent of hard spheres as preparation for Chap. 8 where the range of mixture is expanded. To this end, we investigated the depletion interactions of a pair of pear-shaped particles in a sea of a hard sphere solvent. In the course of this study, we first determined the optimal pear configurations in terms of minimised total excluded volume based on the Bézier curves to predict the equilibrated particle formation. Using numerical calculation techniques, we could compute two global minima; a parallel and antiparallel solution, which both share the same contact point on the pear surface. Both configurations could be related directly to the taper of the particle. Afterwards, the predicted states could be obtained in Monte Carlo simulations of two HPR pear particles dissolved in a hard sphere solvent. However, depletion attraction is weak for the chosen parameters.

In comparison, the PHGO pear particles revealed differences to the predictions. Even though the antiparallel configuration was also reproduced for PHGO pears, the parallel solution was found to be more dominant and shifted from an A- to a V-configuration with a different contact point. We argued that the V-configuration is governed by the PHGO contact function which underestimates the pear overlap slightly and causes overlaps. Moreover, it has been shown that the depletion attraction between two PHGO particles is much stronger than between HPR particles.

The discrepancies in the depletion behaviour also give improved insight into the diminished and aided spontaneous creation of bilayer-phases in monodisperse HPR and PHGO particle systems, respectively. It is more than likely that specific details of the relative positions between neighbouring pear-shaped particles are varied due to the enhanced complexity of the excluded volume effects in one-component assemblies. Nevertheless, we can reason that the quality of the arrangements would not change and hence, general statements about the local formations can be made. Especially three contributions to the stabilisation mechanisms of bilayer configurations are identified.

1. By breaking the duality of the optimal configurations the systems introduce a local polar order. In the PHGO model, this leads to a dominant formation of parallel alignments between adjacent pears. This exact orientational order is also observed in the pair-correlation functions

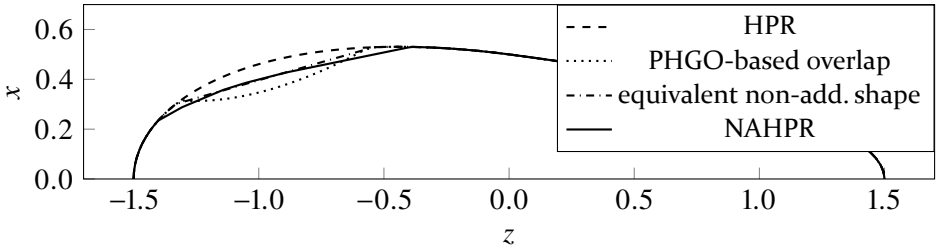

Figure 6.9: The procedure to obtain the second mesh in the NAHPR model which determined the overlap between the blunt ends of two pears with $k = 3$ and $k_\theta = 3.8$. First, two pears are placed symmetrically at an angle $\alpha = 30°$ such that the pears are exactly in contact according to the PHGO contact function. The distance is decreased by $-0.035\sigma_w$ also to compensate the contact overestimation for A-configurations. Afterwards, the overlap is cut from the initial contour (dashed) such that a concavity occurs (dotted line). The equivalent non-additive contour is obtained from its convex hull (dash-dotted). This procedure is repeated for different angles between $\alpha = 30° \pm 15°$. The final contour (solid line) is the basis of the solid of revolution from which the mesh is generated.

weighted with the polar order parameter of the one-component PHGO-particle systems (see Fig. 5.13 in Sec. 5.2). Hence, the system is guided towards the formation of sheets, which are a prerequisite of interdigitated bilayers.

2. The interdigitation is enhanced by the preferred parallel order into V- rather than A-configurations. It is quite intuitive to imagine that sheets, which consist of an array of V-aligned pears, interlock analogous to a zip mechanism in a "zig-zag"-pattern and subsequently develop bilayers.

3. The greater fluctuations of the contact point in HPR systems hinder a targeted alignment of particles. This consequently leads to an increased susceptibility for defects within the bilayers, and a weaker correlation of translational order as those observed in typical smectics let alone gyroid or lamellar phases.

These three factors raise the question of how pear-shaped particles adopting bilayer phases can be realised in experiments. Assuming that colloids interacting via the HPR potential will be more likely to be synthesised in the future[2], the question can be rephrased as such. How does the HPR

[2]This assumption is merely based on the fact that the HPR contact profile resembles the Bézier shaped more closely than the PHGO model. However, if this premise is indeed true cannot be answered to date as modern-day synthesis techniques do not yet offer the amount of detail that is needed.

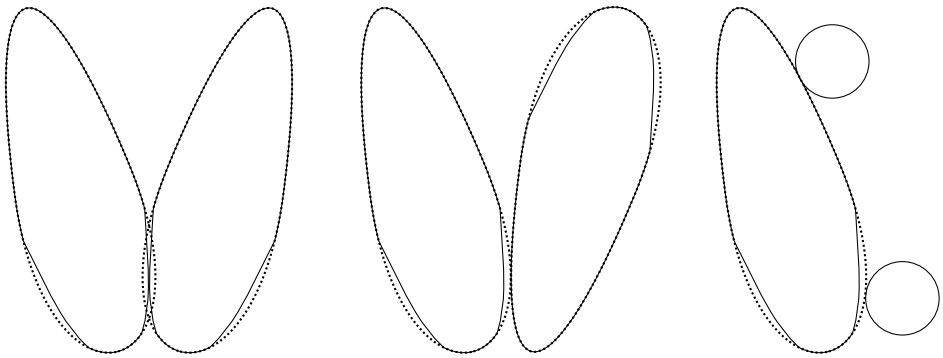

Figure 6.10: The concept of the overlap determination for the NAHPR model. The pear consists of an inner contour (solid line, non-additive part) and an outer contour (dotted line, similar to the HPR model). If the pears coms together with their blunt ends (left) the particles are considered in contact if their inner contours touch. Otherwise (centre) the outer contours determine the overlap. The interactions with hard spheres are also according to the outer contour (right).

contact profile have to be modified to obtain the key characteristics of the PHGO contact function? In the following, we want to propose a promising approach as an outlook and introduce non-additive features to the mesh-description of pears as well.

The non-additive features are added to the blunt ends of the pear particles. Using this approach we specifically try to engineer an HPR potential which favours the formation of V-configurations due to depletion interactions. The mesh which describes the interaction between two blunt ends is based on the distance of two PHGO particles with the largest overlap. As already mentioned this occurs for $\alpha_{\text{overlap}} = 30°$. However, the distance is decreased even a bit further by $-0.035\sigma_w$ to additionally compensate for the contact overestimation for A-configurations which otherwise would not be considered. The contour of the non-additive shape is created by introducing a flat line between the two points where both Bézier curves meet (see Fig. 6.9). Taking this new contour as a basis, we repeat the procedure for different angles $\alpha = 30° \pm 10°$ to allow some flexibility of the adopted orientations. Afterwards, a triangulated mesh of the solid of revolution of the resulting contour is generated. The mesh is implemented into the MC algorithm such that only the blunt ends of the pears are allowed to overlap according to the Bézier shape. To put it differently, the particles interact via the non-additive mesh exclusively if the particles come together with their blunt ends. Otherwise, the overlap is determined by the regular mesh

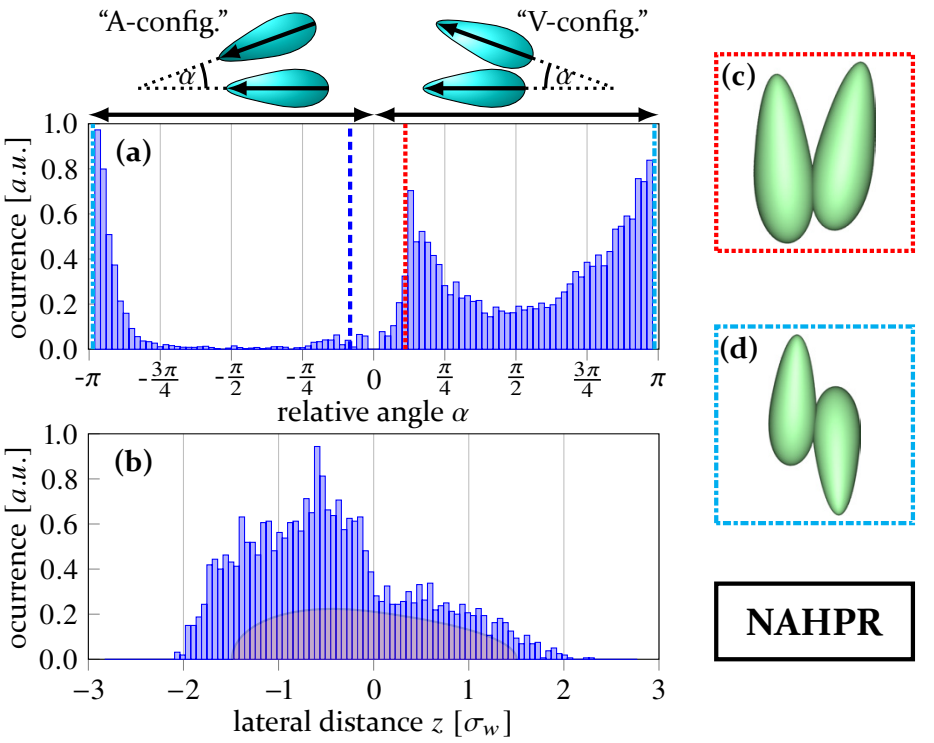

Figure 6.11: The relative orientation (a) and lateral distance distribution (b) of two non-additive HPR particles in a sea of 1498 hard spheres, acting as a solvent at global density ρ_g = 0.45, on the left. The particle parameter are set to $k = 3$, $k_\theta = 3.8$ and $r_{\text{depl}} = 0.31\sigma_w$ ($\frac{V_{\text{depl}}}{V_{\text{pear}}} = 0.08$). Only pair-configurations are considered if the pear-shaped particles are close to each other and the excluded volumes overlap. Positive angles α indicate V-configurations (blunt ends together). Negative α values describe A-configurations (pointy ends together). This is also indicated above the plot. On the right two typical arrangements, extracted from the simulations, are shown. The top snapshot (dotted line, (c)) corresponds to the indicated peak and shows the engineered V-configuration. The bottom configuration (dash-dotted line, (d)) is a defect of the non-additive mesh and contributes next to the anti-parallel solution also to the second indicated peak.

describing the pear surface (see Fig. 6.10). Furthermore, the pear-sphere interactions stay unmodified such that the hard solvent still experiences the HPR pear. We will refer to this model as the non-additive hard pears of revolution (NAHPR) model. In experiments, the underlying contact function might be realised by preparing pear colloids with a rougher surface at the pointy than at the blunt ends. By using different roughness, the strength between different parts of a colloid can be controlled, and therefore an

effective entropic attraction between specific moieties of the colloid can be introduced [240, 549].

After implementing the non-additive contact function, the depletion MC simulations are again repeated with the same parameters. Both Fig. 6.6 and Fig. 6.11 reveal that some of the features of the PHGO model have been adopted by the NAHPR model. By investigating the separation during the MC simulation in Fig. 6.6 it becomes apparent that the depletion interaction increases. Even though the PHGO particles show slightly weaker attraction, the NAHPR particles remain in the zone of influence similarly as soon as they are within their vicinities. More interesting, however, is the orientation distribution for NAHPR particles in contact (see Fig. 6.11a). The non-additivity at the blunt ends indeed stabilises the desired V-configurations creating a dominant peak at around $\alpha = 20°$. Nevertheless, by taking a close look, a small peak at the A-configurations can be observed as well. This leads to the conclusion that two minima for the excluded volume can be obtained within the parallel configurations. The global one is attributed to the V-configuration and the non-additivity, the second minor one can be ascribed to the A-position and the parallel alignment of the pears according to their tapering parameter.

The NAHPR model can also reproduce the lateral distance distribution of the PHGO particle roughly. Even though the distribution in Fig. 6.11b is broader than the one in Fig. 6.8b, most of the contact points are located underneath the centre point of the pear-shaped particle as well. However, the NAHPR model still does not recreate all feature of the PHGO-particles perfectly. For instance, some of the simulations end up in configurations which contribute to the preferred antiparallel alignment but do not coincide with the prediction. Although the prediction is still the dominant configuration, the non-additivity allows the particles also to overlap with the blunt ends in an antiparallel configuration (S-configuration, see Fig. 6.11d) and also introduces in the antiparallel case a secondary minimum.

To put it in a nutshell, the NAHPR particles can recreate some of the features of the PHGO contact function, like the formation of V-configurations, the enhanced depletion attraction or the shift of the contact point towards the blunt ends. Some other features like the symmetry breaking into heavily favoured parallel configuration could not be resolved by the modified model yet. However, the introduction of non-additivity between blunt ends seems

to be a pivotal factor to enable bilayer formation. The present issues might be resolved by further alternations of the NAHPR interactions. One solution might be to add additional angle dependence to the non-additivity, such that blunt ends are only able to overlap if the particles are pointing roughly in the same direction. This would probably diminish the formation of S-configurations. Another approach might be to replace the rounded pear surface with a partially flat surface. This would allow us to control not only the non-additivity attraction but also the depletion attraction via alignment by introducing more or less curvature to the surfaces.

7 Density functional theory of pear-shaped particles

> *"Someone told me that each equation I included in the book would halve the sales."*
>
> – Stephen Hawking

This chapter addresses the differences of the two pear-shape particle models (PHGO and HPR) on the basis of a theory that calculates approximations for the free energy values of the assembled configurations. To this end, we develop a density functional for hard solids of revolution with smooth features (including particles without inversion-symmetric shapes) within the framework of fundamental measure theory. Moreover, this theory is applied to a system of pear-shaped particles described by Bézier-curves and the structure of the isotropic phase of such particles near a hard wall is investigated. This application to the pear-shaped particles can be seen as a preliminary study for possibly higher density phases like the nematic or even the gyroid phase. Here, we can predict a complex orientational ordering within the vicinity of the hard wall which is governed by the particle shape directly. We can identify a good agreement between the theory and our simulations by comparing both approaches, even though the HPR pears showcase better agreement than the PHGO-particles, which implies that the density functional cannot be applied to the PHGO gyroid phase directly. Furthermore, both theory and MC simulations suggest the possibility of the formation of layers, which consist of particles with alternating orientations, due to the lack of particle inversion-symmetry.[1]

[1]This chapter is based, in parts, on the article P.W.A. Schönhöfer, G.E. Schröder-Turk, and M. Marechal, "Density functional theory for hard uniaxial particles: Complex ordering of pear-shaped and spheroidal particles near a substrate", *J. Chem. Phys.* **148**(12):124104, 2018. All simulation methods, numerical procedures and data analyses of this paper were implemented and executed by me. Alongside the senior authors, I was a major contributor to the conceptual questions and research methods addressed in the article, and to the interpretations presented as results. I created all 4 illustrations and graphs in the article, and have written the manuscript, with help and comments from Gerd Schröder-Turk and Matthieu Marechal. Verbatim quotes from that paper may have been used without explicit citations.

So far, this thesis has relied upon MD and MC simulation methods to study colloidal particle assemblies, their capability to form cubic phases and the sensitivity of the phase space in terms of the particle shape. This is reflected by the precedent chapters where our investigations are exclusively assisted by particle simulation methods which generate the particle configurations and act as the backbone for all of our results. An alternative strategy to study the collective interactions between particles in statistical physics, however, is based on theoretical techniques, like density functional theory. The importance of those theories is substantiated not only in better understanding the fundamental principles of self-assembly but also in paving the way for experimental implementations of particle systems. Hereof, both theoretical descriptions and simulations are essential, inexpensive and time efficient early steps to, for example in colloidal physics, test the fitness of new particle shapes to form complicated mesophases and eventually to develop their synthesis. Therefore, the advance of theories is of great interest and is addressed in terms of pear-shaped particles and other solids of revolution in the following chapter.

Density functional theories (DFT) [405] are one of the few microscopic theories that underpin the collective behaviour of particle ensembles in classical statistical mechanics. Classical DFT is based on the similar description of quantum systems by Kohn [550] who demonstrated that all the information of the ground state of an electron system can be derived from an energy functional which is written in terms of the electron density distribution rather than solving the N-particle Schrödinger equation. After it was shown that the same principles also can be applied to electron systems at temperature $T > 0$ [551], DFT has been successfully adopted to ensembles in classical statistical mechanics [405]. Since then DFT has become one of the most commonly used frameworks for describing inhomogeneous classical fluids. Often this theoretical description comes with the benefit of being less time-consuming then state-of-the-art simulation techniques. In addition, free energy-based quantities, such as interfacial tensions [212, 552], can easily be extracted from DFT. However, the construction of functionals and the underlying weighted densities to describe collective phenomena of different liquids is often very complicated and not a straightforward procedure (for a detailed survey of the different proposed weighted densities see Ref. [553]).

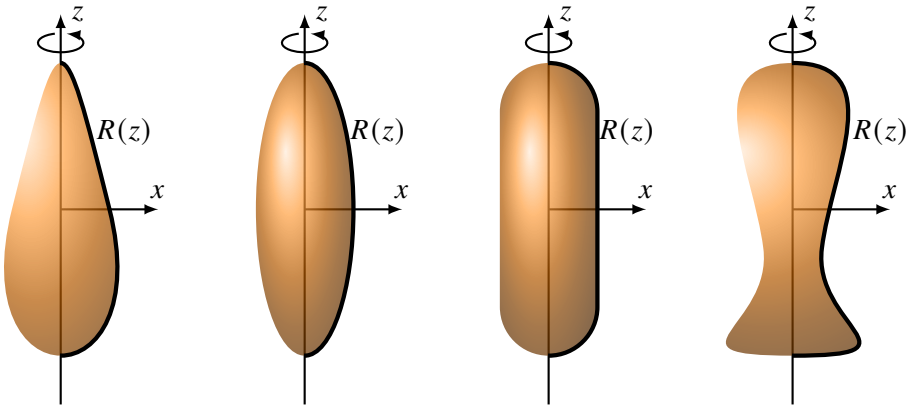

Figure 7.1: Several examples of solids of revolution (from left to right: pear-shaped particle, ellipsoid, spherocylinder, "world-cup trophy"). The radial component of these shapes $R(z)$ are described by a function of the height z and are rotated around the rotation axis to form the bounding particle surface.

A geometry-based approach, namely fundamental measure theory (FMT), was introduced by Rosenfeld for hard spheres [406], modified [554, 555] and later generalized by Hansen-Goos and Mecke for arbitrary convex shapes [210]. Here the functionals are obtained from the fundamental geometrical properties of the individual particles. Previous studies showed that this tool predicts the collective behaviour of several hard particle systems like hard spheres [406, 554, 555], dumbbells [211], spherocylinders [556, 557], polyhedra [212] or even mixtures of the mentioned shapes [558] successfully. In those cases, only a single shape or family of shapes have been considered. An implementation of FMT for general uniaxial shapes, like pear-shaped particles, however, was hitherto not available. Therefore, in the following we first introduce the main ideas of DFT (Sec. 7.1.1) and FMT (Sec. 7.1.2). Afterwards in Sec. 7.2 we develop a new density functional for smooth uniaxial particles in the framework of FMT, where we describe the surface of the particle by a solid of revolution of a Bézier spline (see Fig. 7.1) and thus obtain an implementation for a wide range of uniaxial particles. Finally, we apply this functional to one-component pear-shaped particle and ellipsoid systems and investigate the influence of tapering on the ordering near a hard wall to compare our approach with simulations in Sec. 7.3. In this process, we additionally investigate the differences between PHGO and HPR approach further and discuss the possibility of stabilising the gyroid phase also for hard particle systems due to local orientational correlations.

7.1 Theoretical framework

7.1.1 Density functional theory

This section introduces the density functional theory framework following Evans [405, 553] and Roth [559]. Here we have to revisit the description of the grand canonical potential Ω in Sec. 3.1.2 which describes a particle system in the μVT-ensemble completely. Using Eq. (3.16) and Eq. (3.18) we can write Ω in terms of the equilibrium probability distribution $f_{\mu VT}$ by

$$\Omega(T, V, \mu) = \mathrm{Tr}_{\mathrm{cl}}\, f_{\mu VT}\,(\mathcal{H}_N - \mu N + \beta^{-1} \ln f_{\mu VT}) \tag{7.1}$$

where we again used the classical trace $\mathrm{Tr}_{\mathrm{cl}}$ like already stated in Eq. (3.17). Based on this definition of Ω we can now define a functional

$$\Omega[f] = \mathrm{Tr}_{\mathrm{cl}}\, f(\mathcal{H}_N - \mu N + \beta^{-1} \ln f) \tag{7.2}$$

of any probability density f with $\mathrm{Tr}_{\mathrm{cl}}\, f = 1$ for which holds

$$\Omega[f] = \mathrm{Tr}_{\mathrm{cl}}\, f(\mathcal{H}_N - \mu N + \beta^{-1} \ln f) = \Omega[f_{\mu VT}] + \beta^{-1}\, \mathrm{Tr}_{\mathrm{cl}}\, f(\ln f - \ln f_{\mu VT}). \tag{7.3}$$

Therefore, it can be shown by using Gibbs inequality that for $f \neq f_{\mu VT}$

$$\Omega[f] > \Omega[f_{\mu VT}] \equiv \Omega(T, V, \mu). \tag{7.4}$$

This means that for $f = f_{\mu VT}$ the functional coincides with the grand potential of the equilibrated system. For every other arbitrarily chosen f the functional is always greater than the grand potential.

The equilibrium probability density $f_{\mu VT}$ itself is a functional of the particle number density $\rho(\mathbf{r}, \omega)$, which indicates the local density of the particles with orientation ω at position $\mathbf{r}$. More precisely it can be proven that the external potential term $\mathcal{V}_{\mathrm{ext}}$ of the Hamiltonian $\mathcal{H}_N$ determines the equilibrium number density profile $\rho_{\mu VT}(\mathbf{r}, \omega)$ uniquely [405, 560] such that

$$f_{\mu VT} = f_{\mu VT}[\mathcal{V}_{\mathrm{ext}}] = f_{\mu VT}[\rho_{\mu VT}(\mathbf{r}, \omega)]. \tag{7.5}$$

Consequently, we can also rewrite Eq. (7.2) as $\Omega[\rho(\mathbf{r}, \omega)]$ with

$$\Omega[\rho(\mathbf{r}, \omega) \neq \rho_{\mu VT}(\mathbf{r}, \omega)] > \Omega[\rho_{\mu VT}(\mathbf{r}, \omega)] \equiv \Omega(T, V, \mu). \tag{7.6}$$

An alternative definition of $\Omega[\rho]$ is based on density fields ρ which not necessarily have to be attributed to an external potential [561]. In this Levy method the grand canonical potential functional is defined by

$$\Omega[\rho] = \min_{f \to \rho} \Omega[f] \tag{7.7}$$

where all possible normalised density distributions f are scanned to find the one which minimises the functional and simultaneously keeps

$$\rho(\mathbf{r}, \omega) = \mathrm{Tr}_{\mathrm{cl}}\, f \sum_{i}^{N} \delta(\mathbf{r} - \mathbf{r}_I, \omega - \omega_i) \tag{7.8}$$

fixed. However, Eq. (7.6) holds also for this definition. In general the results from both approaches can be summarized by

$$\left.\frac{\partial \Omega[\rho(\mathbf{r}, \omega)]}{\partial \rho(\mathbf{r}, \omega)}\right|_{\rho(\mathbf{r},\omega)=\rho_{\mu VT}(\mathbf{r},\omega)} = 0 \tag{7.9}$$

where we used the variational principle.

By inserting the general definition of $\mathcal{H}_N$ we can split the functional into different terms

$$\begin{aligned}
\Omega[\rho(\mathbf{r}, \omega)] &= \mathrm{Tr}_{\mathrm{cl}}\, f(\mathcal{T} + \mathcal{U} + \beta^{-1} \ln f) + \mathrm{Tr}_{\mathrm{cl}}\, f(\mathcal{V}_{\mathrm{ext}} - \mu N) = \mathcal{F}_{\mathrm{int}} + \mathcal{F}_{\mathrm{ext}} \\
&= \mathcal{F}_{\mathrm{id}} + \mathcal{F}_{\mathrm{exc}} + \mathrm{Tr}_{\mathrm{cl}}\, f \int \left(\sum_{k=1}^{N} \delta(\mathbf{r} - \mathbf{r}_k, \omega - \omega_k)(\mathcal{V}_{\mathrm{ext}}(\mathbf{r}_k, \omega_k) - \mu) \right) \mathrm{d}\mathbf{r}\, \mathrm{d}\omega \\
&= \mathcal{F}_{\mathrm{id}} + \mathcal{F}_{\mathrm{exc}} + \int \rho(\mathbf{r}, \omega)(\mathcal{V}_{\mathrm{ext}}(\mathbf{r}, \omega) - \mu) \mathrm{d}\mathbf{r}\, \mathrm{d}\omega
\end{aligned} \tag{7.10}$$

with respect to the density profile. The third term in the grand canonical potential is the external term $\mathcal{F}_{\mathrm{ext}}$, where $V_s^{\mathrm{ext}}(\mathbf{r}, \omega)$ is the external potential acting on a particle with orientation ω at position $\mathbf{r}$. The term $\mathcal{F}_{\mathrm{id}}$ can be identified as the free energy of a non-interacting ideal gas [405],

$$\mathcal{F}_{\mathrm{id}} = k_B T \int \mathrm{d}\omega \int \mathrm{d}\mathbf{r}\, \rho(\mathbf{r}, \omega)(\ln[\rho(\mathbf{r}, \omega)\lambda^3] - 1) \tag{7.11}$$

with the Boltzmann constant k_B and the thermal de Broglie wavelength

$$\lambda = \sqrt{\frac{h^2\beta}{2\pi m}} \tag{7.12}$$

of particles with mass m. The excess free energy term $\mathcal{F}_{\text{exc}}$ contains all information about the interparticle interactions and will be covered in great detail in the next sections (see Sec. 7.1.2 and Sec. 7.2). Both theses terms are part of the internal term

$$\mathcal{F}_{\text{int}} = \mathcal{F}_{\text{id}} + \mathcal{F}_{\text{exc}} \tag{7.13}$$

of the functional.

To eventually obtain the thermodynamical properties of the system in terms of the grand potential we have to determine $\rho_{\mu VT}(\mathbf{r}, \omega)$ by inserting Eq. (7.10) into Eq. (7.9)

$$\frac{\partial\Omega[\rho_{\mu VT}(\mathbf{r}, \omega)]}{\partial\rho(\mathbf{r}, \omega)} = 0 = \beta^{-1}\ln\lambda^3\rho_{\mu VT}(\mathbf{r}, \omega) + \frac{\partial\mathcal{F}_{\text{exc}}}{\partial\rho(\mathbf{r}, \omega)} + \mathcal{V}_{\text{ext}}(\mathbf{r}, \omega) - \mu. \tag{7.14}$$

Therefore, we gain a self-consistent equation for the density profile

$$\rho_{\mu VT}(\mathbf{r}, \omega) = \rho_{\text{bulk}}\exp(-\beta\mathcal{V}_{\text{ext}}(\mathbf{r}, \omega) + c^{(1)}(\mathbf{r}, \omega) + \beta\mu) \tag{7.15}$$

with ρ_{bulk} corresponding to a constant bulk density and the one-body direct correlation function

$$c^{(1)}(\mathbf{r}, \omega) = -\beta\frac{\partial\mathcal{F}_{\text{exc}}}{\partial\rho(\mathbf{r}, \omega)}. \tag{7.16}$$

7.1.2 Fundamental measure theory

The difficult task for every density functional theory is to accurately approximate the one direct correlation function $c^{(1)}(\mathbf{r}, \omega)$. As $\mathcal{F}_{\text{exc}}$ can not be derived straightforwardly from the Hamiltonian, different approaches for different particle systems have been developed [553]. For hard particle systems Rosenfeld developed a geometry-based approach, the fundamental measure theory (FMT), which forgoes any empirical assumptions, different from other strategies in DFT, and, thus, is the most suitable for colloidal (hard particle)

systems. In FMT the excess free energy is given by a free energy density Φ, which is a function so-called *weighted densities* $n_\alpha[\rho]$ and reads

$$\mathcal{F}_{\text{exc}} = k_B T \int \mathrm{d}\mathbf{r}\, \Phi\left(\{n_\alpha[\rho](\mathbf{r})\}\right). \tag{7.17}$$

For the exact calculation and the derivation of this free energy density by decomposing the Mayer function, we refer to Ref. [406, 554, 555]. The functions Φ of $n_\alpha[\rho]$ are the same for different versions of FMT,

$$\Phi(\{n_\alpha\}) = -n_0 \log(1-n_3) + \frac{n_{12}}{1-n_3} + \frac{n_{222}}{(1-n_3)^2}, \tag{7.18}$$

however, they differ in the definition of n_{12} and n_{222}. As we will later investigate elongated pear-shaped particles, we use the Tarazona-Rosenfeld-FMT functional, which correctly characterizes the smectic phase of spherocylinders [556, 557], where other definitions [562] usually used for hard spheres were unsuccessful to describe a stable smectic phase with realistic densities and aspect ratios. One of the weighted densities n_3 is defined as the integral of the local density over the volume of the interior $\mathcal{B}(\omega)$ of the particle and over its orientation ω,

$$n_3[\rho](\mathbf{r}) = \int \mathrm{d}\omega \int_{\mathcal{B}(\omega)} \mathrm{d}\mathbf{p}\; \rho(\mathbf{r}-\mathbf{p},\omega). \tag{7.19}$$

For the remaining weighted densities an integral over all points $\mathbf{p}$ on the surface of the particle $\partial\mathcal{B}(\omega)$ with the surface element $\mathrm{d}p^2$ and the particle's orientation has to be calculated. We get

$$n_{\alpha_1\dots\alpha_n}[\rho](\mathbf{r}) = \int_{\partial\mathcal{B}^n} \mathrm{d}\mathfrak{R}^n\; Q_{\alpha_1\dots\alpha_n}(\mathfrak{R}_1,\dots,\mathfrak{R}_n) \prod_{i=1}^{n} \rho(\mathbf{r}-\mathbf{p}_i,\omega_i) \tag{7.20}$$

where we combine the positional and orientational coordinates to $\mathfrak{R}_i = (\omega_i, \mathbf{p}_i)$ for simplicity and introduce a shorthand integral notation

$$\begin{aligned} \int_{\partial\mathcal{B}} \mathrm{d}\mathfrak{R} &\equiv \int \mathrm{d}\omega \int_{\partial\mathcal{B}(\omega)} \mathrm{d}p^2 \quad \text{and} \\ \int_{\partial\mathcal{B}^n} \mathrm{d}\mathfrak{R}^n &\equiv \int_{\partial\mathcal{B}} \mathrm{d}\mathfrak{R}_1 \cdots \int_{\partial\mathcal{B}} \mathrm{d}\mathfrak{R}_n. \end{aligned} \tag{7.21}$$

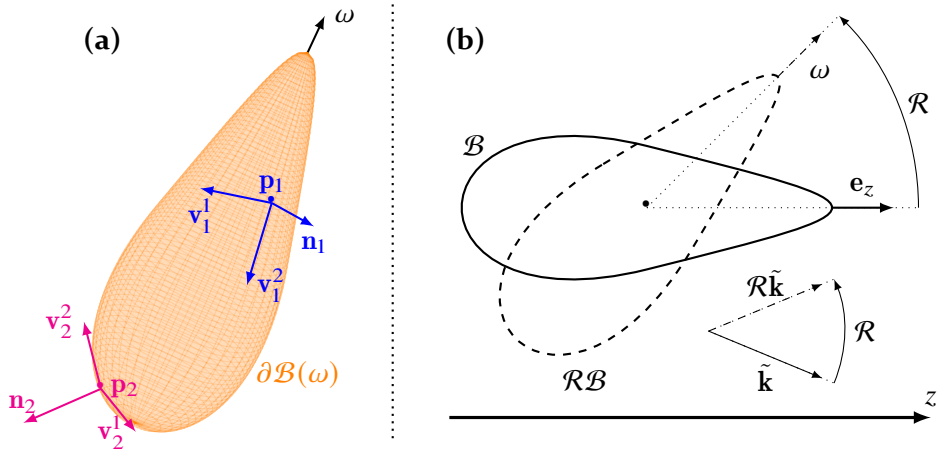

Figure 7.2: (a) The normal directions $\mathbf{n}_i$ and the corresponding vectors $\mathbf{v}_i^1$ and $\mathbf{v}_i^2$ of the principal curvatures at different points $\mathbf{p}_i$ on the pear surface $\partial\mathcal{B}(\omega)$. (b) The weighted functions of the solids of revolution have to be calculated for all orientations ω. The corresponding rotation matrix regarding the unit vector in z-direction $\mathbf{e}_z$ is symbolised by $\mathcal{R}$. Instead of rotating the particles directly the wavenumber vectors are rotated accordingly instead, such that the analytical form $R(z)$ of the surface of revolution in the body fixed frame can be used for all $\mathcal{R}$.

For the Tarazona-Rosenfeld-FMT [554] the functions $Q_\alpha(\mathcal{R}_1,\ldots,\mathcal{R}_n)$ depend on the principal curvatures κ_i^1 and κ_i^2 with Gaussian curvature $K_i{=}\kappa_i^1{\cdot}\kappa_i^2$, the corresponding directions $\mathbf{v}_i^1$ and $\mathbf{v}_i^2$ and the normal $\mathbf{n}_i$ at point $\mathbf{p}_i$ on $\partial\mathcal{B}(\omega)$ (see also Fig. 7.2a):

$$\begin{aligned} Q_0(\mathcal{R}) &= \frac{K}{4\pi}, \\ Q_{12}(\mathcal{R}_1,\mathcal{R}_2) &= \frac{\kappa_1^2(\mathbf{v}_1^1{\cdot}\mathbf{n}_2)^2+\kappa_1^1(\mathbf{v}_1^2\cdot\mathbf{n}_2)^2}{4\pi(1+\mathbf{n}_1\cdot\mathbf{n}_2)}, \\ Q_{222}(\mathcal{R}_1,\mathcal{R}_2,\mathcal{R}_3) &= \frac{3}{16\pi}\left(\mathbf{n}_1\cdot(\mathbf{n}_2\times\mathbf{n}_3)\right). \end{aligned} \tag{7.22}$$

The form for Q_{12} used here is equivalent to the one from Ref. [210]. The computation of Q_{12} and Q_{222} is often involved as we are dealing with high-dimensional integrals. Especially for complex shape it is difficult to calculate the functions directly. However, Hansen-Goos and Mecke [377] proposed to use an expansion of $n_{\alpha_1\ldots\alpha_n}$ and $n_{\alpha_1\ldots\alpha_n}$

$$n_{\alpha_1\ldots\alpha_n}[\rho](\mathbf{r}) = \sum_{k_1,\ldots,k_n} C^{(k_1,\ldots,k_n)}_{\alpha_1\ldots\alpha_n} \prod_{i=1}^{n} n^{(k_i)}_{\alpha_i}[\rho](\mathbf{r}) \tag{7.23}$$

with constants $C^{(k_1,\ldots,k_n)}_{\alpha_1\ldots\alpha_n}$ and the more easily computable weighted densities

$$n^{(k)}_{\alpha}[\rho](\mathbf{r}) = \int_{\mathcal{B}} \mathrm{d}\mathfrak{R}\, w^{(k)}_{\alpha}(\mathfrak{R})\rho(\mathbf{r}-\mathbf{p},\omega). \tag{7.24}$$

The functions $w^{(k)}_{\alpha}(\mathbf{p},\omega)$ are called weight functions that can be expressed as an expansion of Q_{12} in the orthogonal spherical harmonics $Y^m_l(\mathbf{n}_2)$. Based on the fact that $Q_{12}(\mathfrak{R}_1,\mathfrak{R}_2) = Q_{12}(\mathfrak{R}_1,\mathbf{n}_2)$ only depends on $\mathbf{n}_2$ in terms of $\mathfrak{R}_2$ we get, following Ref. [563],

$$\begin{aligned} w^{(l,m)}_1(\mathfrak{R}) &= \int_{S^2} \mathbf{dn}\; Q(\mathfrak{R},\mathbf{n}) Y^m_l(\mathbf{n}) N^0_l, \\ w^{(l,m)}_2(\mathfrak{R}) &= \frac{Y^{m*}_l(\mathbf{n}(\mathfrak{R}))}{N^0_l} \end{aligned} \tag{7.25}$$

with $k = (l,m)$ and the factors $N^m_l = \sqrt{\frac{2l+1}{4\pi}\frac{(l-m)!}{(l+m)!}}$. Furthermore, $w^{(k)}_{\alpha}(\mathbf{p},\omega)$ can be brought into the following analytical form

$$w^{(l,m)}_{\alpha}(\mathfrak{R}) = \sum_{n=-l}^{l} \mathcal{D}^l_{mn}(\mathcal{R}_T(\mathfrak{R})) W^{(\alpha)}_{ln}(\mathfrak{R}) \quad \text{for } \alpha = 1,2, \tag{7.26}$$

where $\mathcal{D}^l_{mn}$ are the Wigner-D matrices, $\mathcal{R}_T(\mathfrak{R})$ denotes the orientation of the axis system $\{\mathbf{v}^1,\mathbf{v}^2,\mathbf{n}\}$ and

$$\begin{aligned} W^{(1)}_{ln}(\mathfrak{R}) &= \begin{cases} \frac{H(\mathfrak{R})}{4\pi}\delta_{n,0} & l = 0 \\ -\frac{H(\mathfrak{R})}{4\pi}\delta_{n,0} & l = 1 \\ -(-1)^l \Delta\kappa(\mathfrak{R}) N^0_l N^2_l [\delta_{n,2} - \delta_{n,-2}] & l \geq 2 \end{cases} \\ W^{(2)}_{ln}(\mathfrak{R}) &= \delta_{n,0} \end{aligned} \tag{7.27}$$

with the mean curvature $H = \frac{1}{2}(\kappa^1+\kappa^2)$ and $\Delta\kappa = \frac{1}{2}(\kappa^1-\kappa^2)$. For detailed step by step deviation of Eq. (7.25) into Eq. (7.26), we refer to Ref. [222, 377, 563].

For n_{12} the constant is defined as

$$C_{12}^{(l_1,m_1,l_2,m_2)} = \delta_{l_1,l_2}\delta_{m_1,m_2} \tag{7.28}$$

as a consequence of symmetry under a rotation of the whole system including the density profile and the external potential. The constant for n_{222} is defined as

$$C_{222}^{(l_1,m_1,l_2,m_2,l_3,m_3)} = \int_{(S^2)^3} \mathrm{d}\mathbf{n}^3 Q_{222}(\mathbf{n}^3) \prod_{i=1}^{3} Y_{l_i}^{m_i}(\mathbf{n}_i) N_{l_i}^0. \tag{7.29}$$

It can be shown that only a finite number of these terms are nonzero [222], which is an advantage of Tarazona-Rosenfeld-FMT compared to the other version also derived in Ref. [554]. We truncate the expansion of n_{12} at the order $l_{\max} = 8$, so $C_{12}^{(l_1,m_1,l_2,m_2)} = 0$ for $l_1, l_2 > l_{\max}$ as we do not observe any changes in the results for $l > 8$ and the numerical errors are negligible compared to differences between simulation and theory.

7.2 Fundamental measure theory for solids of revolution

Here we apply fundamental measure theory to smooth uniaxial particles (solids of revolution) by deriving a new functional. We consider a general cross-section with a plane containing the rotation axis by prescribing its boundary for example by a Beziér spline. Usually, the radial component of a solid of revolution is written as a function $R(z)$ of the position along the symmetry axis. Kinks in the boundary can also be implemented in the manner of Ref [211], but we consider only smooth contours here. Examples of solids of revolution are presented pictorially in Fig. 7.1 and via a formula for pear-shaped particles in the next section (see Eq. (7.38)).

To implement the weighted densities n_0, $n_1^{(k)}$, $n_2^{(k)}$ and n_3 efficiently, we first calculate the Fourier transforms of the weight functions

$$\hat{w}_\alpha^{(l,m)}(\mathbf{k},\omega) = \frac{1}{(2\pi)^3} \int_{\partial\mathcal{B}(\omega)} \mathrm{d}^2\mathbf{p}\; w_\alpha^{(l,m)}(\mathbf{p},\omega) \exp(-\mathrm{i}\mathbf{k}\cdot\mathbf{p}) \tag{7.30}$$

where we use $w_\alpha^{(l,m)} = w_\alpha \delta_{0,l}\delta_{0,m}$ for $\alpha = 0, 3$ to unify the notation, before exploiting the convolution theorem in Eq. (7.24)

$$\hat{n}_\alpha^{(l,m)}(\mathbf{k}) = \int \mathrm{d}\omega\ \hat{w}_\alpha^{(l,m)}(\mathbf{k},\omega)\hat{\rho}(\mathbf{k},\omega). \tag{7.31}$$

To calculate the Fourier transforms in Eq. (7.30) we replace ω by the Euler angles ϕ, θ and χ and the corresponding rotation matrices $\mathcal{R}$. Thus the weight functions of the differently oriented particles described by the volume of their interior $\mathcal{RB}$

$$(\hat{w}^{\mathcal{RB}})_\alpha^{(l,m)}(\mathcal{R}\mathbf{k}) = \sum_{n=-l}^{l} \mathcal{D}_{mn}^{l}(\mathcal{R})(\hat{w}^{\mathcal{B}})_\alpha^{(l,n)}(\mathbf{k}) \tag{7.32}$$

are written in terms of the weight functions in the body-fixed frame $(\hat{w}^{B})_\alpha^{(l,m)}(\tilde{\mathbf{k}})$ where the surfaces of the particles are defined as $\mathbf{p}(z,\phi') = (R(z)\cos\phi', R(z)\sin\phi', z)$. In other words the integral is calculated by rotating the wavenumber vector $\mathbf{k}$ and keeping the particle orientation fixed instead of rotating the particle itself and calculating the surface points $\mathbf{p}$ for any possible ω (see Fig. 7.2b). In doing so we can derive benefit from the area element of the surface of revolution [564]

$$\mathrm{d}S_z = R(z)\ \mathrm{d}s\ \mathrm{d}\phi' = R(z)\sqrt{1+R'(z)^2}\ \mathrm{d}z\ \mathrm{d}\phi' \tag{7.33}$$

and simplify the integral of Eq. (7.30) further. For $\alpha = 0, 1, 2$ the Fourier transforms of the weight functions in the body-fixed frame using Eq. (7.26) and Eq. (7.30) result in

$$(\hat{w}^{\mathcal{B}})_\alpha^{(l,m)}(\tilde{\mathbf{k}}) =$$
$$2\pi \int \mathrm{d}z\ R(z)\sqrt{1+R'(z)^2} \sum_{n=-l}^{l} \mathcal{D}_{mn}^{l}(0,\theta'(z),0) W_{\alpha n}^{(\alpha)}(z) J_m(k_\perp R(z)) \exp(-\mathrm{i}k_z z) \tag{7.34}$$

where $J_m(z)$ is the m-th Bessel function, $k_\perp = \sqrt{k_x^2 + k_y^2}$, $R'(z)$ is the derivative of $R(z)$ and $\theta'(z)$ (see also Fig. 7.3) denotes the polar angle of the normal vector

$$\theta'(z) = \begin{cases} \arctan(\frac{1}{R'(z)}) & R'(z) > 0 \\ \frac{\pi}{2} & R'(z) = 0 \\ \pi + \arctan(\frac{1}{R'(z)}) & R'(z) < 0. \end{cases} \tag{7.35}$$

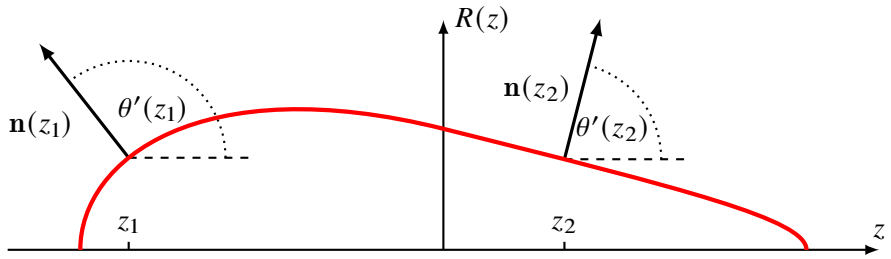

Figure 7.3: The polar angles $\theta'(z_i)$ of the normal vector $\mathbf{n}(z_i)$ at different heights z_i of a pear-shaped particle in the body fixed frame which is described by the radial function $R(z)$.

Here, we define $W^{(0)}_{l,m} = \frac{K}{4\pi}\delta_{0,l}\delta_{0,m}$ and used $\mathcal{D}^0_{00}(\mathcal{R}) = 1$, such that w_0 also obeys Eq. (7.26) for $\alpha = 0$. For $\alpha = 3$ we get

$$(\hat{w}^{\mathcal{B}})_3(\tilde{\mathbf{k}}) = 2\pi \int \mathrm{d}z\; R(z) J_1(k_\perp R(z)) \exp(-\mathrm{i}k_z z). \tag{7.36}$$

Additionally, for solids of revolution we can write the principal curvatures in terms of $R(z)$ as [564]

$$\begin{aligned} \kappa^1(z) &= \frac{R''(z)}{(R'(z)^2+1)^{\frac{3}{2}}} \\ \kappa^2(z) &= -\frac{1}{R(z)\sqrt{R'(z)^2+1}}. \end{aligned} \tag{7.37}$$

We perform the integral over z in Eq. (7.34) numerically, once for every k_z and ω at the beginning of the calculation.

7.3 Ordering of pear-shaped particle systems near hard substrates

7.3.1 Fundamental measure theory of pear-shaped particles

In our calculations we investigate a variety of one-component pear-shaped particle fluids enclosed within two hard walls. Such confined isotropic fluids are often used as reference systems to test the quality and accuracy of the derived functional [210, 211, 212, 377, 565] as the problem reduces effectively to one dimensions (see in the following Eq. (7.42)). Hence, in this chapter we favour this low-density system as a preliminary study over the more complex higher density phases, like the nematic, smectic or gyroid phase which we

analyse in the rest of this thesis. To this end, the contour of the pear-shaped solids of revolution are defined as described in Sec. 2.1 by two Beziér curves which form the top and the bottom of the particle. Using the anchor points in Eq. (2.2) and Eq. (2.3), we can convert the Bezier-curve representation into a description based on the radial function

$$R_{\text{pear}}(z) = 0.5d\left((1-t(z))^3 + C(z)\cdot t(z)(1-t(z))(1-2t(z)) - t(z)^3\right) \tag{7.38}$$

with

$$t(z) = 0.5\left(1-\sqrt{1-\frac{2|z|}{d\cdot k}}\right) \tag{7.39}$$

and

$$C(z) = \begin{cases} C_1 = \frac{3k_\theta - 2k}{k_\theta} & \text{for } z \geq 0 \\ C_2 = \frac{3k_\theta + 2k}{k_\theta} & \text{for } z < 0. \end{cases} \tag{7.40}$$

Furthermore, we introduce an external potential $\mathcal{V}^{\text{ext}}(\mathbf{r},\omega)$ which is infinite if a pear at position $\mathbf{r}$ with orientation ω overlaps with one of the walls at $z=0$ and $z=L$ with L being the distance between the walls and zero otherwise. This contact distance $\sigma_{\text{wall}}(\theta)$ between pears and the wall can be calculated analytically based on the Bezier description of the particles:

$$\sigma_{\text{wall}}(\theta) = \inf_t \sigma_w \begin{cases} ((1-t)^3 + C_1 t(1-t)(1-2t) - t^3)\sin\theta + 4kt(1-t)\cos\theta) \\ \qquad \text{for } \theta \geq \arctan(2k_\theta) \\ (((1-t)^3 + C_2 t(1-t)(1-2t) - t^3)\sin\theta - 4kt(1-t)\cos\theta) \\ \qquad \text{for } \theta < \arctan(2k_\theta) \end{cases} \tag{7.41}$$

The problem is effectively reduced to a one-dimensional problem. Eq. (7.31) then becomes

$$\hat{n}_\alpha^{(l,m)}(k_z\mathbf{e}_z) = 2\pi\delta_{m,0}\int\int \mathrm{d}\phi\sin\theta\ \mathrm{d}\theta\ (\hat{w}^{\mathcal{R}(\theta,\phi)\mathcal{B}})_\alpha^{(l,0)}(k_z\mathbf{e}_z)\ \hat{\rho}_{\mathcal{R}(\theta,\phi)B}(k_z\mathbf{e}_z) \tag{7.42}$$

as the Fourier transform of the density profile is nonzero only if $\mathbf{k} = k_z \mathbf{e}_z$ points towards the z-direction perpendicular to the wall.

Finally, the grand potential Eq. (7.1) and its functional derivative with respect to the density profile Eq. (7.16) are calculated using Eq. (7.32) and (7.42). The grand potential is minimized for a fixed mean packing fraction ρ_g with respect to the density profile using Picard iteration [559, 566]. We fix the average packing fraction instead of the chemical potential or bulk density in the middle between the walls ρ_{bulk} to avoid the statistical error of measuring ρ_{bulk} in the simulations where the number of particles and thus ρ_g is fixed. This might complicate the comparison between simulations and FMT. However, in the following we measure ρ_{bulk} in the FMT calculations to allow comparison of our work with future DFT or simulation studies that fix μ.

The Picard iteration is executed as follows

I. Set initial choice of ρ_g and density profiles $\rho^{(0)}(z, \omega)$ accordingly:

$$\rho^{(0)}(z, \omega) = \rho_{\text{bulk}} \exp(-\beta \mathcal{V}_{\text{ext}}(z, \omega)).$$

II. Calculate $\tilde{\rho}^{(i)}(z, \omega)$ by using $\rho^{(i)}(z, \omega)$:

$$\tilde{\rho}^{(i)}(z, \omega) = \rho_{\text{bulk}} \exp(-\beta \mathcal{V}_{\text{ext}}(z, \omega) + c^{(1)}(\rho^{(i)}(z, \omega)) + \beta \mu_{\text{ext}}).$$

III. Determine $\tilde{\rho}^{(i)}(z) = \int \mathrm{d}\omega \; \rho^{(i)}(z, \omega)$ and rescale $\tilde{\rho}^{(i)}(z, \omega)$ such that ρ_g stays constant for every step.

IV. Mix solutions with parameter $\alpha = 0.01$:

$$\rho^{(i+1)}(z, \omega) = (1 - \alpha)\rho^{(i)}(z, \omega) + \alpha \tilde{\rho}^{(i)}(z, \omega).$$

V. Go back to step II. until $\tilde{\rho}^{(i)}(z, \omega)$ converges.

7.3.2 Comparison between fundamental measure theory and Monte Carlo results

To evaluate the results of the FMT algorithm we perform Monte Carlo simulations on the same system using both the modified hard-Gaussian-overlap contact function σ^{PHGO} for pear-shaped particles and the HPR approach to determine overlapping particles. The distance $L = 20\sigma_w$ between the walls

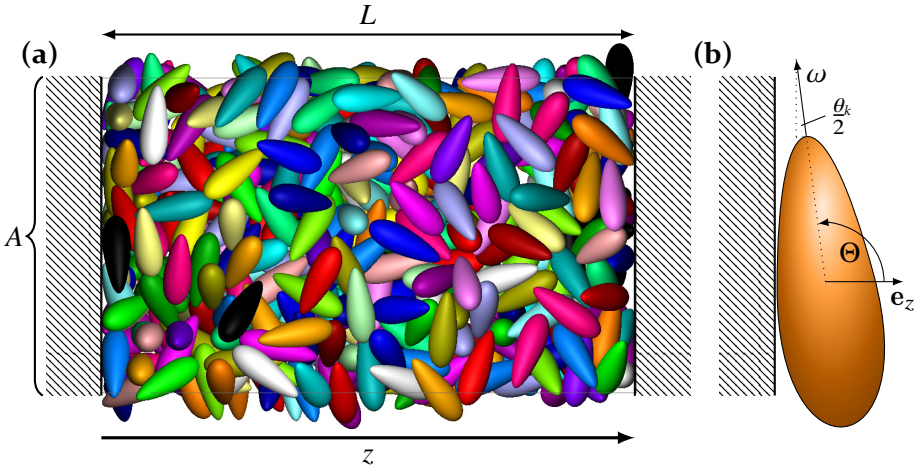

Figure 7.4: (a) Snapshot of a Monte Carlo simulation of hard pear-shaped particles in between two hard walls at an average volume density $\rho_g = 0.3$. The walls have the area A and are placed parallel to one another on the left and right-hand side of the simulation box at a distance $L = 20{\cdot}\sigma_w$. The boundary conditions in the transversal directions are periodic. The simulation box contains 500 particles with $k = 3.0$ and $k_\theta = 3.8$. (b) A pear-shaped particle close to the wall. In this domain the particles only can adopt certain angles Θ as the overlap between wall and particle is prohibited. Here Θ can be related to the tapering angle θ_k.

in units of the width of the pear-shaped particle σ_w is chosen large enough such that the fluid behaves like a bulk-fluid in the middle of the system.

The average packing fraction

$$\rho_g = V_{\text{pear}} \frac{N}{L{\cdot}A} = 0.3 \tag{7.43}$$

is set to a value that corresponds to the isotropic disordered phase, if the fluid was in the bulk, for both simulation sets and FMT (for the PHGO and the HPR model of pear-shaped particles the transition to orientationally-ordered phases like gyroid or nematic occurs for $\rho_g \approx 0.53$ and $\rho_g \approx 0.56$, respectively; see Fig. 5.1 and Fig. 5.10). The parameter V_{pear} is the volume of a pear-shaped particle, A the area of the walls and $N = 500$ the number of particles in the system (see Fig. 7.4a). To analyse the effect of both particle parameters k and k_θ independently, we investigate the behaviour of five different pear-shaped particle systems $(k,k_\theta,\rho_{\text{bulk}})$={(2.5,3.8,0.3077), (3.0,2.5,0.3076), (3.0,3.8,0.3078), (3.0,∞,0.3079), (3.5,3.8,0.3079)} ($k_\theta = \infty$ corresponds to spheroids).

Fig. 7.5 shows the local packing fraction

$$\rho(z) = \frac{V_{\text{pear}}}{A} \sum_{i=1}^{N} \langle \delta(z - z_i) \rangle, \tag{7.44}$$

where z_i is the distance between the centre of the particle i and the wall. For all five pear-shaped particle systems, the results obtained from FMT and the simulations are in very good agreement. Both methods clearly reveal distinct layering of the particles for each parameter set, indicated by the different peak-profiles. This also implies that both pear-shaped particle models generate equal results. Hence, the density profiles for diluted systems at low global densities seem to be insensitive to the non-additivity effects of the PHGO model, which we discussed in Sec. 2.2.1, and are indistinguishable in terms of local densities. Note that the similarities, however, might be hidden behind the interaction between particles and wall. In both cases, the contact is determined in the same way, where overlaps, such as those observed in the PHGO model, do not occur (see Eq. (7.41)). However, this does not change the fact that the profiles also coincide further away from the substrate.

The shapes of the peaks in Fig. 7.5 result from two competing phenomena. Firstly, particles from the bulk of the system apply pressure on the first layer of pear-shaped particles close to the wall and as a result, push those particles even further towards the restricting boundary. The other effect is the loss of rotational entropy, which is caused by the exclusion of certain prohibited orientations which would cause an overlap with the wall. This second mechanism, which pushes the particles away from the wall, highly depends on the specific shape of the particles. Keeping the aspect ratio of the pear-shaped particles constant we detect a broad first and second peak for strongly tapered particles (see Fig. 7.5b). The density profile for less tapered pear-shaped particles exhibits sharper features (Fig. 7.5c) and eventually forms two distinct peaks with the first peak increasing in height for spheroids with $k_\theta = \infty$ in Fig. 7.5e. The peaks indicate that the range of preferred arrangements at the wall is narrower than for tapered pear-shaped particles. The same broadening of peaks can also be achieved by decreasing the aspect ratio at constant tapering parameter (see Fig. 7.5a,c,d). However, this is caused by a more prominent change in the density profile. On the one hand, the second peak becomes more dominant for more elongated particles, on the other hand, it is shifted further apart from the wall and the first peak, with its position being equal to half of the length of the pear. Thus,

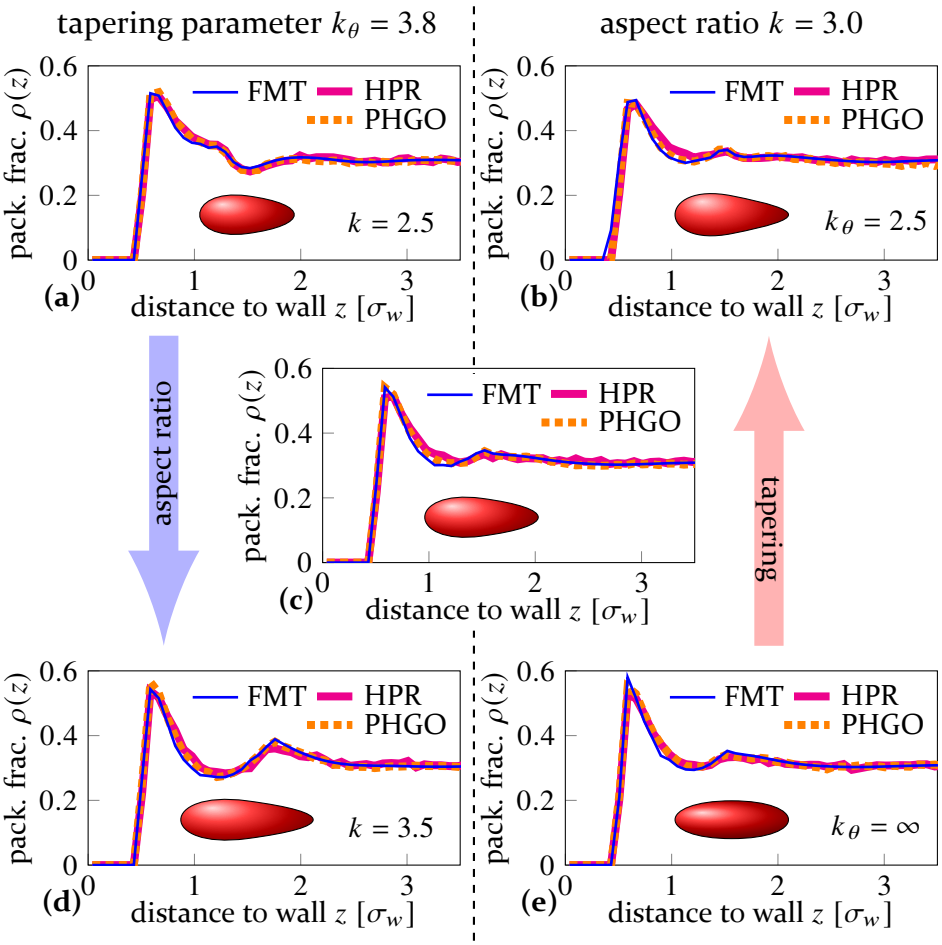

Figure 7.5: Density profile of hard pear-shaped particles close to a hard wall. The results obtained by both Monte Carlo simulation (HPR and PHGO model) and FMT are shown. The mean density is set to $\rho_g = 0.3$. The shapes underneath the plots indicate the cross-sections of the corresponding rotationally symmetric pear-shaped particles. All hard particle systems show a complex ordering at the first layers near the hard surface. a) $k = 2.5$, $k_\theta = 3.8$, $\rho_{\text{bulk}} = 0.3077$ b) $k = 3.0$, $k_\theta = 2.5$, $\rho_{\text{bulk}} = 0.3076$ c) $k = 3.0$, $k_\theta = 3.8$, $\rho_{\text{bulk}} = 0.3078$ d) $k = 3.5$, $k_\theta = 3.8$, $\rho_{\text{bulk}} = 0.3079$ e) $k = 3.0$, $k_\theta = \infty$, $\rho_{\text{bulk}} = 0.3079$ (spheroid)

in Fig. 7.5a both peaks are close together such that they merge and form one broad peak. Interestingly, this density profile shows a distinct dip where a second peak is observed in all other density profiles.

To investigate the orientational order in more detail we determine a polar profile

$$P_z(z) = \frac{\langle \sum_{i=1}^{N} \cos(\Theta_i)\delta(z - z_i)\rangle}{\langle \sum_{i=1}^{N} \delta(z - z_i)\rangle}, \tag{7.45}$$

where Θ_i is the angle between the orientation ω_i of the i-th pear and the normal of the boundaries pointing in the z-direction $\mathbf{e}_z$ for the wall $z = 0$ and in the $(-z)$-direction $-\mathbf{e}_z$ for the wall $z = L$ (see Fig. 7.4b). The polar parameter P_z contains the information about the alignment of the pear-shaped particles towards the wall, where for positives values the particles tend to point away from the walls with their thin ends, whereas for negative values the majority of particles are tilted towards the wall. The profiles are shown in Fig. 7.6.

For all systems, the positions and heights of the first dips are in good agreement for both pear-shaped particle models used in simulations and the derived theory. Nevertheless, it becomes apparent that the orientational order profile reacts more sensitively on subtle changes of the particle shape than the density profile. Only the simulation results created with the HPR approach show exactly the same orientational behaviour as FMT, whereas the theory underestimates the magnitude of the peak observed for the PHGO model, where the particles are facing away from the walls. Overall, the orientational alignment is enhanced by using the non-additive PHGO contact function. This is in accordance with our earlier discussed observations, where non-additivity tends to alter the local arrangements, especially the relative orientations between neighbouring particles (see Sec. 6.3.2). However, also for the hard particle system the orientational order, which seems to be prerequisite to create highly complex structures like the gyroid and other bilayers structures, is clearly present. Thus, it appears conceivable to potentially magnify the local orientational correlations of colloids, change the mesoscopic length scale and eventually stabilise the gyroid phase by using particles which are based on the hard-core pear potential. How exactly this can be realised in experiments, however, has to be covered in future studies.

By comparing the different shapes, we can see that the aspect ratio only slightly changes the profile and governs the position of the peak (see Fig. 7.6a,c,d). A more drastic alternation in the orientational order of the layers close to the wall becomes apparent by changing the tapering parameter. Starting from a non-tapered spheroid (see Fig. 7.6e) $P_z(z)$ stays constant at 0

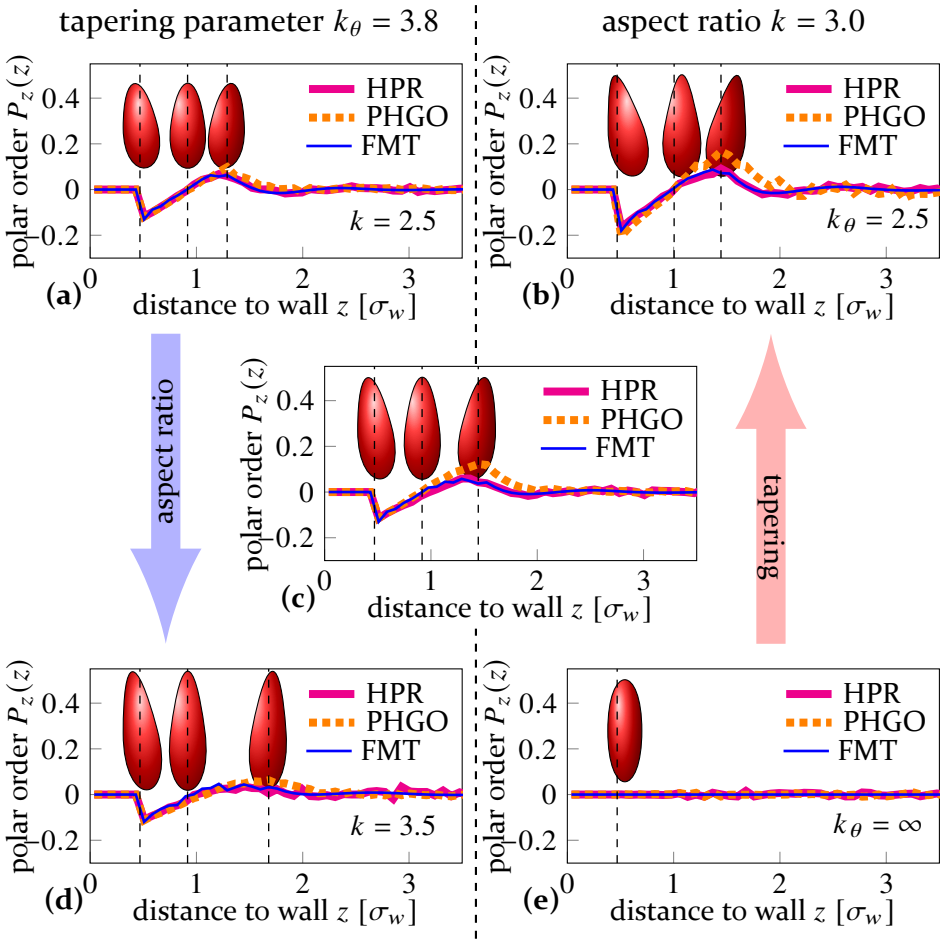

Figure 7.6: Polar profile $P_z(z)$ of hard pear-shaped particles close to a hard w all. Negative values correspond to the sharp end angled towards the substrate. The results obtained by both Monte Carlo simulation (HPR and PHGO model) and FMT are shown. The mean density is set to $\rho_g = 0.3$. All hard particle systems show a complex ordering at the first layers near the hard surface. a) $k = 2.5$, $k_\theta = 3.8$, $\rho_{\text{bulk}} = 0.3077$ b) $k = 3.0$, $k_\theta = 2.5$, $\rho_{\text{bulk}} = 0.3076$ c) $k = 3.0$, $k_\theta = 3.8$, $\rho_{\text{bulk}} = 0.3078$ d) $k = 3.5$, $k_\theta = 3.8$, $\rho_{\text{bulk}} = 0.3079$ e) $k = 3.0$, $k_\theta = \infty$, $\rho_{\text{bulk}} = 0.3079$ (spheroid). The pear profiles indicate the mean orientation of the layers towards the hard wall (parallel to dotted lines) according to the orientational order profile of the MC simulations of pears interacting via the PHGO contact function.

due to the inversion-symmetry of the particles. Note that this does not mean that all orientations are equally probable. Close to the walls, the spheroids align along the wall and, therefore, perpendicular to its normal. By increasing the head-tail asymmetry of the pear-shaped particles, they arrange such

that the particles in the first layer point slightly towards the wall. The angle between their rotational axis and the substrate results from the configuration of the particles which fits closest along the wall and hence can be identified exactly as their tapering angle θ_k as indicated in Fig. 7.6 (see also Fig. 7.4). Thus the taper of the pear-shaped particle can be seen as a mechanism to align the elongated particles at a certain angle to a hard surface. Further away from the wall, approximately in the second layer of particles, all tapered pear-shaped particles tend to face away from the wall as $P_z(z)$ changes from negative to positive values. This can be seen as a precursor for a potential smectic arrangement which was found in our previous computational studies of the PHGO model (see Sec. 5.1.1) at higher densities. In those smectic bilayer phases, the pear-shaped particles form interdigitating sheets with particles alternatingly facing in opposite directions. The observation that the first layer of pear-shaped particles faces slightly towards and the second layer slightly away from the wall supports the conclusion that the same alternation of directions occurs at low densities close to a hard surface.

7.4 Conclusion and outlook

We have introduced a fundamental measure density functional for arbitrary solids of revolution. We have applied this approach to a pear-shaped particle fluid, where the shape of the particle is parametrised by two Beziér curves. We showed that pear-shaped particle fluids interacting with a hard planar substrate demonstrate a different degree of orientational order compared to spheroids despite only slight differences between both shapes. The pear-shaped particles are aligned towards the wall, where the orientation is determined by the tapering angle of the particle. The orientational order profiles of tapered particles also indicate an alternating orientational arrangement between the first and second layer even at low densities (this may be the precursor to the development of interdigitating bilayers). It has been shown that this interdigitating behaviour – and consequently the tapering of the particle – is crucial to stabilise smectic or even gyroid phases. Yet, we can observe that this precursor is much stronger for PHGO particles than the one predicted for a more accurate description of the pear-shape both in theory (FMT) and simulation (HPR). As the nematic phase probably also occurs at a system of hard-core pear-shaped particles near a hard wall similar to previous computational observations [567, 568, 569] and even experimental indications [230] in systems of hard spherocylinders, we can think of the alignment of particles at the wall due to their taper as a mechanism

to control the direction of the smectic phase. In experiments, it should be possible to alter the direction of tapered colloids by introducing a hard interface to the liquid.

Finally, the small but important differences between the HPR and PHGO models covered in earlier chapters are also reflected in the results of this chapter. While the hard-mesh and the theory show similar orientational ordering at the substrate, the PHGO model exhibits a more prominent and distinct orientational order profile. Even though the slightly different alignment does not change the positional order on the microscopic level, like the density profile at a hard wall, by a great margin, they again indicate the earlier observed distinct mesoscopic behaviours of both models.

In the context of the whole thesis, the obvious question emerges why we have not used FMT to analyse the gyroid structures? The answer is that for once the density functional describes the HPR rather than the PHGO model more accurately. As we have not observed the gyroid phase in the HPR model (see Fig. 5.10) the introduced density functional, applied to pear-shaped particles at high densities, probably does not reproduce the PHGO gyroid phase directly but has to be modified first.

The second and more significant issue is the dimensionality of the PHGO gyroid problem. In isotropic systems at a hard wall, the density functional reduces effectively to a one-dimensional problem. To analyse the gyroid phase, we have to consider all three translational degrees of freedom as the underlying minimal surface structure is triply periodic. Also the two orientational degrees of freedom come into addition, such that the overall problem is five-dimensional. This makes the computation of the free energy highly complex, numerically very challenging and, therefore, very slow. However, it might be possible to find a parametrisation for the particle coordinates based on our observations in Sec. 4.3.4. Here, we identified the gyroid phase as a warped smectic bilayer phase, which could help us to lower the dimensionality by relating the particles to the minimal surface. Yet, how exactly the minimal surface and pears can be related for the FMT calculations is highly non-trivial.

Overall, MC simulations seem currently to be more efficient and hence, more preferential over DFT techniques to analyse gyroid-like phases. However, despite all these issues, FMT might be a valid tool to determine if HPR pear-shaped particles can assemble into a (meta-)stable gyroid phase in the

future, nevertheless. As an initial step, we can try to identify suitably shaped particles that form a globally aligned smectic bilayer phase (which is much easier to calculate numerically than the gyroid phase using FMT), as observed in Sec. 5.1, instead of a nematic or isotropic phase. In case some of the shapes induce the right intra-layer order (like the right amount of interdigitation as observed in Sec. 4.3.1), we can follow up these calculations with particle-resolved computer simulations to see if the layers are flat or curved. The accuracy of the FMT demonstrated in this chapter and [222, 377, 556, 557] shows that this is a promising route.

8 Mixtures of PHGO-pears and hard-core spheres

"A Double Diamond works wonders!"

– Ind Coope Star Brewery

This chapter mainly addresses the formation of the $Pn\bar{3}m$ double diamond in PHGO pear-shaped particle systems upon addition of a hard sphere solvent. In the first part, the geometrical differences and transition pathways between the double gyroid and the double diamond are introduced on a mathematical basis. We discuss the strategies how systems in chemistry overcome geometrical constraints and normally favour the double gyroid over the double diamond. In line with these geometric arguments, our simulations show that a $Pn\bar{3}m$ double diamond structure in the "dry mixture limit" where only a small amount of sphere solvent is introduced to the PHGO particle system. Curiously, the mechanism to generate regions of high negative Gaussian curvature is based on placing the spherical solvent close to the minimal surface within the pear-bilayer formation. Lastly, we describe our preliminary exploration of diluted mixtures. In the course of this, we show that the mixture phases separate for high packing fractions. Furthermore, we obtain micellar structures in systems dominated by the sphere solvent, which themselves form ordered structures and thus, indicate hierarchical self-assembly in PHGO particle systems.[1]

[1]This chapter is based, in parts, on the article P.W.A. Schönhöfer, D.J. Cleaver, and G.E. Schröder-Turk, "Double diamond phase in pear-shaped nanoparticle systems with hard sphere solvent", *J. Phys. D: Appl. Phys.* **51**:464003, 2018. All simulation methods, numerical procedures and data analyses of this paper were implemented and executed by me (with the MD code based on earlier code by Laurence Ellison). Alongside the senior authors, I was a major contributor to the conceptual questions and research methods addressed in the article and to the interpretations presented as results. I created 5 illustrations and graphs in the article, and have written the manuscript, with help and comments from Gerd Schröder-Turk and Douglas Cleaver. Verbatim quotes from that paper may have been used without explicit citations.

Up to this point in the thesis, we have focused on the ability of PHGO particles to self-assemble into gyroid bilayer phases. Next to confirming the existence of such a phase in Chap. 4, we answered the question of both how and why these specific particles create double gyroid structures in contrast to HPR pears (see Chap. 5 and Chap. 6). Although the gyroid is a very fascinating structure, it is not the only cubic bicontinuous architecture which takes a prominent role in self-assembly, with other known structures being the diamond [165, 166, 170], primitive [168, 191] and hexagonal [163, 188] surfaces. We now address the formation of the Pn$\bar{3}$m double diamond phase in PHGO particle systems.

Hence, this chapter is structured as followed. In Sec. 8.1 we first introduce the mathematics behind the transformations between cubic bicontinuous phases. In Sec. 8.2 we show that small quantities of the sphere solvent in the PHGO pear system tend to stabilise the *Pn*$\bar{3}$*m* double diamond phase (in addition to the double gyroid phase). However, we can demonstrate that, in contrast to the lipid-water and copolymer systems, the solvent does not assemble within the channel domain, but the heterogeneities are differently resolved by placing the supplementary material in the dividing matrix instead. In Sec. 8.3 we broaden our studies and determine the phase behaviour for a range of pear-sphere mixtures with different solvent concentrations. We observe that for high enough sphere concentrations the system phase separates for high packing fractions into regions dominated by pears and spheres, respectively. Here, the concentration correlates with the transition packing fraction. Lastly, we show in Sec. 8.3.2 that pear-shaped particles cluster together in systems primarily dominated by spheres by forming "inverse" micellar configurations. Although this assembly can again be associated with the non-additive features of the PHGO particle system, the micelle entities showcase interesting collective behaviours with other micelles and open up the possibility of hierarchical self-assembly in colloidal systems.

Note here that this chapter should not be misunderstood as an attempt to complete study of the pear-sphere mixture. The overall focus of this thesis is the study of the self-assembly of bicontinuous structures in pear-shaped particle systems. Therefore, we address only a limited specific range of the vast parameter space of the pear-sphere mixture.

8.1 Geometric properties of and structural transformation between diamond and gyroid

8.1.1 Curvature and domain size heterogeneity

To find promising strategies to generate double diamond phase we have to familiarise ourselves with the geometric differences between gyroid and diamond structures. Topologically, the gyroid, diamond and primitive surface are equivalent with a common genus 3 [570]. However, in terms of geometry, the three surfaces exhibit clear distinction. Some of those differences, like the connectivity of the network domains, have been already addressed in Sec. 1.2. One aspect, which is believed to take a crucial role in the stability of such structures in multi particle systems, is homogeneity.

The homogeneity of a surface is measured in terms of the variations of the Gaussian curvature ΔK. Triply-periodic minimal surfaces (TPMS) are, like all other hyperbolic surfaces embedded in Euclidean space, inevitably heterogeneous and cannot have constant Gaussian curvature $K(p)$ at every point p on the surface [369, 370] (most evident in the presence of $K = 0$ flat points on TPMS). The curvature heterogeneity is also inherited by space tilings which are based on TPMS surfaces, which can be seen in Sec. 4.3.4. There, we introduced Steiner's theorem [395] which describes the space $\mathrm{d}V(p)$ between an infinitesimal surface patch $\mathrm{d}A(p)$ at point p on the surface and its counterpart $\mathrm{d}A'(p)$ on the parallel surface at a distance l. As we have shown in that chapter the volume and – for incompressible molecules like lipids and di-block copolymers more importantly – the volume shape, indicated by $\mathrm{d}A'$, depend on $K(p)$:

$$\mathrm{d}A' = \mathrm{d}A \cdot (1 + K \cdot l^2) \tag{8.1}$$

which is a special case of Eq. (4.8) where we have used that the mean curvature is zero, $H(p) = 0$. This suggests that the inhomogeneities in K propagate to the Steiner cells (see definition in Sec. 4.3.4) and, hence, leads to variations in $\mathrm{d}A'$ as well. Moreover, the bicontinuous surface structures are heterogeneous in regard to channel sizes [70, 91, 167]. Speaking in more mathematical terms, the distance $l = d_{\mathrm{MS}}(p)$ between the triply-periodic minimal surface and its medial axis is not uniform either (see definition off the medial surface in Sec. 1.2.2). In general, the parameter $d_{\mathrm{MS}}(p)$ can be interpreted as the local channel radius of the labyrinthine domains. Consequently, the variation Δl of a surface is referred to as its packing homogeneity.

Both the packing homogeneity and the homogeneity in regard to the Gaussian curvature are believed to be an indicator of the likeliness of the self-assembly of the associated surface structures [571, 572]. Hyde used the curvature homogeneity to predict the energy difference between bicontinuous lipid-water mesophases [50, 573]. Similarly, the curvature variations have been accounted for in the Helfrich curvature energy formalism of such phases [246, 574]. In principle, the higher the degree of heterogeneity is featured by the minimal surface the greater is the variation of volume shape which has to be adopted by the constituent particles within the systems, according to the Steiner cells. Therefore, the distribution of distances and Gaussian curvature also yield a description of packing frustration. To compensate these packing frustrations, the molecules either have to adopt different shapes in different parts of the cubic phase (shape parameter [244, 423]) or, like the PHGO pear-shaped particles, have to arrange in an interdigitated bilayer formation which can modulate the bilayer thickness according to d_{MS}.

It has been shown that the gyroid is the most homogeneous surface among large classes of the TPMS structures [91, 167]. Both the Gaussian curvature and the domain sizes exhibit the least variance. This might be an explanation of why the gyroid is the most prominent TPMS structure in chemistry and biology. Specifically, as these observations are in line with normal (Q_I) cubic phases in dry soap, which only forms the spatially most homogeneous case the gyroid (Q_I^{250}) [77]. The second most homogeneous surface is the diamond structure. Hence, it is not surprising that the most common and most studied transition between TPMS, both experimentally [309, 575, 576] and theoretically [88, 91] is between the double gyroid and the $Pn\bar{3}m$ double diamond phase.

8.1.2 Structural transition models

We briefly introduce the different pathways, which have been suggested between bicontinuous surface structures. One possible mathematical way to continuously transform the gyroid into the diamond surface and vice versa was already indicated in Sec. 1.2. Here we have introduced in Eq. (1.2) that the G-, D-, and also the P-surface can be parametrised by the Weierstrass representation. Moreover, it was discussed that these three minimal surfaces even share the same Weierstrass function (see Eq. (1.3)), up to the prefactor $\exp(\mathrm{i}\theta_B)$. Taking the Weierstrass representation into account one of these

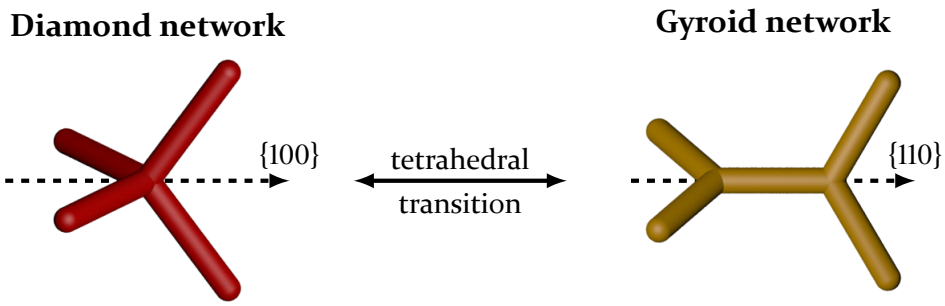

Figure 8.1: The pictorial pathway of the tetrahedral transition between the diamond and gyroid minimal surface structures described by Squires *et al.* [309] and Oka [576] based on the studies by Fodgen and Hyde [88, 91]. The diamond network transforms into the gyroid network by splitting the four-branched nodes into two three-branched nodes and separating them in the {100}-direction.

double symmetric structures can be transferred continuously into another by only shifting one single parameter: the Bonnet angle θ_B. This transition is known as the Bonnet transformation [67].

While a Bonnet transformation from the diamond ($\theta_B = 0$) to the gyroid ($\theta_B \approx 38°$) is mathematically a viable route, the Bonnet pathway causes the minimal surface to self-intersect in the course of the transformation. Self-intersections, however, would imply that biological and chemical systems transitioning from one bicontinuous geometry to another have to introduce cuts and subsequent folds to the minimal surface. Those rearrangements would lead to a temporary loss of the bicontinuous nature of the structure and consequently, a change in topology during the process. Finally, the surface would have to be recombined to generate the new minimal surface morphology which then again separates space into two domains. Hence, the Bonnet transformation and the requisite dissolution and reformation of bilayers seem to be unrealistically complicated, hardly practical via self-assembly and thus is considered as unphysical [575]. Moreover, the transition is presumed to be too fast to involve cuts and fusion of bilayer surfaces [577]

Fodgen and Hyde introduced two alternative continuous transition pathways, neither of which require self-intersections but conserve topology and zero-mean curvature during all stages of the transition [88, 91]. Moreover, these methods additionally fulfil the same length ratio between the unit cell sizes of the cubic phases like the Bonnet transformation, also known

as the Bonnet ratio [578, 579]. Based on the descriptions by Fodgen and Hyde, Squires *et al.* [309] and later Oka [576] developed a pictorial representation of the mechanisms (see Fig. 8.1). The first proposed pathway involves stretches of the unit cell of the diamond into a tetrahedral shape which corresponds to a distortion into the {100}-direction of the diamond. Using this technique the four-armed junctions of the diamond are effectively split into two three-armed junctions of the gyroid, which are connected by a link, then corresponding to the {110}-direction (see also Ref. [167] for the transition mechanism of the associated geometrically centred skeletons). A similar idea was already suggested earlier by Sadoc and Charvolin [580]. The second transition route from the diamond to the gyroid, which is induced by rhombohedral distortions of the unit cell and contains the P-surface structure as an intermediate state, was considered energetically less favourable in regards to curvature and packing homogeneity [91]. Here, we also remark mathematical studies by Chen and Weber on further transition models [94].

8.1.3 Phase stability and phase transitions between diamond and gyroid in soft matter physics

Despite all the different routes mentioned above, the exact structural transformation at the phase transition between different cubic bicontinuous structures is still not a completely solved phenomenon in soft-matter systems. Those transformations are, for example, observed in various lipid [309, 581] and copolymer systems [310, 582, 583, 584, 585]. Nevertheless, it is still valuable to take a closer look at how the double diamond is induced in amphiphilic systems to implement a suitable plan to form cubic phases other than the gyroid by pear-shaped particle in PHGO systems. In Sec. 1.3.2 we already commented briefly on mechanisms both observed in the lipid-water and copolymer systems. In both cases, the greater spatial heterogeneity of the diamond is accommodated by introducing additional material. For instance, in lipid-water systems the aqueous channels are swollen by increasing the water concentration [163, 165] and, therefore, shift for the gyroid into a morphology with $Pn\bar{3}m$ symmetry (see Fig. 8.2). On the other hand, in copolymer melts the extra material is added in the form of homopolymers which stabilise the double diamond [71, 190]. The additional particles accumulate at the backbone of the labyrinth-like domains which otherwise cannot be homogeneously occupied by the di-block copolymers without causing unphysical gaps or greatly penalised chain stretches to reach the distant regions of the channel domain.

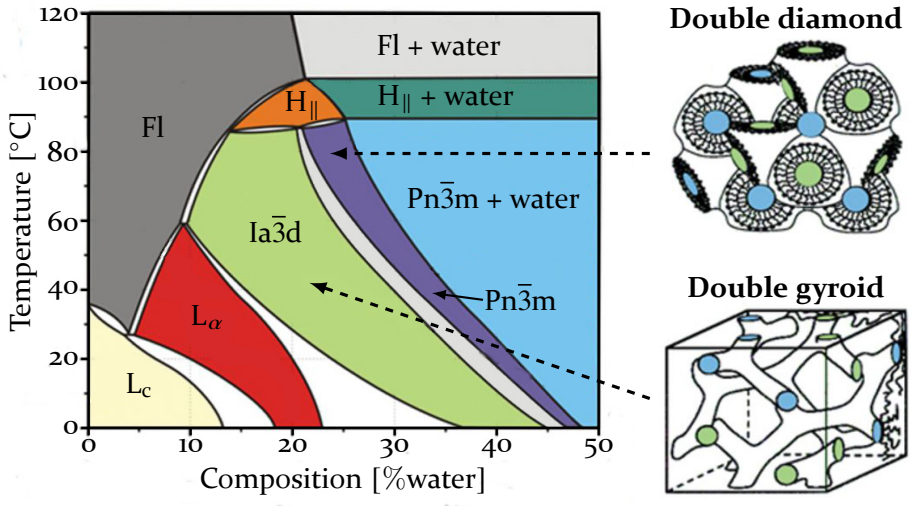

Figure 8.2: The phase diagram of lipid-water systems in terms of water concentration and temperature is shown. By increasing the water content form the Ia$\bar{3}$d double gyroid structure the bilayer arrangement eventually transitions into the Pn$\bar{3}$m double diamond configuration. Adapted, with permission, from from [165].

Inspired by those findings, we attempt to tweak the self-assembly of the PHGO particle model such that the system equilibrates into a diamond formation instead of the gyroid. Thus, we extend the monodisperse PHGO particle systems in the following and inject solvent particles into our simulations. We use the simplest solvent model, spherical particles, that interact via hard interactions with the pear-shaped particles and with each other (hard sphere fluid). Spheres are a convenient way to include additional matter without unnecessarily complicating the mixture by a second aspherical colloid and to potentially resolve the geometrical frustrations which prevent the formation of the double diamond in the one-component system.

8.2 The dry limit of PHGO pear-sphere-mixtures: The Pn$\bar{3}$m diamond

In the first part of this section, we acquaint ourselves with the additional particle species by staying close to the one-component pear-shaped particle system and studying the "dry limit" of the mixture with the sphere solvent at very low sphere concentrations. The motive behind restricting us to very

low solvent volume concentrations Φ_{sph} is driven by the intention to create a double diamond bilayer structure similar to the observed gyroid structure. Here, we make two intuitive guesses which probably have to be fulfilled in the case that the double diamond is indeed achievable by adding a second particle species. If the number of spherical particles is too small, the solvent can not take effect and only leads to defects in the gyroid. The second aspect to consider is that an exceeding sphere concentration likely leads to the spheres interfering with the pear arrangement by a greater margin and, hence, destroying the integrity of the pear bilayers. But also two-phase coexistence or phase separation might be possible (see Sec. 8.3). We show that $\Phi_{\text{sph}} = 1\text{–}2\ \%$ spheres stabilize the double diamond phase.

8.2.1 Double diamond structures in PHGO pear-sphere-mixtures

Simulation set-up

To gather the simulation data, we perform MD and MC simulations of pear-shaped particles with a small concentration of hard spheres. For the interactions between the particles we use both hard-core (MC) and the WCA potential (MD) with the PHGO approximation (see Eq. (2.17)). Here we want to highlight again that even though this overlap function results in a sufficiently accurate hard body interaction between pears and spheres, the pear-pear interaction reveals some inaccuracies in terms of the Beziér curve representation. Those can cause the blunt ends of pears to slightly overlap and reach areas which cannot be obtained by hard spheres (see especially Sec. 2.2 for a detailed study). Moreover, the overlap volume of two pears is overestimated when the particles are neither parallel nor antiparallel. The simulations are carried out using the same methodology as in Sec. 4.1, adjusted to include the hard-sphere solvent. The system is set up within a cubic box with three-dimensional periodic boundary conditions and volume V_{box} and analysed at an overall global packing fraction

$$\rho_g = \frac{N_{\text{pear}} \cdot V_{\text{pear}} + N_{\text{sph}} \cdot V_{\text{sph}}}{V_{\text{box}}} = 0.56. \tag{8.2}$$

The particle volume ratio between a single solvent sphere and a pear-shaped colloid is chosen to be $v = \frac{V_{\text{p}}}{V_{\text{sp}}} = 9$ such that the spheres are small enough to accommodate geometrical defects. Furthermore, the aspect ratio of the pear-shaped particles k is set to 2.75 and the tapering parameter k_θ

tapering angle is set to 3 (this corresponds to a tapering angle of 19°). Here, we decided to deviate from the otherwise used reference pear-shape with $k = 3$ and $k_\theta = 3.8$, as the system with slightly shorter particles, seems to equilibrate into a diamond-like structure faster, such that we were able to obtain more data. However, the following observations also hold for particles with the reference pear-shape used for the gyroid simulations in Sec. 4.1. The smaller particle shape is shown, to scale, in Fig. 8.3.

The mixture is in the dry limit with a low number of spheres $N_{\text{sph}} = 90$ and a majority of pears $N_{\text{pear}} = 890$ ($n = \frac{N_{\text{pear}}}{N_{\text{sph}}} = \frac{89}{9}$).[2] The number of particles are not randomly chosen. Instead they are selected such that the simulation box theoretically holds a 2×2×2 double diamond unit cell arrangement, in case that the pear-shaped particle systems satisfy the Bonnet ratio $\frac{a_G}{a_D} = 1.576$ [67, 90, 578]. Here, a_G denotes the unit cell size of the gyroid phase in the monodisperse PHGO particle system which has been obtained in Sec. 4.2.2 whereas a_D symbolises the equivalent unit cell size of the anticipated double diamond phase. Additionally, the MD simulations are performed in the NVT-ensemble with adjustable walls, time steps $\Delta t = 0.0015$ and dimensionless temperature $T = 1$ (the Boltzman constant is set to $k_B = 1$). All simulations are run for $20,000,000$ time steps. The systems seem to reach sufficient equilibration to identify the diamond phase after around $5,000,000$ steps.

The simulations are initiated from a low density $\rho_g = 0.3$ and slowly compressed to the final packing fraction (see Eq. (8.2)) where the double gyroid forms in a monodisperse pear-particle system ($\rho > 0.54$). Similarly to the previous simulations, we can ensure by advancing the assemblies from an unordered isotropic phase that the developed diamond macrostructure is not enforced by the initial conditions. Additionally, we also produced an artificial smectic phase as an initial starting structure which proves to be unstable and eventually turns also into the double diamond structure.

Stability of the double diamond

In all our simulations, generated from different isotropic initial configurations a similar spatial arrangement of pear-shaped particles as described previously for the double gyroid is obtained after equilibration (see Fig. 8.3).

[2] For pears with $k = 3$ and $k_\theta = 3.8$ the combination of $N_{\text{sph}} = 82$ and $N_{\text{pear}} = 820$ has to be used to get similar results

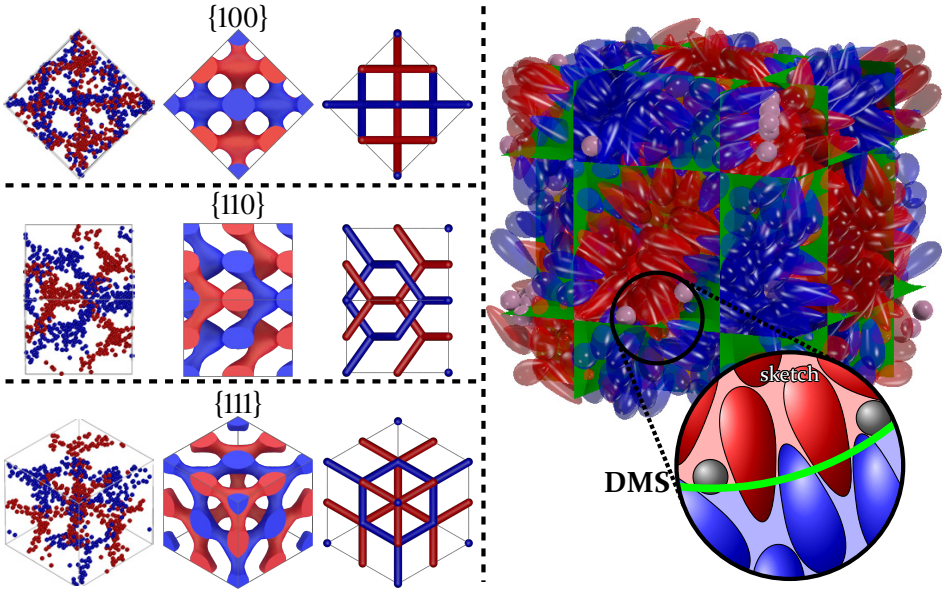

Figure 8.3: An assembly of 890 pear-shaped particles and 90 hard-core spheres forming the 2×2×2 unit cell of the double diamond structure ($k = 2.75$, $\alpha = 19°$, $\rho = 0.56$, $v = 9$,$n = \frac{89}{9}$). Positions of the blunt ends determine to which of the two distinct domains (red/blue) the particle belongs. The green surface represents the double diamond minimal surface (DMS) which separates these domains. The spherical segment is a two-dimensional sketch, recreated from the indicated part in the pear-shaped particle system to highlight the special arrangement of particles. On the left, only the position of the blunt ends is depicted as spheres to showcase the labyrinth-like channels (first column). The system is shown in the {100}-, {110}- and {111}-direction and compared with the channel domain (second column) and the skeletal-graph (third column) of the double diamond structure.

The particles interdigitate with their thin ends at the minimal surface interface and form two network domains with their blunt ends as sketched in Fig. 8.3. The interdigitation, where pears effectively protrude through the minimal surface, collectively leads to an effectively wider space per molecule near the minimal surface. Like in the gyroid phase this finding is fundamentally different to the intuitive interpretation of the molecular shape concept [50, 244], which holds for lipid or diblock copolymer systems, where for negatively curved surfaces the space occupied by an individual particle is largest near the membrane and decreases in the normal direction (see Sec. 4.3.4).

The resemblance to the double diamond structure becomes visible by applying the clustering algorithm, described in Sec. 3.4.4, to the particle mixture and extracting both labyrinth domains. In particular, this procedure

reveals that the morphology indeed corresponds to a 2×2×2 unit cell of the bicontinuous Pn$\bar{3}$m double diamond network structure. The two networks are shown on the left-hand side of Fig. 8.3, where only the positions of the blunt ends are depicted by spheres. The resulting set of points can be divided nicely into two regions by the double diamond minimal surface. Additionally, the set exhibits the typical 4-branched notes and the 2- and 6-fold rotation symmetry along the {100}- and {111}-direction, respectively (see Fig. 8.3). The two-dimensional projections of the point cloud encoding the blunt end coordinates lead to square ({100}-direction) and hexagonal ({111}-direction) patterns. Those match perfectly with the graph of the cubic diamond structure. Likewise, the 2D projections in the {110}-direction coincide to a high degree as well.

We have observed the spontaneous formation of the double diamond structure in simulation boxes of size $(1a_D)^3$ and $(2a_D)^3$. For a simulation box with size $(4a_d)^3$ ($N_{\text{pear}} = 7120$, $N_{\text{sph}} = 720$), we have not achieved a clear identification of the symmetry of the double diamond via compression form an isotropic phase. Even though we still observe interdigitation, the system forms single nodes characteristic for both the double diamond (four branched nodes) and the double gyroid (three branched nodes). This observation is also made for large systems where the number of particles is not roughly commensurate with the Bonnet ratio. Those findings lead to the assumption that the particle number/size ratio to form a pure double diamond phase might not be chosen perfectly. Smaller systems (like the 2×2×2 system) can distribute the extra material more easily within the simulation box and consequently, conform to a potential lack of additional material better. In contrast, an insufficient distribution of the solvent spheres within larger systems can locally cause areas with a deficit concentration of spheres expressed in the formation of a gyroid-like architecture, and some areas with a larger concentration of spheres sufficient to enable stabilisation of a diamond-like channel system (the mechanism will be discussed in the next section).

Another explanation, why the diamond phase is not observed for large systems, might be that the diamond phase is dynamically harder to reach and needs many computational steps to equilibrate. To resolve this possible issue, we create another simulation run where we already start from a 4×4×4 double diamond unit cell arrangement. Here, a snapshot of the equilibrated 2×2×2 diamond system is copied eight times, where each copy serves as a

basis for one octant of the initialised 4×4×4 configuration. By propagating this system in time, the double diamond stays stable even after 20,000,000 simulation steps (see Fig. 8.4), but also exhibits the fluid characteristics of a liquid crystal phase. Even though this should not be interpreted as a final proof that the double diamond is indeed the final state of initially disordered systems, these simulations indicate that the diamond phase is at least metastable.

$Pn\bar{3}m$ symmetry

Furthermore, evidence of the double diamond structure and the $Pn\bar{3}m$ symmetry is provided by the three-dimensional structure factor $\mathbf{S(k)}$ of the 4×4×4 unit cell arrangement. For this we apply the same Fast Fourier Transformation algorithm as described in Sec. 4.2.1 to the density profile of the blunt end point cloud which represents the two channel domains. In Fig. 8.4 representative 2D projections of the resulting scattering pattern are depicted. They reveal a 6- and 3-fold rotational symmetry (plane orbifold group: $*632$) in the {111}-direction, 4-fold rotational symmetry in the {100}-direction (plane

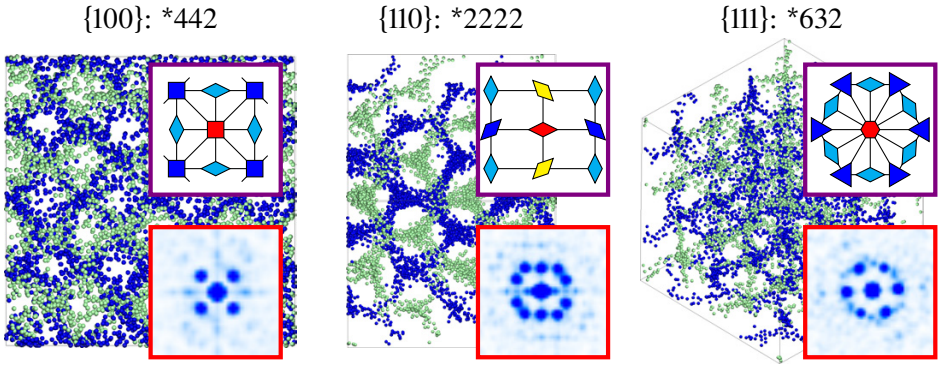

Figure 8.4: A representative snapshot (only the positions of the blunt ends are considered) of a system of $N_{\text{pear}} = 7120$ PHGO particles and $N_{\text{sphere}} = 720$ spheres in a 4×4×4 unit cell arrangement of the double diamond ($\rho_g = 0.56$). The pears ($k = 2.75$ and $k_\theta = 3.0$) are $v = 9$ times larger in volume than the spheres. Already starting from a double diamond, the system seems thermodynamically stable. The high-symmetry projections of the three-dimensional scattering patterns are depicted in the red boxes. They reveal a 4-fold symmetry in the {100}-direction, a 2-fold symmetry in the {110}-direction and a 6-fold symmetry in the {111}-direction characteristic for the $Pn\bar{3}m$ double diamond. In the violet, boxes are the corresponding cell structures of the symmetry groups. Hexagons represent 6-fold rotations, squares 4-fold rotations, triangles 3-fold rotations and rhombi 2-fold rotations. The black lines describe mirror lines [586, 587, 588, 589].

orbifold group: ∗442) and a 2-fold symmetry in the {110}-direction (plane orbifold group: ∗2222).

Moreover, the reciprocal lattice vectors are determined via the three-dimensional scattering data. As the lattice vectors form a primitive cubic lattice in Fourier-space, also the channel structure in real space follows a primitive cubic symmetry. Thus, we identify the space group as Pn$\bar{3}$m, matching the symmetry group of the double diamond.

8.2.2 Stabilisation mechanism of the double diamond

To investigate why the double diamond is favoured over the gyroid, we have to take a closer look at the position of the spherical solvent particles. Like the arrangement of the pear-shaped particles also the dominant location of the solvent particles in the simulations turns out to interestingly differ from intuition and earlier findings in other double diamond forming systems where the packing frustration is released by the solvent/additional material by swelling the network domain. In our simulation, this would correspond to the hard spheres accumulating at the blunt ends of the pear-particles and fill space within the channel domains.

The two-dimensional pear-sphere pair correlation function, however, reveals a mostly opposite behaviour (see Fig. 8.5). In the isotropic phase, the spheres distribute uniformly around the pear particles without any significant preference for specific locations (Fig. 8.5a). By increasing the density, however, the spheres are 'pushed' towards the thin ends of the pears where, as seen in Fig. 8.5b, a higher concentration of spheres can be observed. This observation coincides with the aggregation of spheres around the minimal surface (Fig. 8.6a shows a symmetric bell-shaped distribution), such that the solvent fills additional space where the pears interdigitate. Note here that this mechanism benefits from the earlier addressed small disparities between the perfect hard body interactions and the used PHGO potential. Consequently, we have to take the role of minor non-additivity effects between pear-shaped particles into account, which probably enhance the overall tendency of spheres to gather around the thin rather than the blunt ends of pears.

To determine the location of the spheres in more detail, we identify the Gaussian curvature of each point on the diamond minimal surface which

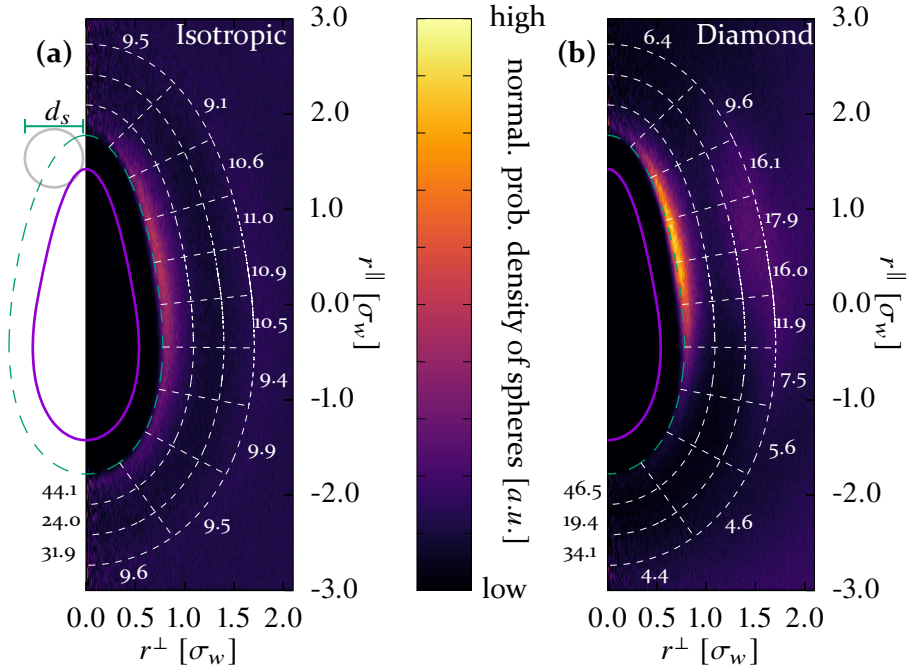

Figure 8.5: The two-dimensional pear-sphere-correlation function $g(z, r)$ of a system in the isotropic phase at $\rho_g = 0.45$ (a) and the cubic diamond phase at $\rho_g = 0.56$ (b) is shown. z is the distance between the pear's and spheres central position along the orientation vector of the pear-shaped particle. r is the radial component of the distance between the pear and sphere centre. The dashed white lines determine the parallel surface of the pear particles. The small numbers indicate the distribution of spherical particles within a given radial (black) or polar (white) sector in percentage. Only particles lying within the outmost drawn parallel surface are considered.

is closest to the centre of a hard sphere. Fig. 8.6b indicates that the majority of spheres are located around areas with high negative Gaussian curvature. This observation is consistent with the local effect of spheres on their surrounding pear particles. By aggregating close to the thin ends of the pears the spheres act as 'disruptive' elements between the interdigitating pear sheets and hinder pears from protruding into the opposite domain (see the sketch in Fig. 8.3). However, they can also be seen as a filler material which allows neighbouring pears to arrange in a much wider angle and, therefore, induces a greater amount of negative curvature in the system.

This mechanism bears some similarity to lipid bilayers which encapsulate biomolecules like peptides or proteins [590, 591]. In these systems, it is widely assumed that the proteins are inserted within the membrane-like

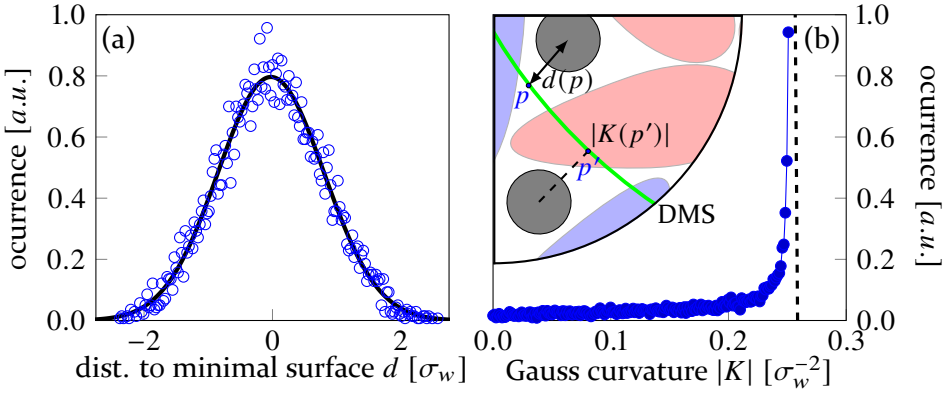

Figure 8.6: (a) The distribution of spheres around the diamond minimal surface is displayed. Therefore, the distance $d(x) := \inf\{\text{dist}(x, q)|q \in \text{DMS}\}$ of each solvent particle to its closest point $p \in$ DMS where $\text{dist}(x, p) = d(x)$ on the diamond minimal surface (DMS – indicated in green) is calculated. Positive/Negative distances imply that the sphere lies in the red/blue channel domain. The black line indicates a Gaussian fit to highlight the bell-shaped distribution. (b) The position distribution of the spheres in regards to Gaussian curvature is plotted. Here, the absolute value of the Gaussian curvature $|K(p)|$ at its closest point p on the DMS is assigned to each solvent particle $|K(x)| := |K(p)|$. The dashed line indicates the maximal curvature which also responds to the maximal curvature in the gyroid phase in Sec. 4.3.4.

'wedges' and act as either curvature relief or a curvature generation agents [592, 593, 594]. The resemblance becomes even more apparent by considering studies of monoolein bilayer phases which transition from the gyroid to the diamond morphology by integrating specific membrane proteins into the bilayers [595, 596]. It has been suggested theoretically and computationally that in those systems the additives separate into specific locations on the minimal surface, like the areas of lowest or highest negative Gaussian curvature [597, 598, 599]. However, experimental studies on encapsulated biomolecules within the diamond phase indicate in contrast that proteins do not showcase any preferential segregation in terms of Gaussian curvature [600, 601].

The integration of spheres into the "pear-bilayer" to create curvature might also be an explanation for the stabilisation and preference of the double diamond phase over the double gyroid. In one of our earlier chapters, in particular Sec. 4.3.4, we determined a correlation between the interdigitation depth and the local Gaussian curvature of the system. The further pears reach into the realm of the opposite channel system; the more curvature is contributed to the interface between both pear particle clusters. In case of

the gyroid and diamond minimal surface formed by the pear-shaped particle systems, the maximum negative Gaussian curvature is roughly the same. As we set up the simulation box such that the unit cell length between the diamond a_D (half of the simulation box size) and the gyroid phase of the monodisperse pear-shaped particle system a_G corresponds to the ratio obtained by the Bonnet transformation the underlying minimal surfaces are isometric. Isometric minimal surfaces are locally indistinguishable and, therefore, preserve area and Gaussian curvature [90].

However, the isometry between both structures causes two issues in forming the diamond structure, which can not be resolved solely by pear particles simultaneously. In the diamond phase, pears are not able to interdigitate as deeply as in the gyroid phase without creating gaps in the channel domain. Similarly, by filling the gaps with their blunt ends, the pear bilayers are less interdigitated such that they lose their capability to generate enough curvature via interdigitation. Consequently, there are technically two possible mechanisms of how additional material can stabilise the double diamond:

1. The spheres fill the gaps in the channel domains, such that the pears can penetrate the minimal surface efficiently.

2. The pears occupy the space around the labyrinthine backbone of the double diamond with their blunt ends. The system then compensates its loss in creating high negative Gaussian curvature by interdigitation by placing the solvent at the minimal surface and by increasing the amount of curvature locally accordingly (probably more favourable).

8.3 The dilute limit of PHGO pear-sphere mixtures

Our strategy to induce new phases upon the addition of a spherical solvent turned out to be fruitful, evident in the formation of the double diamond phase. However, so far only a tiny fragment of the parameter space of the pear-sphere system has been investigated. Therefore, the behaviour of more diluted mixtures with a solvent size of $v = 9$ outside the dry mixture limit is analysed in the following by changing the number ration n and the solvent content is increased over 2 % in our simulations.[3] Here, we want to

[3]Another route to change the sphere volume concentration is by shifting the size ratio between pear-shaped particles and hard spheres v. Although this strategy is very intriguing and should be investigated in the future, we decide to take the alternative and more obvious path by changing the number ration n instead. This approach is probably the more physical

stress that the self-imposed limitation to only study the n-dependence, implies that we cannot explain pear-sphere mixtures fully in the next sections.[4] Thus, the following should be seen as a larger preliminary investigation for future studies to come.

8.3.1 Phase separation

In this part of our studies, several MD simulations with different sphere concentrations are performed where the total number of particles N=N_{pear}+N_{sph} = 2500 is kept constant. However, we first cover a range where the pear-shaped particles with $k = 3$ and $k_\theta = 3.8$ are still the dominant component ($\Phi_{\text{sph}} < 0.15$) to increase the solvent contribution to the free energy slowly. We start from a wholly mixed isotropic phase and compress the systems to densities where the spontaneous formation of the PHGO particles into TPMS structures has been observed. Otherwise, the same protocol as in the dry limit has been used.

All systems within this composition range reveal warped, interdigitated bilayer phases, which are of the same essence as those observed in the gyroid and diamond phase. This can be seen in the first column of Fig. 8.7, where some representative structures are depicted for a global density of $\rho_g = 0.56$. However, already at first glance, it is evident that the bilayer formations do not exhibit the same degree of symmetry and are traversed by the sphere solvent. This behaviour is also shown by the density distribution of the blunt ends. Even though the coordinates of the blunt ends still suggest a complex channel network with 3- and 4-branched nodes, the clustering algorithm fails to separate the pear-shaped particles into two distinct clusters and instead detects a single large, self-intertwined and disordered "sponge"-like network structure (see the second column in Fig. 8.7).

Those observations lead to the conclusion that for mixtures with $\Phi_{\text{sph}} > 0.02$ the systems apparently cannot accommodate the additional spheres within the ordered gyroid or diamond configurations. However, the spheres are not randomly distributed within the simulation box either. From the

method as it can be interpreted as simply increasing or decreasing the content of the same solvent species.

[4] To achieve such a complete description, additional comprehensive studies of different combinations of v, k and k_θ have to be executed, which are not subject to this chapter.

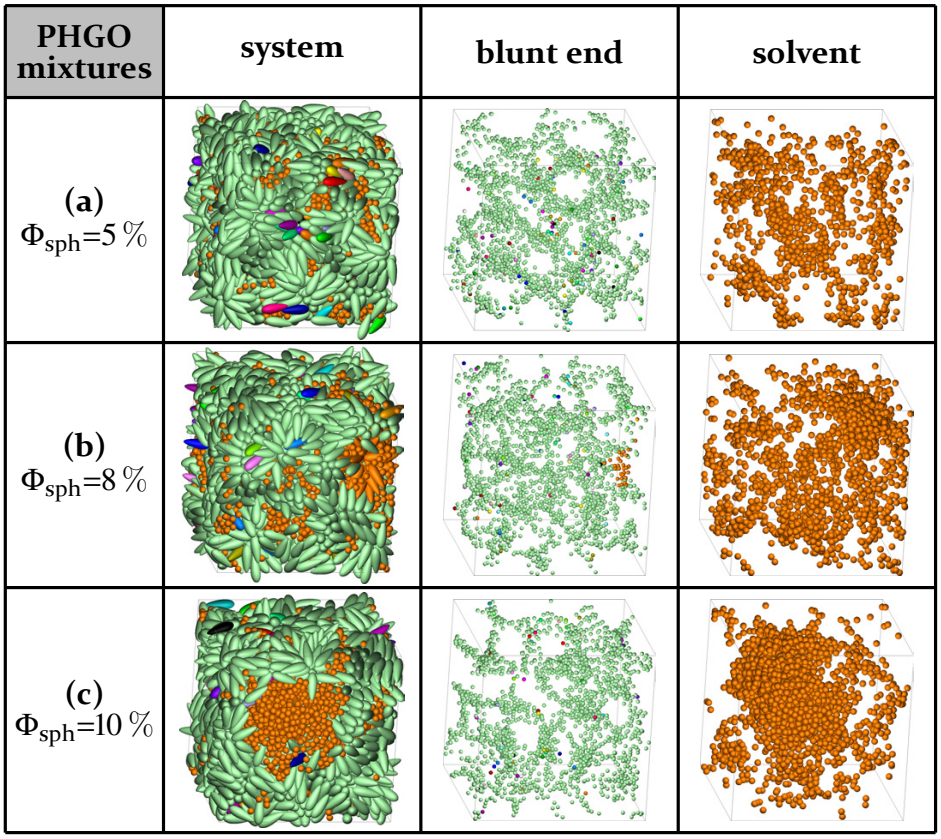

Figure 8.7: Representative mixtures of PHGO pear-shaped particles ($k = 3, k_\theta = 5.4$) with a hard sphere solvent ($v = 9$) at a global density $\rho_g = 0.56$ for solvent concentrations $\Phi_{\text{sph}} = 0.05$ (first row: $N_{\text{pear}} = 2164, N_{\text{pear}} = 1025$), $\Phi_{\text{sph}} = 0.08$ (second row: $N_{\text{pear}} = 2096, N_{\text{pear}} = 1640$) and $\Phi_{\text{sph}} = 0.10$ (third row: $N_{\text{pear}} = 2050, N_{\text{pear}} = 2050$). The structures are illustrated in the cluster representation (first column) and the blunt end representation (second column) where the colors indicate the cluster affiliation. In the third column only the sphere solvent is shown.

illustrations in the third column in Fig. 8.7 one gains the impression that the solvent particles form local clusters which become larger for higher solvent concentrations.

To investigate this further, we determine the number of sphere clusters M and the number of spheres within the largest cluster m for the different concentrations during the compression process. Here we implement a similar clustering algorithm as described in Sec. 3.4.4, with the only difference

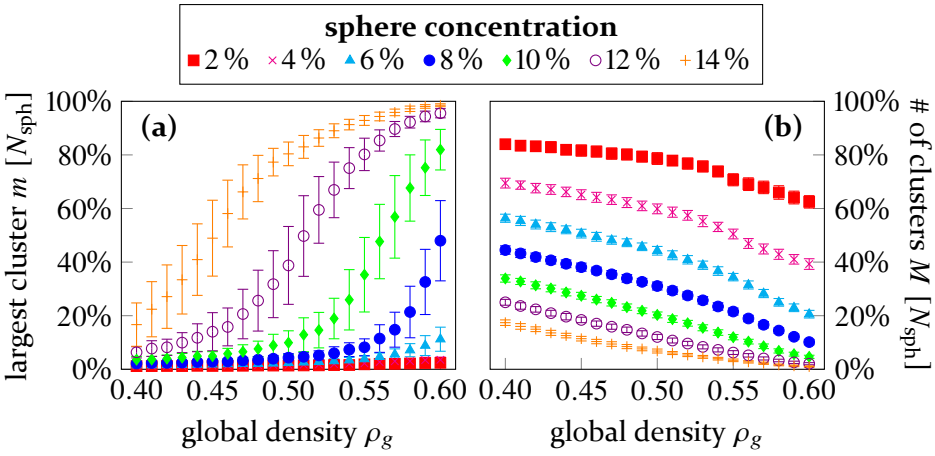

Figure 8.8: The phase separation in mixtures of PHGO particles ($k = 3$ and $k_\theta = 3.8$) and a hard sphere solvent (pear-sphere volume ratio $v = 9$) is traced for different solvent concentrations Φ_{sph} during the compression. Here the process of (a) the number of spheres within the larges sphere cluster m in % of the total particle number N_{sph} and (b) the number of sphere clusters M is determined. The number of overall particles within the simulation box is set to $N = N_{pear} = N_{sph} = 2500$, for all systems. All systems exhibit demixing upon compression.

that instead of the position of the pear blunt ends the coordinates of the solvent spheres generate the point pattern to be clustered. Here, the sphere particles are assigned to the same group if they are within a cut-off radius which we set to $r_{cut} = 3r_{sph}$.

The results are plotted in Fig. 8.8. For low densities, all mixtures exhibit many small clusters where most of them consist only of one single sphere. Hence, no particular clustering mechanism is indicated. The predominant amount of single particle clusters implies that the pears and spheres do not phase separate in the low density state. However, when compressing the system and especially when the pears begin to arrange into bilayers (indicated by the kink in M Fig. 8.8b), also the spheres start to accumulate leading to larger and fewer clusters. Here we also note that systems with smaller solvent concentration tend to aggregate into multiple clusters of equal size, whereas for a more significant amount of spheres ($\Phi_{sph} > 0.08$) the entropy is maximised by generating one single large sphere domain. Hence, the system divides the two particle species by forming regions dominated by pears and regions enriched by spheres. Note that finite size effects have to be considered here. It might be possible that the demixing is hindered by fixed finite

number of particles N_{pear} and N_{sph} within the simulation such that the plots in Fig. 8.8 might vary.

This mechanism gives the pears an environment to locally assemble into curved bilayers which are hardly disrupted by the solvent. However, those bilayers have to accommodate the large sphere clusters which act as notable defects in the network structure and destroy the integrity of the highly symmetric TPMS configurations. A similar kind of phase separation is also observed in mixtures of hard spheres and aspherical particles where hard rod-like particles shed the hard sphere solvent into separate regions to form nematic phases [482, 489, 494]. Also in simulations of mixtures of spheres and HGO ellipsoids, which are the inversion symmetric equivalent of the PHGO pear-shaped particles, phase separation has been detected [602].

8.3.2 "Inverse" micelle structures

The phase separation in the previous systems and the spontaneous cleansing of solvent particles from the pear-enriched regions are distinct indications that the assembly into interdigitated bilayers is an entropically very favourable PHGO pear-shaped particle arrangement. The formation of network-like domains, on the other hand, is only feasible in mixtures consisting predominantly out of pear-shaped particles. It is quite intuitive to assume that there have to be enough pear-shaped particles present to enable the collective generation of elaborate labyrinthine network structures. Thus, we are interested in mixtures on the other end of the concentration spectrum where the spherical solvent embodies the dominant particle species and the number of pears is insufficient for channel creations.

In Sec. 6.3.2 we already discussed one variant of highly diluted mixtures, namely two PHGO pear-shaped particles within a pool of spheres. Here, we observed that the pears either arrange in an anti-parallel or a V-configuration (see Fig. 6.8c+d) due to depletion attractions which are consistent with the interactions between two neighbouring pears within bilayers. Proceeding from this extreme limit we perform MD simulations with $\Phi_{\text{sph}} = 0.9$ ($N_{\text{pear}} = 50$, $N_{\text{sph}} = 4050$) to investigate how those two-particle-interactions change by adding more of the minority component. The pear shape is defined by $k = 3$ and $k_\theta = 3.8$. The other parameters are the same as previously.

The simulations start from the isotropic phase ($\rho_g = 0.2$) and are first slowly compressed to a global density of $\rho_g = 0.42$, where the pear-shaped

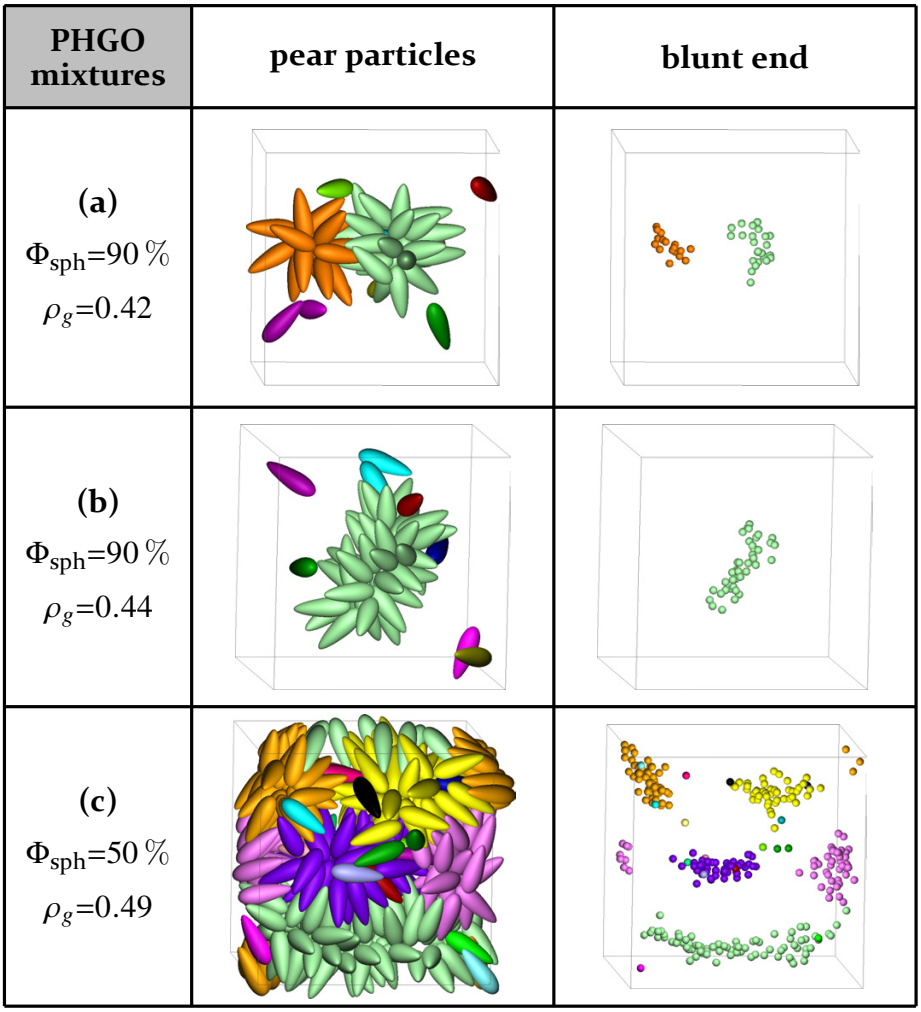

Figure 8.9: The formation of inverse micelles in pear-sphere-mixtures dominated by the hard sphere solvent (Φ_{sph} = 0.9, N_{pear} = 50, N_{sph} = 4050) at (a) a global density ρ_g= 0.42 where two separate micelles are observed, and (b) at ρ_g= 0.42 where the two clusters merge into a single strand-like micelle. (c) The inverse micelles form larger geometries in systems with a higher pear content (Φ_{sph} = 0.5, N_{pear} = 304, N_{sph} = 2736) and indicate hierarchical self-assembly. The shape of the pears is defined by k = 3 and k_θ = 3.8. The volume ratio between pears and spheres is set to v = 9. Only the pear-shaped particles are depicted. In the simulations the void space is filled with the solvent.

particles start to accumulate noticeably. After equilibration, the pear-shaped particles form two clusters which we will refer to as “inverse micelles” and are shown in Fig. 8.9a. Here the particles come together with their thicker

moiety which effectively constitutes the centres of the spherical, micellar mesostructures. On the other hand, the pear-shaped particles face the solvent with their thin parts and, thus, establish a spiky interface between the inside of the inverse micelle and the diluted outside. Each of these micelles consists of roughly 19 ± 4 pears.[5]

The observed assembly into inverse micelles is again contrary to the formation of micelles, for example in lipid-water systems above a critical micelle concentration [603, 604, 605]. Additionally, it can also be described as counterintuitive. By simple geometric arguments based on excluded volume ideas (see also Chap. 6), amphiphilic liquid crystal particles adopt local morphologies with a shape parameter which is tapered towards and not away from the centre of the micelle [50]. With this shape parameter, the molecules can successfully fill the inside of the micelle and additionally create a compact packing (see Fig. 1.1). The pears expose a larger surface area to the solvent by placing the pointy tips at the outside rather than the blunt ends. This specific orientation suggests a higher surface tension.

However, the inverse micelle formation is in accordance with the depletion behaviour of PHGO particles and hence, has to be attributed to the non-additive features of the PHGO contact function once more. The highly anisotropic effective attraction of the PHGO pears causes the spheres to accumulate near their tips. Thus the whole micelle cluster can be interpreted as an array of pairs of particles each arranged in the V-configuration which is stabilised due to the non-additive overlaps of the pears' blunt ends.

The simulations are reminiscent of micellar formations which have been observed in colloidal systems of asymmetric dumbbells [240]. Here, the surface of the smaller spherical part is roughened, such that the depletion interactions between the two smooth components (the larger spheres) are greater than between other parts of the dumbbell. This effect can be nicely compared to the non-additive features in our simulations and even seen as a valid realisation of non-additivity in experiments in general. The difference in surface roughness leads to similar clusters of dumbells where the larger spheres are placed in the centre.

After the two micelles are formed both mesostructures act as collective entities, approach each other, and eventually interdigitate with their spikes.

[5] We have analysed a total of 1000 micelles formed in 20 different simulation runs

This attraction is attributed to their depletion forces. By increasing the density over $\rho_g > 0.44$ the micelles merge into a larger, elongated spiky assembly (see Fig. 8.9b). In those configurations, the blunt ends meet on a line rather than one central point. It might be possible to relate this arrangement of the bunt ends to packings of hard or soft spheres within a tight cylindrical confinement [606, 607, 608, 609, 610]. Here, the achiral spheres break symmetry spontaneously by building chiral arrangements for some ratios between sphere radius and the radius of the confining cylinder. Also, some of the elongated pear micelles exhibit a slight twist along the prolate axis which might be referred to one of the aforementioned sphere packings as an underlying configuration. However, it is challenging to determine this twist exactly as the elongated inverse micelles are very short and their backbones are not necessarily straight but can be bent.

The clustering and merging of the micellar entities suggest that the self-assembly processes of highly diluted PHGO particle systems follow a hierarchical protocol. First, the pears produce some micellar structures which then themselves act as components for larger geometries. The hierarchical self-assembly becomes even more apparent by shifting the mixture concentration in favour of the pear-shaped particles to $\Phi_{\text{sph}} = 0.5$. In this regime, the system forms a block of pears which consist of multiple small inverse micelle clusters. It is conceivable that for larger system sizes this configuration equilibrates into a gyroid or diamond structure surrounded by the sphere solvent, comparable to cubosomes [76, 164, 611, 612, 613, 614, 615]. This hypothesis, however, can not be resolved in this thesis due to computational constraints.

8.4 Conclusion and outlook

To summarise, we have shown that the introduction of small quantities of hard spheres appears to stabilise the bicontinuous $Pn\bar{3}m$ cubic diamond phase in pear-shaped particle systems (note the caveat of equilibration issues for large systems $> 2\times2\times2$ in Table 8.1). In this stabilisation process, the system showcases a new way to overcome the additional spatial heterogeneities in relation to the double gyroid phase, namely by placing the spheres around the minimal surface and aiding the system to create surfaces of higher negative Gaussian curvature.

Pear shape		Particle number		Protocol	$Pn\bar{3}m$ phase	Unit cell	Ref.
k	k_θ	N_{pear}	N_{sph}				
2.75	3.0	894	89	compression	✓	2×2×2	Fig. 8.3
				init. smectic	✓		
		7152	712	compression	✗	–	
				init. smectic	✗	–	
				init. diamond	✓	4×4×4	Fig. 8.4
3.0	3.8	820	82	compression	✓	2×2×2	
				init. smectic	✓		
		6560	656	compression	✗	–	
				init. smectic	✗	–	
				init. diamond	✓	4×4×4	

Table 8.1: Simulation protocols where the formation of the $Pn\bar{3}m$ double diamond phase in PHGO pear-sphere mixtures are successfully achieved (✓) and where the spontaneous organisation failed (✗). The list is dedicated to mixture with a hard sphere solvent $v = 9$. The diamond phase is obtained at a density of around $\rho_g = 0.56$.

This observation gives rise to an alternative perspective on self-assembly processes. In terms of new synthesis strategies, our results can give an outlook to new possible methods to form the double diamond out of the gyroid morphology. For example, some molecules forming cubosomes can swell specific domains of the bicontinuous structure by addition of a low concentration of a solvent [613, 615]. Designing molecules with solvophilic ends which are placed within the separating matrix domain rather than within the channel domain may bear the capability to form double diamond nanostructures in a similar fashion as the pear-shaped particle system.

Furthermore, we have shown that pear-dominated mixtures phase separate into pear and multiple sphere enriched domains for sphere concentrations $\Phi_{sph} > 0.08$. Even though neither the diamond nor the gyroid structure could be recognised, the demixing was identified as a mechanism to facilitate the spontaneous and advantageous formation of warped bilayer structures. In this way the sphere solvent does not interrupt the interdigitation of pears, however, acts as several defect agents, which have to be incorporated by the bilayers and consequently alter or randomise the underlying network morphology.

Lastly, we also studied highly diluted mixtures, where the PHGO pear-shaped particles are the minority component and unable to form network structures. We observed the formation of inverse micelles, where the thicker moiety forms the centre. This mesostructure could be attributed to the presence of non-additive features in the PHGO contact function. The slight overlaps of the pear shapes enable the particles to assemble in a geometrically counterintuitive fashion in contrast to micelles in nature and chemistry, which adopt a shape parameter with the thick ends at the micelle-solvent interface. The micelles themselves act as colloidal particles and assemble into even larger structures indicating hierarchical self-assembly.

The observed self-assembly in a hierarchical order raises the question if also the gyroid in the monodisperse PHGO particle system and the diamond in the dry mixture limit can be recognised as hierarchically structured phases? We also observed a significant clue in the isotropic phase in Sec. 5.1, which reinforces this assumption. At densities slightly below the transition density between isotropic and gyroid phase, we reported the existence of small thread-like pear clusters which were identified as precursors of interdigitated bilayer formation. Those small clusters, however, can be equally constructed as a first stage of the self-assembly which then combine into the final bicontinuous channel structure. More efforts are needed to examine if the gyroid is indeed built form specific sub-cluster components.[6]

Inverse micelle stability in two-dimensional NAHPR pear-shaped particle systems

As a closing remark, we want to take up the threads of the discussions made in Sec. 6.4 and address once more the potential route how to realise phases, observed in PHGO particle systems, using pear interactions based on the HPR model. In this chapter, we established the approach to introduce non-additive features to the HPR contact function to which we then referred to as the NAHPR-model. We have shown that some of the depletion behaviours of the PHGO particles have been successfully mimicked, whereas other issues

[6] One possible method is the analysis of topological properties of the gyroid using persistent homology [616, 617, 618]. This mathematical tool, where information about topological features like rings and cavities embedded within a structure can be extracted, has been successfully applied to characterise microscopic order and shapes in granular, colloidal and amorphous materials [619, 620, 621, 622, 623, 624, 625] and have been used to identify hierarchical structures [626]. Thus, persistent homology seems to be an auspicious next step to investigate the gyroid phase further.

could not be resolved yet. However, especially the replicated formation of the V-configuration, where particles are in a splayed position, raises some promising arguments that the NAHPR model might also be suitable to form inverse micelle structures.

Therefore, we present some preliminary studies on the inverse micelle formation in the NAHPR-model. The procedure to obtain the NAHPR contact function is explained in Sec. 6.4. However, due to the numerically very demanding calculations of the contact function during the simulations, we reduce the complexity in the following significantly by only analysing two-dimensional NAHPR pear-disk mixtures. With those simulations, we obviously are not able to reproduce the exact three-dimensional behaviour of diluted pear mixtures. Nevertheless, these results shed light on the possibilities provided by non-additivity and have to be seen as preparatory work for studies to come. Hence, Monte Carlo simulations are performed with $N_{\text{pear}} = 12$, $N_{\text{disk}} = 15000$ and $a = \frac{A_{\text{pear}}}{A_{\text{disk}}} = 15$ which corresponds to $\Phi_{\text{disk}} = 0.98$.[7]

The pear shape is defined by $k = 2.75$ and $k_\theta = 1.9$. This particle outline is chosen such that the 12 pears are pieces of a perfect two-dimensional micelle as depicted in Fig. 8.10a$_1$ and are theoretically capable of forming this structure without any geometrical defects. Similarly the angle $\alpha_{\text{overlap}} = 30$, where the non-additivity is added at blunt ends, is chosen to allow for the formation of circular inverse structures without defects. Using the NAHPR approach, it becomes apparent that constructing two-dimensional inverse micelles by pears without large overlaps is impossible. Therefore, we try to generate the closest structural relative which pear constituents manage to form without large overlaps, namely inverse vesicles (see Fig. 8.10b$_1$).

The first simulation sets are initiated from an isotropic phase and slowly compressed to a global density of $\rho_g = 0.5$. We observe that the pears come together due to depletion forces and eventually form clusters. However, the clusters are not identified as inverse micelle structure but rather as arrays of pears where neighbouring particles are either in the V-configuration or the S-configuration (see Fig. 8.10a$_3$). This S-arrangement, where the pears overlap with their blunt ends in an antiparallel fashion, prevents the self-assembly of inverse micelles as an antiparallel pear-pair cannot be extended

[7] Φ_{disk} is now defined as an area fraction.

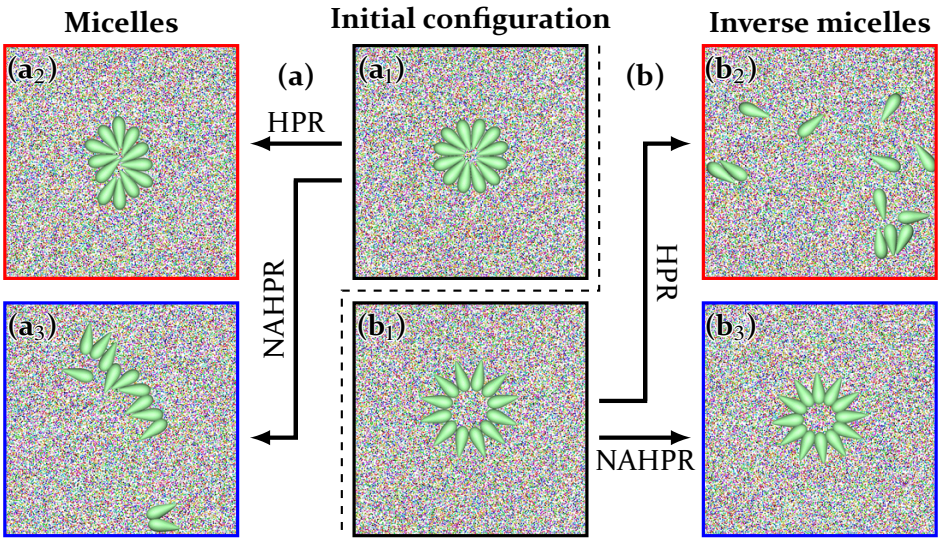

Figure 8.10: The metastable configurations of highly diluted 2D pear-disk mixtures in the HPR- (red) and the NAHPR- (blue) model. (a) The first set of MC simulations proceeds from an artificial micelle configuration (a_1) at $\rho_g = 0.5$, which stays stable in the HPR-model (a_2) but diffuses in the NAHPR model (a_3). (b) The second set of MC simulations proceeds from an artificial inverse vesicular configuration (b_1) at the same global density, which shows in contrast stability in the NAHPR-model (b_3) but destabilises for HPR particles (b_2). The parameters of the mixtures are set up to $N_{\text{pear}} = 12$, $N_{\text{disk}} = 15000$, $k = 2.75$, $k_\theta = 1.9$, $a = \frac{A_{\text{pear}}}{A_{\text{disk}}} = 15$ and $\Phi_{\text{disk}} = 0.98$ in both simulation sets.

by further pear-shaped particles to an inverse vesicle. Thus, neither the "normal" micelle nor the inverse vesicle cluster can be obtained via compression.

To show, however, that the inverse vesicle can be generated by non-additive interactions we perform another two sets of simulations. Here, we generate both an non-overlapping micellar (see Fig. 8.10a_1) and non-overlapping vesicular (see Fig. 8.10b_1) starting configuration at $\rho_g = 0.5$ and simply run the MC simulations. Additionally, the same simulations are performed using HPR-particles as a comparison. It becomes apparent that the simulations, proceeding from the artificial micelle, is stable in the HPR-mixture and only slightly deforms (see Fig. 8.10a_2), whereas, for NAHPR particles the system diffuses into arrays of particles which have also been observed via compression (Fig. 8.10a_3). The exact opposite behaviour is obtained starting from the vesicle. Here, the HPR particles quickly separate and form small clusters (see Fig. 8.10b_2). In contrast, the NAHPR particles indeed keep the collective

shape and create a metastable vesicle (see Fig. 8.10b$_3$). These distinctions between HPR and NAHPR particles open up the possibility for an exciting mechanism. It seems to be feasible to switch the orientation of the particles within a micelle by turning the non-additive features of the pear colloid on and off. However, here we first have to find a way for the particles to assemble spontaneously.

Thus, we have shown that the addition of non-additivity to the HPR model does not only replicate some of the depletion interactions of PHGO pears but also shows promising potential to adopt more complex multi-particle interactions like the formation of micellar structures. However, there are still issues which have to be resolved. Firstly, the simulations have to be extended to three dimensions to investigate if circular inverse structures can also be obtained with additional degrees of freedom. Secondly, the self-assembly has to be enhanced by preventing the particles from forming S-configurations. Some possible solutions to this problem were already proposed in Sec. 6.4. However, maybe the issues with the S-configurations are not as severe in 3D. By opening up the possibility to expand into the third dimension, the particles have more ways to adapt to geometrical defects. Thus, the S-arrangement might not necessarily be an exclusion criterion for three-dimensional inverse micelles.

9 Conclusion and outlook

> *"May you find inspiration in the big picture, but may you find love in the details."*
>
> – Adrienne Maloof

The overall goal of this PhD project was to achieve a deeper understanding of the self-assembly processes of aspherical particles with hard (but possibly non-additive) interactions, with a particular emphasis on the formation of bicontinuous cubic phases. Our results on pear-shaped particle systems can be summarised as follows:

9.1 There are many ways to skin a cat

Is entropic pear-particle self-assembly fundamentally different to other mechanisms that form the gyroid?

The focus of this thesis was placed on the inter-particle arrangements within bicontinuous cubic phases. In that process, we recreated the Ia$\bar{3}$d double gyroid phase in a system of pear-shaped particles, which was observed earlier by Ellison *et al.* [241], using the PHGO pear-shape approximation (which features small non-additive properties facilitating the gyroid formation) and significantly extended its geometric study in Chap. 4. Moreover, we managed to stabilise a Pn$\bar{3}$m double diamond structure with similar architecture and micelle-like arrangements by introducing a hard sphere solvent to the pear system in Chap. 8. The most significant findings are listed below:

- **Confirmation of the Ia$\bar{3}$d gyroid liquid-crystal phases in the PHGO approximation (both with and without WCA method):** The gyroid structure is stabilised by the PHGO pear-shaped particles forming space-filling bilayers where the two opposite leaflets interdigitate with the thin ends of the pears and where the blunt ends create the bicontinuous network domain. The gyroid phase has been identified as a warped smectic phase where the particles align with the local normal direction of the dividing minimal surface. Comparing local properties

between the gyroid minimal surface and the particle assembly, we detected a novel technique based on the special collective interdigitation arrangement to create negatively curved surfaces via the modulation of the penetration depth of the leaflets. We showed that this stabilisation mechanism is fundamentally different from amphiphilic gyroid assemblies, where the stabilisation stems from the arrangement of single particles.

- **Pn$\bar{3}$m diamond symmetry upon addition of a small concentration of a hard sphere solvent to the PHGO pear-shaped particle system:** The diamond particle arrangement is similar to the one observed in the gyroid phase as the particles again form interdigitated bilayers. We recognised the hard spheres as curvature inducing agents which accumulate at the interface between the channel domains and aid the system to resolve geometric heterogeneities. This strategy resonates with the interdigitation mechanism of the pears and hence showcases a new way to create diamond surface structures.

- **Inverse micelle formation in the dilute limit of PHGO pear-shaped particles in a bath of hard spheres:** The pear-shaped particles equilibrate into an inverse micelle formation favoured by the non-additive properties of the PHGO model. The larger micelles themselves function as constituents of even larger self-assembled structures indicating hierarchical self-assembly. This observation leads to the hypothesis that also the minimal surface phases are hierarchically assembled geometries.

These results help us to assess the possibilities of entropically driven self-assembly. Even though non-additive features seem to be necessary, all the complex phases mentioned above are created with a potential governed exclusively by the excluded volumes of the pear-shaped particles. Here, we have to mention that the non-additivity enforces a polarity between neighbouring particles. The blunt ends tend to "overlap', which favours the formation of bilayers and eventually cubic phases. Therefore, it is possible to describe the non-additivity also as an "effective" or "entropic amphiphilicity". However, in contrast to lipids and copolymers, where the polar order between neighbouring molecules is energetically favoured, the PHGO pear-shaped particle are "amphiphilic" only by maximising entropy!

Our results also shed light on a more fundamental question in soft matter. The theoretical descriptions of self-assembled triply-periodic minimal

surfaces often rest on the assumption that structures with similar morphologies are created by a similar mechanism. The resemblance of the architecture of the gyroid phase in lipid-water and di-block copolymer systems strengthened this conjecture even further. In both the lipidic and copolymeric cases, the final negatively curved surface is constructed as a result of the amphiphilic molecules adopting tapered shapes fitting the Steiner's cell of the surface (see Sec. 4.3.4) and arranging accordingly.

The question as to whether there is more than one mechanism towards the gyroid, is crucial in particular when considering the lipid-based membrane phases in biology [62, 171, 172]. Because of their lipid/water nature, it is often assumed or implied that they result from similar self-assembly mechanism as the bicontinuous phases in synthetic lipid-water systems. Yet, there are huge differences, e.g. in length scale, which can not (yet) be reconciled. In this context, our demonstration here that the gyroid can also result from an entropic maximisation of degrees of freedom (with at best minimal entropic amphiphilicity), leading to interdigitating bilayers and a collective (and maybe hierarchical) process, is an important caution in this respect: Just because the resulting structure is the same does not necessarily imply the same formation mechanism. For the gyroid (and its sister structures), that assumption presumably stems from its unconventional and unfamiliar structure. Our work here and the many examples where the gyroid now forms, is starting to challenge this notion. Surely, in the more familiar spherical geometry, we would have never made that assumption: You would be labelled a fool if you assumed that, just because of their common spherical shape, soap bubbles and planets result from the same formation mechanism.

Thus, we have to change the posing of the question: Is there only one natural mechanism to form gyroid-like structures, which is shown in lipid bilayer systems? Or is there an underlying, more generic optimisation principle behind the geometry of the gyroid, by being the (potentially) best albeit not perfect solution to construct a surface with constant negative Gaussian curvature[1] and also by revealing the most homogeneous domain sizes, that there is more than one way to achieve it, for example, by the mechanism present in the PHGO pear-shaped particle systems.

[1]This would make the gyroid to the negatively curved equivalent of a sphere which has constant radius and, therefore, constant positive Gaussian curvature.

9.2 The devil is in the details

The sensitivity of structure formation to details of the particle shape

The second overarching topic of this thesis concerned the stability of the gyroid phase with respect to particle shape. It hence fits closely with the broader topic of how self-assembly (in particular in hard core systems) is sensitive to the details of the particle shape [221, 234, 238, 254, 627, 628, 629, 630, 631, 632, 633, 634]. In particular, we compared two hard pear-shaped particle models and their abilities to form the double gyroid spontaneously in Chap. 5. One is the pear hard Gaussian overlap (PHGO) particle, which closely approximates the pear-shape but also features non-additive properties. The other model represents the exact pear shape perfectly and is called hard pear of revolution (HPR) model. Furthermore, we compare the two models by probing their depletion behaviour in Chap. 6 and by contrasting them with a density functional for hard pear-shaped particles in Chap. 7. The main results of the comparison are listed in the following:

- **Comparison between the PHGO and HPR model based on the phase diagram:** We generated both phase diagrams in terms of global density and particle shape (degree of tapering) for hard pear-shaped particles with aspect ratio 3 using various protocols for the spontaneous formation. The PHGO phase diagram reveals isotropic, nematic and monolayer smectic (small taper), bilayer smectic (high taper) and gyroid phases (intermediate taper). The HPR phase diagram only provides isotropic and nematic phases. However, it also showcases that the particles destabilise the nematic order such that the transition occurs at larger densities. Pears of revolution with approximately the same degree of taper additionally reveal a local arrangement which can be identified as precursors of bilayer formation. The pair correlation functions indicate that the spontaneous formation of bilayers (and thus of the gyroid) benefits from the small non-additive properties of the PHGO model.
- **Comparison between the PHGO and HPR model based on the depletion behaviour:** The indication of non-additivity playing a significant role in the local arrangement of PHGO particles was confirmed by testing the depletion interactions of both pear-shaped particle models. We showed that the HPR particles behave according to the excluded volume principle considering the pear shape. In contrast,

the PHGO particles arranged in a splayed position where the particles take advantage of the non-additivity of the underlying contact function. This formation is in accordance with the constellation between neighbouring particles within the bilayers of the gyroid. We also suggested a third model (NAHPR) based on the HPR model, which additionally provides non-additive properties. The depletion interactions of these particles show that the NAHPR model adopts important features to enable bilayer formation like the splay between neighbouring particles.

- **The PHGO and HPR model in comparison with density functional theory:** We developed a density functional for arbitrarily shaped hard solids of revolution and applied it to different pear-shaped particle systems with the same features as the HPR particles at a hard wall. We predicted an orientational alignment and layering of the particles close to the wall with very weak indications for bilayer-like staggering. This behaviour has been recreated by simulations of the HPR model perfectly and of the PHGO particles sufficiently, whereas the latter reveals an enhanced bilayer-like staggering.

This PhD project contributes to a very general question [221, 234, 238, 254, 627, 628, 629, 630, 631, 632, 633, 634]: How sensitive is self-assembly to slight shape changes? This conundrum is a rather practical one which becomes more apparent by rephrasing it to: How much can the experimentally synthesised colloid deviate from the computed particle shape to still show the same assembled structure?

Hard core systems are by design reduced to the shape of the inherent particles. Therefore, presumably the sensitivity to shape detail is most clearly observed in these systems. The difference of the hard core PHGO and HPR phase diagram, despite the close resemblance of the models, indicate very prominently that shape details are of greatest relevance and have to be taken with caution when attempting the transition from the numerically computed particle to a synthesised colloid with the same behaviour.

Those observations are in accordance with other hard particle systems, which have been studied by investigating the intermediate stages of interpolations between two shapes. It has been shown, for example, that in systems of hard cubes, rounded edges have a significant influence on the cubical ordering of the crystalline phase [234, 254, 627, 628]. In addition to these

superballs also various families of truncated [221, 238, 629, 630, 631] polyhedra, elongated and twisted triangular prisms [632], discs with adjustable thickness [633] and very recently also dimpled spheres with various dimple sizes [634] have been studied. Here it has been indicated that especially more complex particle arrangements (among which we would also count cubic phases) are stable within a narrow window of shapes which makes them even more prone to small shape changes.

We have to come to the conclusion that the shape of a particle cuts both ways. The shape is considered as maybe the most fundamental property to induce order effects in multi-particle systems. This is highlighted by the plethora of different phases which we have addressed in the course of this thesis and which can be created by adjusting the form of particles accordingly, including the gyroid phase in the PHGO particles. For the assembly of specific ordered structures some shape features can be even attributed as necessary traits [221, 247]. To obtain, for example, smectic order, hard-core particles like spherocylinders [213, 237], rigid sphere-beads [216, 217], helices [218], triangular prisms [219, 221, 222] or cuboids [223] have to be of certain length.

On the other hand, structure formation seems to be also highly sensitive to variations such that we can not claim that a given approximate shape is also a sufficient trait to create specific structures. Like the close resemblance between the shapes in the PHGO and HPR particle model is a red herring and does not guarantee the same phase behaviour, also the difference between spherocylinders (which do have a smectic phase [237]) and ellipsoids (which do not have a smectic phase [214]), emphasises the care of details which have to be taken. Thus, to create specific structures, we can surely make educated guesses about the shape of the building blocks and narrow down the particle shapes in question. However, to guarantee its spontaneous formation, we have to take more than a coarse-grained look. Consequently, we can include another statement to the ones above: The shape of a particle is the most likely reason why and why not a specific ordered structure is observed!

9.3 Future projects

We finish this thesis with some speculations and ideas for various future projects that extend the presented results. Note that a couple of intriguing research topics have already been mentioned in the outlook sections of the

previous chapters as food for thought. Here, we will revisit and significantly extend these ideas.

9.3.1 Phase diagram extension

An obvious next step is to attempt completing the phase diagrams of the HPR and PHGO particle models. Although we have already presented two phase diagrams in terms of global density and tapering parameter in Chap. 5, we only considered a small fraction of the available parameter space of the system by restricting the aspect ratio to $k = 3$, for which – in combination with $k_\theta = 3.8$ – it was already known that the gyroid structure forms in the PHGO pear-shaped particle system [241]. The dimensionality of this space can be further extended by considering mixtures of pear-shaped particles and the hard spherical solvent into account. Therefore, it would be interesting to investigate if pear-shaped particle systems reveal an even greater zoo of liquid crystal phases next to bi- and monolayer smectic, nematic, Ia$\bar{3}$d double gyroid, Pn$\bar{3}$m double diamond, "inverse" micellar or pear-sphere coexistence. Next to the global density ρ_g to regulate between isotropic and ordered phases and the tapering parameter k_θ, three other parameters (aspect ratio k, sphere number concentration n and sphere size v) complete the parameter space of hard pear-sphere mixtures. However, before this major task of covering the whole phase diagram should be tackled, it is advisable to reduce the numerical complexity of calculating the contact functions first, as a significant number of simulations have to be performed. Especially the overlap determination by creating surface meshes for the HPR particles (see Sec. 2.2.1) is rather slow. However, even if the five-dimensional phase diagram will not be completed in the near future, already slight adjustments, some of which we suggest in the following, to the already obtained phase diagram might give valuable additional insight.

A good example is the variation of the pear-shape in its aspect ratio rather than in its tapering angle, on which we mainly focused on in this thesis. Especially by starting from a PHGO pear ensemble which forms the gyroid, we would be able to determine the upper and lower bound of the Ia$\bar{3}$d phase in terms of elongation besides the already ascertained smallest and highest tapering angle. It is very reasonable to assume that highly elongated PHGO particles do not assemble into the gyroid and even destabilise bilayer structures. This conjecture is substantiated by the observation that for very long pears ($k \to \infty$) the maximum tapering angle becomes very small such that its

particle-shape hardly deviates from an ellipsoid of equal length. This suggests that the pears have to transition for a specific k into a nematic phase which was determined for infinitely long hard rods [203]. Some preliminary studies of PHGO particle systems with $k = 3.5$ and $k_\theta = 3$ indicate that the gyroid phase is still stable such that the transition has to occur at higher values.

Also for short particles, the gyroid presumably destabilises. It is known that elongated particles like ellipsoids or rods have to feature a minimum length of $k_{\text{crit}} = 2.75$ to obtain global orientational order like nematic order [213, 214]. This implies that also PHGO particles have to provide a sufficient degree of asphericity to avoid an otherwise disordered isotropic phase. Furthermore, the influence of taper on the nematic phase could be investigated in similar studies of the HPR model. Here two different effects seem likely. One possible outcome is that the influence of polar alignment, which is weakly indicated by strongly tapered HPR particles in the nematic phase (see correlation functions in Fig. 5.13), becomes stronger such that global orientational order is also stabilised for $k_{\text{crit}} < 2.75$ (maybe even gyroid- or sponge-like structures; see next section). Alternatively, the critical length is shifted to higher values as the taper introduces a curvature to the system. The latter is probably more realistic, based on our observations so far as in Fig. 5.12 the transition between isotropic and nematic phases occurs at higher densities for smaller k_θ.

Another question, which might be resolved in the course of extending the phase diagram, is if also the $Im\bar{3}m$ primitive surface structure [48, 51] can be formed by PHGO particles. Note that in copolymer systems, the $Pn\bar{3}m$ (diamond) and the $Im\bar{3}m$ (primitive) have been stabilised by Finnefrock *et. al* [191] upon addition of nanoparticles. To create primitive surface structures the system has to overcome even higher spatial heterogeneities than in the diamond phase [70, 91, 167] which hints towards larger hard sphere agents $v > 9$ that relieve this issue. However, considering the position of the spheres in the diamond phase close to the surface matrix (see Fig. 8.6) such large solvent particles could alternatively disrupt the bilayer architecture instead.

9.3.2 Disordered warped smectics and sponge phases

An intriguing phenomenon among cubic phases in soft matter physics is the swelling of bicontinuous phases into L_3 sponge phases [165, 371, 427]. The sponge phase can be interpreted as a disordered cubic phase where a lipid bilayer separates a bicontinuous aqueous channel network but lacks long-range order. The sponge usually forms by adding organic [165, 427, 428, 429, 430] or polymeric solvents [431, 432, 433, 434] to ordered cubic phases which cause the lipidic membranes to swell.

In pear-shaped particle systems, we have not observed a bicontinuous disordered structure yet. The closest approach, which we have observed in pear-shaped particle systems so far, is the pear-sphere mixture of Sec. 8.3 with an intermediate concentration of the hard spherical solvent. However, in these systems, only one single network structure could be extracted (see Fig. 8.8). Another and a more auspicious path to obtain disordered minimal surfaces in the pear-shaped particle system might be the highly tapered HPR particles in Fig. 5.10. The grey area indicates an isotropic region of particles with short-range transitional-order and orientational order, which we have identified as a precursor for bilayer-like arrangements. Considering that PHGO particles indeed form gyroid-like phases, it might be feasible to assign pears only a small amount of non-additivity to their blunt ends (for example by using the NAHPR model) such that the next neighbour correlation is strong enough to enable bilayer formation but fails to enforce global order. This behaviour would be reminiscent of observations of sponge phases in X-ray scattering experiments where the scattering pattern shows

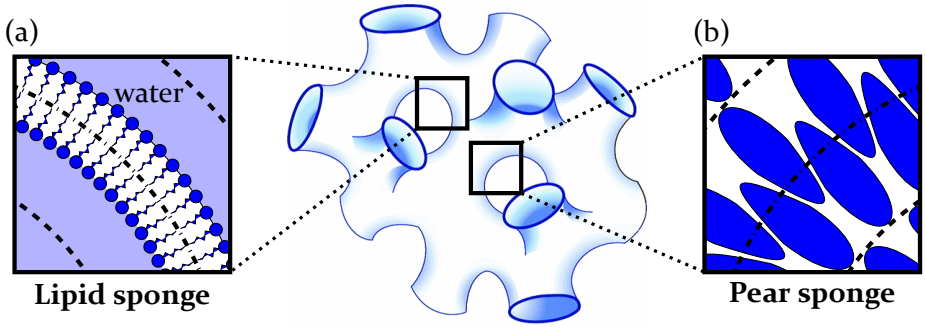

Figure 9.1: Sketch of (a) lipidic L_3 spong phases and of (b) how the pear-shaped particles might arrange within a potential sponge-like phase. The sketch of the sponge is adapted with permission from Ref. [433].

two characteristic diffuse peaks [372, 635, 636]. One corresponds to the next neighbour correlation of particles within the same leaflet. The other one is related to bilayer distances.

Alternatively, we could try to take the reverse route and somehow decrease the non-additivity of the PHGO model and destabilise their long-range order. Here, the potentially hierarchical architecture of the minimal surfaces might be beneficial as it gives rise for the formation of intermediate bilayer-like structures which then randomly attach to a sponge-like mesostructure. This would suggest that the sponge phases are not fully disordered but might bear some hidden order. Here we want to refer to the interludes in Sec. 3.4.6, where hidden order in the form of hyperuniformity [360] and its relation to sponge phases is addressed. Lastly, we have to mention that it is reasonable to assume that in these disordered minimal surface phases the PHGO particles also align with the normal of the minimal surface. Hence, the sponge phase could be again identified as warped smectic, giving this phase the nicely counterintuitively sounding name "disordered (warped) smectic".

9.3.3 Chiral gyroid phases

A recurrent question in the context of gyroid-like phases is chirality, discussed in particular in terms of optical properties [46, 185, 637] and in terms of an observed, but unexplained enantiomeric imbalance in the single gyroid in butterfly nanostructures [183, 638].

While the PHGO hard-pear system described in this thesis adopts only the achiral gyroid phase with symmetry $Ia\bar{3}d$,[2] it may also inform on the issue of chiral generalisations. While synthetic self-assembly protocols exist to generate chiral single gyroids with symmetry $I4_132$ [639] or solid replicas thereof [185], these do not break the chiral symmetry, that is, left-handed and right-handed enantiomers occur with equal probability. In these systems, the two network-like domains are chemically distinct, say A and C, yet the probability for each of A and C to be the right-hand gyroid network is equal[3]. The open question is what is required to make the A moiety adopt the, say, right-handed network with a higher probability than the left-handed one?

[2] The symmetry group has elements that exchange the two domains of opposed handedness, resulting in an achiral composition of two chiral domains

[3] Note that more complicated chiral gyroid-like arrangements have been observed in simulations [640] or analysed in terms of geometric free energy concepts [89]

It has been demonstrated that molecular twist in copolymeric components can affect the mesoscopic structural chirality (and enantiomeric type) of the self-assembled nanostructure [641]. The $Ia\bar{3}d$ gyroid phase described in this thesis is interesting in the sense that the pear-shaped particles naturally subdivide into two groups, each occupying one of the two labyrinthine domains. It is, though, conceivable that a small adaption of the particles to embed chiral character may lead to an adapted mesoscale geometry (where the labyrinthine domain that "matches" one particle enantiomeric type is different from the other, e.g. higher density); only one of the two enantiomers of the $I4_132$ gyroid would then form. Further, if a mixture of both enantiomeric particle types were considered, it is conceivable that a chiral microphase separation may result, with right-hand particles occupying the right-hand domain and left-hand particles the left-hand domain, again producing only one of the two enantiomers of the $I4_132$ single gyroid. In that regard, we want to mention the investigations of systems of achiral molecules with chiral conformers by Dressel and Tschierske [642, 643, 644]. Those molecules form conglomerates of dominantly left-handed and right-handed liquids which are immiscible before they combine into a gyroid phase by cooling the system (see Fig. 9.2a). This "pre-separation" of chirality and subsequent "soaking-up" of the chiral domains also suggests the separation of chiral conformers into the bicontinuous domains of the gyroid.

Particle activity might guide us to a practical solution path on how to implement chirality into our system. So far we have restricted ourselves to the analysis of the collective behaviour and self-assembly of nanoparticle systems in equilibrium. However, especially in biology but also in chemistry and soft matter, interesting physical phenomena occur as a result of non-equilibrium effects. One possible way a particle system can be brought into a state of constant non-equilibrium, next to being exposed to fluctuating external forces [646, 647, 648, 649], is an inherent activity of the particles [252, 650, 651, 652, 653, 654, 655, 656, 657, 658]. In these systems, the particles are not only subject to conservative forces based on the inter-particle interactions but also create internal forces. On the microscopic level, these forces can be experienced as both self-propelled translational and rotational motions. On the more interesting mesoscopic lengthscale particle activity can cause complex physics like pattern formations [650, 651], active turbulence [652, 653], swarming behaviour [654, 655] or clustering [656, 657].

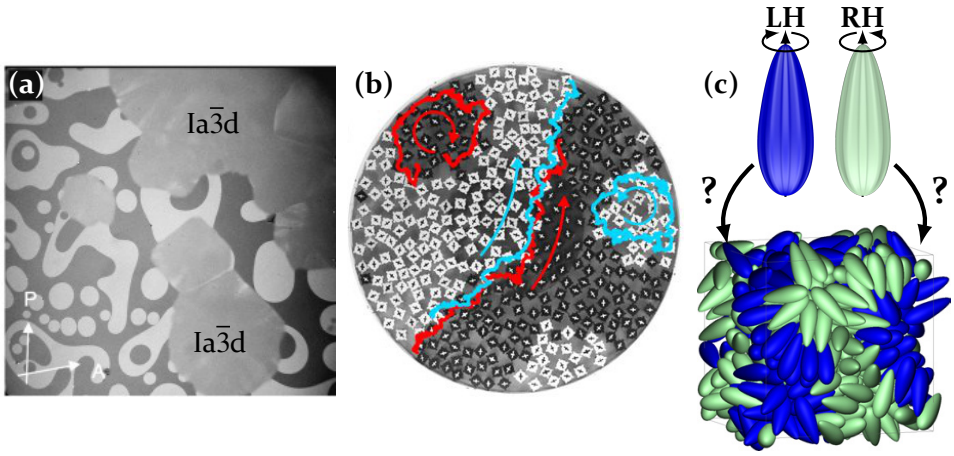

Figure 9.2: (a) Achiral molecules forming left-handed and right-handed domains of their chiral conformers before transitioning into the gyroid phase upon cooling. The chirality of the domains (dark or bright) is visualised via uncrossed polarizers. Their orientations are indicated by (P) and (A). The image is obtained with permission from Ref. [642]. (b) An experiment of two-dimensional active rotating particles shows spontaneous phase separation into domains of clockwise (black) and counter-clockwise (white) rotating particles. Image adapted with permission from Ref. [645]. (c) Thought experiment to introduce chirality to pear-shaped particle systems via activity. The particles are divided into groups of self-propelled left-handed (LH) and right-handed (RH) rotating pears. Their interactions are coupled with the rotation due to the grooved particle surface. By adding this feature, we might be able to obtain a phase separation within the gyroid phase where RH pears form the RH channel domain and where the LH domain contains only LH particles.

To apply activity to the pear-shaped particle system, we can assign a handedness to individual colloids by including a self-propelled rotational motion, which couples with the inter-particle interactions, to the pear-shaped particles. Those non-linear interactions are typically realised by introducing a friction term between neighbouring colloids [659, 660] or via geometric modulations and appendages [645, 651]. The latter strategy can presumably be applied to the pear-shaped particles in the form of grooves (see Fig. 9.2c), but as we have discussed in length in the earlier chapters, those morphological changes might have unforeseeable consequences to the gyroid stability. In terms of our thought experiment, the active form of introducing chirality would imply that pears rotating clockwise around the symmetry axis and pears rotating anti-clockwise segregate into two separate subgroups each occupying space within the appropriate channel domains as indicated in Fig. 9.2c. This implementation of activity seems very promising as rotating hard particle systems are known to phase separate due to spinodal

decomposition when activity is increased and the system is brought into constant non-equilibrium [645, 651, 661] (see Fig. 9.2b). However, here we also have to bear the possibility of subsequent remixing in mind when the particles reach a turbulent state for high activity [658].

Consequently, we might be able to observe a spontaneous clustering of left- and right-handed particles into separate srs-domains in between the unsorted equilibrium gyroid phase at the low activity limit and a dynamically mixed state in non-equilibrium at the high activity limit. In this medium activity range, it is very likely that we have to add another layer of complexity to prevent complete spinodal decomposition. Therefore, some mechanism like an intrinsic motor within particles, which switches the rotational activity on and off periodically, might be necessary. Whether such specific demixing can occur due to entropy alone is an interesting question for future research.

9.3.4 Active robot particles with non-additive interactions to probe two-dimensional micelle formation

Active particles can also be useful to answer other questions which have been arisen during this PhD project. In the course of this thesis, we have provided some suggestions on how to realise pear-shaped particles in an experimental setup. For example, we have discussed possible future experimental implementations by introducing the NAHPR model (see in Sec. 6.4 and Sec. 8.4) and also argued in Sec. 5.3 about suitable synthesis strategies of pear-shaped colloids on the microscopic level, like introducing a short-ranged attractive potential, modulating the surface roughness or utilising the curvature of the colloid. Here we indicated which specific issues have to be considered in manufacturing pears to achieve liquid crystal phases like the double gyroid. So far, however, we have omitted another interesting model on the macroscopic scale, which shows great potential to materialise two-dimensional pear-shaped particle systems with the right non-additive features and to recreate at least some of our results in the laboratory: an adaption of the "vibrot" particles [662].

In recent years the collective behaviour of animals or bacterial colonies has been studied by a collaboration of robots, which mimic physical phenomena out of equilibrium like swarming and flocking [645, 662, 663, 664]. Rather simplistic examples to conceptualise those robots are known as bristle-bots or vibrots [662, 665] (see Fig. 9.3a+b). These walking automatons consist

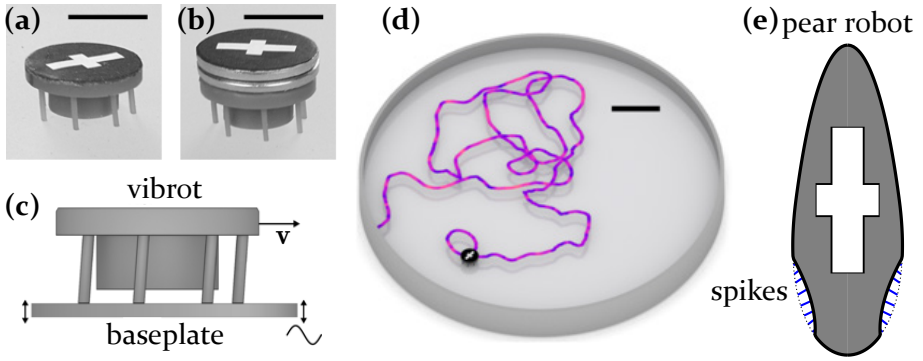

Figure 9.3: Two versions of 3D-printed vibrots: (a) reference vibrot and (b) vibrot with additional hard body layer. Scale bar: 1 cm. (c) Sketch of the vibrot mechanism powered by a vibrating baseplate. (d) Exemplary particle trajectory. Particle image marks the starting point of the trajectory. Scale bar: 4 cm. (e) Possible design of a pear-shaped robot which copies the properties of the NAHPR model. The non-additivity is modelled by a region of spikes (blue) which is pervious for spikes of other pear-shaped vibrots but not for their hard body (black). The images (a-d) are adapted with permission from Ref. [671].

of hard bodies and elastic legs, which act like springs and allow to convert vibrations into motion. The self-propulsion is excited either by a motor on the top of each robot causing it to vibrate and therefore to jump [663] or by a vibrating plate having the same effect on the particle [662, 666] (see Fig. 9.3c). The specific type of motion depends on the arrangement and tilt of the legs. For so-called walkers, tilted legs are placed parallel to another which then induce translational forces. To create rotating vibrots, the tilted legs are arranged in a circular fashion such that a torque is applied to the particle. The two-dimensional trajectories of these active particles are similar to those of mechanically shaken polar discs [667, 668]. A 3D printed version of a vibrot is illustrated in Fig. 9.3.

The intensity of the self-propelled forces of the vibrots depends on different properties, like the leg inclination, frequency and amplitude of the vibration and the elasticity and friction coefficients of the legs [662, 663, 669, 670]. However, the system also inherits a non-deterministic component on the long time-scale which is caused by both surface inhomogeneities and elastic instabilities of the legs [669, 671] (see Fig. 9.3d). These cause the vibrots to bounce more irregularly and reorientate randomly with every jump. Therefore, the vibrots are often considered as active Brownian particles on the macroscopic level [671, 672, 673, 674].

In principle, the shape of the robots can be chosen arbitrarily. Due to the advances in 3D printing also pear-shaped robot seem feasible and an exciting opportunity for a future project. In these systems, the hard body of the robot would have to be printed according to the Bézier curve representation. Note here that we are not particularly interested in the activity as a self-propelled rotation. Instead, we suggest to utilise the "activity" of the vibrots as an ability to insert energy into the microscopic degrees of freedom. This implies that the legs of the pear-shaped robots probably have to be hardly inclined or tilted in different directions to reduce the "active' part of the self-propulsion, which is then dominated by the Brownian like motion. As this system is two-dimensional, cubic phases like the gyroid cannot be recreated with this approach. Nevertheless, other experiments to observe some indications of particle interdigitation or the formation of micellar and vesicular structures in equilibrium when adding a second species of circular vibrots (see Sec. 8.4), seem to be viable for those robot systems.

Design 1: Prickly pear-shaped vibrots

Another benefit of this approach is that the non-additive features, like those present in the PHGO and the NAHPR particle model, can probably be implemented. One idea is to introduce a "prickly" pear-shaped robot. Here non-additivity is modelled by a region of spikes, which is pervious by thorns of other robots, leading to an effective "overlap" of the pear shapes, but cannot be penetrated by their hard bodies (see Fig. 9.3e). Here, we have to consider that the spikes should not be too dense, which would prevent the full penetration of spikes or causes the particles to wedge. On the downside, if the spikes are distributed only sparsely, also the hard body can enter the non-additive region. Nevertheless, it seems feasible that we can effectively replicate the NAHPR model by vibrots with spikes in appropriate distances and even suppress unwanted effects like the S-configuration (where the non-additive regions overlap and the particles are antiparallel to each other; see also Fig. 6.11d) by changing the angle of the thorns.

The prickly pear approach might also be suitable for the realisation of non-additivity in colloidal particle systems. In that regard, some synthesis techniques to generate star-like nanoparticles with a spiky exterior have been reported [675, 676, 677, 678]. To apply this idea to the pear-shape, we would have to design pear-shaped colloids with a thinner upper half with a smooth surface and a blunt bottom half featuring small spikes. Similar

to the proposed mechanism for vibrots, the spikes might allow the pears to penetrate the blunt end with their prickly side but prevents the smooth end to enter this very same region. We have to keep in mind, however, that a rough surface reduces the effective depletion attraction between colloids [240, 549]. This might counteract the benefit of partially penetrable thick ends.

Design 2: Layered pear-shaped vibrots

We also suggest an alternative design for pear-shaped robots by using the third dimension for the overlap of two robots. By partitioning the hard body of the pear-shaped robots into a lower and an upper part (the two body parts are indicated in Fig. 9.3b), we can effectively assign two different shapes to the vibrots. Hence, we might be able to copy the NAHPR contact profile by choosing one of the layers as the outer contour and the other layer as the inner contour of the NAHPR pear as described in Fig. 6.9. Then, two pear robots would interact mainly via the outer contour layers except when they approach with the blunt ends leading to a suitable "overlap".

Here we have to keep in mind that this method is probably only practicable if the inner and outer contour is engraved in opposite layers for neighbouring particles. Otherwise, if, for example, the inner contour layer forms the top for all particles, the robots would not be able to take advantage of the "non-additivity" as the contact of their lower layer, formed like the regular pear, prevents this more compact arrangement. Consequently, the robots have to be divided into two groups with some inner contours printed at the top (lock-particle) and some at the bottom (key-particle) of the hard body. Even though this probably leads to incompatibility issues (lock-lock or key-key) for multi-particle systems, like those forming vesicles, it will be sufficient to study the depletion behaviour in principle. In order for us to study the depletion interactions, only two pear-shaped robots within a "solvent" of hard circular vibrots are needed, where the incompatibility vanishes by choosing one lock- and one key-robot and where we can hopefully recreate the V-configurations determined in Fig. 6.11c.

The Gyroid - from curious oddity to household name

To sum things up, we have managed to uncover some open questions in soft matter physics by studying the pear-shaped particle system whereas others are still to be revealed. Even though we do not dare a prognosis when (and if) the gyroid out of pear-shaped particles becomes a reality, it is hard to avoid philosophising about the prospects. When Alan Schoen was the first to described the gyroid 50 years ago, probably not even he could have foreseen the impact of this geometry in soft matter physics or the possibility of its formation in entropically dominated pear-shaped particle systems. Starting as a curiosity known to only a handful of scientists, the gyroid has become almost a household name across a greater range of disciplines (including engineering, materials science, physics, chemistry and biology). So what can come next? We hope that the results of this thesis will help to further promote this geometry in science, including the colloid community. It will hopefully be a useful piece of the bigger puzzle why and how bicontinuous geometries form and what purposes they can serve, in both man-made and natural nanostructured materials.

Bibliography

[1] G. A. Garzon and R. E. Wrolstad. Comparison of the stability of pelargonidin-based anthocyanins in strawberry juice and concentrate. *J. Food Sci.*, 67(4):1288–1299, 2002.

[2] R. A. Grange, C. R. Hribal, and L. F. Porter. Hardness of tempered martensite in carbon and low-alloy steels. *Metall. Trans. A*, 8(11):1775–1785, 1977.

[3] J. Kepler and C. Frisch. *Joannis Kepleri astronomi opera omnia*, volume 5. Heyder & Zimmer, 1864.

[4] Credit: Felver Alfonzo. Acueducto romano (segovia, españa). `https://commons.wikimedia.org/wiki/File:Acueducto_Romano_(Segovia,_España).jpg`, 2009.

[5] A. J. Katz and A. H. Thompson. Quantitative prediction of permeability in porous rock. *Phys. Rev. B*, 34(11):8179, 1986.

[6] P. R. King, J. S. Andrade Jr, S. V. Buldyrev, N. Dokholyan, Y. Lee, S. Havlin, and H. E. Stanley. Predicting oil recovery using percolation. *Physica A*, 266(1-4):107–114, 1999.

[7] J. B. Walsh. Effect of pore pressure and confining pressure on fracture permeability. In *Int. J. Rock Mech. Min. Sci. Geomech. Abstr.*, volume 18, pages 429–435. Elsevier, 1981.

[8] R. M. Iverson. The physics of debris flows. *Rev. Geophys.*, 35(3):245–296, 1997.

[9] S. J. Friedmann, N. Taberlet, and W. Losert. Rock-avalanche dynamics: insights from granular physics experiments. *Int. J. Earth Sci.*, 95(5):911–919, 2006.

[10] D. Kadau, H. J. Herrmann, J. S. Andrade, A. D. Araújo, L. J. C. Bezerra, and L. P. Maia. Living quicksand. *Granular Matter*, 11(1):67–71, 2009.

[11] T. Aste and T. Di Matteo. Emergence of Gamma distributions in granular materials and packing models. *Phys. Rev. E*, 77(2):021309, 2008.

[12] F. M. Schaller, M. Neudecker, M. Saadatfar, G. W. Delaney, G. E. Schröder-Turk, and M. Schröter. Local origin of global contact numbers in frictional ellipsoid packings. *Phys. Rev. Lett.*, 114(15):158001, 2015.

[13] D. W. Thompson. *On Growth and Form*. Cambridge University Press, 1917.

[14] T. Darmanin and F. Guittard. Superhydrophobic and superoleophobic properties in nature. *Mater. Today*, 18(5):273–285, 2015.

[15] H. Peisker and S. N. Gorb. Always on the bright side of life: anti-adhesive properties of insect ommatidia grating. *J. Exp. Biol.*, 213(20):3457–3462, 2010.

[16] R. Dewan, S. Fischer, V. B. Meyer-Rochow, Y. Özdemir, S. Hamraz, and D. Knipp. Studying nanostructured nipple arrays of moth eye facets helps to design better thin film solar cells. *Bioinspir. Biomim.*, 7(1):016003, 2011.

[17] M. Plotkin, I. Hod, A. Zaban, S. A. Boden, D. M. Bagnall, D. Galushko, and D. J. Bergman. Solar energy harvesting in the epicuticle of the oriental hornet (Vespa orientalis). *Naturwissenschaften*, 97(12):1067–1076, 2010.

[18] J. S. Ishay. Hornet flight is generated by solar energy: UV irradiation counteracts anaesthetic effects. *Microscopy*, 53(6):623–633, 2004.

[19] Jacques Livage. Bioinspired nanostructured materials. *C. R. Chimie*, 21(10):969–973, 2018.

[20] L. De Stefano, I. Rea, I. Rendina, M De Stefano, and L. Moretti. Lensless light focusing with the centric marine diatom Coscinodiscus walesii. *Opt. Express*, 15(26):18082–18088, 2007.

[21] J. Hazel, M. Stone, M. S. Grace, and V. V. Tsukruk. Nanoscale design of snake skin for reptation locomotions via friction anisotropy. *J. Biomech.*, 32(5):477–484, 1999.

[22] K. Autumn, C. Majidi, R. E. Groff, A. Dittmore, and R. Fearing. Effective elastic modulus of isolated gecko setal arrays. *J. Exp. Biol.*, 209(18):3558–3568, 2006.

[23] K. Autumn and N. Gravish. Gecko adhesion: evolutionary nanotechnology. *Philos. Trans. Royal Soc. A*, 366(1870):1575–1590, 2008.

[24] M. Srinivasarao. Nano-optics in the biological world: beetles, butterflies, birds, and moths. *Chem. Rev.*, 99(7):1935–1962, 1999.

[25] P. Vukusic and J. R. Sambles. Photonic structures in biology. *Nature*, 424(6950):852, 2003.

[26] A. R. Parker and H. E. Townley. Biomimetics of photonic nanostructures. *Nat. Nanotechol.*, 2(6):347, 2007.

[27] J. D. Joannopoulos, S. G. Johnson, J. N. Winn, and R. D. Meade. *Photonic crystals: molding the flow of light*. Princeton university press, 2011.

[28] C. Isenberg. *The science of soap films and soap bubbles*. Courier Corporation, 1992.

[29] Credit: Pashminu. Single light soap bubble photograph taken under macro photography. `https://commons.wikimedia.org/wiki/File:Macro_Photography_of_a_soap_bubble.jpg`, 2015.

[30] Credit: Marco Roosink. Pauwenogen. `https://pixabay.com/de/photos/peacock-augen-pauwenogen-tooi-2254989/`, 2017.

[31] E. Moyroud, T. Wenzel, R. Middleton, P. J. Rudall, H. Banks, A. Reed, G. Mellers, P. Killoran, M. M. Westwood, U. Steiner, S. Vignolini, and B. J. Glover. Disorder in convergent floral nanostructures enhances signalling to bees. *Nature*, 550(7677):469, 2017.

[32] J. Zi, X. Yu, Y. Li, X. Hu, C. Xu, X. Wang, X. Liu, and R. Fu. Coloration strategies in peacock feathers. *Proc. Natl. Acad. Sci. USA*, 100(22):12576–12578, 2003.

[33] P. Vukusic, J. R. Sambles, C. R. Lawrence, and R. J. Wootton. Quantified interference and diffraction in single Morpho butterfly scales. *Proc. R. Soc. London. Ser.B*, 266(1427):1403–1411, 1999.

[34] V. Sharma, M. Crne, J. O. Park, and M. Srinivasarao. Structural origin of circularly polarized iridescence in jeweled beetles. *Science*, 325(5939):449–451, 2009.

[35] V. Sharma, M. Crne, J. O. Park, and M. Srinivasarao. Bouligand structures underlie circularly polarized iridescence of scarab beetles: A closer view. *Mater. Today*, 1(Suppl):161–171, 2014.

[36] L. D'Alba, V. Saranathan, J. A. Clarke, J. A. Vinther, R. O. Prum, and M. D. Shawkey. Colour-producing β-keratin nanofibres in blue penguin (Eudyptula minor) feathers. *Biol. Lett.*, 7(4):543–546, 2011.

[37] B. D. Wilts, K. Michielsen, J. Kuipers, H. De Raedt, and D. G. Stavenga. Brilliant camouflage: photonic crystals in the diamond weevil, Entimus imperialis. *Proc. R. Soc. London. Ser.B*, page rspb20112651, 2012.

[38] B. D. Wilts, K. Michielsen, H. De Raedt, and D. G. Stavenga. Hemispherical Brillouin zone imaging of a diamond-type biological photonic crystal. *J. R. Soc. Interface*, 9(72):1609–1614, 2012.

[39] M. Burresi, L. Cortese, L. Pattelli, M. Kolle, P. Vukusic, D. S. Wiersma, U. Steiner, and S. Vignolini. Bright-white beetle scales optimise multiple scattering of light. *Sci. Rep.*, 4:6075, 2014.

[40] B. D. Wilts, K. Michielsen, H. De Raedt, and D. G. Stavenga. Sparkling feather reflections of a bird-of-paradise explained by finite-difference time-domain modeling. *Proc. Natl. Acad. Sci. USA*, 111(12):4363–4368, 2014.

[41] V. Saranathan, A. E. Seago, A. Sandy, S. Narayanan, S. G. J. Mochrie, E. R. Dufresne, H. Cao, C. O. Osuji, and R. O. Prum. Structural diversity of arthropod biophotonic nanostructures spans amphiphilic phase-space. *Nano Lett.*, 15(6):3735–3742, 2015.

[42] L. A. Taylor and K. J. McGraw. Animal coloration: sexy spider scales. *Curr. Biol.*, 17(15):R592–R593, 2007.

[43] L. M. Mäthger, G. R. R. Bell, A. M. Kuzirian, J. J. Allen, and R. T. Hanlon. How does the blue-ringed octopus (Hapalochlaena lunulata) flash its blue rings? *J. Exp. Biol.*, 215(21):3752–3757, 2012.

[44] S. Vignolini, P. J. Rudall, A. V. Rowland, A. Reed, E. Moyroud, R. B. Faden, J. J. Baumberg, B. J. Glover, and U. Steiner. Pointillist structural color in Pollia fruit. *Proc. Natl. Acad. Sci. USA*, 109(39):15712–15715, 2012.

[45] G. E. Schröder-Turk, S. Wickham, H. Averdunk, F. Brink, J. D. F. Gerald, L. Poladian, M. C. J. Large, and S. T. Hyde. The chiral structure of porous chitin within the wing-scales of Callophrys rubi. *J. Struct. Biol.*, 174(2):290–295, 2011.

[46] M. Saba, B. D. Wilts, J. Hielscher, and G. E. Schröder-Turk. Absence of circular polarisation in reflections of butterfly wing scales with chiral gyroid structure. *Mater. Today*, 1:193–208, 2014.

[47] B. D. Wilts, B. A. Zubiri, M. A. Klatt, B. Butz, M. G. Fischer, S. T. Kelly, E. Spiecker, U. Steiner, and G. E. Schröder-Turk. Butterfly gyroid nanostructures as a time-frozen glimpse of intracellular membrane development. *Sci. Adv.*, 3(4):e1603119, 2017.

[48] J. C. Nitsche. *Lectures on minimal surfaces: vol. 1*. Cambridge university press, 1989.

[49] A. Fogden and S. T. Hyde. Parametrization of triply periodic minimal surfaces. II. Regular class solutions. *Acta Crystallogr., Sect. A: Found. Crystallogr.*, 48(4):575–591, 1992.

[50] S. T. Hyde, Z. Blum, T. Landh, S. Lidin, B. W. Ninham, S. Andersson, and K. Larsson. *The language of shape: the role of curvature in condensed matter: physics, chemistry and biology*. Elsevier, 1996.

[51] E. A. Lord and A. L. Mackay. Periodic minimal surfaces of cubic symmetry. *Current Science*, pages 346–362, 2003.

[52] A. H. Schoen. Reflections concerning triply-periodic minimal surfaces. *Interface Focus*, 2(5):658–668, 2012.

[53] H. Karcher. The triply periodic minimal surfaces of Alan Schoen and their constant mean curvature companions. *Manuscripta Math.*, 64(3):291–357, 1989.

[54] K. Große-Brauckmann. Gyroids of constant mean curvature. *Exp. Math.*, 6(1):33–50, 1997.

[55] K. Grosse-Brauckmann. Triply periodic minimal and constant mean curvature surfaces. *Interface Focus*, 2(5):582–588, 2012.

[56] M. Saba, M. Thiel, M. D. Turner, S. T. Hyde, M. Gu, K. Grosse-Brauckmann, D. N. Neshev, K. Mecke, and G. E. Schröder-Turk. Circular dichroism in biological photonic crystals and cubic chiral nets. *Phys. Rev. Lett.*, 106(10):103902, 2011.

[57] B. D. Dolan, J. A .and Wilts, S. Vignolini, J. J. Baumberg, U. Steiner, and T. D. Wilkinson. Optical properties of gyroid structured materials: from photonic crystals to metamaterials. *Adv. Opt. Mater.*, 3(1):12–32, 2015.

[58] M. P. Do Carmo. *Differential Geometry of Curves and Surfaces: Revised and Updated Second Edition*. Courier Dover Publications, 2016.

[59] H. Nissen. Crystal orientation and plate structure in echinoid skeletal units. *Science*, 166(3909):1150–1152, 1969.

[60] Y. Deng and M. Mieczkowski. Three-dimensional periodic cubic membrane structure in the mitochondria of amoebaeChaos carolinensis. *Protoplasma*, 203(1-2):16–25, 1998.

[61] L. Norlén and A. Al-Amoudi. Stratum corneum keratin structure, function, and formation: the cubic rod-packing and membrane templating model. *J. Invest. Dermatol.*, 123(4):715–732, 2004.

[62] Z. A. Almsherqi, S. D. Kohlwein, and Y. Deng. Cubic membranes: a legend beyond the Flatland* of cell membrane organization. *J. Cell Biol.*, 173(6):839–844, 2006.

[63] E. Selstam, J. Schelin, W. P. Williams, and A. P. R. Brain. Structural organisation of prolamellar bodies (PLB) isolated from Zea mays. parallel TEM, SAXS and absorption spectra measurements on samples subjected to freeze–thaw, reduced pH and high-salt perturbation. *Biochim. Biophys. Acta, Biomembr.*, 1768(9):2235–2245, 2007.

[64] T. Zhan, W. Lv, and Y. Deng. Multilayer gyroid cubic membrane organization in green alga Zygnema. *Protoplasma*, 254(5):1923–1930, 2017.

[65] J. M. Seddon and R. H. Templer. Cubic phases of self-assembled amphiphilic aggregates. *Phil. Trans. R. Soc. Lond. A*, 344(1672):377–401, 1993.

[66] S. T. Hyde. Bicontinuous structures in lyotropic liquid crystals and crystalline hyperbolic surfaces. *Curr. Opin. Solid State Mater. Sci.*, 1(5):653–662, 1996.

[67] S. T. Hyde and S. Andersson. A cubic structure consisting of a lipid bilayer forming an infinite periodic minimum surface of the gyroid type in the glycerolmonooleat-water system. *Z. Kristallogr. - Cryst. Mater.*, 168(1-4):213–220, 1984.

[68] D. A. Hajduk, P. E. Harper, S. M. Gruner, C. C. Honeker, G. Kim, E. L. Thomas, and L. J. Fetters. The gyroid: a new equilibrium morphology in weakly segregated diblock copolymers. *Macromolecules*, 27(15):4063–4075, 1994.

[69] I. W. Hamley and I. W. Hamley. *The physics of block copolymers*, volume 19. Oxford University Press Oxford, 1998.

[70] G. E. Schröder-Turk, A. Fogden, and S. T. Hyde. Local v/a variations as a measure of structural packing frustration in bicontinuous mesophases, and geometric arguments for an alternating $Im\bar{3}$ (I-WP) phase in block-copolymers with polydispersity. *Euro. Phys. J. B*, 59(1):115–126, 2007.

[71] F. J. Martínez-Veracoechea and F. A. Escobedo. Bicontinuous phases in diblock copolymer/homopolymer blends: simulation and self-consistent field theory. *Macromolecules*, 42(5):1775–1784, 2009.

[72] M. Müller and D. Sun. Directing the self-assembly of block copolymers into a metastable complex network phase via a deep and rapid quench. *Phys. Rev. Lett.*, 111(26):267801, 2013.

[73] D. Sun and M. Müller. Process-accessible states of block copolymers. *Phys. Rev. Lett.*, 118:067801, Feb 2017.

[74] P. Barois, S. T. Hyde, B. Ninham, and T. Dowling. Observation of two phases within the cubic phase region of a ternary surfactant solution. *Langmuir*, 6(6):1136–1140, 1990.

[75] T. Ichikawa, M. Yoshio, A. Hamasaki, J. Kagimoto, H. Ohno, and T. Kato. 3D interconnected ionic nano-channels formed in polymer films: Self-organization and polymerization of thermotropic bicontinuous cubic liquid crystals. *J. Am. Chem. Soc.*, 133(7):2163–2169, 2011.

[76] H. M. G. Barriga, M. N. Holme, and M. M. Stevens. Cubosomes; the next generation of smart lipid nanoparticles? *Angew. Chem.*, 58(10):2958–2978, 2019.

[77] V. Luzzati and P. A. Spegt. Polymorphism of lipids. *Nature*, 215(5102):701, 1967.

[78] X. Zeng, G. Ungar, and M. Impéror-Clerc. A triple-network tricontinuous cubicliquid crystal. *Nat. Mater.*, 4(7):562, 2005.

[79] C. T. Kresge, M. E. Leonowicz, W. J. Roth, J. C. Vartuli, and J. S. Beck. Ordered mesoporous molecular sieves synthesized by a liquid-crystal template mechanism. *Nature*, 359(6397):710, 1992.

[80] X. Zou, T. Conradsson, M. Klingstedt, M. S. Dadachov, and M. O'Keeffe. A mesoporous germanium oxide with crystalline pore walls and its chiral derivative. *Nature*, 437(7059):716, 2005.

[81] Credit: EPINET. Minimal surface soap film. `http://epinet.anu.edu.au/mathematics/minimal_surfaces`, 2018.

[82] Credit: AGPapa. Hyperbolic paraboloid. `https://www.thingiverse.com/thing:183812`, 2013.

[83] H. A. Schwarz. Fortgesetzte untersuchungen über specielle minimalflächen. In *Gesammelte Mathematische Abhandlungen*, pages 126–148. Springer, 1890.

[84] P. J. F. Gandy, D. Cvijović, A. L. Mackay, and J. Klinowski. Exact computation of the triply periodic D (diamond') minimal surface. *Chem. Phys. Lett.*, 314(5-6):543–551, 1999.

[85] P. J. F. Gandy and J. Klinowski. Exact computation of the triply periodic G (gyroid') minimal surface. *Chem. Phys. Lett.*, 321(5-6):363–371, 2000.

[86] P. J. F. Gandy and J. Klinowski. Exact computation of the triply periodic Schwarz P minimal surface. *Chem. Phys. Lett.*, 322(6):579–586, 2000.

[87] A. H. Schoen. Infinite periodic minimal surfaces without self-intersections. *NASA Technical Note*, pages TD–5541, 1970.

[88] A. Fogden and S. T. Hyde. Continuous transformations of cubic minimal surfaces. *Eur. Phys. J. B*, 7(1):91–104, 1999.

[89] G. E. Schröder-Turk, L. De Campo, M. E. Evans, M. Saba, S. C. Kapfer, T. Varslot, K. Grosse-Brauckmann, S. Ramsden, and S. T. Hyde. Polycontinuous geometries for inverse lipid phases with more than two aqueous network domains. *Faraday Discuss.*, 161:215–247, 2013.

[90] G. E. Schröder, S. J. Ramsden, A. G. Christy, and S. T. Hyde. Medial surfaces of hyperbolic structures. *Eur. Phys. J. B*, 35:551–564, 2003.

[91] G. E. Schröder-Turk, A. Fogden, and S. T. Hyde. Bicontinuous geometries and molecular self-assembly: comparison of local curvature and global packing variations in genus-three cubic, tetragonal and rhombohedral surfaces. *Eur. Phys. J. B*, 54(4):509–524, 2006.

[92] S. Fujimori and M. Weber. A construction method for triply periodic minimal surfaces. *OCAMI Studies*, 3:79–90, 2009.

[93] H. Chen. Minimal twin surfaces. *Exp. Math.*, pages 1–16, 2017.

[94] H. Chen and M. Weber. A new deformation family of Schwarz'D surface. *arXiv preprint arXiv:1804.01442*, 2018.

[95] H. Chen and M. Weber. An orthorhombic deformation family of Schwarz'H surfaces. *arXiv preprint arXiv:1807.10631*, 2018.

[96] S. G. Markande, M. Saba, G. E. Schröder-Turk, and E. A. Matsumoto. A chiral family of triply-periodic minimal surfaces derived from the quartz network. *arXiv preprint arXiv:1805.07034*, 2018.

[97] K. A. Brakke. The surface evolver. *Exp. Math.*, 1(2):141–165, 1992.

[98] K. A. Brakke. The surface evolver. `http://facstaff.susqu.edu/brakke/evolver/evolver.html`, 2013.

[99] J. Klinowski, A. L. Mackay, and H. Terrones. Curved surfaces in chemical structure. *Phil. Trans. R. Soc. Lond. A*, 354(1715):1975–1987, 1996.

[100] P. J. F. Gandy, S. Bardhan, A. L. Mackay, and J. Klinowski. Nodal surface approximations to the P, G, D and I-WP triply periodic minimal surfaces. *Chem. Phys Lett.*, 336(3-4):187–195, 2001.

[101] R. Nesper and S. Leoni. On tilings and patterns on hyperbolic surfaces and their relation to structural chemistry. *ChemPhysChem*, 2(7):413–422, 2001.

[102] H. G. von Schnering and R. Nesper. Nodal surfaces of Fourier series: fundamental invariants of structured matter. *Z. Phys. B*, 83(3):407–412, 1991.

[103] J. Hielscher, C. Pouya, P. Vukusic, and G. E. Schröder-Turk. Harmonic distortions enhance circular dichroism of dielectric single gyroids. *Opt. Express*, 25(5):5001–5017, 2017.

[104] A. Tagliasacchi, T. Delame, M. Spagnuolo, and A. Amenta, N.and Telea. 3d skeletons: A state-of-the-art report. *Comput. Graph. Forum*, 35(2):573–597, 2016.

[105] H. Chen and C. Jin. Competition brings out the best: modelling the frustration between curvature energy and chain stretching energy of lyotropic liquid crystals in bicontinuous cubic phases. *Interface Focus*, 7(4):20160114, 2017.

[106] M. D. Turner, M. Saba, Q. Zhang, B. P. Cumming, G. E. Schröder-Turk, and M. Gu. Miniature chiral beamsplitter based on gyroid photonic crystals. *Nat. Photonics*, 7(10):801, 2013.

[107] G. Shambat, M. S. Mirotznik, G. W. Euliss, V. Smolski, E. G. Johnson, and R. A. Athale. Photonic crystal filters for multi-band optical filtering on a monolithic substrate. *J. Nanophotonics*, 3(1):031506, 2009.

[108] J. Wu, D. Day, and M. Gu. A microfluidic refractive index sensor based on an integrated three-dimensional photonic crystal. *Appl. Phys. Lett.*, 92(7):071108, 2008.

[109] R. V. Nair and R. Vijaya. Photonic crystal sensors: An overview. *Prog. Quantum Electron.*, 34(3):89–134, 2010.

[110] P. Lodahl, S. Mahmoodian, S. Stobbe, A. Rauschenbeutel, P. Schneeweiss, J. Volz, H. Pichler, and P. Zoller. Chiral quantum optics. *Nature*, 541(7638):473, 2017.

[111] S. Torquato, S. Hyun, and A. Donev. Multifunctional composites: optimizing microstructures for simultaneous transport of heat and electricity. *Phys. Rev. Lett.*, 89(26):266601, 2002.

[112] E. J. W. Crossland, M. Kamperman, M. Nedelcu, C. Ducati, U. Wiesner, D.-M. Smilgies, G. E. S. Toombes, M. A. Hillmyer, S. Ludwigs, U. Steiner, and H. J. Snaith. A bicontinuous double gyroid hybrid solar cell. *Nano Lett.*, 9(8):2807–2812, 2008.

[113] L. Sagalowicz and M. E. Leser. Delivery systems for liquid food products. *Curr. Opin. Colloid Interface Sci.*, 15(1-2):61–72, 2010.

[114] K.-H. Shen, J. R. Brown, and L. M. Hall. Diffusion in lamellae, cylinders, and double gyroid block copolymer nanostructures. *ACS Macro Lett.*, 7(9):1092–1098, 2018.

[115] S. C. Kapfer, S. T. Hyde, K. Mecke, C. H. Arns, and G. E. Schröder-Turk. Minimal surface scaffold designs for tissue engineering. *Biomaterials*, 32(29):6875–6882, 2011.

[116] L. Wang, J. Lau, E. L. Thomas, and M. C. Boyce. Co-continuous composite materials for stiffness, strength, and energy dissipation. *Adv. Mater.*, 23(13):1524–1529, 2011.

[117] S. N. Khaderi, V. S. Deshpande, and N. A. Fleck. The stiffness and strength of the gyroid lattice. *Int. J. Solids Struct.*, 51(23-24):3866–3877, 2014.

[118] D. W. Abueidda, M. Bakir, R. K. A. Al-Rub, J. S. Bergström, N. A. Sobh, and I. Jasiuk. Mechanical properties of 3D printed polymeric cellular materials with triply periodic minimal surface architectures. *Mater. Design*, 122:255–267, 2017.

[119] H. Zhang, X. Yu, and P. V. Braun. Three-dimensional bicontinuous ultrafast-charge and-discharge bulk battery electrodes. *Nat. Nanotechnol.*, 6(5):277, 2011.

[120] J. H. Pikul, H. G. Zhang, J. Cho, P. V. Braun, and W. P. King. High-power lithium ion microbatteries from interdigitated three-dimensional bicontinuous nanoporous electrodes. *Nat. Commun.*, 4:1732, 2013.

[121] S. Choudhury, M. Agrawal, P. Formanek, D. Jehnichen, D. Fischer, B. Krause, V. Albrecht, M. Stamm, and L. Ionov. Nanoporous cathodes for high-energy Li–S batteries from gyroid block copolymer templates. *ACS Nano*, 9(6):6147–6157, 2015.

[122] T.-S. Wei, B. Y. Ahn, J. Grotto, and J. A. Lewis. 3D printing of customized Li-ion batteries with thick electrodes. *Adv. Mater.*, 30(16):1703027, 2018.

[123] S. Zekoll, C. Marriner-Edwards, A. K. O. Hekselman, J. Kasemchainan, C. Kuss, D. E. J. Armstrong, D. Cai, R. J. Wallace, F. H. Richter, J. H. J. Thijssen, and P. G. Bruce. Hybrid electrolytes with 3D bicontinuous ordered ceramic and polymer microchannels for all-solid-state batteries. *Energ. Environ. Sci.*, 11(1):185–201, 2018.

[124] E. Goi, B. Cumming, and M. Gu. Impact of cubic symmetry on optical activity of dielectric 8-srs networks. *Appl. Sci.*, 8(11):2104, 2018.

[125] J.-H. Jang, C. K. Ullal, M. Maldovan, T. Gorishnyy, S. Kooi, C. Y. Koh, and E. L. Thomas. 3D micro-and nanostructures via interference lithography. *Adv. Funct. Mater.*, 17(16):3027–3041, 2007.

[126] M. Campbell, D. N. Sharp, M. T. Harrison, R. G. Denning, and A. J. Turberfield. Fabrication of photonic crystals for the visible spectrum by holographic lithography. *Nature*, 404(6773):53, 2000.

[127] J. A. Rogers, K. E. Paul, R. J. Jackman, and G. M. Whitesides. Generating 90 nanometer features using near-field contact-mode photolithography with an elastomeric phase mask. *J. Vac. Sci. Technol. B*, 16(1):59–68, 1998.

[128] S. Jeon, J.-U. Park, R. Cirelli, S. Yang, C. E. Heitzman, P. V. Braun, P. J. A. Kenis, and J. A. Rogers. Fabricating complex three-dimensional nanostructures with high-resolution conformable phase masks. *Proc. Natl. Acad. Sci. USA*, 101(34):12428–12433, 2004.

[129] D. N. Sharp, A. J. Turberfield, and R. G. Denning. Holographic photonic crystals with diamond symmetry. *Phys. Rev. B*, 68(20):205102, 2003.

[130] O. Toader, T. Y. M. Chan, and S. John. Photonic band gap architectures for holographic lithography. *Phys. Rev. Lett.*, 92(4):043905, 2004.

[131] C. K. Ullal, M. Maldovan, E. L. Thomas, G. Chen, Y.-J. Han, and S. Yang. Photonic crystals through holographic lithography: Simple cubic, diamond-like, and gyroid-like structures. *Appl. Phys. Lett.*, 84(26):5434–5436, 2004.

[132] J. H. Moon, J. Ford, and S. Yang. Fabricating three-dimensional polymeric photonic structures by multi-beam interference lithography. *Polym. Adv. Technol.*, 17(2):83–93, 2006.

[133] J. S. King, E. Graugnard, O. M. Roche, D. N. Sharp, J. Scrimgeour, R. G. Denning, A. J. Turberfield, and C. J. Summers. Infiltration and inversion of holographically defined polymer photonic crystal templates by atomic layer deposition. *Adv. Mater.*, 18(12):1561–1565, 2006.

[134] J. H. Moon, Y. Xu, Y. Dan, S.-M. Yang, A. T. Johnson, and S. Yang. Triply periodic bicontinuous structures as templates for photonic crystals: A pinch-off problem. *Adv. Mater.*, 19(11):1510–1514, 2007.

[135] M. Miyake, Y.-C. Chen, P. V. Braun, and P. Wiltzius. Fabrication of three-dimensional photonic crystals using multibeam interference lithography and electrodeposition. *Adv. Mater.*, 21(29):3012–3015, 2009.

[136] J.-H. Lee, Y.-S. Kim, K. Constant, and K.-M. Ho. Woodpile metallic photonic crystals fabricated by using soft lithography for tailored thermal emission. *Adv. Mater.*, 19(6):791–794, 2007.

[137] J. Fischer and M. Wegener. Three-dimensional optical laser lithography beyond the diffraction limit. *Laser Photonics Rev.*, 7(1):22–44, 2013.

[138] T. F. Scott, B. A. Kowalski, A. C. Sullivan, C. N. Bowman, and R. R. McLeod. Two-color single-photon photoinitiation and photoinhibition for subdiffraction photolithography. *Science*, 324(5929):913–917, 2009.

[139] Z. Gan, Y. Cao, B. Jia, and M. Gu. Dynamic modeling of superresolution photoinduced-inhibition nanolithography. *Opt. Express*, 20(15):16871–16879, 2012.

[140] L. Lu, Z. Wang, D. Ye, L. Ran, L. Fu, J. D. Joannopoulos, and M. Soljačić. Experimental observation of Weyl points. *Science*, 349(6248):622–624, 2015.

[141] M. D. Turner, G. E. Schröder-Turk, and M. Gu. Fabrication and characterization of three-dimensional biomimetic chiral composites. *Optics Express*, 19(10):10001–10008, 2011.

[142] B. P. Cumming, G. E. Schröder-Turk, S. Debbarma, and M. Gu. Bragg-mirror-like circular dichroism in bio-inspired quadruple-gyroid 4srs nanostructures. *Light: Science & Applications*, 6(1):e16192, 2017.

[143] M. Saba, M. D. Turner, K. Mecke, M. Gu, and G. E. Schröder-Turk. Group theory of circular-polarization effects in chiral photonic crystals with four-fold rotation axes applied to the eight-fold intergrowth of gyroid nets. *Phys. Rev. B*, 88(24):245116, 2013.

[144] F. Turella, B. P. Cumming, G. E. Schröder-Turk, and M. Gu. Observation of optical activity in dielectric biomimetic 8-srs networks. *Opt. Lett.*, 40(20):4795–4798, 2015.

[145] S. Peng, R. Zhang, V. H. Chen, E. T. Khabiboulline, P. Braun, and H. A. Atwater. Three-dimensional single gyroid photonic crystals with a mid-infrared bandgap. *ACS Photonics*, 3(6):1131–1137, 2016.

[146] B. P. Cumming, G. E. Schröder-Turk, and M. Gu. Metallic gyroids with broadband circular dichroism. *Opt. Lett.*, 43(4):863–866, 2018.

[147] S. Wong, M. Deubel, F. Pérez-Willard, S. John, G. A. Ozin, M. Wegener, and G. von Freymann. Direct laser writing of three-dimensional photonic crystals with a complete photonic bandgap in chalcogenide glasses. *Adv. Mater.*, 18(3):265–269, 2006.

[148] E. Nicoletti, G. Zhou, B. Jia, M. J. Ventura, D. Bulla, B. Luther-Davies, and M. Gu. Observation of multiple higher-order stopgaps from three-dimensional chalcogenide glass photonic crystals. *Opt. Lett.*, 33(20):2311–2313, 2008.

[149] B. P. Cumming, M. D. Turner, G. E. Schröder-Turk, S. Debbarma, B. Luther-Davies, and M. Gu. Adaptive optics enhanced direct laser writing of high refractive index gyroid photonic crystals in chalcogenide glass. *Opt. Express*, 22(1):689–698, 2014.

[150] Z. Qin, G. S. Jung, M. J. Kang, and M. J. Buehler. The mechanics and design of a lightweight three-dimensional graphene assembly. *Sci. Adv.*, 3(1):e1601536, 2017.

[151] L. Wu, J. He, W. Shang, T. Deng, J. Gu, H. Su, Q. Liu, W. Zhang, and D. Zhang. Optical functional materials inspired by biology. *Adv. Opt. Mater.*, 4(2):195–224, 2016.

[152] Credit: Dr. Feodor Oestreicher. Synthesevorschrift zur herstellung des raumtemperaturflüssigkristalles. `http://fluessigkristalle.com/synthese.htm`, 2019.

[153] J. T. Kajiya and J. T. Whitted. Liquid crystal display (LCD), May 27 2014. US Patent 8,736,802.

[154] D. Yang. *Fundamentals of liquid crystal devices*. John Wiley & Sons, 2014.

[155] B. B. Lahiri, S. Bagavathiappan, T. Jayakumar, and J. Philip. Medical applications of infrared thermography: a review. *Infrared Phys. Technol.*, 55(4):221–235, 2012.

[156] P. T. Ireland and T. V. Jones. Liquid crystal measurements of heat transfer and surface shear stress. *Meas. Sci. Technol.*, 11(7):969, 2000.

[157] P. G. de Gennes. *The Physics of Liquid Crystals*. Clarendon Press Oxford, 1974.

[158] O. Lehmann. über krystallinische Flüssigkeiten. *Ann. Phys.*, 277(11):525–537, 1890.

[159] F. Reinitzer. Beiträage zur Kenntniss des Cholesterins. *Monatsh. Chem.*, 9:421–441, 1888.

[160] M. G. Friedel. Les états mésomorphes de la matière. *Ann. Phys.*, 18:273–474, 1922.

[161] S. Chandrasekhar and G. S. Ranganath. Discotic liquid crystals. *Rep. Prog. Phys.*, 53(1):57, 1990.

[162] V. Luzzati, A. Tardieu, T. Gulik-Krzywicki, E. Rivas, and F. Reiss-Husson. Structure of the cubic phases of lipid–water systems. *Nature*, 220(5166):485, 1968.

[163] J. Briggs, H. Chung, and M. Caffrey. The temperature-composition phase diagram and mesophase structure characterization of the monoolein/water system. *J. Phys. II*, 6(5):723–751, 1996.

[164] K. Larsson. Cubic lipid-water phases: structures and biomembrane aspects. *J. Phys. Chem.*, 93(21):7304–7314, 1989.

[165] V. Cherezov, J. Clogston, M. Z. Papiz, and M. Caffrey. Room to move: crystallizing membrane proteins in swollen lipidic mesophases. *J. Mol. Biol.*, 357(5):1605–1618, 2006.

[166] B. Ericsson, K. Larsson, and K. Fontell. A cubic protein-monoolein-water phase. *Biochim. Biophys. Acta, Biomembr.*, 729(1):23–27, 1983.

[167] G. E. Schröder. *Skeletons in the labyrinth: Medial Representations and packing properties of bicontinuous space partitions*. PhD thesis, The Australian National University, 2005.

[168] W. Buchheim and K. Larsson. Cubic lipid-protein-water phases. *J. Colloid Interface Sci.*, 117:582–583, 1987.

[169] E. L. Snapp, R. S. Hegde, M. Francolini, F. Lombardo, S. Colombo, E. Pedrazzini, N. Borgese, and J. Lippincott-Schwartz. Formation of stacked ER cisternae by low affinity protein interactions. *J. Cell Biol.*, 163(2):257–269, 2003.

[170] Z. Almsherqi, S. Hyde, M. Ramachandran, and Y. Deng. Cubic membranes: a structure-based design for DNA uptake. *J. Royal Soc. Interface*, 5(26):1023–1029, 2008.

[171] T. Landh. From entangled membranes to eclectic morphologies: cubic membranes as subcellular space organizers. *FEBS Lett.*, 369(1):13–17, 1995.

[172] Z. A. Almsherqi, T. Landh, S. D. Kohlwein, and Y. Deng. Cubic membranes: the missing dimension of cell membrane organization. *Int. Rev. Cell Mol. Biol.*, 274:275–342, 2009.

[173] B. E. S Gunning. Membrane geometry of "open" prolamellar bodies. *Protoplasma*, 215(1-4):4–15, 2001.

[174] Z. Almsherqi, F. Margadant, and Y. Deng. A look through 'lens' cubic mitochondria. *Interface Focus*, 2(5):539–545, 2012.

[175] Q. Xiao, Z. Wang, D. Williams, P. Leowanawat, M. Peterca, S. E. Sherman, S. Zhang, D. A. Hammer, P. A. Heiney, S. R. King, D. M. Markovitz, S. André, H.-J. Gabius, M. L. Klein, and V. Percec. Why do membranes of some unhealthy cells adopt a cubic architecture? *ACS Cent. Sci*, 2(12):943–953, 2016.

[176] Z. A. Almsherqi, C. S. McLachlan, P. Mossop, K. Knoops, and Y. Deng. Direct template matching reveals a host subcellular membrane gyroid cubic structure that is associated with SARS virus. *Redox Rep.*, 10(3):167–171, 2005.

[177] Y. Deng, Z. A. Almsherqi, M. M. L. Ng, and S. D. Kohlwein. Do viruses subvert cholesterol homeostasis to induce host cubic membranes? *Trends Cell Biol.*, 20(7):371–379, 2010.

[178] K. Takei, G. A. Mignery, E. Mugnaini, T. C. Südhof, and P. De Camilli. Inositol 1, 4, 5-trisphosphate receptor causes formation of er cisternal stacks in transfected fibroblasts and in cerebellar purkinje cells. *Neuron*, 12(2):327–342, 1994.

[179] Y. Deng and Z. A. Almsherqi. Evolution of cubic membranes as antioxidant defence system. *Interface Focus*, 5(4):20150012, 2015.

[180] V. Saranathan, C. O. Osuji, S. G. J. Mochrie, H. Noh, S. Narayanan, A. Sandy, E. R. Dufresne, and R. O. Prum. Structure, function, and self-assembly of single network gyroid (I4132) photonic crystals in butterfly wing scales. *Proc. Natl. Acad. Sci. USA*, 107(26):11676–11681, 2010.

[181] H. Ghiradella. Insect cuticular surface modifications: scales and other structural formations. In *Adv. In. Insect Phys.*, volume 38, pages 135–180. Elsevier, 2010.

[182] Y. Tan, J. Gu, X. Zang, W. Xu, K. Shi, L. Xu, and D. Zhang. Versatile fabrication of intact three-dimensional metallic butterfly wing scales with hierarchical sub-micrometer structures. *Angew. Chem.*, 123(36):8457–8461, 2011.

[183] C. Mille, E. C. Tyrode, and R. W. Corkery. 3D titania photonic crystals replicated from gyroid structures in butterfly wing scales: approaching full band gaps at visible wavelengths. *RSC Adv.*, 3(9):3109–3117, 2013.

[184] L. Wu, W. Wang, W. Zhang, H. Su, Q. Liu, J. Gu, T. Deng, and D. Zhang. Highly sensitive, reproducible and uniform SERS substrates with a high density of three-dimensionally distributed hotspots: gyroid-structured au periodic metallic materials. *NPG Asia Mater.*, 10(1):e462, 2018.

[185] S. Vignolini, N. A. Yufa, P. S. Cunha, S. Guldin, I. Rushkin, M. Stefik, K. Hur, U. Wiesner, J. J. Baumberg, and U. Steiner. A 3D optical metamaterial made by self-assembly. *Adv. Mater.*, 24(10):OP23–OP27, 2012.

[186] H.-Y. Hsueh, H.-Y. Chen, Y.-C. Ling, W.-S. Huang, Y.-C. Hung, S. Gwo, and R.-M. Ho. A polymer-based SERS-active substrate with gyroid-structured gold multibranches. *J. Mater. Chem. C*, 2(23):4667–4675, 2014.

[187] S. Salvatore, S. Vignolini, J. Philpott, M. Stefik, U. Wiesner, J. J. Baumberg, and U. Steiner. A high transmission wave-guide wire network made by self-assembly. *Nanoscale*, 7(3):1032–1036, 2014.

[188] M. W. Matsen and M. Schick. Stable and unstable phases of a diblock copolymer melt. *Phys. Rev. Lett.*, 72(16):2660, 1994.

[189] Y. Mai and A. Eisenberg. Self-assembly of block copolymers. *Chem. Soc. Rev.*, 41(18):5969–5985, 2012.

[190] M. W. Matsen. Phase behavior of block copolymer/homopolymer blends. *Macromolecules*, 28(17):5765–5773, 1995.

[191] A. C. Finnefrock, R. Ulrich, G. E. S. Toombes, S. M. Gruner, and U. Wiesner. The plumber's nightmare: 1 a new morphology in block copolymer-ceramic nanocomposites and mesoporous aluminosilicates. *J. Am. Chem. Soc.*, 125(43):13084–13093, 2003.

[192] M. G. Fischer, L. De Campo, J. J. K. Kirkensgaard, S. T. Hyde, and G. E. Schröder-Turk. The tricontinuous 3 ths (5) phase: A new morphology in copolymer melts. *Macromolecules*, 47(21):7424–7430, 2014.

[193] A. M. Urbas, M. Maldovan, P. DeRege, and E. L. Thomas. Bicontinuous cubic block copolymer photonic crystals. *Adv. Mater.*, 14(24):1850–1853, 2002.

[194] T.-H. Lin, Y. Li, C.-T. Wang, H.-C. Jau, C.-W. Chen, C.-C. Li, H. K. Bisoyi, T. J. Bunning, and Q. Li. Red, green and blue reflections enabled in an optically tunable self-organized 3D cubic nanostructured thin film. *Adv. Mater.*, 25(36):5050–5054, 2013.

[195] H. K. Bisoyi and Q. Li. Light-driven liquid crystalline materials: from photo-induced phase transitions and property modulations to applications. *Chem. Rev.*, 116(24):15089–15166, 2016.

[196] E. L. Lin, W. L. Hsu, and Y. W. Chiang. Trapping structural coloration by a bioinspired gyroid microstructure in solid state. *ACS Nano*, 12(1):485–493, 2018.

[197] S. Park, Y. Kim, W. Lee, S.-M. Hur, and D. Y. Ryu. Gyroid structures in solvent annealed PS-b-PMMA films: Controlled orientation by substrate interactions. *Macromolecules*, 50(13):5033–5041, 2017.

[198] D. H. Everett. *Basic principles of colloid science*. Royal society of chemistry, 2007.

[199] M. Kardar. *Statistical physics of particles*. Cambridge University Press, 2007.

[200] R. K. Pathria and P. D. Beale. *Statistical mechanics*. Elsevier, Oxford, 2011.

[201] D. P. Landau and K. Binder. *A guide to Monte Carlo simulations in statistical physics*. Cambridge University Press, 2014.

[202] V. N. Manoharan. Colloidal matter: Packing, geometry, and entropy. *Science*, 349(6251):1253751, 2015.

[203] L. Onsager. The effects of shape on the interaction of colloidal particles. *Ann. N. Y. Acad. Sci.*, 51(4):627–659, 1949.

[204] G. D. Scott and D. M. Kilgour. The density of random close packing of spheres. *J. Phys. D: Appl. Phys.*, 2(6):863, 1969.

[205] P. N. Pusey, E. Zaccarelli, C. Valeriani, E. Sanz, W. C. K. Poon, and M. E. Cates. Hard spheres: crystallization and glass formation. *Philos. Trans. Royal Soc. A*, 367(1909):4993–5011, 2009.

[206] B. J. Alder and T. E. Wainwright. Phase transition for a hard sphere system. *J. Chem. Phys.*, 27(5):1208–1209, 1957.

[207] P. N. Pusey and W. Van Megen. Phase behaviour of concentrated suspensions of nearly hard colloidal spheres. *Nature*, 320(6060):340, 1986.

[208] S. C. Kapfer and W. Krauth. Two-dimensional melting: From liquid-hexatic coexistence to continuous transitions. *Phys. Rev. Lett.*, 114(3):035702, 2015.

[209] E. P. Bernard and W. Krauth. Two-step melting in two dimensions: First-order liquid-hexatic transition. *Phys. Rev. Lett.*, 107(15):155704, 2011.

[210] H. Hansen-Goos and K. Mecke. Tensorial density functional theory for non-spherical hard-body fluids. *J. Phys. Condens. Matter.*, 22:364107, 2010.

[211] M. Marechal, H. H. Goetzke, A. Härtel, and H. Löwen. Inhomogeneous fluids of colloidal hard dumbbells: fundamental measure theory and Monte Carlo simulations. *J. Chem. Phys.*, 135(23):234510, 2011.

[212] M. Marechal and H. Löwen. Density functional theory for hard polyhedra. *Phys. Rev. Lett.*, 110:137801, 2013.

[213] J. A. C. Veerman and D. Frenkel. Phase diagram of a system of hard spherocylinders by computer simulation. *Phys. Rev. A*, 41(6):3237, 1990.

[214] D. Frenkel, B. M. Mulder, and J. P. McTague. Phase diagram of a system of hard ellipsoids. *Phys. Rev. Lett.*, 52(4):287, 1984.

[215] G. A. Few and M. Rigby. Equation of state for systems of hard non-spherical molecules. *Chem. Phys. Lett.*, 20(5):433–435, 1973.

[216] M. Whittle and A. J. Masters. Liquid crystal formation in a system of fused hard spheres. *Mol. Phys.*, 72(2):247–265, 1991.

[217] C. Vega, C. McBride, and L. G. MacDowell. Liquid crystal phase formation for the linear tangent hard sphere model from Monte Carlo simulations. *J. Chem. Phys.*, 115(9):4203–4211, 2001.

[218] H. B. Kolli, E. Frezza, G. Cinacchi, A. Ferrarini, A. Giacometti, T. S. Hudson, C. De Michele, and F. Sciortino. Self-assembly of hard helices: a rich and unconventional polymorphism. *Soft Matter*, 10(41):8171–8187, 2014.

[219] B. S. John, C. Juhlin, and F. A. Escobedo. Phase behavior of colloidal hard perfect tetragonal parallelepipeds. *J. Chem. Phys.*, 128(4):044909, 2008.

[220] M. Dennison, K. Milinković, and M. Dijkstra. Phase diagram of hard snowman-shaped particles. *J. Chem. Phys.*, 137(4):044507, 2012.

[221] P. F. Damasceno, M. Engel, and S. C. Glotzer. Predictive self-assembly of polyhedra into complex structures. *Science*, 337(6093):453–457, 2012.

[222] M. Marechal, S. Dussi, and M. Dijkstra. Density functional theory and simulations of colloidal triangular prisms. *J. Chem. Phys.*, 146(12):124905, 2017.

[223] S. Dussi, N. Tasios, T. Drwenski, R. van Roij, and M. Dijkstra. Hard competition: stabilizing the elusive biaxial nematic phase in suspensions of colloidal particles with extreme lengths. *Phys. Rev. Lett.*, 120(17):177801, 2018.

[224] J. K. G. Dhont, M. P. Lettinga, Z. Dogic, T. A. J. Lenstra, H. Wang, S. Rathgeber, P. Carletto, L. Willner, H. Frielinghaus, and P. Lindner. Shear-banding and microstructure of colloids in shear flow. *Faraday Discuss.*, 123:157–172, 2003.

[225] T. Divoux, M. A. Fardin, S. Manneville, and S. Lerouge. Shear banding of complex fluids. *Annu. Rev. Fluid Mech.*, 48:81–103, 2016.

[226] J. Kim, R. J. Larsen, and D. A. Weitz. Synthesis of nonspherical colloidal particles with anisotropic properties. *J. Am. Chem. Soc.*, 128(44):14374–14377, 2006.

[227] A. Perro, S. Reculusa, E. Bourgeat-Lami, E. Duguet, and S. Ravaine. Synthesis of hybrid colloidal particles: From snowman-like to raspberry-like morphologies. *Colloids and Surfaces A, Physicochem. Eng. Asp.*, 284:78–83, 2006.

[228] K. M. Keville, E. I. Franses, and J. M. Caruthers. Preparation and characterization of monodisperse polymer microspheroids. *J. Colloid Interface Sci.*, 144(1):103–126, 1991.

[229] A. Mohraz and M. J. Solomon. Direct visualization of colloidal rod assembly by confocal microscopy. *Langmuir*, 21(12):5298–5306, 2005.

[230] A. Kuijk, D. V. Byelov, A. V. Petukhov, A. van Blaaderen, and A. Imhof. Phase behavior of colloidal silica rods. *Faraday Discuss.*, 159:181–199, 2012.

[231] S. Mehra, E. M. Chan, and A. Salleo. Modular synthetic design enables precise control of shape and doping in colloidal zinc oxide nanorods. *J. Mater. Chem. C*, 3:7172–7179, 2015.

[232] T. S. Ahmadi, Z. L. Wang, T. C. Green, A. Henglein, and M. A. El-Sayed. Shape-controlled synthesis of colloidal platinum nanoparticles. *Science*, 272(5270):1924–1925, 1996.

[233] A. R. Tao, S. Habas, and P. Yang. Shape control of colloidal metal nanocrystals. *small*, 4(3):310–325, 2008.

[234] L. Rossi, V. Soni, D. J. Ashton, D. J. Pine, A. P. Philipse, P. M. Chaikin, M. Dijkstra, S. Sacanna, and W. T. M. Irvine. Shape-sensitive crystallization in colloidal superball fluids. *Proc. Natl. Acad. Sci. USA*, page 201415467, 2015.

[235] J. A. Champion, Y. K. Katare, and S. Mitragotri. Making polymeric micro- and nanoparticles of complex shapes. *Proc. Natl. Acad. Sci. USA*, 104(29):11901–11904, 2007.

[236] S. C. Glotzer and M. J. Solomon. Anisotropy of building blocks and their assembly into complex structures. *Nat. Mater.*, 6(8):557, 2007.

[237] P. Bolhuis and D. Frenkel. Tracing the phase boundaries of hard spherocylinders. *J. Chem. Phys.*, 106(2):666–687, 1997.

[238] D. Klotsa, E. R. Chen, M. Engel, and S. C. Glotzer. Intermediate crystalline structures of colloids in shape space. *Soft Matter*, 14(43):8692–8697, 2018.

[239] A. Walther and A. H. E. Müller. Janus particles. *Soft Matter*, 4(4):663–668, 2008.

[240] D. J. Kraft, R. Ni, F. Smallenburg, M. Hermes, K. Yoon, D. A. Weitz, A. van Blaaderen, J. Groenewold, M. Dijkstra, and W. K. Kegel. Surface roughness directed self-assembly of patchy particles into colloidal micelles. *Proc. Natl. Acad. Sci. USA*, 109(27):10787–10792, 2012.

[241] L. J. Ellison, D. J. Michel, F. Barmes, and D. J. Cleaver. Entropy-driven formation of the gyroid cubic phase. *Phys. Rev. Lett.*, 97(23):237801, 2006.

[242] R. Berardi, M. Ricci, and C. Zannoni. Ferroelectric nematic and smectic liquid crystals from tapered molecules. *ChemPhysChem*, 2(7):443–447, 2001.

[243] F. Barmes, M. Ricci, C. Zannoni, and D. J. Cleaver. Computer simulations of hard pear-shaped particles. *Phys. Rev. E*, 68:021708, 2003.

[244] J. N. Israelachvili, D. J. Mitchell, and B. W. Ninham. Theory of self-assembly of hydrocarbon amphiphiles into micelles and bilayers. *J. Chem. Soc., Faraday Trans. 2*, 72:1525–1568, 1976.

[245] W. Helfrich. Elastic properties of lipid bilayers: theory and possible experiments. *Z. Naturforsch. C*, 28(11-12):693–703, 1973.

[246] U. S. Schwarz and G. Gompper. Stability of inverse bicontinuous cubic phases in lipid-water mixtures. *Phys. Rev. Lett.*, 85(7):1472, 2000.

[247] G. van Anders, D. Klotsa, A. S. Karas, P. M. Dodd, and S. C. Glotzer. Digital alchemy for materials design: Colloids and beyond. *ACS Nano*, 9(10):9542–9553, 2015.

[248] D. Höhner, S. Wirtz, and V. Scherer. Experimental and numerical investigation on the influence of particle shape and shape approximation on hopper discharge using the discrete element method. *Powder Technol.*, 235:614–627, 2013.

[249] F. M. Schaller, S. C. Kapfer, J. E. Hilton, P. W. Cleary, K. Mecke, C. De Michele, T. Schilling, M. Saadatfar, M. Schröter, G. W. Delaney, and G. E. Schröder-Turk. Non-universal Voronoi cell shapes in amorphous ellipsoid packs. *Europhys. Lett.*, 111(2):24002, 2015.

[250] I. S. Aranson and L. S. Tsimring. Patterns and collective behavior in granular media: Theoretical concepts. *Rev. Mod. Phys.*, 78(2):641, 2006.

[251] M. Gonzalez-Pinto, F. Borondo, Y. Martínez-Ratón, and E. Velasco. Clustering in vibrated monolayers of granular rods. *Soft Matter*, 13(14):2571–2582, 2017.

[252] M. C. Bott, F. Winterhalter, M. Marechal, A. Sharma, J. M. Brader, and R. Wittmann. Isotropic-nematic transition of self-propelled rods in three dimensions. *Phys. Rev. E*, 98(1):012601, 2018.

[253] A. Haji-Akbari, M. Engel, and S. C. Glotzer. Phase diagram of hard tetrahedra. *J. Chem. Phys.*, 135(19):194101, 2011.

[254] R. Ni, A. P. Gantapara, J. de Graaf, R. van Roij, and M. Dijkstra. Phase diagram of colloidal hard superballs: from cubes via spheres to octahedra. *Soft Matter*, 8(34):8826–8834, 2012.

[255] W. M. Gelbart and A. Gelbart. Effective one-body potentials for orientationally anisotropic fluids. *Mol. Phys.*, 33(5):1387–1398, 1977.

[256] J. S. Ketchel and P. M. Larochelle. Collision detection of cylindrical rigid bodies using line geometry. In *ASME 2005 International Design Engineering Technical Conferences and Computers and Information in Engineering Conference*, pages 811–825. American Society of Mechanical Engineers, 2005.

[257] X. Zheng and P. Palffy-Muhoray. Distance of closest approach of two arbitrary hard ellipses in two dimensions. *Phys. Rev. E*, 75(6):061709, 2007.

[258] X. Zheng, W. Iglesias, and P. Palffy-Muhoray. Distance of closest approach of two arbitrary hard ellipsoids. *Phys. Rev. E*, 79:057702, May 2009.

[259] C. Vega, E. P. A. Paras, and P. A. Monson. Solid–fluid equilibria for hard dumbbells via Monte Carlo simulation. *J. Chem. Phys.*, 96(12):9060–9072, 1992.

[260] K. Milinković, M. Dennison, and M. Dijkstra. Phase diagram of hard asymmetric dumbbell particles. *Phys. Rev. E*, 87(3):032128, 2013.

[261] C. Jennings, M. Ramsay, T. Hudson, and P. Harrowell. Packing concave molecules in crystals and amorphous solids: on the connection between shape and local structure. *Mol. Phys.*, 113(17-18):2755–2769, 2015.

[262] H. Kruggel-Emden, S. Rickelt, S. Wirtz, and V. Scherer. A study on the validity of the multi-sphere discrete element method. *Powder Technol.*, 188(2):153–165, 2008.

[263] D. Markauskas, R. Kačianauskas, A. Džiugys, and R. Navakas. Investigation of adequacy of multi-sphere approximation of elliptical particles for DEM simulations. *Granular Matter*, 12(1):107–123, 2010.

[264] D. Höhner, S. Wirtz, H. Kruggel-Emden, and V. Scherer. Comparison of the multi-sphere and polyhedral approach to simulate non-spherical particles within the discrete element method: Influence on temporal force evolution for multiple contacts. *Powder Technol.*, 208(3):643–656, 2011.

[265] S. Gottschalk, M. C. Lin, and D. Manocha. OBBTree: A hierarchical structure for rapid interference detection. In *Proc. of ACM Siggraph'96*, pages 171–180. ACM, 1996.

[266] T. C. Hudson, M. C. Lin, J. Cohen, S. Gottschalk, and D. Manocha. V-COLLIDE: accelerated collision detection for VRML. In *Proc. of VRML*, pages 117–ff. ACM, 1997.

[267] P. Jiménez, F. Thomas, and C. Torras. 3D collision detection: a survey. *Computers & Graphics*, 25(2):269–285, 2001.

[268] L. Filion, M. Marechal, B. van Oorschot, D. Pelt, F. Smallenburg, and M. Dijkstra. Efficient method for predicting crystal structures at finite temperature: Variable box shape simulations. *Phys. Rev. Lett.*, 103(18):188302, 2009.

[269] J. de Graaf, R. van Roij, and M. Dijkstra. Dense regular packings of irregular nonconvex particles. *Phys. Rev. Lett.*, 107(15):155501, 2011.

[270] J. Vieillard-Baron. Phase transitions of the classical hard-ellipse system. *J. Chem. Phys.*, 56(10):4729–4744, 1972.

[271] J. W. Perram and M. S. Wertheim. Statistical mechanics of hard ellipsoids. I. Overlap algorithm and the contact function. *J. Comp. Phys.*, 58(3):409–416, 1985.

[272] B. J. Berne and P. Pechukas. Gaussian model potentials for molecular interactions. *J. Chem. Phys.*, 56(8):4213–4216, 1972.

[273] D. J. Cleaver, C. M. Care, M. P. Allen, and M. P. Neal. Extension and generalization of the Gay-Berne potential. *Phys. Rev. E*, 54(1):559, 1996.

[274] P. Ballone, G. Pastore, G. Galli, and D. Gazzillo. Additive and non-additive hard sphere mixtures: Monte Carlo simulation and integral equation results. *Mol. Phys.*, 59(2):275–290, 1986.

[275] E. Lomba, M. Alvarez, L. L. Lee, and N. G. Almarza. Phase stability of binary non-additive hard-sphere mixtures: A self-consistent integral equation study. *J. Chem. Phys.*, 104(11):4180–4188, 1996.

[276] R. Roth and R. Evans. The depletion potential in non-additive hard-sphere mixtures. *Europhys. Lett.*, 53(2):271, 2001.

[277] P. Hopkins and M. Schmidt. Binary non-additive hard sphere mixtures: fluid demixing, asymptotic decay of correlations and free fluid interfaces. *J. Phys. Condens. Matter.*, 22(32):325108, 2010.

[278] K. Zhang, M. Fan, Y. Liu, J. Schroers, M. D. Shattuck, and C. S. O'Hern. Beyond packing of hard spheres: The effects of core softness, non-additivity, intermediate-range repulsion, and many-body interactions on the glass-forming ability of bulk metallic glasses. *J. Chem. Phys*, 143(18):184502, 2015.

[279] P. N. Pusey and W. van Megen. In S. A. Safran and N. A. Clark, editors, *Physics of Complex and Supramolecular Fluids*, pages 673–698. Wiley, New York, 1987.

[280] W. C. K. Poon, E. R. Weeks, and C. P. Royall. On measuring colloidal volume fractions. *Soft Matter*, 8(1):21–30, 2012.

[281] C. P. Royall, W. C. K. Poon, and E. R. Weeks. In search of colloidal hard spheres. *Soft Matter*, 9(1):17–27, 2013.

[282] J. D. Weeks, D. Chandler, and H. C. Andersen. Role of repulsive forces in determining the equilibrium structure of simple liquids. *J. Chem. Phys.*, 54(12):5237–5247, 1971.

[283] J. G. Gay and B. J. Berne. Modification of the overlap potential to mimic a linear site–site potential. *J. Chem. Phys.*, 74(6):3316–3319, 1981.

[284] G. C. Shearman, O. Ces, R. H. Templer, and J. M. Seddon. Inverse lyotropic phases of lipids and membrane curvature. *J. Phys. Condens. Matter.*, 18(28):S1105, 2006.

[285] J. A. Anderson, E. Jankowski, T. L. Grubb, M. Engel, and S. C. Glotzer. Massively parallel Monte Carlo for many-particle simulations on GPUs. *J. Comput. Phys.*, 254:27–38, 2013.

[286] T. L. Hill. *An introduction to statistical thermodynamics*. Courier Corporation, 1986.

[287] J. P. Hansen and I. R. McDonald. *Theory of simple liquids*. Elsevier, 1986.

[288] P. Walters. *An introduction to ergodic theory*, volume 79. Springer Science & Business Media, 2000.

[289] W. Feller. *An introduction to probability theory and its applications*, volume 2. John Wiley & Sons, 2008.

[290] J. W. Gibbs. *Elementary principles in statistical mechanics*. Scribner, 1902.

[291] H. Dominguez, E. Velasco, and J. Alejandre. Stress anisotropy in liquid crystalline phases. *Mol. Phys.*, 100(16):2739–2744, 2002.

[292] M. P. Allen and D. J. Tildesley. *Computer simulation of liquids*. Oxford university press, 1991.

[293] D. Frenkel and B. Smit. *Understanding Molecular Simulation: From Algorithms to Applications*. Computational Science Serie, Academic Press, Orlando, 2002.

[294] K. Singer, A. Taylor, and J. V. L. Singer. Thermodynamic and structural properties of liquids modelled by '2-Lennard-Jones centres' pair potentials. *Mol. Phys.*, 33(6):1757–1795, 1977.

[295] L. Verlet. Computer" experiments" on classical fluids. I. Thermodynamical properties of Lennard-Jones molecules. *Phys. Rev.*, 159(1):98, 1967.

[296] D. J. Evans and B. L. Holian. The Nose–Hoover thermostat. *J. Chem. Phys.*, 83(8):4069–4074, 1985.

[297] W. Smith. Elements of Molecular Dynamics. published online at `http://scc.acad.bg/ncsa/articles/library/Library2016_Supercomputers-at-Work/Molecular_Dynamics/Elements-of-Molecular-Dynamics-Smith%20.pdf`, 2014.

[298] B. D. Lubachevsky. How to simulate billiards and similar systems. *J. Comput. Phys.*, 94(2):255–283, 1991.

[299] P. A. Gagniuc. *Markov chains: from theory to implementation and experimentation*. John Wiley & Sons, 2017.

[300] E. P. Bernard, W. Krauth, and D. B. Wilson. Event-chain Monte Carlo algorithms for hard-sphere systems. *Phys. Rev. E*, 80(5):056704, 2009.

[301] Kapfer S. and W. Krauth. Irreversible local Markov chains with rapid convergence towards equilibrium. *Phys. Rev. Lett.*, 119(24), Dec 2017.

[302] N. Metropolis, A. W. Rosenbluth, M. N. Rosenbluth, A. H. Teller, and E. Teller. Equation of state calculations by fast computing machines. *J. Chem. Phys.*, 21(6):1087–1092, 1953.

[303] P. M. Chaikin, T. C. Lubensky, and T. A. Witten. *Principles of condensed matter physics*, volume 1. Cambridge university press Cambridge, 1995.

[304] R. Eppenga and D. Frenkel. Monte carlo study of the isotropic and nematic phases of infinitely thin hard platelets. *Mol. Phys.*, 52(6):1303–1334, 1984.

[305] A. Avgeropoulos, B. J Dair, N. Hadjichristidis, and E. L. Thomas. Tricontinuous double gyroid cubic phase in triblock copolymers of the ABA type. *Macromolecules*, 30(19):5634–5642, 1997.

[306] B. Chu and B. S. Hsiao. Small-angle X-ray scattering of polymers. *Chem. Rev.*, 101(6):1727–1762, 2001.

[307] R. Roy, J. K. Park, W.-S. Young, S. E. Mastroianni, M. S. Tureau, and T. H. Epps III. Double-gyroid network morphology in tapered diblock copolymers. *Macromolecules*, 44(10):3910–3915, 2011.

[308] I. Vukovic, T. P. Voortman, D. H. Merino, G. Portale, P. Hiekkataipale, J. Ruokolainen, G. ten Brinke, and K. Loos. Double gyroid network morphology in supramolecular diblock copolymer complexes. *Macromolecules*, 45(8):3503–3512, 2012.

[309] A. M. Seddon, J. Hallett, C. Beddoes, T. S. Plivelic, and A. M. Squires. Experimental confirmation of transformation pathways between inverse double diamond and gyroid cubic phases. *Langmuir*, 30(20):5705–5710, 2014.

[310] X. Cao, D. Xu, Y. Yao, L. Han, O. Terasaki, and S. Che. Interconversion of triply periodic constant mean curvature surface structures: From double diamond to single gyroid. *Chem. Mat.*, 28(11):3691–3702, 2016.

[311] A. S. Clarke and J. D. Wiley. Numerical simulation of the dense random packing of a binary mixture of hard spheres: Amorphous metals. *Phys. Rev. B*, 35(14):7350, 1987.

[312] V. A. Luchnikov, N. N. Medvedev, L. Oger, and J.-P. Troadec. Voronoi-delaunay analysis of voids in systems of nonspherical particles. *Phys. Rev. E*, 59(6):7205, 1999.

[313] T. Aste, T. Di Matteo, M. Saadatfar, T. J. Senden, M. Schröter, and H. L. Swinney. An invariant distribution in static granular media. *Europhys. Lett.*, 79(2):24003, 2007.

[314] A. van Blaaderen and P. Wiltzius. Real-space structure of colloidal hard-sphere glasses. *Science*, 270(5239):1177–1179, 1995.

[315] Á. G. Marín, H. Gelderblom, D. Lohse, and J. H. Snoeijer. Order-to-disorder transition in ring-shaped colloidal stains. *Phys. Rev. Lett.*, 107(8):085502, 2011.

[316] A. L. Thorneywork, J. L. Abbott, D. G. A. L. Aarts, and R. P. A. Dullens. Two-dimensional melting of colloidal hard spheres. *Phys. Rev. Lett.*, 118(15):158001, 2017.

[317] G. W. Brodland and J. H. Veldhuis. Computer simulations of mitosis and interdependencies between mitosis orientation, cell shape and epithelia reshaping. *J. Biomech.*, 35(5):673–681, 2002.

[318] F. Dupuis, J.-F. Sadoc, R. Jullien, B. Angelov, and J.-P. Mornon. Voro3D: 3D Voronoi tessellations applied to protein structures. *Bioinformatics*, 21(8):1715–1716, 2004.

[319] A. Poupon. Voronoi and Voronoi-related tessellations in studies of protein structure and interaction. *Curr. Opin. Struct. Biol.*, 14(2):233–241, 2004.

[320] S. M. Zehnder, M. Suaris, M. M. Bellaire, and T. E. Angelini. Cell volume fluctuations in MDCK monolayers. *Biophys. J.*, 108(2):247–250, 2015.

[321] D. Bi, X. Yang, M. C. Marchetti, and M. L. Manning. Motility-driven glass and jamming transitions in biological tissues. *Phys. Rev. X*, 6(2):021011, 2016.

[322] A. Rahman. Liquid structure and self-diffusion. *J. Chem. Phys.*, 45(7):2585–2592, 1966.

[323] P. Ziherl and R. D. Kamien. Soap froths and crystal structures. *Phys. Rev. Lett.*, 85(16):3528, 2000.

[324] F. W. Starr, S. Sastry, J. F. Douglas, and S. C. Glotzer. What do we learn from the local geometry of glass-forming liquids? *Phys. Rev. Lett.*, 89(12):125501, 2002.

[325] M. E. Evans, A. M. Kraynik, D. A. Reinelt, K. Mecke, and G. E. Schröder-Turk. Networklike propagation of cell-level stress in sheared random foams. *Phys. Rev. Lett.*, 111(13):138301, 2013.

[326] S. C. Takatori, W. Yan, and J. F. Brady. Swim pressure: stress generation in active matter. *Phys. Rev. Lett.*, 113(2):028103, 2014.

[327] M. Ramella, W. Boschin, D. Fadda, and M. Nonino. Finding galaxy clusters using Voronoi tessellations. *Astron. Astrophys.*, 368(3):776–786, 2001.

[328] N. Hamaus, B. D. Wandelt, P. M. Sutter, G. Lavaux, and M. S. Warren. Cosmology with void-galaxy correlations. *Phys. Rev. Lett.*, 112(4):041304, 2014.

[329] E. Wigner and F. Seitz. On the constitution of metallic sodium. *Phys. Rev.*, 43(10):804, 1933.

[330] H. Brumberger and J. Goodisman. Voronoi cells: An interesting and potentially useful cell model for interpreting the small-angle scattering of catalysts. *J. Appl. Crystallogr.*, 16(1):83–88, 1983.

[331] N. Pittet. Dynamical percolation through the Voronoitessellations. *J. Phys. A*, 32(25):4611, 1999.

[332] Z. Hou, D. Guo, J. Cao, and Y. Chang. A method based on the centroid of segregation points: A Voronoi polygon application to solidification of alloys. *J. Alloys Compd.*, 762:508–519, 2018.

[333] S. Johnson. *The ghost map: The story of London's most terrifying epidemic–and how it changed science, cities, and the modern world*. Riverhead Books, 2006.

[334] G. Voronoi. Nouvelles applications des paramètres continus à théorie des formes quadratiques. Deuxième Mémoire. Recherches sur les parallélo̊edres primitifs. *J. Reine Angew. Math.*, 136:67–182, 1909.

[335] A. Okabe, B. Boots, K. Sugihara, and S. N. Chiu. *Spatial tessellations: concepts and applications of Voronoi diagrams*, volume 501. John Wiley & Sons, 2009.

[336] W. Fischer, E. Koch, and E. Hellner. Zur Berechnung von Wirkungsbereichen in Strukturen anorganischer Verbindungen. *Neues Jahrb. Mineral., Monatsh.*, 1971:227–237, 1971.

[337] P. F. Ash and E. D. Bolker. Generalized dirichlet tessellations. *Geometriae Dedicata*, 20(2):209–243, 1986.

[338] P. Richard, L. Oger, J.-P. Troadec, and A. Gervois. Geometrical characterization of hard-sphere systems. *Phys. Rev. E*, 60(4):4551, 1999.

[339] F. M. Schaller, S. C. Kapfer, M. E. Evans, M. J. F. Hoffmann, T. Aste, M. Saadatfar, K. Mecke, G. W. Delaney, and G. E. Schröder-Turk. Set Voronoi diagrams of 3D assemblies of aspherical particles. *Philosophical Magazine*, 93(31-33):3993–4017, 2013.

[340] E. Preteux. Watershed and skeleton by influence zones: A distance-based approach. *J. Math. Imaging Vis.*, 1(3):239–255, 1992.

[341] S. Weis, P. W. A. Schönhöfer, F. M. Schaller, M. Schröter, and G. E. Schröder-Turk. Pomelo, a tool for computing generic Set Voronoi diagrams of aspherical particles of arbitrary shape. In *Europhys. J, Web Conf.*, volume 140, page 06007. EDP Sciences, 2017.

[342] P. W. A. Schönhöfer and S. Weis. Pomelo: A generic Set-Voronoi tool. `http://www.theoriel.physik.uni-erlangen.de/research/pomelo/index.html`, 2018.

[343] P. W. A. Schönhöfer, L. J. Ellison, M. Marechal, D. J. Cleaver, and G. E. Schröder-Turk. Purely entropic self-assembly of the bicontinuous Ia$\bar{3}$d gyroid phase in equilibrium hard-pear systems. *Interface Focus*, 7:20160161, 2017.

[344] A. Giustiniani, S. Weis, C. Poulard, P. H. Kamm, F. García-Moreno, M. Schröter, and W. Drenckhan. Skinny emulsions take on granular matter. *Soft Matter*, 14(36):7310–7323, 2018.

[345] S. Weis, G. Schröder-Turk, and M. Schröter. Structural similarity between dry and wet sphere packings. *arXiv preprint arXiv:1808.04342*, 2018.

[346] S. Zhao, T. M. Evans, and X. Zhou. Three-dimensional voronoi analysis of monodisperse ellipsoids during triaxial shear. *Powder Technol.*, 323:323–336, 2018.

[347] N. N. Thyagu, M. Neudecker, S. Weis, F. M. Schaller, and M. Schröter. Local analysis of the history dependence in tetrahedra packings. *arXiv preprint arXiv:1501.04472*, 2015.

[348] J. D. Treado, Z. Mei, L. Regan, and C. S. O'Hern. Void distributions reveal structural link between jammed packings and protein cores. *Phys. Rev. E*, 99(2):022416, 2019.

[349] M. A. Klatt, J. Lovrić, D. Chen, S. C. Kapfer, F. M. Schaller, P. W. A. Schönhöfer, B. S. Gardiner, A.-S. Smith, G. E. Schröder-Turk, and S. Torquato. Universal hidden order in amorphous cellular geometries. *Nat. Commun.*, 10(1):811, 2019.

[350] D. Weaire. *The Kelvin Problem*. Taylor & Francis, London, 1997.

[351] Denis Weaire and Robert Phelan. A counter-example to Kelvin's conjecture on minimal surfaces. *Phil. Mag. Lett.*, 69(2):107–110, 1994.

[352] T. Aste and D. Weaire. *The Pursuit of Perfect Packing*. Taylor & Francis, New York, 2 edition, 2008.

[353] T. C. Hales. A proof of the Kepler conjecture. *Ann. Math.*, 162:1065–1185, 2005.

[354] S. Torquato. Reformulation of the covering and quantizer problems as ground states of interacting particles. *Phys. Rev. E*, 82(5):056109, 2010.

[355] A. Gersho. Asymptotically optimal block quantization. *IEEE Trans. Inf. Theory*, 25(4):373–380, 1979.

[356] Q. Du, V. Faber, and M. Gunzburger. Centroidal Voronoi tessellations: Applications and algorithms. *SIAM Rev.*, 41(4):637–676, 1999.

[357] G. M. Grason, B. A. DiDonna, and R. D. Kamien. Geometric theory of diblock copolymer phases. *Phys. Rev. Lett.*, 91(5):058304, 2003.

[358] S. Lloyd. Least squares quantization in PCM. *IEEE Trans. Inf. Theory*, 28(2):129–137, 1982.

[359] Q. Du, M. Emelianenko, and L. Ju. Convergence of the Lloyd algorithm for computing centroidal Voronoi tessellations. *SIAM J. Num. Anal.*, 44(1):102–119, 2006.

[360] S. Torquato and F. H. Stillinger. Local density fluctuations, hyperuniformity, and order metrics. *Phys. Rev. E*, 68(4):041113, 2003.

[361] L. Berthier, P. Chaudhuri, C. Coulais, O. Dauchot, and P. Sollich. Suppressed compressibility at large scale in jammed packings of size-disperse spheres. *Phys. Rev. Lett.*, 106(12):120601, 2011.

[362] Y. Jiao, T. Lau, H. Hatzikirou, M. Meyer-Hermann, J. C. Corbo, and S. Torquato. Avian photoreceptor patterns represent a disordered hyperuniform solution to a multiscale packing problem. *Phys. Rev. E*, 89(2):022721, 2014.

[363] K. J. Schrenk and D. Frenkel. Communication: Evidence for non-ergodicity in quiescent states of periodically sheared suspensions. *J. Chem. Phys.*, 143(24), 2015.

[364] E. Tjhung and L. Berthier. Hyperuniform density fluctuations and diverging dynamic correlations in periodically driven colloidal suspensions. *Phys. Rev. Lett.*, 114(14):148301, 2015.

[365] J. H. Weijs, R. Jeanneret, R. Dreyfus, and D. Bartolo. Emergent hyperuniformity in periodically driven emulsions. *Phys. Rev. Lett.*, 115(10):108301, 2015.

[366] S. Ghosh and J. L. Lebowitz. Fluctuations, large deviations and rigidity in hyperuniform systems: a brief survey. *Indian J. Pure Appl. Math.*, 48(4):609–631, 2017.

[367] S. R. Sellers, W. Man, S. Sahba, and M. Florescu. Local self-uniformity in photonic networks. *Nat. Commun.*, 8:14439, 2017.

[368] J. D. Bernal and J. Mason. Packing of spheres: co-ordination of randomly packed spheres. *Nature*, 188(4754):910, 1960.

[369] D. Hilbert. über Flächen von konstanter Gaußscher Krümmung. *Trans. Amer. Math. Soc.*, 2:87–99, 1901.

[370] M. E. Evans and G. E. Schröder-Turk. In a material world. Hyperbolische Geometrie in biologischen Materialien. *Mitteilungen der DMV*, 22(3):158–166, 2014.

[371] D. Anderson, H. Wennerstroem, and U. Olsson. Isotropic bicontinuous solutions in surfactant-solvent systems: the L3 phase. *J. Phys. Chem.*, 93(10):4243–4253, 1989.

[372] D. Roux, M. E. Cates, U. Olsson, R. C. Ball, F. Nallet, and A. M. Bellocq. Light scattering from a surfactant "sponge" phase: Evidence for a hidden symmetry. *Europhys. Lett.*, 11(3):229, 1990.

[373] L. J. Ellison. *Computer simulations of tapered particles*. PhD thesis, MERI, Sheffield Hallam University, 2008.

[374] S. T. Hyde, M. O'Keeffe, and D. M. Proserpio. A short history of an elusive yet ubiquitous structure in chemistry, materials, and mathematics. *Angew. Chem. Int. Ed.*, 47(42):7996–8000, 2008.

[375] S. T. Hyde and G. E. Schröder-Turk. Geometry of interfaces: topological complexity in biology and materials. *Interface Focus*, 2(5):529–538, 2012.

[376] R. Lipowsky and E. Sackmann. *Structure and Dynamics of Membranes*, volume 1. Elsevier, 1995.

[377] H. Hansen-Goos and K. Mecke. Fundamental measure theory for inhomogeneous fluids of nonspherical hard particles. *Phys. Rev. Lett.*, 102(1):018302, 2009.

[378] D. Fischermeier, E.and Bartuschat, T. Preclik, M. Marechal, and K. Mecke. Simulation of a hard-spherocylinder liquid crystal with the pe. *Comput. Phys. Commun.*, 185(12):3156–3161, 2014.

[379] B. M. Mladek, P. Charbonneau, and D. Frenkel. Phase coexistence of cluster crystals: beyond the Gibbs phase rule. *Phys. Rev. Lett.*, 99(23):235702, 2007.

[380] Y. Zhuang, K. Zhang, and P. Charbonneau. Equilibrium phase behavior of a continuous-space microphase former. *Phys. Rev. Lett.*, 116(9):098301, 2016.

[381] B. Widom. Some topics in the theory of fluids. *J. Chem. Phys.*, 39(11):2808–2812, 1963.

[382] J. G. Powles, W. A. B. Evans, and N. Quirke. Non-destructive molecular-dynamics simulation of the chemical potential of a fluid. *Mol. Phys.*, 46(6):1347–1370, 1982.

[383] W. P. Thurston. The geometry and topology of three-manifolds. Lecturenotes, Princeton University Princeton, NJ, November 1980.

[384] J. H. Conway and D. H. Huson. The orbifold notation for two-dimensional groups. *Struct. Chem.*, 13(3-4):247–257, 2002.

[385] H. Chung and M. Caffrey. The neutral area surface of the cubic mesophase: location and properties. *Biophys. J.*, 66(2):377–381, 1994.

[386] C. Song, P. Wang, and H. A. Makse. A phase diagram for jammed matter. *Nature*, 453(7195):629, 2008.

[387] R. Kurita and E. R. Weeks. Experimental study of random-close-packed colloidal particles. *Phys. Rev. E*, 82(1):011403, 2010.

[388] K. A. Newhall, I. Jorjadze, E. Vanden-Eijnden, and J. Brujic. A statistical mechanics framework captures the packing of monodisperse particles. *Soft Matter*, 7(24):11518–11525, 2011.

[389] F. M. Schaller, R. F. B. Weigel, and S. C. Kapfer. Densest local structures of uniaxial ellipsoids. *Phys. Rev. X*, 6(4):041032, 2016.

[390] P. W. A. Schönhöfer. Making sense of a pear-shaped world. `http://gerdschroeder-turk.org/2019/04/30/making-sense-of-a-pear-shaped-world-by-philipp-schonhofer/`, 2019.

[391] I. Prasad, Y. Seo, L. M. Hall, and G. M. Grason. Intradomain textures in block copolymers: multizone alignment and biaxiality. *Phys. Rev. Lett.*, 118(24):247801, 2017.

[392] M. Poppe, C. Chen, F. Liu, S. Poppe, and C Tschierske. Formation of a cubic liquid crystalline nanostructure with π-conjugated fluorinated rods on the gyroid minimal surface. *Chem. Eur. J.*, 23(30):7196–7200, 2017.

[393] M. Poppe, C. Chen, H. Ebert, S. Poppe, M. Prehm, C. Kerzig, F. Liu, and C. Tschierske. Transition from nematic to gyroid-type cubic soft self-assembly by side-chain engineering of π-conjugated sticky rods. *Soft matter*, 13(24):4381–4392, 2017.

[394] S. Poppe, C. Chen, F. Liu, and C. Tschierske. A skeletal double gyroid formed by single coaxial bundles of catechol based bolapolyphiles. *Chem. Comm.*, 54(79):11196–11199, 2018.

[395] L. A. Santaló. *Integral geometry and geometric probability*. Cambridge university press, 2004.

[396] A. Perera. Fluids of hard natural and Gaussian ellipsoids: A comparative study by integral equation theories. *J. Chem. Phys.*, 129(19):194504, 2008.

[397] S. M. Shamid, D. W. Allender, and J. V. Selinger. Predicting a polar analog of chiral blue phases in liquid crystals. *Phys. Rev. Lett.*, 113(23):237801, 2014.

[398] C. A. Tyler and D. C. Morse. Linear elasticity of cubic phases in block copolymer melts by self-consistent field theory. *Macromolecules*, 36(10):3764–3774, 2003.

[399] R. P. S. Fartaria and M. B. Sweatman. Density minimum in the isotropic–nematic transition of hard cut-spheres. *Chem. Phys. Lett.*, 478(4-6):150–154, 2009.

[400] R. P. S. Fartaria, N. Javid, J. Sefcik, and M. B. Sweatman. Simulation of scattering and phase behavior around the isotropic–nematic transition of discotic particles. *J. Colloid Interface Sci.*, 377(1):94–104, 2012.

[401] E. de Miguel and E. Martín del Río. The isotropic–nematic transition in hard Gaussian overlap fluids. *J. Chem. Phys.*, 115(19):9072–9083, 2001.

[402] E. de Miguel and E. Martín del Río. Equation of state for hard Gaussian overlap fluids. *J. Chem. Phys.*, 118(4):1852–1858, 2003.

[403] D. Frenkel and A. J. C. Ladd. New monte carlo method to compute the free energy of arbitrary solids. application to the fcc and hcp phases of hard spheres. *J. Chem. Phys.*, 81(7):3188–3193, 1984.

[404] M. A. Bates and D. Frenkel. Infinitely thin disks exhibit a first order nematic-columnar phase transition. *Phys. Rev. E*, 57(4):4824, 1998.

[405] R. Evans. The nature of the liquid-vapour interface and other topics in the statistical mechanics of non-uniform, classical fluids. *Adv. Phys.*, 28:143, 1979.

[406] Y. Rosenfeld. Free-energy model for the inhomogeneous hard-sphere fluid mixture and density-functional theory of freezing. *Phys. Rev. Lett.*, 63:980, 1989.

[407] A. K. Khandpur, S. Foerster, F. S. Bates, I. W. Hamley, A. J. Ryan, W. Bras, K. Almdal, and K. Mortensen. Polyisoprene-polystyrene diblock copolymer phase diagram near the order-disorder transition. *Macromolecules*, 28(26):8796–8806, 1995.

[408] D. A. Hajduk, H. Takenouchi, M. A. Hillmyer, F. S. Bates, M. E. Vigild, and K. Almdal. Stability of the perforated layer (PL) phase in diblock copolymer melts. *Macromolecules*, 30(13):3788–3795, 1997.

[409] D. Yao, K. Zhang, and Y. Chen. Microphase separation of poly (tert-butyl methacrylate)-block-polystyrene diblock copolymers to form perforated lamellae. *Polymer*, 94:1–7, 2016.

[410] H. F. Scherk. Bemerkungen über die kleinste Fläche innerhalb gegebener Grenzen. *J. reine angew. Math.*, 13:185–208, 1835.

[411] H. Karcher. Embedded minimal surfaces derived from Scherk's examples. *Manuscripta Math.*, 62(1):83–114, 1988.

[412] E. L. Thomas, D. M. Anderson, C. S. Henkee, and D. Hoffman. Periodic area-minimizing surfaces in block copolymers. *Nature*, 334(6183):598, 1988.

[413] S. P. Gido and E. L. Thomas. Lamellar diblock copolymer grain boundary morphology. 2. Scherk twist boundary energy calculations. *Macromolecules*, 27(3):849–861, 1994.

[414] R. D. Kamien and T. C. Lubensky. Minimal surfaces, screw dislocations, and twist grain boundaries. *Phys. Rev. Lett.*, 82(14):2892, 1999.

[415] H. Ogawa and N. Uchida. Numerical simulation of the twist-grain-boundary phase of chiral liquid crystals. *Phys. Rev. E*, 73(6):060701, 2006.

[416] H. Jinnai, K. Sawa, and T. Nishi. Direct observation of twisted grain boundary in a block copolymer lamellar nanostructure. *Macromolecules*, 39(17):5815–5819, 2006.

[417] C. D. Santangelo and R. D. Kamien. Triply periodic smectic liquid crystals. *Phys. Rev. E*, 75(1):011702, 2007.

[418] E. A. Matsumoto, R. D. Kamien, and G. P. Alexander. Straight round the twist: frustration and chirality in smectics-A. *Interface Focus*, 7(4):20160118, 2017.

[419] S. T. Hyde. Identification of lyotropic liquid crystalline mesophases. *Handbook of applied surface and colloid chemistry*, 2:299–332, 2001.

[420] B. W. Ninham, K. Larsson, and P Lo Nostro. Two sides of the coin. part 1. lipid and surfactant self-assembly revisited. *Colloids Surf. B Biointerfaces*, 152:326–338, 2017.

[421] M. Youssef, T. Hueckel, G. Yi, and S. Sacanna. Shape-shifting colloids via stimulated dewetting. *Nat. Commun.*, 7:12216, 2016.

[422] X. Zheng, M. Liu, M. He, D. J. Pine, and M. Weck. Shape-shifting patchy particles. *Angew. Chem.*, 129(20):5599–5603, 2017.

[423] S. Svenson. Self-assembly and self-organization: Important processes, but can we predict them? *J. Disper. Sci. Technol.*, 25(2):101–118, 2004.

[424] A. N. Semenov. Theory of block copolymer interfaces in the strong segregation limit. *Macromolecules*, 26(24):6617–6621, 1993.

[425] G. Odriozola. Revisiting the phase diagram of hard ellipsoids. *J. Chem. Phys.*, 136(13):134505, 2012.

[426] I. Dozov. On the spontaneous symmetry breaking in the mesophases of achiral banana-shaped molecules. *Europhys. Lett.*, 56(2):247, 2001.

[427] S. Engström, K. Alfons, M. Rasmusson, and H. Ljusberg-Wahren. Solvent-induced sponge (L_3) phases in the solvent-monoolein-water system. *Prog. Colloid Polym. Sci.*, 108:93–98, 1998.

[428] H. Evertsson, P. Stilbs, G. Lindblom, and S. Engström. Nmr self diffusion measurements of the monooleoylglycerol/poly ethylene glycol/water l3 phase. *Colloids Surf. B*, 26(1-2):21–29, 2002.

[429] S. Abe and H. Takahashi. A comparative study of the effects of dimethylsulfoxide and glycerol on the bicontinuous cubic structure of hydrated monoolein and its phase behavior. *Chem. Phys. Lipids*, 147(2):59–68, 2007.

[430] A. B. Wöhri, L. C. Johansson, P. Wadsten-Hindrichsen, W. Y. Wahlgren, G. Fischer, R. Horsefield, G. Katona, M. Nyblom, F. Öberg, G. Young, R. J. Cogdell, N. J. Fraser, S. Engström, and R. Neutze. A lipidic-sponge phase screen for membrane protein crystallization. *Structure*, 16(7):1003–1009, 2008.

[431] T. Landh. Phase behavior in the system pine needle oil monoglycerides-poloxamer 407-water at 20. degree. *J. Phys. Chem.*, 98(34):8453–8467, 1994.

[432] J. Barauskas, A. Misiunas, T. Gunnarsson, F. Tiberg, and M. Johnsson. "sponge" nanoparticle dispersions in aqueous mixtures of diglycerol monooleate, glycerol dioleate, and polysorbate 80. *Langmuir*, 22(14):6328–6334, 2006.

[433] R. Iñiguez-Palomares, H. Acuña-Campa, and A. Maldonado. Effect of polymer on the elasticity of surfactant membranes: A light scattering study. *Phys. Rev. E*, 84(1):011604, 2011.

[434] M. Valldeperas, M. Wiśniewska, M. Ram-On, E. Kesselman, D. Danino, T. Nylander, and J. Barauskas. Sponge phases and nanoparticle dispersions in aqueous mixtures of mono-and diglycerides. *Langmuir*, 32(34):8650–8659, 2016.

[435] J. P. Rolland, B. W. Maynor, L. E. Euliss, A. E. Exner, G. M. Denison, and J. M. DeSimone. Direct fabrication and harvesting of monodisperse, shape-specific nanobiomaterials. *J. Am. Chem. Soc.*, 127(28):10096–10100, 2005.

[436] S. H. Lee, S. J. Gerbode, B. S. John, A. K. Wolfgang, F. A. Escobedo, I. Cohen, and C. M. Liddell. Synthesis and assembly of nonspherical hollow silica colloids under confinement. *J. Mater. Chem.*, 18(41):4912–4916, 2008.

[437] L. Chen, H. Z. An, and P. S. Doyle. Synthesis of nonspherical microcapsules through controlled polyelectrolyte coating of hydrogel templates. *Langmuir*, 31(33):9228–9235, 2015.

[438] W. K. Kegel, D. Breed, M. Elsesser, and D. J. Pine. Formation of anisotropic polymer colloids by disparate relaxation times. *Langmuir*, 22(17):7135–7136, 2006.

[439] J.-G. Park, J. D. Forster, and E. R. Dufresne. Synthesis of colloidal particles with the symmetry of water molecules. *Langmuir*, 25(16):8903–8906, 2009.

[440] A. Perro, E. Duguet, O. Lambert, J.-C. Taveau, E. Bourgeat-Lami, and S. Ravaine. A chemical synthetic route towards "colloidal molecules". *Angew. Chem.*, 121(2):367–371, 2009.

[441] B. Peng and A. Imhof. Surface morphology control of cross-linked polymer particles via dispersion polymerization. *Soft Matter*, 11(18):3589–3598, 2015.

[442] J.-B. Fan, H. Liu, Y. Song, Z. Luo, Z. Lu, and S. Wang. Janus particles synthesis by emulsion interfacial polymerization: Polystyrene as seed or beyond? *Macromolecules*, 51(5):1591–1597, 2018.

[443] I. Lesov, Z. Valkova, E. Vassileva, G. S. Georgiev, K. Ruseva, M. Simeonov, S. Tcholakova, N. D. Denkov, and S. K. Smoukov. Bottom-up synthesis of polymeric micro-and nanoparticles with regular anisotropic shapes. *Macromolecules*, 51(19):7456–7462, 2018.

[444] C. I. Zoldesi, C. A. van Walree, and A. Imhof. Deformable hollow hybrid silica/siloxane colloids by emulsion templating. *Langmuir*, 22(9):4343–4352, 2006.

[445] H. Shin and C. Kim. Preparation of spheroidal and ellipsoidal particles from spherical polymer particles by extension of polymer film. *Colloid Polym. Sci.*, 290(13):1309–1315, 2012.

[446] Y. Yin, Y. Lu, B. Gates, and Y. Xia. Template-assisted self-assembly: a practical route to complex aggregates of monodispersed colloids with well-defined sizes, shapes, and structures. *J. Am. Chem. Soc.*, 123(36):8718–8729, 2001.

[447] D. Dendukuri, D. C. Pregibon, J. Collins, T. A. Hatton, and P. S. Doyle. Continuous-flow lithography for high-throughput microparticle synthesis. *Nat. Mater.*, 5:365–367, 2006.

[448] J. Guan, N. Ferrell, L. J. Lee, and D. J. Hansford. Fabrication of polymeric microparticles for drug delivery by soft lithography. *Biomaterials*, 27(21):4034–4041, 2006.

[449] G. C. Le Goff, J. Lee, A. Gupta, W. A. Hill, and P. S. Doyle. High-throughput contact flow lithography. *Adv. Sci.*, 2(10):1500149, 2015.

[450] H. N. W. Lekkerkerker and R. Tuinier. *Colloids and the depletion interaction*, volume 833. Springer, Dordrecht, the Netherlands, 2011.

[451] S. Asakura and F. Oosawa. On interaction between two bodies immersed in a solution of macromolecules. *J. Chem. Phys.*, 22(7):1255–1256, 1954.

[452] S. Asakura and F. Oosawa. Interaction between particles suspended in solutions of macromolecules. *J. Polym. Sci.*, 33(126):183–192, 1958.

[453] A. Vrij. Polymers at interfaces and the interactions in colloidal dispersions. *Pure Appl. Chem.*, 48(4):471–483, 1976.

[454] B. Widom and J. S. Rowlinson. New model for the study of liquid–vapor phase transitions. *J. Chem. Phys.*, 52(4):1670–1684, 1970.

[455] R. D. Kamien. Entropic attraction and ordering. In G. Gompper and M. Schick, editors, *Soft Matter, Volume 3: Colloidal Order: Entropic and Surface Forces*, pages 1–40. Wiley-VCH, Weinheim, Germany, 2007.

[456] Y. Mao, M. E. Cates, and H. N. W. Lekkerkerker. Depletion force in colloidal systems. *Phys. A*, 222(1-4):10–24, 1995.

[457] B. Götzelmann, R. Evans, and S. Dietrich. Depletion forces in fluids. *Phys. Rev. E*, 57(6):6785, 1998.

[458] T. Biben, P. Bladon, and D. Frenkel. Depletion effects in binary hard-sphere fluids. *J. Phys. Condens. Matter*, 8(50):10799, 1996.

[459] R. Dickman, P. Attard, and V. Simonian. Entropic forces in binary hard sphere mixtures: Theory and simulation. *J. Chem. Phys.*, 107(1):205–213, 1997.

[460] X. L. Chu, A. D. Nikolov, and D. T. Wasan. Effects of particle size and polydispersity on the depletion and structural forces in colloidal dispersions. *Langmuir*, 12(21):5004–5010, 1996.

[461] J. C. Crocker, J. A. Matteo, A. D. Dinsmore, and A. G. Yodh. Entropic attraction and repulsion in binary colloids probed with a line optical tweezer. *Phys.,Rev. Lett.*, 82(21):4352, 1999.

[462] R. Roth, R. Evans, and S. Dietrich. Depletion potential in hard-sphere mixtures: Theory and applications. *Phys. Rev. E*, 62(4):5360, 2000.

[463] A. A. Louis, E. Allahyarov, H. Löwen, and R. Roth. Effective forces in colloidal mixtures: From depletion attraction to accumulation repulsion. *Phys. Rev. E*, 65(6):061407, 2002.

[464] E. Eisenriegler, A. Hanke, and S. Dietrich. Polymers interacting with spherical and rodlike particles. *Phys. Rev. E*, 54(2):1134, 1996.

[465] D. G. A. L. Aarts, R. Tuinier, and H. N. W. Lekkerkerker. Phase behaviour of mixtures of colloidal spheres and excluded-volume polymer chains. *J. Phys. Condens. Matter*, 14(33):7551, 2002.

[466] Y. Mao, M. E. Cates, and H. N. W. Lekkerkerker. Theory of the depletion force due to rodlike polymers. *J. Chem. Phys.*, 106(9):3721–3729, 1997.

[467] R. Roth. Depletion potentials in colloidal mixtures of spheres and rods. *J. Phys. Condens. Matter*, 15(1):S277, 2002.

[468] W. Li, T. Yang, and H.-R. Ma. Depletion potentials in colloidal mixtures of hard spheres and rods. *J. Chem. Phys.*, 128(4):044910, 2008.

[469] M. Piech and J. Y. Walz. Depletion interactions produced by nonadsorbing charged and uncharged spheroids. *J. Colloid Interface Sci.*, 232(1):86–101, 2000.

[470] L. Harnau and S. Dietrich. Depletion potential in colloidal mixtures of hard spheres and platelets. *Phys. Rev. E*, 69(5):051501, 2004.

[471] Y.-X. Yu and J. Wu. Density functional theory for inhomogeneous mixtures of polymeric fluids. *J. Chem. Phys.*, 117(5):2368–2376, 2002.

[472] M. Oettel, H. Hansen-Goos, P. Bryk, and R. Roth. Depletion interaction of two spheres—full density functional theory vs. morphometric results. *Europhys. Lett.*, 85(3):36003, 2009.

[473] E. Evans and D. Needham. Attraction between lipid bilayer membranes in concentrated solutions of nonadsorbing polymers: comparison of mean-field theory with measurements of adhesion energy. *Macromolecules*, 21(6):1822–1831, 1988.

[474] P. D. Kaplan, L. P. Faucheux, and A. J. Libchaber. Direct observation of the entropic potential in a binary suspension. *Phys.,Rev. Lett.*, 73(21):2793, 1994.

[475] A. D. Dinsmore, P. B. Warren, W. C. K. Poon, and A. G. Yodh. Fluid-solid transitions on walls in binary hard-sphere mixtures. *Europhys. Lett.*, 40(3):337, 1997.

[476] W. Knoben, N. A..M. Besseling, and M. A. Cohen Stuart. Direct measurement of depletion and hydrodynamic forces in solutions of a reversible supramolecular polymer. *Langmuir*, 23(11):6095–6105, 2007.

[477] T. Biben and J.-P. Hansen. Phase separation of asymmetric binary hard-sphere fluids. *Phys. Rev. Lett.*, 66(17):2215, 1991.

[478] H. N. W. Lekkerkerker and A. Stroobants. On the spinodal instability of highly asymmetric hard sphere suspensions. *Phys. A*, 195(3-4):387–397, 1993.

[479] Y. Rosenfeld. Phase separation of asymmetric binary hard-sphere fluids: self-consistent density functional theory. *Phys. Rev. Lett.*, 72(24):3831, 1994.

[480] Y. Rosenfeld. Phase separation of asymmetric binary hard-sphere fluids: Self-consistent density functional theory. *J. Phys. Chem.*, 99(9):2857–2864, 1995.

[481] A. Imhof and J. K. G. Dhont. Experimental phase diagram of a binary colloidal hard-sphere mixture with a large size ratio. *Phys. Rev. Lett.*, 75(8):1662, 1995.

[482] M. Dijkstra, R. van Roij, and R. Evans. Phase diagram of highly asymmetric binary hard-sphere mixtures. *Phys. Rev. E*, 59(5):5744, 1999.

[483] R. Tuinier, J. Rieger, and C. G. De Kruif. Depletion-induced phase separation in colloid–polymer mixtures. *Adv. Colloid Interface Sci.*, 103(1):1–31, 2003.

[484] S. Sacanna, W. T. M. Irvine, P. M. Chaikin, and D. J. Pine. Lock and key colloids. *Nature*, 464(7288):575, 2010.

[485] Y. Wang, Y. Wang, X. Zheng, G.-R. Yi, S. Sacanna, David J. Pine, and M. Weck. Three-dimensional lock and key colloids. *J. Am. Chem. Soc.*, 136(19):6866–6869, 2014.

[486] E. Eisenriegler, A. Bringer, and R. Maassen. Polymer depletion interaction of small mesoscopic particles: Effects beyond leading order and anisotropic particles. *J. Chem. Phys.*, 118(17):8093–8105, 2003.

[487] W. Li and H. R. Ma. Depletion force and torque on an ellipsoid. *J. Chem. Phys.*, 119(1):585–589, 2003.

[488] R. Roth, R. H. H. G. van Roij, D. Andrienko, K. R. Mecke, and S. Dietrich. Entropic torque. *Phys. Rev. Lett.*, 89(8):088301, 2002.

[489] M. Adams, Z. Dogic, S. L. Keller, and S. Fraden. Entropically driven microphase transitions in mixtures of colloidal rods and spheres. *Nature*, 393(6683):349, 1998.

[490] G. H. Koenderink, G. A. Vliegenthart, S. G. J. M. Kluijtmans, A. van Blaaderen, A. P. Philipse, and H. N. W. Lekkerkerker. Depletion-induced crystallization in colloidal rod-sphere mixtures. *Langmuir*, 15(14):4693–4696, 1999.

[491] A. Suzuki, M. Yamazaki, and T. Ito. Osmoelastic coupling in biological structures: formation of parallel bundles of actin filaments in a crystalline-like structure caused by osmotic stress. *Biochemistry*, 28(15):6513–6518, 1989.

[492] M. Adams and S. Fraden. Phase behavior of mixtures of rods (tobacco mosaic virus) and spheres (polyethylene oxide, bovine serum albumin). *Biophys. J.*, 74(1):669–677, 1998.

[493] M. A. Bates and D. Frenkel. Phase behavior of model mixtures of colloidal disks and polymers. *Phys. Rev. E*, 62(4):5225, 2000.

[494] Z. Dogic, K. R. Purdy, E. Grelet, M. Adams, and S. Fraden. Isotropic-nematic phase transition in suspensions of filamentous virus and the neutral polymer dextran. *Phys. Rev. E*, 69(5):051702, 2004.

[495] S. Belli, M. Dijkstra, and R. H. H. G. van Roij. Depletion-induced biaxial nematic states of boardlike particles. *J. Phys. Condens. Matter*, 24(28):284128, 2012.

[496] R. Aliabadi, M. Moradi, and S. Varga. Tracking three-phase coexistences in binary mixtures of hard plates and spheres. *J. Chem. Phys.*, 144(7):074902, 2016.

[497] Á. G. García, J. Opdam, and R. Tuinier. Phase behaviour of colloidal superballs mixed with non-adsorbing polymers. *Euro. Phys. J. E*, 41(9):110, 2018.

[498] Á. G. García, R. Tuinier, J. V. Maring, J. Opdam, H. H. Wensink, and H. N. W. Lekkerkerker. Depletion-driven four-phase coexistences in discotic systems. *Mol. Phys.*, pages 1–16, 2018.

[499] S. S. Cohen. The isolation and crystallization of plant viruses and other protein macro molecules by means of hydrophilic colloids. *J. Biol. Chem.*, 144(2):353–362, 1942.

[500] T. G. Mason. Osmotically driven shape-dependent colloidal separations. *Phys. Rev. E*, 66(6):060402, 2002.

[501] D. Baranov, A. Fiore, M. van Huis, C. Giannini, A. Falqui, U. Lafont, H. Zandbergen, M. Zanella, R. Cingolani, and L. Manna. Assembly of colloidal semiconductor nanorods in solution by depletion attraction. *Nano Lett.*, 10(2):743–749, 2010.

[502] K. Park, H. Koerner, and R. A. Vaia. Depletion-induced shape and size selection of gold nanoparticles. *Nano Lett.*, 10(4):1433–1439, 2010.

[503] A. Kulkarni and C. Zukoski. Depletion interactions and protein crystallization. *J. Cryst. Growth*, 232(1-4):156–164, 2001.

[504] S. Tanaka and M. Ataka. Protein crystallization induced by polyethylene glycol: A model study using apoferritin. *J. Chem. Phys.*, 117(7):3504–3510, 2002.

[505] S. B. Zimmerman and S. O. Trach. Estimation of macromolecule concentrations and excluded volume effects for the cytoplasm of Escherichia coli. *J. Mol. Bio.*, 222(3):599–620, 1991.

[506] R. J. Ellis and A. P. Minton. Cell biology: join the crowd. *Nature*, 425(6953):27, 2003.

[507] G. Rivas, F. Ferrone, and J. Herzfeld. Life in a crowded world: Workshop on the biological implications of macromolecular crowding. *EMBO rep.*, 5(1):23–27, 2004.

[508] R. J. Ellis. Macromolecular crowding: obvious but underappreciated. *Trends Biochem. Sci.*, 26(10):597–604, 2001.

[509] D. Marenduzzo, K. Finan, and P. R. Cook. The depletion attraction: an underappreciated force driving cellular organization. *J. Cell. Biol.*, 175(5):681–686, 2006.

[510] P. Chien and L. M. Gierasch. Challenges and dreams: physics of weak interactions essential to life. *Mol. Biol. Cell*, 25(22):3474–3477, 2014.

[511] S. B. Zimmerman and A. P. Minton. Macromolecular crowding: biochemical, biophysical, and physiological consequences. *Annu. Rev. Biophys. Biomol. Atruct.*, 22(1):27–65, 1993.

[512] J. Herzfeld. Entropically driven order in crowded solutions: from liquid crystals to cell biology. *Acc. Chem. Res.*, 29(1):31–37, 1996.

[513] I. M. Kuznetsova, K. K. Turoverov, and V. N. Uversky. What macromolecular crowding can do to a protein. *Int. J. Mol. Sci*, 15(12):23090–23140, 2014.

[514] G. Rivas and A. P. Minton. Macromolecular crowding in vitro, in vivo, and in between. *Trends Biochem. Sci.*, 41(11):970–981, 2016.

[515] B. van den Berg, R. J. Ellis, and C. M. Dobson. Effects of macromolecular crowding on protein folding and aggregation. *EMBO J.*, 18(24):6927–6933, 1999.

[516] R. J. Ellis. Protein folding: inside the cage. *Nature*, 442(7101):360, 2006.

[517] A. Maritan, C. Micheletti, A. Trovato, and J. R. Banavar. Optimal shapes of compact strings. *Nature*, 406(6793):287, 2000.

[518] Y. Snir and R. D. Kamien. Entropically driven helix formation. *Science*, 307(5712):1067–1067, 2005.

[519] M. Hosek and J. X. Tang. Polymer-induced bundling of F actin and the depletion force. *Phys. Rev. E*, 69(5):051907, 2004.

[520] F. Hilitski, A. R. Ward, L. Cajamarca, M. F. Hagan, G. M. Grason, and Z. Dogic. Measuring cohesion between macromolecular filaments one pair at a time: depletion-induced microtubule bundling. *Phys. Rev. Lett.*, 114(13):138102, 2015.

[521] A. P. Minton. The influence of macromolecular crowding and macromolecular confinement on biochemical reactions in physiological media. *J. Bio. Chem.*, 276(14):10577–10580, 2001.

[522] H.-X. Zhou, G. Rivas, and A. P. Minton. Macromolecular crowding and confinement: biochemical, biophysical, and potential physiological consequences. *Annu. Rev. Biophys.*, 37:375–397, 2008.

[523] I. Oh, S. Choi, Y. J. Jung, and J. S. Kim. Entropic effect of macromolecular crowding enhances binding between nucleosome clutches in heterochromatin, but not in euchromatin. *Sci. Rep.*, 8(1):5469, 2018.

[524] G. Wieczorek and P. Zielenkiewicz. Influence of macromolecular crowding on protein-protein association rates—a Brownian dynamics study. *Biophys. J.*, 95(11):5030–5036, 2008.

[525] E. A. Cino, M. Karttunen, and W.-Y. Choy. Effects of molecular crowding on the dynamics of intrinsically disordered proteins. *PLoS One*, 7(11):e49876, 2012.

[526] N. F. Dupuis, E. D. Holmstrom, and D. J. Nesbitt. Molecular-crowding effects on single-molecule rna folding/unfolding thermodynamics and kinetics. *Proc. Natl. Acad. Sci. USA*, 111(23):8464–8469, 2014.

[527] M. T. Record Jr., E. S. Courtenay, S. Cayley, and H. J. Guttman. Biophysical compensation mechanisms buffering e. coli protein–nucleic acid interactions against changing environments. *Trends Biochem. Sci.*, 23(5):190–194, 1998.

[528] A. P. Minton. How can biochemical reactions within cells differ from those in test tubes? *J. Cell. Sci.*, 119(14):2863–2869, 2006.

[529] F.-X. Theillet, A. Binolfi, T. Frembgen-Kesner, K. Hingorani, M. Sarkar, C. Kyne, C. Li, P. B. Crowley, L. Gierasch, G. J. Pielak, A. H. Elcock, A. Gershenson, and P. Selenko. Physicochemical properties of cells and their effects on intrinsically disordered proteins (IDPs). *Chem. Rev.*, 114(13):6661–6714, 2014.

[530] SideFX. Houdini 17: procedural content creation tools for film, TV and gamedev. `https://www.sidefx.com`, 2018.

[531] P.-M. König, R. Roth, and S. Dietrich. Depletion forces between nonspherical objects. *Phys. Rev. E*, 74(4):041404, 2006.

[532] J. R. Henderson. Statistical mechanics of fluids at spherical structureless walls. *Mol. Phys.*, 50(4):741–761, 1983.

[533] M. Kinoshita. Interaction between big bodies with high asphericity immersed in small spheres. *Chem. Phys. Lett.*, 387(1-3):47–53, 2004.

[534] C. H. Bennett. Efficient estimation of free energy differences from Monte Carlo data. *J. Comput. Phys.*, 22(2):245–268, 1976.

[535] W. Li and H. R. Ma. Depletion potential near curved surfaces. *Phys. Rev. E*, 66(6):061407, 2002.

[536] F. Wang and D. P. Landau. Efficient, multiple-range random walk algorithm to calculate the density of states. *Phys. Rev. Lett.*, 86(10):2050, 2001.

[537] M. S. Shell, P. G. Debenedetti, and A. Z. Panagiotopoulos. Generalization of the Wang-Landau method for off-lattice simulations. *Phys. Rev. E*, 66(5):056703, 2002.

[538] H. Miao, Y. Li, and H. Ma. Depletion interaction between two ellipsoids. *J. Chem. Phys.*, 140(15):154904, 2014.

[539] H. W. Hatch, W. P. Krekelberg, S. D. Hudson, and V. K. Shen. Depletion-driven crystallization of cubic colloids sedimented on a surface. *J. Chem. Phys.*, 144(19):194902, 2016.

[540] Z. Jin and J. Wu. Hybrid MC - DFT method for studying multidimensional entropic forces. *J. Phys. Chem. B*, 115(6):1450–1460, 2011.

[541] W. Kob and H. C. Andersen. Testing mode-coupling theory for a supercooled binary Lennard-Jones mixture I: The van Hove correlation function. *Phys. Rev. E*, 51(5):4626, 1995.

[542] H. W. Sheng, M. J. Kramer, A. Cadien, T. Fujita, and M. W. Chen. Highly optimized embedded-atom-method potentials for fourteen fcc metals. *Phys. Rev. B*, 83(13):134118, 2011.

[543] M. Matsuoka. Solid liquid equilibria of binary organic mixtures. *Bunri Gijutsu*, 7:245–249, 1977.

[544] S. Punnathanam and P. A. Monson. Crystal nucleation in binary hard sphere mixtures: A Monte Carlo simulation study. *J. Chem. Phys.*, 125(2):024508, 2006.

[545] A. Widmer-Cooper and P. Harrowell. Structural phases in non-additive soft-disk mixtures: Glasses, substitutional order, and random tilings. *J. Chem. Phys.*, 135(22):224515, 2011.

[546] L. V. Woodcock. Nonadditive hard-sphere reference model for ionic liquids. *Ind. Eng. Chem. Res.*, 50(1):227–233, 2010.

[547] M. Dijkstra. Phase behavior of nonadditive hard-sphere mixtures. *Phys. Rev. E*, 58(6):7523, 1998.

[548] A. A. Louis, R. Finken, and J. P. Hansen. Crystallization and phase separation in nonadditive binary hard-sphere mixtures. *Phys. Rev. E*, 61(2):R1028, 2000.

[549] K. Zhao and T. G. Mason. Directing colloidal self-assembly through roughness-controlled depletion attractions. *Phys. Rev. Lett.*, 99(26):268301, 2007.

[550] P. Hohenberg and W. Kohn. Inhomogeneous electron gas. *Phys. Rev.*, 136(3B):B864, 1964.

[551] N. D. Mermin. Thermal properties of the inhomogeneous electron gas. *Phys. Rev.*, 137(5A):A1441, 1965.

[552] A. Härtel, M. Oettel, R. E. Rozas, S. U. Engelhaaf, J. Horbach, and H. Löwen. Tension and stiffness of the hard sphere crystal-fluid interface. *Phys. Rev. Lett.*, 108:226101, 2012.

[553] R. Evans. Density functionals in the theory of nonuniform fluids. In *Fundamentals of inhomogeneous fluids*, pages 85–176. Marcel Dekker, New York, 1992.

[554] P. Tarazona and Y. Rosenfeld. From zero-dimension cavities to free-energy functionals for hard disks and hard spheres. *Phys. Rev. E*, 55:R4873, 1997.

[555] H. Hansen-Goos and R. Roth. Density functional theory for hard-sphere mixtures: the White Bear version mark II. *J. Phys. Condens. Matter*, 18:8413, 2006.

[556] R. Wittmann, M. Marechal, and K. Mecke. Fundamental measure theory for smectic phases: Scaling behavior and higher order terms. *J. Chem. Phys.*, 141(19):064103, 2014.

[557] R. Wittmann, M. Marechal, and K. Mecke. Fundamental measure theory for non-spherical hard particles: predicting liquid crystal properties from the particle shape. *J. Phys. Condens. Matter*, 28:244003, 2016.

[558] A. Esztermann, H. Reich, and M. Schmidt. Density functional theory for colloidal mixtures of hard platelets, rods, and spheres. *Phys. Rev. E*, 73:011409, 2006.

[559] Roth R. Introduction to density functional theory of classical systems: Theory and applications. Lecturenotes, ITAP Universität Stuttgart, November 2006.

[560] J. T. Chayes, L. Chayes, and E. H. Lieb. The inverse problem in classical statistical mechanics. *Commun. Math. Phys.*, 93(1):57–121, 1984.

[561] W. S. B. Dwandaru and M. Schmidt. Variational principle of classical density functional theory via levy's constrained search method. *Phys. Rev. E*, 83(6):061133, 2011.

[562] P. Tarazona. Density functional for hard sphere crystals: A fundamental measure approach. *Phys. Rev. Lett.*, 84:694, 2000.

[563] M. S. Wertheim. Fluids of hard convex molecules. *Mol. Phys.*, 83:519, 1994.

[564] E. Abbena, S. Salamon, and A. Gray. *Modern differential geometry of curves and surfaces with Mathematica*. 3rd edition CRC Press, Boca Raton, 2006.

[565] R. Roth, R. Evans, A. Lang, and G. Kahl. Fundamental measure theory for hard-sphere mixtures revisited: the white bear version. *J. Phys. Condens. Matter.*, 14(46):12063, 2002.

[566] R. Roth. Fundamental measure theory for hard-sphere mixtures: a review. *J. Phys. Condens. Matter.*, 22:063102, 2010.

[567] M. Dijkstra, R. van Roij, and R. Evans. Wetting and capillary nematization of a hard-rod fluid: A simulation study. *Phys. Rev. E*, 63(5):051703, 2001.

[568] S. V. Savenko and M. Dijkstra. Sedimentation and multiphase equilibria in suspensions of colloidal hard rods. *Phys. Rev. E*, 70:051401, 2004.

[569] M. Dijkstra and R. van Roij. Entropic wetting in colloidal suspensions. *J. Phys. Condens. Matter.*, 17:3507–3514, 2005.

[570] L. De Campo, O. Delgado-Friedrichs, S. T. Hyde, and M. O'Keeffe. Minimal nets and minimal minimal surfaces. *Acta Cryst. A*, 69(5):483–489, 2013.

[571] P. M. Duesing, R. H. Templer, and J. M. Seddon. Quantifying packing frustration energy in inverse lyotropic mesophases. *Langmuir*, 13(2):351–359, 1997.

[572] U. S. Schwarz and G. Gompper. Bending frustration of lipid- water mesophases based on cubic minimal surfaces1. *Langmuir*, 17(7):2084–2096, 2001.

[573] S. T. Hyde. Curvature and the global structure of interfaces in surfactant-water systems. *J. Phys. Colloq.*, 51(C7):C7–209, 1990.

[574] W. Helfrich and H. Rennschuh. Landau theory of the lamellar-to-cubic phase transition. *J. Phys. Colloq.*, 51(C7):C7–189, 1990.

[575] A. M. Squires, R. H. Templer, J. M. Seddon, J. Woenkhaus, R. Winter, T. Narayanan, and S. Finet. Kinetics and mechanism of the interconversion of inverse bicontinuous cubic mesophases. *Phys. Rev. E*, 72(1):011502, 2005.

[576] T. Oka. Transformation between inverse bicontinuous cubic phases of a lipid from diamond to gyroid. *Langmuir*, 31(41):11353–11359, 2015.

[577] A. Squires, R. H. Templer, O. Ces, A. Gabke, J. Woenckhaus, J. M. Seddon, and R. Winter. Kinetics of lyotropic phase transitions involving the inverse bicontinuous cubic phases. *Langmuir*, 16(8):3578–3582, 2000.

[578] J. M. Seddon, A. M. Squires, C. E. Conn, O. Ces, A. J. Heron, X. Mulet, G. C. Shearman, and R. H. Templer. Pressure-jump X-ray studies of liquid crystal transitions in lipids. *Philos. Trans. Royal Soc. A*, 364(1847):2635–2655, 2006.

[579] G. E. Schröder, S. J. Ramsden, A. Fogden, and S. T. Hyde. A rhombohedral family of minimal surfaces as a pathway between the P and D cubic mesophases. *Physica A*, 339(1-2):137–144, 2004.

[580] J.-F. Sadoc and J. Charvolin. Infinite periodic minimal surfaces and their crystallography in the hyperbolic plane. *Acta Crystallogr. Sect. A: Found. Crystallogr.*, 45(1):10–20, 1989.

[581] J. M. Seddon and R. H. Templer. *Structure and dynamics of membranes*. Elsevier, Amsterdam, 1995.

[582] C. Chu, W. Lin, J. Tsai, C. Lai, S. Lo, H. Chen, and T. Hashimoto. Order–order transition between equilibrium ordered bicontinuous nanostructures of double diamond and double gyroid in stereoregular block copolymer. *Macromolecules*, 45(5):2471–2477, 2012.

[583] H. Takagi, K. Yamamoto, and S. Okamoto. Ordered-bicontinuous-double-diamond structure in block copolymer/homopolymer blends. *Europhys. Lett.*, 110(4):48003, 2015.

[584] W. Mao, X. Cao, Q. Sheng, L. Han, and S. Che. Silica scaffold with shifted "plumber's nightmare" networks and their interconversion into diamond networks. *Angew. Chem.*, 129(36):10810–10815, 2017.

[585] C.-H. Lin, T. Higuchi, H.-L. Chen, J.-C. Tsai, H. Jinnai, and T. Hashimoto. Stabilizing the ordered bicontinuous double diamond structure of diblock copolymer by configurational regularity. *Macromolecules*, 51(11):4049–4058, 2018.

[586] I. Honma, H. S. Zhou, D. Kundu, and A. Endo. Structural control of surfactant-templated hexagonal, cubic, and lamellar mesoporous silicate thin films prepared by spin-casting. *Adv. Mater.*, 12(20):1529–1533, 2000.

[587] S. A. El-Safty and T. Hanaoka. Monolithic nanostructured silicate family templated by lyotropic liquid-crystalline nonionic surfactant mesophases. *Chem. Mater.*, 15(15):2892–2902, 2003.

[588] C. Gao, Y. Sakamoto, K. Sakamoto, O. Terasaki, and S. Che. Synthesis and characterization of mesoporous silica AMS-10 with bicontinuous cubic $Pn\bar{3}m$ symmetry. *Angew. Chem. Int. Ed.*, 45(26):4295–4298, 2006.

[589] B. D. Wilts and V. Saranathan. A literal elytral rainbow: tunable structural colors using single diamond biophotonic crystals in pachyrrhynchus congestus weevils. *Small*, 14(46):1802328, 2018.

[590] K.A Lundstrom. The future of G protein-coupled receptors as targets in drug discovery. *IDrugs*, 8(11):909–913, 2005.

[591] C. E. Conn and C. J. Drummond. Nanostructured bicontinuous cubic lipid self-assembly materials as matrices for protein encapsulation. *Soft Matter*, 9(13):3449–3464, 2013.

[592] H. T. McMahon and J. L. Gallop. Membrane curvature and mechanisms of dynamic cell membrane remodelling. *Nature*, 438(7068):590, 2005.

[593] J. Zimmerberg and M. M. Kozlov. How proteins produce cellular membrane curvature. *Nat. Rev. Mol. Cell Bio.*, 7(1):9, 2006.

[594] S. A. Rautu, G. Rowlands, and M. S. Turner. Membrane composition variation and underdamped mechanics near transmembrane proteins and coats. *Phys. Rev. Lett.*, 114(9):098101, 2015.

[595] C. E. Conn, C. Darmanin, S. M. Sagnella, X. Mulet, T. L. Greaves, J. N. Varghese, and C. J. Drummond. Incorporation of the dopamine D2L receptor and bacteriorhodopsin within bicontinuous cubic lipid phases. 1. relevance to in meso crystallization of integral membrane proteins in monoolein systems. *Soft Matter*, 6(19):4828–4837, 2010.

[596] C. E. Conn, C. Darmanin, S. M. Sagnella, X. Mulet, T. L. Greaves, J. N. Varghese, and C. J. Drummond. Incorporation of the dopamine D2L receptor and bacteriorhodopsin within bicontinuous cubic lipid phases. 2. relevance to in meso crystallization of integral membrane proteins in novel lipid systems. *Soft Matter*, 6(19):4838–4846, 2010.

[597] M. Grabe, J. Neu, G. Oster, and P. Nollert. Protein interactions and membrane geometry. *Biophys. J.*, 84(2):854–868, 2003.

[598] F. Paillusson, M. R. Pennington, and H. Kusumaatmaja. Phase separation on bicontinuous cubic membranes: symmetry breaking, reentrant, and domain faceting. *Phys. Rev. Lett.*, 117(5):058101, 2016.

[599] P. Fonda, M. Rinaldin, D. J. Kraft, and L. Giomi. Interface geometry of binary mixtures on curved substrates. *Phys. Rev. E*, 98(3):032801, 2018.

[600] L. van 't Hag, L. de Campo, C. J. Garvey, G. C. Feast, A. E. Leung, N. R. Yepuri, R. Knott, T. L. Greaves, N. Tran, S. L. Gras, C. J. Drummond, and C. E. Conn. Using SANS with contrast-matched lipid bicontinuous cubic phases to determine the location of encapsulated peptides, proteins, and other biomolecules. *J. Phys. Chem. Lett.*, 7(14):2862–2866, 2016.

[601] L. van't Hag, K. Knoblich, S. A. Seabrook, N. M. Kirby, S. T. Mudie, D. Lau, X. Li, S. L. Gras, X. Mulet, M. E. Call, C. J. Drummond, and C. E. Conn. Exploring the in meso crystallization mechanism by characterizing the lipid mesophase microenvironment during the growth of single transmembrane α-helical peptide crystals. *Philos. Trans. Royal Soc. A*, 374(2072):20150125, 2016.

[602] D. Antypov and D. J. Cleaver. Orientational and phase-coexistence behaviour of hard rod–sphere mixtures. *Chem. Phys. Lett.*, 377(3-4):311–316, 2003.

[603] E. Ruckenstein and R. Nagarajan. Critical micelle concentration. Transition point for micellar size distribution. *J. Phys. Chem.*, 79(24):2622–2626, 1975.

[604] A. Ben-Naim and F. H. Stillinger. Critical micelle concentration and the size distribution of surfactant aggregates. *J. Phys. Chem.*, 84(22):2872–2876, 1980.

[605] L. Leibler, H. Orland, and J. C. Wheeler. Theory of critical micelle concentration for solutions of block copolymers. *J. Chem. Phys.*, 79(7):3550–3557, 1983.

[606] G. T. Pickett, M. Gross, and H. Okuyama. Spontaneous chirality in simple systems. *Phys. Rev. Lett.*, 85(17):3652, 2000.

[607] M. A. Lohr, A. M. Alsayed, B. G. Chen, Z. Zhang, R. D. Kamien, and A. G. Yodh. Helical packings and phase transformations of soft spheres in cylinders. *Phys. Rev. E*, 81(4):040401, 2010.

[608] A. Mughal, H. K. Chan, D. Weaire, and S. Hutzler. Dense packings of spheres in cylinders: Simulations. *Phys. Rev. E*, 85(5):051305, 2012.

[609] D. A. Wood, C. D. Santangelo, and A. D. Dinsmore. Self-assembly on a cylinder: A model system for understanding the constraint of commensurability. *Soft Matter*, 9(42):10016–10024, 2013.

[610] L. Fu, W. Steinhardt, H. Zhao, J. E. S. Socolar, and P. Charbonneau. Hard sphere packings within cylinders. *Soft Matter*, 12(9):2505–2514, 2016.

[611] S. Andersson, M. Jacob, S. Lidin, and K. Larsson. Structure of the cubosome - a closed lipid bilayer aggregate. *Z. Kristallog.*, 210:315–318, 1995.

[612] B. Angelov, A. Angelova, B. Papahadjopoulos-Sternberg, S. Lesieur, J.-F. Sadoc, M. Ollivon, and P. Couvreur. Detailed structure of diamond-type lipid cubic nanoparticles. *J. Am. Chem. Soc.*, 128(17):5813–5817, 2006.

[613] D. Demurtas, P. Guichard, I. Martiel, R. Mezzenga, C. Hébert, and L. Sagalowicz. Direct visualization of dispersed lipid bicontinuous cubic phases by cryo-electron tomography. *Nat. Commun.*, 6:8915, 2015.

[614] H. Kim and C. Leal. Cuboplexes: Topologically active siRNA delivery. *ACS Nano*, 9(10):10214–10226, 2015.

[615] H. Kim, Z. Song, and C. Leal. Super-swelled lyotropic single crystals. *Proc. Natl. Acad. Sci. USA*, 114(41):10834–10839, 2017.

[616] V. Robins. Towards computing homology from finite approximations. In *Topology Proc.*, volume 24, pages 503–532, 1999.

[617] H. Edelsbrunner, D. Letscher, and A Zomorodian. Topological persistence and simplification. *Discrete Comput. Geom.*, 28:511–533, 2002.

[618] G. Carlsson. Topology and data. *Bull. Am. Math. Soc.*, 46(2):255–308, 2009.

[619] M. Kramar, A. Goullet, L. Kondic, and K. Mischaikow. Persistence of force networks in compressed granular media. *Phys. Rev. E*, 87(4):042207, 2013.

[620] T. Nakamura, Y. Hiraoka, A. Hirata, E. G. Escolar, and Y. Nishiura. Persistent homology and many-body atomic structure for medium-range order in the glass. *Nanotechnology*, 26(30):304001, 2015.

[621] Y. Lee, S. D. Barthel, P. Dłotko, S. M. Moosavi, K. Hess, and B. Smit. Quantifying similarity of pore-geometry in nanoporous materials. *Nat. Commun.*, 8:15396, 2017.

[622] M. Saadatfar, H. Takeuchi, V. Robins, N. Francois, and Y. Hiraoka. Pore configuration landscape of granular crystallization. *Nat. Commun.*, 8:15082, 2017.

[623] A. L. Herring, V. Robins, and A. P. Sheppard. Topological persistence for relating microstructure and capillary fluid trapping in sandstones. *Water Resour. Res.*, 2018.

[624] F. Jiang, T. Tsuji, and T. Shirai. Pore geometry characterization by persistent homology theory. *Water Resour. Res.*, 54(6):4150–4163, 2018.

[625] V. Lotito and T. Zambelli. Pattern formation in binary colloidal assemblies: hidden symmetries in a kaleidoscope of structures. *Langmuir*, 34(26):7827–7843, 2018.

[626] Y. Hiraoka, T. Nakamura, A. Hirata, E. G. Escolar, K. Matsue, and Y. Nishiura. Hierarchical structures of amorphous solids characterized by persistent homology. *Proc. Natl. Acad. Sci. USA*, 113(26):7035–7040, 2016.

[627] R. D. Batten, F. H. Stillinger, and S. Torquato. Phase behavior of colloidal superballs: Shape interpolation from spheres to cubes. *Phys. Rev. E*, 81(6):061105, 2010.

[628] Y. Zhang, F. Lu, D. van der Lelie, and O. Gang. Continuous phase transformation in nanocube assemblies. *Phys. Rev. Lett.*, 107(13):135701, 2011.

[629] P. F. Damasceno, M. Engel, and S. C. Glotzer. Crystalline assemblies and densest packings of a family of truncated tetrahedra and the role of directional entropic forces. *ACS Nano*, 6(1):609–614, 2011.

[630] A. P. Gantapara, J. de Graaf, R. van Roij, and M. Dijkstra. Phase diagram and structural diversity of a family of truncated cubes: Degenerate close-packed structures and vacancy-rich states. *Phys. Rev. Lett.*, 111(1):015501, 2013.

[631] C. X. Du, G. van Anders, R. S. Newman, and S. C. Glotzer. Shape-driven solid–solid transitions in colloids. *Proc. Natl. Acad. Sci. USA*, 114(20):E3892–E3899, 2017.

[632] S. Dussi and M. Dijkstra. Entropy-driven formation of chiral nematic phases by computer simulations. *Nat. Commun.*, 7:11175, 2016.

[633] M. Marechal and M. Dijkstra. Phase behavior and structure of colloidal bowl-shaped particles: Simulations. *Phys. Rev. E*, 82(3):031405, 2010.

[634] D. Wan, C. X. Du, G. van Anders, and S. C. Glotzer. FCC-to-BCC phase transitions in convex and concave hard particle systems. *arXiv preprint arXiv:1901.09523*, 2019.

[635] N. Lei, C. R. Safinya, D. Roux, and K. S. Liang. Synchrotron X-ray-scattering studies on the sodium dodecyl sulfate–water–pentanol–dodecane L3 sponge phase. *Phys. Rev. E*, 56(1):608, 1997.

[636] B. Angelov, A. Angelova, R. Mutafchieva, S. Lesieur, U. Vainio, V. M. Garamus, G. V. Jensen, and J. S. Pedersen. SAXS investigation of a cubic to a sponge (L_3) phase transition in self-assembled lipid nanocarriers. *Phys. Chem. Chem. Phys.*, 13(8):3073–3081, 2011.

[637] S. S. Oh, A. Demetriadou, S. Wuestner, and Or. Hess. On the origin of chirality in nanoplasmonic gyroid metamaterials. *Adv. Mater.*, 25(4):612–617, 2013.

[638] B. Winter, B. Butz, C. Dieker, G. E. Schröder-Turk, K. Mecke, and E. Spiecker. Coexistence of both gyroid chiralities in individual butterfly wing scales of Callophrys rubi. *Proc. Natl. Acad. Sci. USA*, 112(42):12911–12916, 2015.

[639] T. H. Epps, E. W. Cochran, T. S. Bailey, R. S. Waletzko, C. M. Hardy, and F. S. Bates. Ordered network phases in linear poly (isoprene-b-styrene-b-ethylene oxide) triblock copolymers. *Macromolecules*, 37(22):8325–8341, 2004.

[640] J. J. K. Kirkensgaard, M. E. Evans, L. De Campo, and S. T. Hyde. Hierarchical self-assembly of a striped gyroid formed by threaded chiral mesoscale networks. *Proc. Natl. Acad. Sci. USA*, 111(4):1271–1276, 2014.

[641] W. Zhao, T. P. Russell, and G. M. Grason. Chirality in block copolymer melts: mesoscopic helicity from intersegment twist. *Phys. Rev. Lett.*, 110(5):058301, 2013.

[642] C. Dressel, F. Liu, M. Prehm, X. Zeng, G. Ungar, and C. Tschierske. Dynamic mirror-symmetry breaking in bicontinuous cubic phases. *Angew. Chem. Int. Ed.*, 53(48):13115–13120, 2014.

[643] C. Dressel, T. Reppe, M. Prehm, M. Brautzsch, and C. Tschierske. Chiral self-sorting and amplification in isotropic liquids of achiral molecules. *Nat. Chem.*, 6(11):971, 2014.

[644] C. Tschierske and G. Ungar. Mirror symmetry breaking by chirality synchronisation in liquids and liquid crystals of achiral molecules. *ChemPhysChem*, 17(1):9–26, 2016.

[645] C. Scholz, M. Engel, and T. Pöschel. Rotating robots move collectively and self-organize. *Nat. Commun.*, 9(1):931, 2018.

[646] U. Erdmann, W. Ebeling, L. Schimansky-Geier, and F. Schweitzer. Brownian particles far from equilibrium. *Euro. Phys. J. B*, 15(1):105–113, 2000.

[647] F. Zamponi, F. Bonetto, L. F. Cugliandolo, and J. Kurchan. A fluctuation theorem for non-equilibrium relaxational systems driven by external forces. *J. Stat. Mech.*, 2005(09):P09013, 2005.

[648] C. Micheletti, G. Bussi, and A. Laio. Optimal langevin modeling of out-of-equilibrium molecular dynamics simulations. *J. Chem. Phys.*, 129(7):074105, 2008.

[649] I. S. Aranson. Collective behavior in out-of-equilibrium colloidal suspensions. *C. R. Phys.*, 14(6):518–527, 2013.

[650] D. Saintillan and M. J. Shelley. Instabilities, pattern formation, and mixing in active suspensions. *Phys. Fluids*, 20(12):123304, 2008.

[651] N. H. P. Nguyen, D. Klotsa, M. Engel, and S. C. Glotzer. Emergent collective phenomena in a mixture of hard shapes through active rotation. *Phys. Rev. Lett.*, 112(7):075701, 2014.

[652] H. H. Wensink, J. Dunkel, S. Heidenreich, K. Drescher, R. E. Goldstein, H. Löwen, and J. M. Yeomans. Meso-scale turbulence in living fluids. *Proc. Natl. Acad. Sci. USA*, 109(36):14308–14313, 2012.

[653] L Giomi. Geometry and topology of turbulence in active nematics. *Phys. Rev. X*, 5(3):031003, 2015.

[654] A. Czirók and T. Vicsek. Collective behavior of interacting self-propelled particles. *Physica A*, 281(1-4):17–29, 2000.

[655] H. H. Wensink and H. Löwen. Emergent states in dense systems of active rods: from swarming to turbulence. *J. Phys. Condens. Matter*, 24(46):464130, 2012.

[656] J. Tailleur and M. E. Cates. Statistical mechanics of interacting run-and-tumble bacteria. *Phys. Rev. Lett.*, 100(21):218103, 2008.

[657] J. Bialké, T. Speck, and H. Löwen. Active colloidal suspensions: Clustering and phase behavior. *J. Non-Cryst. Solids*, 407:367–375, 2015.

[658] J. Dunkel, S. Heidenreich, K. Drescher, H. H. Wensink, M. Bär, and R. E. Goldstein. Fluid dynamics of bacterial turbulence. *Phys. Rev. Lett.*, 110(22):228102, 2013.

[659] N. V. Brilliantov, F. Spahn, J.-M. Hertzsch, and T. Pöschel. Model for collisions in granular gases. *Phys. Rev. E*, 53(5):5382, 1996.

[660] H. Pourtavakoli, E. J. R. Parteli, and T Pöschel. Granular dampers: does particle shape matter? *New J. Phys.*, 18(7):073049, 2016.

[661] K. Yeo, E. Lushi, and P. M. Vlahovska. Collective dynamics in a binary mixture of hydrodynamically coupled microrotors. *Phys. Rev. Lett.*, 114(18):188301, 2015.

[662] E. Altshuler, J. M. Pastor, A. Garcimartín, I. Zuriguel, and D. Maza. Vibrot, a simple device for the conversion of vibration into rotation mediated by friction: preliminary evaluation. *PLoS One*, 8(8):e67838, 2013.

[663] L. Giomi, N. Hawley-Weld, and L. Mahadevan. Swarming, swirling and stasis in sequestered bristle-bots. *Proc. R. Soc. A*, 469(2151):20120637, 2013.

[664] M. Rubenstein, A. Cornejo, and R. Nagpal. Programmable self-assembly in a thousand-robot swarm. *Science*, 345(6198):795–799, 2014.

[665] L. Bobadilla, K. Gossman, and S. M. LaValle. Manipulating ergodic bodies through gentle guidance. In *Robot Motion and Control 2011*, pages 273–282. Springer, 2012.

[666] J.-C. Tsai, F. Ye, J. Rodriguez, J. P. Gollub, and T. C. Lubensky. A chiral granular gas. *Phys. Rev. Lett.*, 94(21):214301, 2005.

[667] J. Deseigne, O. Dauchot, and H. Chaté. Collective motion of vibrated polar disks. *Phys. Rev. Lett.*, 105(9):098001, 2010.

[668] J. Deseigne, S. Léonard, O. Dauchot, and H. Chaté. Vibrated polar disks: spontaneous motion, binary collisions, and collective dynamics. *Soft Matter*, 8(20):5629–5639, 2012.

[669] C. Scholz, S. D'Silva, and T. Pöschel. Ratcheting and tumbling motion of vibrots. *New J. Phys.*, 18(12):123001, 2016.

[670] N. Koumakis, A. Gnoli, C. Maggi, A. Puglisi, and R. Di Leonardo. Mechanism of self-propulsion in 3D-printed active granular particles. *New J. Phys.*, 18(11):113046, 2016.

[671] C. Scholz, S. Jahanshahi, A. Ldov, and H. Löwen. Inertial delay of self-propelled particles. *Nat. Commun.*, 9(1):5156, 2018.

[672] J. Stenhammar, A. Tiribocchi, R. J. Allen, D. Marenduzzo, and M. E. Cates. Continuum theory of phase separation kinetics for active brownian particles. *Phys. Rev. Lett.*, 111(14):145702, 2013.

[673] U. Basu, S. N. Majumdar, A. Rosso, and G. Schehr. Active brownian motion in two dimensions. *Phys. Rev. E*, 98(6):062121, 2018.

[674] Y. Lanoiselée, G. Briand, O. Dauchot, and D. S. Grebenkov. Statistical analysis of random trajectories of vibrated disks: towards a macroscopic realization of brownian motion. *Phys. Rev. E*, 98(6):062112, 2018.

[675] Z. X. Yang, W. Zhong, C. T. Au, X. Du, H. A. Song, X. S. Qi, X. J. Ye, M. H. Xu, and Y. W. Du. Novel photoluminescence properties of magnetic Fe/ZnO composites: self-assembled ZnO nanospikes on Fe nanoparticles fabricated by hydrothermal method. *J. Phys. Chem. C*, 113(51):21269–21273, 2009.

[676] B. L. Sanchez-Gaytan and S.-J. Park. Spiky gold nanoshells. *Langmuir*, 26(24):19170–19174, 2010.

[677] I. W. Guo, I. C. Pekcevik, M. C. P. Wang, B. K. Pilapil, and B. D. Gates. Colloidal core–shell materials with 'spiky' surfaces assembled from gold nanorods. *Chem. Commun.*, 50(60):8157–8160, 2014.

[678] H.-J. Chen, C. Yang, T. Hang, G. Liu, J. Wu, D. Lin, A. Zhang, Y. Li, B. Yang, and X. Xie. Nanospikes-mediated anomalous dispersities of hydropobic micro-objects and their application for oil emulsion cleaning. *Sci. Rep.*, 8(1):12600, 2018.

Acknowledgements

In the four years journey of my PhD project, I quickly realised that great research makes or breaks depending on the people which you are surrounded by. I feel fortunate to have found a variety of colleagues, friends and fellow researchers who supported me in shaping the content of this thesis and turned my time as a PhD student into such an enjoyable and rewarding experience. Therefore, in the following, I would like to express my deepest gratitude to all those who helped me creating this thesis.

Having the advantage to perform a PhD at two different universities, I find myself in the lucky situation to thank 4(.5) inspiring supervisors. Without them, this project could not have been nearly as successful:

My biggest thanks are addressed to my supervisor at Murdoch, Prof Dr Gerd Schröder-Turk who took me under his wings four years ago to work on this PhD project. To be honest, it is quite challenging to keep this paragraph short, but I give it a try. Gerd sparked my excitement for soft matter physics with his competent advice, critical questions and his unfailing support. He always took his time for intriguing discussions and motivated me with his enthusiasm to think outside the box and tackle new ideas. Even during the ups and downs, which I faced in my project, he has been a constant mentor, encouraged me to participate at different conferences and introduced me to fascinating people. I also valued his critical eye on this manuscript, which elevated the quality of this thesis to a level I would not have thought of. Furthermore, Gerd not only gave me the opportunity to join him in Australia, but he and his family also tried everything possible (and succeeded) to transform Western Australia into something like a second home. Whether it was discussing science over a beer in a pub, inviting me to dinner, catching waves or exploring the beauty of WA together. And even though Gerd supports the wrong football team, I am glad to call him not only a mentor but also a friend.

I would also like to thank my supervisor at Erlangen, Dr Mathieu Marechal. Matthieu has been a big inspiration and a linchpin for the success of this project. Especially in the beginning of my PhD in Erlangen, but also later during my time in Australia (despite the unfavourable time difference), he gave me valuable insight into the physics of liquid crystal self-assembly, both computationally and theoretically. His door was always open for discussions, which often lead to new ideas and a deeper understanding of the pear-shaped particle system. I also greatly benefited from him sharing his computational skills and his knowledge about density functional theory.

Moreover, I want to gratefully acknowledge the support by Prof Dr Klaus Mecke. Having been the primary supervisor of my Bachelor's and Master's project, Klaus not only initiated my excitement for research but also continued to make me reflect on my scientific thinking during this project. Klaus' advice and insightful comments have been of incredible value and had a significant impact on the quality of my project. I also want to thank him as chair of the Institute for Theoretical Physics I. He both provided a welcoming and inspiring work environment and aided me to communicate my research, for example, by creating the opportunity to attend various conferences.

Special thanks go to Dr. Mark Lukas who added the truly mathematical point of view to my project. He was always open for questions and stood out as a critical proof-reader for my manuscripts and papers with special care for details.

Lastly, I want to give thanks to my unofficial supervisor Prof Dr Doug Cleaver. He launched the research on pear-shaped particle systems and also boosted this project right from the beginning. I was fortunate to visit him and his group in Sheffield within the very first days of my PhD and a couple of times afterwards. Doug was essential for me to settle into the problem and fueled my research in many discussions and emails. My visits to Sheffield have been highlights every single time, also from a collegial point of view. I am very grateful to him for inviting me to his home, pretty much on the very first day of my PhD, and for our countless discussions about the latest news in football. Well, surviving South Central and early morning cockerels together is a bonding life experience apparently.

In addition to my supervisors, there are lots of different other people to thank. So I hope I do not forget anybody:

Many cheers go to the people at MERI at Sheffield Hallam University and, in particular, Dr Laurence Ellison, my predecessor of studying pear gyroid phases and an important pillar to the success of my PhD. He thankfully provided me with parts of his former Molecular Dynamics code and, consequently, kickstarted my project. Talking to Laurence and discussing my latest achievements has been simultaneously helpful and of great pleasure. Moreover, I have to thank him and his wife Jenny for hosting my stays in Sheffield by welcoming me to their home and showing me around town; quite often with a couple of beers, takeaway Chinese and/or pub-quiz wins. I am also grateful to Dr Alireza Dastan, who helped me with my Monte Carlo simulations.

I would like to thank the whole group of Theorie 1 in Erlangen, a bunch of people who create a fantastic working atmosphere. I have to thank especially Dr Simon Weis for extending the fruit basket and creating our Set-Voronoi tool kit POMELO with me. I learned a lot from our joint programming sessions and enjoyed working on this great software tool. I have never conceptualised and written code with someone else, which made this a worthwhile and even more fun experience. Here, I also want to mention and thank Dr Fabian Schaller and Dr Sebastian Kapfer, who gave great advice during the creation of POMELO. I have to thank Margret Heinen-Krumreich and Ingrid Hofmann for their patient help with the extensive paperwork associated with my double degree arrangement. Thanks also to the admins at Theorie 1, first Matthias Hofmann and Markus Spanner, later Johannes Hielscher and Felix Winterhalter for keeping up the computer infrastructure and immediate help when it was necessary!

Many thanks go to my friends and colleagues at SEIT at Murdoch University, especially the staff and students at Maths & Stats with its chair Prof Dr Graeme Hocking, who all turned working on my research in Australia into an absolute joy. First I thank Tobias Hain for many discussions about my project and science in general, but also for his comments about mushy pears over a couple of beers in many of WA's bars. I also have to thank Azin Azadi. Without her, my time at Murdoch would have been not even half as fun. I am also grateful for my coffee companion and Murdoch office mate Novia Minaee, always causing good mood and being a great mental support.

Sincere gratitude also goes to Dr Ross Bowden, who greatly helped me to settle into Murdoch and WA with our intriguing conversation about science, cinema, sports and much more. Thanks to Prof Dr Nicola Armstrong and Kris Parker for providing and giving me access to Hypatia. Special thanks also to Kellie O'Toole and Rosie Price for keeping bureaucracy at a pleasant minimum at Murdoch.

I thank and specifically name the people who volunteered proof-reading and commented on this manuscript: Ross Bowden, Novia Minaee, Wilfried Schönhöfer, Johannes Hielscher, Mark Lukas, Doug Cleaver, Matthieu Marechal and Gerd Schröder-Turk. I also want to thank some people I have not mentioned yet but who contributed to this project with fruitful discussions, inspiring comments and thought-provoking impulses, including Prof Dr Ana-Sunčana Smith, Prof Dr Michael Schmiedeberg, Prof Dr Bruce Gardiner, Prof Dr Peter Harrowell, Prof Dr John Seddon, Prof Dr Goran Ungar, Prof Dr Greg Grason, Prof Dr Elisabetta Matsumoto, Prof Dr Lisa Manning, Prof Dr Stephen Hyde, Prof Dr Jacob Kirkensgaard, Dr Drew Parsons, Dr Bodo Wilts, Dr Myfanwy Evans, Dr Christian Scholz, Dr Michael Klatt, Dr Matthias Merkel and Benedikt Kolbe.

Furthermore, this PhD thesis would not have been feasible without the financial support of the following institutes:
I thank Universities Australia and the German Academic Exchange Service (DAAD) for travel funds through a collaboration funding scheme, specifically the grant "Absorption and confinement of complex fluids'. Further thanks go to the Australian Institute of Physics, Murdoch University, the Murdoch graduate office and the Friedrich-Alexander University for conference travel support. Moreover, I am grateful for the Cluster of Excellence "Engineering of Advanced Materials" (EAM) and the DFG through the ME1361/11-2 grant and through the research group "Geometry and Physics of Spatial Random Systems" (GPRSR) for funding. I thank the Pawsey supercomputing centre for a grant for computational time at one of their supercomputers. Last but not least, I thankfully acknowledge a Murdoch University postgraduate research scholarship.

Finally, I want to send my deepest gratitude to my family: My grandmother who probably would have also sent me cake to Australia! My mother, with whom I can share both the good and the bad times! My brother, who joins in every nonsense! And my father, to whom I dedicate this thesis! Without

the knowledge about their support and the assurance that I can always seek their advice, even when we are 13,600 km apart, this PhD would not have been possible.

The ambition to recreate highly complex and functional nanostructures found in living organisms marks one of the pillars of today's research in bio- and soft matter physics. Here, self-assembly has evolved into a prominent strategy in nanostructure formation and has proven to be a useful tool for many complex structures. However, it is still a challenge to design and realise particle properties such that they self-organise into a desired target configuration. One of the key design parameters is the shape of the constituent particles.

This thesis focuses in particular on the shape sensitivity of liquid crystal phases by addressing the entropically driven colloidal self-assembly of tapered ellipsoids, reminiscent of „pear-shaped" particles. Therefore, we analyse the formation of the gyroid and of the accompanying bilayer architecture, reported earlier in the so-called pear hard Gaussian overlap (PHGO) approximation, by applying various geometrical tools like Set-Voronoi tessellation and clustering algorithms. Using computational simulations, we also indicate a method to stabilise other bicontinuous structures like the diamond phase. Moreover, we investigate both computationally and theoretically (density functional theory) the influence of minor variations in shape on different pear-shaped particle systems, including the stability of the PHGO gyroid phase. We show that the formation of the gyroid is due to small non-additive properties of the PHGO potential. This phase does not form in pears with a „true" hard pear-shaped potential.

Overall our results allow for a better general understanding of necessity and sufficiency of particle shape in regards to colloidal self-assembly processes. Furthermore, the pear-shaped particle system sheds light on a unique collective mechanism to generate bicontinuous phases. It suggests a new alternative pathway which might help us to solve still unknown characteristics and properties of naturally occurring gyroid-like nano- and microstructures.

ISBN 978-3-96147-268-0

9 783961 472680

FAU UNIVERSITY PRESS 2019